

INFORMATION TO USERS

This manuscript has been reproduced from the microfilm master. UMI films the text directly from the original or copy submitted. Thus, some thesis and dissertation copies are in typewriter face, while others may be from any type of computer printer.

The quality of this reproduction is dependent upon the quality of the copy submitted. Broken or indistinct print, colored or poor quality illustrations and photographs, print bleedthrough, substandard margins, and improper alignment can adversely affect reproduction.

In the unlikely event that the author did not send UMI a complete manuscript and there are missing pages, these will be noted. Also, if unauthorized copyright material had to be removed, a note will indicate the deletion.

Oversize materials (e.g., maps, drawings, charts) are reproduced by sectioning the original, beginning at the upper left-hand corner and continuing from left to right in equal sections with small overlaps.

Photographs included in the original manuscript have been reproduced xerographically in this copy. Higher quality 6" x 9" black and white photographic prints are available for any photographs or illustrations appearing in this copy for an additional charge. Contact UMI directly to order.

ProQuest Information and Learning
300 North Zeeb Road, Ann Arbor, MI 48106-1346 USA
800-521-0600

UMI[®]

University of Alberta

**Conservation Equations for
Subcritical Flow in Open Channel Junctions**

by



Shazy Abdel Fattah Shabayek

A thesis submitted to the

Faculty of Graduate Studies and Research

In partial fulfilment of the requirements for the degree of

Doctor of Philosophy

in

Water Resources Engineering

Department of Civil and Environmental Engineering

Edmonton, Alberta

Spring 2002



**National Library
of Canada**

**Acquisitions and
Bibliographic Services**

**395 Wellington Street
Ottawa ON K1A 0N4
Canada**

**Bibliothèque nationale
du Canada**

**Acquisitions et
services bibliographiques**

**395, rue Wellington
Ottawa ON K1A 0N4
Canada**

Your file Votre référence

Our file Notre référence

The author has granted a non-exclusive licence allowing the National Library of Canada to reproduce, loan, distribute or sell copies of this thesis in microform, paper or electronic formats.

The author retains ownership of the copyright in this thesis. Neither the thesis nor substantial extracts from it may be printed or otherwise reproduced without the author's permission.

L'auteur a accordé une licence non exclusive permettant à la Bibliothèque nationale du Canada de reproduire, prêter, distribuer ou vendre des copies de cette thèse sous la forme de microfiche/film, de reproduction sur papier ou sur format électronique.

L'auteur conserve la propriété du droit d'auteur qui protège cette thèse. Ni la thèse ni des extraits substantiels de celle-ci ne doivent être imprimés ou autrement reproduits sans son autorisation.

0-612-68623-X

Canada

University of Alberta
Library Release Form

Name of Author: Shazy Shabayek
Title of Thesis: Conservation Equations for Subcritical Flow
in Open Channel Junctions
Degree: Doctor of Philosophy
Year this degree Granted: 2002

Permission is hereby granted to the University of Alberta library to reproduce single copies of this thesis and to lend or sell such copies for private, scholarly, or scientific research purposes only.

The author reserves all other publication and other rights in association with the copyright in this thesis, and except as herein before provided, neither the thesis nor any substantial portion thereof may be printed or otherwise reproduced in any material form whatever without the author's prior written permission.


.....*Shazy Shabayek*.....

110 RH, Michener Park
Edmonton, Alberta
Canada, T6H 4M4

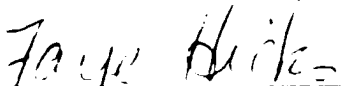
Date:*02 April 2002*.....

University of Alberta
Faculty of Graduate Studies and Research

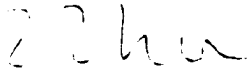
The undersigned certify that they have read, and recommend to the Faculty of Graduate Studies and Research for acceptance, a thesis entitled **“CONSERVATION EQUATIONS FOR SUBCRITICAL FLOW IN OPEN CHANNEL JUNCTIONS”** submitted by **Shazy Abd El Fattah Ibrahim Shabayek** in partial fulfillment of the requirements for the degree of **Doctor of Philosophy in Water Resources Engineering**.



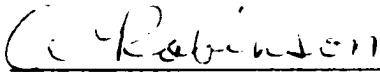
Dr. Peter Steffler
(Co-Supervisor)



Dr. Faye Hicks
(Co-Supervisor)



Dr. David Zhu



Dr. Aminah Robinson



Dr. Suzanne Kresta



Dr. Willi H. Hager
(External Examiner)

Date: March 26, 2002

بِسْمِ اللَّهِ الرَّحْمَنِ الرَّحِيمِ
أَوَلَمْ يَرَ الَّذِينَ كَفَرُوا أَنَّ السَّمَاوَاتِ
وَالْأَرْضَ كَانَتَا رَتْقًا فَفَتَقْنَاهُمَا وَجَعَلْنَا مِنَ الْمَاءِ
كُلَّ شَيْءٍ حَيٍّ أَفَلَا يُؤْمِنُونَ .

(سورة البقرة - آية ٢٤)

In the Name of Allah, the Most Gracious, the Most Merciful

*"Do not those who disbelieve see that the
heavens and the earth were joined together
then We (God Almighty) tore them asunder?
And We made of water every living thing
Will they not then believe?"*

The Quran, 21: 30

ABSTRACT

In this study, a one-dimensional theoretical model for subcritical flows in open channel junctions is developed. These junctions are encountered in open channel networks; typical examples include conveyance structures in urban water treatment plants, irrigation and drainage canals and natural river systems. In addition to the external boundary conditions for the whole network and the interior conservation equations (St. Venant equations) for each computational channel segment, a set of compatibility relationships or interior boundary conditions is also required for each junction.

Currently, most numerical models of open channel networks provide the required equations by applying mass and energy conservation principles at the junctions. Since energy losses and differences in velocity heads are difficult to evaluate, the interior boundary conditions may simply diminish to the equality of water surface elevations and the continuity of discharge. Thus, physical effects considered significant enough to be included in the channel reaches of these network models are neglected when handling the junctions. Further, equality of the water surface elevations may be unrealistic for dynamic unsteady flow applications such as ice jam release surges or dam break floods in tributary channels as well as abrupt gate closure in irrigation networks.

The purpose of this study is to provide a framework that leads to an improved set of internal boundary conditions, consistent with the level of approximation embodied in the St. Venant equations. Thus, it can be incorporated as an enhancement in the current open channel network models. The proposed model is based on applying the momentum

principle together with mass continuity through the junction. Two control volumes are considered: one for the main channel flow, and the other for the lateral channel flow. The control volumes are bounded by streamlines such that there are no lateral mass fluxes. Conservation of longitudinal momentum is applied to each control volume in the respective streamwise directions. An attempt to model all the interacting forces between the two control volumes and the separation zone shear forces for the combining and the dividing junctions is performed. The weight component in the direction of the slope and the boundary friction force are accounted for in the analysis.

Predictions based on the proposed approach are shown to compare favourably with existing experimental data. Comparisons with previous theories, and conventional junction modelling approaches showed that the proposed model predictions were either as good as the other theories or rather superior. The main advantage of the proposed model is that application of the momentum principle in the streamwise direction makes handling of the junctions dynamically consistent with that of the channel reaches in a network model. Including the boundary friction force in the model allows the model to be scaled up to real world applications. Eventually, with the addition of terms for storage of mass and momentum, the model can be extended to unsteady dynamic junction flow situations.

ACKNOWLEDGMENT

First and foremost I am thankful to Allah the Almighty for His continuous Grace and Mercy.

I would like to express my sincere gratitude to my supervisors Dr. Peter Steffler and Dr. Faye Hicks for their patience, continuous support and valuable advice throughout the course of this study. Their interest in the topic was inspiring and made this work a success. My special thanks are due to their time and effort in reviewing the thesis.

I wish to acknowledge Dr. Willi Hager, my external examiner, for taking time to review the thesis. His interest and insight on this topic proved most valuable.

I wish to extend my thanks to Dr. Suzanne M. Kresta, Dr. A. Robinson, and Dr. D. Z. Zhu for their effort in reading this thesis thoroughly and providing many helpful comments and suggestions.

This research was financially supported through scholarships from: the Natural Sciences and Engineering Research Council of Canada; the Province of Alberta; and the University of Alberta (Faculty of Graduate Studies). All are most gratefully acknowledged.

Special thanks are to my husband, Samir, to my children, Ahmed, Maha, and Rana, and to my mother in law, for their patience, support and encouragement during this work.

I wish to extend a warm thank you to my father, brothers and cousin, Eman, for their always being there.

Table of Contents

Chapter 1

Introduction	1
1.1 General.....	1
1.2 Organization of the Thesis.....	4
References.....	6

Chapter 2

Literature Review	7
2.1 Introduction.....	7
2.2 Combining Open Channel Junctions.....	7
2.2.1 Subcritical Combining Flow Studies.....	8
2.2.2 Flow Structure at Combining Open Channel Junctions.....	15
2.2.3 Energy Losses at Open Channel Junctions.....	17
2.2.4 Separation Zone Formation in Combining Junction Flows...	17
2.2.5 Unsteady Flow in Open Channel Junctions.....	18
2.3 Dividing Flow in Open Channel Junctions.....	18
2.3.1 Subcritical Dividing Junction Flow Studies.....	19
2.4 Numerical Modeling of Open Channel Networks.....	28
2.5 Summary and Comments.....	30
References.....	34

Chapter 3

Theoretical Model for Combining Flows.....	41
3.1 Introduction.....	41
3.2 Proposed Theoretical Approach.....	42
3.2.1 Hydrostatic Pressure Forces.....	44
3.2.2 Pressure Forces due to Convergence.....	44
3.2.3 Weight.....	49
3.2.4 Boundary Friction Forces.....	49
3.2.5 Interfacial Shear Force.....	50
3.2.6 Separation Zone Shear Force.....	54
3.2.7 Governing Equations.....	55
3.3 Results and Discussion.....	57
3.3.1 Calibration of the Interfacial Shear Coefficient, K^* , and the Separation Shear Coefficient K	57
3.3.2 The Final Model Results.....	59
3.4 Comparison with Previous Theories.....	62
3.5 Summary and Conclusions.....	65
References.....	67
APPENDIX	
Alternate Control Volume Configurations.....	68

Chapter 4

Theoretical Model for Subcritical Dividing Flows

4.1	Introduction.....	105
4.2	Proposed Theoretical Approach.....	106
4.2.1	Hydrostatic Pressure Forces.....	108
4.2.2	Pressure Force due to Divergence.....	108
4.2.3	Weight.....	110
4.2.4	Boundary Friction Forces.....	111
4.2.5	Lateral Channel Separation Zone Shear Force.....	111
4.2.6	Centrifugal Force.....	114
4.2.7	Main Channel Separation Zone Shear Force.....	117
4.2.8	Governing Equations.....	119
4.3	Results and Discussion.....	121
4.3.1	Calibration of the Separation Coefficients, K_{d1} and K_{d2} , and the Centrifugal Coefficient, C	122
4.3.2	The Final Model Results.....	124
4.4	Comparison with Previous Theories and Energy Approaches.....	125
4.5	Summary and Conclusions.....	129
	References.....	130

Chapter 5

Applications

5.1	Introduction.....	168
-----	-------------------	-----

5.2	Design Charts.....	168
5.3	Junction Formulation in an Open Channel Network Model.....	171
5.3.1	Setup.....	171
5.3.2	Results.....	175
5.4	Summary and Conclusions.....	180

Chapter 6

Conclusions and Recommendations.....	205
Recommendations for Future Research.....	209

List of Tables

<u>Table</u>	<u>Title</u>	<u>Page</u>
2.1	Experimental Details for Previous Combining Flow Studies.....	39
2.2	Experimental Details for Previous Dividing Flow Studies.....	39
3.1	Comparing the Interfacial Shear Coefficient, K^* , for the Two Interfacial Shear Velocity Models.....	69
3.2	Comparing the Interfacial Length Models Using the Data of Hsu et al. (1998).....	70
3.3	Calibrated and Empirical Values of K^* and K	71
4.1	Calibrated Coefficients and Least Square Error for the Different Centrifugal Formulations.....	132
4.1	Calibrated Coefficients and Least Square Error for the Different Centrifugal Formulations (<i>cont.</i>).....	133
4.2	Calibrated Coefficients and Least Square Error for the Different Main Channel Separation Formulations	134
4.2	Calibrated Coefficients and Least Square Error for the Different Main Channel Separation Formulations (<i>Cont.</i>).....	135
4.3	The Calibrated Coefficients for Previous Studies.....	136
5.1	The Lengths of the Control volumes for the Irrigation Network ($x=1$).....	182
5.2	The Lengths of the Control volumes for the River Cutoff ($x=1$).....	182
5.3	Discharge Ratios for the Irrigation System by Applying Momentum at the Junctions (No Backwater Effects).....	183
5.4	The Effect of Including the Combining and Dividing Coefficients for the Momentum Approach on the Discharge Ratio (No Backwater Effects).....	184
5.5	Comparing the Momentum Approach Results with the Conservation of Energy and the Equal Water Surface Elevation Approaches at the Junctions (with Backwater Effects).....	185

5.5	Comparing the Momentum Approach Results with the Conservation of Energy and the Equal Water Surface Elevation Approaches at the Junctions (with Backwater Effects) (<i>cont.</i>).....	186
5.6	Discharge Ratios for the Irrigation Network by Applying Equal Water Surface Elevation at the Junctions.....	187
5.7	Discharge Ratios for the Irrigation Network by Applying Equal Energy at the Junctions.....	188
5.8	Discharge Ratios for the River Cutoff by Applying Momentum at the Junctions (No Backwater Effects).....	189
5.9	The Effect of Including the Combining and Dividing Coefficients for the Momentum Approach on the Discharge Ratio (No Backwater Effects).....	190
5.10	Comparing the Momentum Approach Results with the Conservation of Energy and the Equal Water Surface Elevation Approaches at the Junctions (with Backwater Effects).....	191
5.11	Discharge Ratios for the River Cutoff by Applying Equal Water Surface Elevation at the Junctions.....	192
5.12	Discharge Ratios for the River Cutoff by Applying Equal Energy at the Junctions.....	193

List of Figures

<u>Figure</u>	<u>Title</u>	<u>Page</u>
2.1	Combining Junction Geometry and Notation.....	40
2.2	Dividing Junction Geometry and Notation.....	40
3.1	Combining Open Channel Junction with the Control Volumes and Notation.....	72
3.2	Curvilinear Coordinate System and the Pressure Force due to Convergence.....	73
3.3	Comparing the Different Theories for Pressure Force B ($\delta=30^\circ$).....	74
3.4	Comparing the Different Theories for Pressure Force B ($\delta=45^\circ$)	75
3.5	Comparing the Different Theories for Pressure Force B ($\delta=60^\circ$)	76
3.6	Comparing the Different Theories for Pressure Force B ($\delta=90^\circ$)	77
3.7	Comparing the Different Theories for Pressure Force B ($\delta=135^\circ$)	78
3.8(a-b)	Comparing the Different Theories for Pressure Force B (a) The Main Channel Depth Ratio η_1	79
	(b) The Lateral Channel Depth Ratio η_2	79
3.9	Including the Effects of Interfacial Shear and Friction ($\delta=30^\circ$)...	80
3.10	Including the Effects of Interfacial Shear and Friction ($\delta=45^\circ$)...	81
3.11	Including the Effects of Interfacial Shear and Friction ($\delta=60^\circ$)...	82
3.12	Including the Effects of Interfacial Shear and Friction ($\delta=90^\circ$)...	83
3.13	Including the Effects of Interfacial Shear and Friction ($\delta=135^\circ$)..	84
3.14	Comparing the Theories for Interfacial Shear Length, L_i (a) The Main Channel Depth Ratio η_1	85
	(b) The Lateral Channel Depth Ratio η_2	85

3.15(a-b)	(a) Variation of K^* with the Junction Angle.....	86
	(b) Variation of K with the Junction Angle.....	86
3.16(a-b)	The Final Model Results Comparison with Hsu et al. (1998).....	87
3.17(a-d)	The Final Model Results. Comparison with Webber and Greated (1966) $\delta=30^\circ$	88
3.18(a-d)	The Final Model Results. Comparison with Webber and Greated (1966) $\delta=60^\circ$	89
3.19(a-d)	The Final Model Results. Comparison with Webber and Greated (1966) $\delta=90^\circ$	90
3.20(a-c)	The Final Model Results. Comparison with Webber and Greated (1966) $\zeta=0.5$	91
3.21(a-c)	The Final Model Results. Comparison with Taylor (1944) $\delta=45^\circ$	92
3.22(a-c)	The Final Model Results. Comparison with Taylor (1944) $\delta=135^\circ$	93
3.23(a-c)	The Final Model Results. Comparison with Gurram (1994) $\delta=30^\circ$	94
3.24(a-c)	The Final Model Results. Comparison with Gurram (1994) $\delta=60^\circ$	95
3.25(a-b)	The Final Model Results. Comparison with Gurram (1994) $\delta=90^\circ$	96
3.26	Comparing the Different Theories ($\delta=30^\circ, K^*=0.26, K=0.09$)....	97
3.27	Comparing the Different Theories ($\delta=45^\circ, K^*=0.23, K=0.23$)....	98
3.28	Comparing the Different Theories ($\delta=60^\circ, K^*=0.21, K=0.37$)....	99
3.29	Comparing the Different Theories ($\delta=90^\circ, K^*=0.17, K=0.64$)....	100
3.30	Comparing the Different Theories ($\delta=135^\circ, K^*=0.1, K=1.06$)....	101
3.31	Comparison with the Theory of Hsu et al. (1998) (a) The Main Channel Depth Ratio η_1	102

	(b) The Lateral Channel Depth Ratio η_2	102
3.32	Combining Junction with Three Control Volumes Configuration.	103
3.33	Combining Junction with Four Control Volumes Configuration...	104
4.1	Dividing Open Channel Junction with the Control Volumes and Notation.....	137
4.2	Comparing the Different Formulations for the Divergence Pressure.....	138
4.3	Comparisons Between Taylor's (1944) Data and the Model Predictions Using Eqs. (4.8) and (4.9) for the Pressure and Eq. (4.17) for the Lateral Channel Separation Shear.....	139
4.4	Comparisons Between Taylor's (1944) Data and the Model Predictions Using Eqs. (4.6) and (4.7) for the Pressure and Eq. (4.17) for the Lateral Channel Separation Shear.....	140
4.5	Comparisons Between Taylor's (1944) Data and the Model Predictions Using Eqs. (4.10) and (4.11) for the Pressure and Eq. (4.17) for the Lateral Channel Separation Shear.....	141
4.6	Comparisons Between Taylor's (1944) Data and the Model Predictions Using Eqs. (4.8) and (4.9) for the Pressure and Eq. (4.18) for the Lateral Channel Separation Shear.....	142
4.7	Comparisons Between Taylor's (1944) Data and the Model Predictions Using Eqs. (4.6) and (4.7) for the Pressure and Eq. (4.18) for the Lateral Channel Separation Shear.....	143
4.8	Comparisons Between Taylor's (1944) Data and the Model Predictions Using Eqs. (4.10) and (4.11) for the Pressure and Eq. (4.18) for the Lateral Channel Separation Shear.....	144
4.9	The Model Predictions for the Main Channel Depth Ratio, η_1 , Using Eqs. (4.8) and (4.9) for the Pressure and Eq. (4.17) for the Lateral Channel Separation Shear	145
4.10	Junction Geometry for Two Lateral Channels' Take-off (Symmetrical Junction).....	146
4.11	Junction Geometry and Control Volumes Configuration for High Discharge Ratios.....	147

4.12 (a-c)	The Final Model Results. Comparison with Taylor's (1944) Data	148
4.13 (a-c)	The Final Model Results. Comparison with Law's (1965) Data...	149
4.14 (a-c)	The Final Model Results. Comparison with Grace's (1958) Data for $\delta=30^\circ$ and $\omega_2=1.0$	150
4.15 (a-c)	The Final Model Results. Comparison with Grace's (1958) Data for $\delta=60^\circ$ and $\omega_2=1.0$	151
4.16 (a-c)	The Final Model Results. Comparison with Grace's (1958) Data for $\delta=90^\circ$ and $\omega_2=1.0$	152
4.17 (a-c)	The Final Model Results. Comparison with Grace's (1958) Data for $\delta=120^\circ$ and $\omega_2=1.0$	153
4.18 (a-c)	The Final Model Results. Comparison with Grace's (1958) Data for $\delta=30^\circ$ and $\omega_2=0.4$	154
4.19(a-c)	Comparing the Proposed Theory with Law's (1965) Theory, Tran's (1989) Theory and the Energy Approach Using Taylor's (1944) Data $Fr_1=0.632$	155
4.20(a-c)	Comparing the Proposed Theory with Law's (1965) Theory, Tran's (1989) Theory and the Energy Approach Using Taylor's (1944) Data $Fr_1=0.447$	156
4.21(a-c)	Comparing the Proposed Theory with Law's (1965) Theory, Tran's (1989) Theory and the Energy Approach Using Taylor's (1944) Data $Fr_1=0.374$	157
4.22(a-c)	Comparing the Proposed Theory with Law's (1965) Theory, Tran's (1989) Theory and the Energy Approach Using Taylor's (1944) Data $Fr_1=0.2$	158
4.23(a-c)	Comparing the Proposed Theory with Law's (1965) Theory, Tran's (1989) Theory and the Energy Approach Using Law's (1965) Data $0.70 \leq Fr_1 < 0.83$	159
4.24(a-c)	Comparing the Proposed Theory with Law's (1965) Theory, Tran's (1989) Theory and the Energy Approach Using Law's (1965) Data $0.61 \leq Fr_1 < 0.69$	160
4.25(a-c)	Comparing the Proposed Theory with Law's (1965) Theory, Tran's (1989) Theory and the Energy Approach Using	

	Law's (1965) Data $0.52 \leq Fr_1 < 0.60$	161
4.26(a-c)	Comparing the Proposed Theory with Law's (1965) Theory, Tran's (1989) Theory and the Energy Approach Using Law's (1965) Data $0.40 \leq Fr_1 < 0.50$	162
4.27(a-c)	Comparing the Proposed Theory with Law's (1965) Theory, Tran's (1989) Theory and the Energy Approach Using Law's (1965) Data $0.30 \leq Fr_1 < 0.40$	163
4.28(a-c)	Comparing the Proposed Theory with Law's (1965) Theory, Tran's (1989) Theory and the Energy Approach Using Law's (1965) Data $0.22 \leq Fr_1 < 0.29$	164
4.29(a-c)	Comparing the Proposed Theory with Law's (1965) Theory, Tran's (1989) Theory and the Energy Approach Using Law's (1965) Data $0.15 \leq Fr_1 < 0.19$	165
4.30(a-c)	Comparing the Proposed Theory with Law's (1965) Theory, Tran's (1989) Theory and the Energy Approach Using Using Grace's (1944) Data $0.20 \leq Fr_1 < 0.28$	166
4.31(a-c)	Comparing the Proposed Theory with Law's (1965) Theory, Tran's (1989) Theory and the Energy Approach Using Using Grace's (1944) Data $0.11 \leq Fr_1 < 0.20$	167
5.1	Junction Geometry and Notation.....	194
5.2	Design Chart for an Asymmetrical Junction Geometry $\omega_1=1, \omega_2=1, C=12, K_{d2}=0.8, K_{d1}=0.1, C=0.1, a_1=8, n=0.6$	195
5.3	Design Chart for a Symmetrical Junction Geometry $\omega_1=1, \omega_2=1, C=12, K_{d2}=0.4, K_{d1}=0.4, C=0, a_1=8, n=0.6$	196
5.4	Design Chart for an Asymmetrical Junction Geometry $\omega_1=1, \omega_2=0.5, C=12, K_{d2}=0.8, K_{d1}=0.1, C=0.1, a_1=8, n=0.6$	197
5.5	Design Chart for an Asymmetrical Junction Geometry $\omega_1=1, \omega_2=1.5, C=12, K_{d2}=0.8, K_{d1}=0.1, C=0.1, a_1=8, n=0.6$	198
5.6	Design Chart for a Large Scale River Junction $\omega_1=1, \omega_2=1, C=12, K_{d2}=0.8, K_{d1}=0.1, C=0.1, a_1=100, n=0.6$	199
5.7	Design Chart for a Large Scale River Junction $\omega_1=1, \omega_2=1, C=20, K_{d2}=0.8, K_{d1}=0.1, C=0.1, a_1=100, n=0.6$	200

5.8	Irrigation Network.....	201
5.9	River Cutoff.....	202
5.10	The Variation of ξ with the Upstream Froude Number for the Dividing Junction in the Irrigation Network.....	203
5.11	The Variation of ξ with the Upstream Froude Number for the Dividing Junction in the River Cutoff.....	204

NOTATION*

Symbol	Description
<i>A</i>	average area of cross section (L^2);
<i>a</i>	aspect ratio;
<i>B</i>	pressure force due to change in control volume width (MLT^{-2});
<i>b</i>	width of channel (L);
<i>C</i>	centrifugal coefficient;
<i>C_f</i>	shear coefficient;
<i>C_c</i>	Chezy coefficient;
<i>c</i>	Law's (1965) contraction coefficient for the lateral channel separation zone;
<i>db</i>	incremental change in the width of the control volume (L);
<i>ds</i>	incremental distance in the streamwise direction [3,4] (L), length of the channel segment in the streamwise direction [5] (L);
<i>dy</i>	depth increment on the dividing stream line (L);
<i>dz</i>	difference in bed elevation for the control volume (L);
<i>Fr</i>	Froude number;
<i>F_b</i>	boundary friction force (MLT^{-2});
<i>F_s</i>	separation shear force (MLT^{-2});
<i>F_c</i>	centrifugal force (MLT^{-2});
<i>g</i>	gravitational acceleration (LT^{-2});
<i>h</i>	width of separation zone (L);
I	upstream junction point;
<i>K_c</i>	conveyance ratio;
<i>K'</i>	coefficient of the interfacial shear;
<i>K</i>	separation zone shear coefficient;
<i>k</i>	Taylor's (1944) kineticity coefficient;
<i>K_{d1}</i>	main channel separation zone coefficient;

* The number in the square brackets [] denotes relevant chapter number

K_{d2}	lateral channel separation zone coefficient;
L	length of the control volume (L);
L_i	length of the interface between the two control volumes (L);
L_s	length of the separation shear interface (L);
M	water mass in the lateral channel control volume (M);
m	downstream limit of the control volume in streamwise direction;
n	upstream limit of the control volume in streamwise direction [3,4], power of the discharge in the rating curve equation [5];
P	hydrostatic pressure force (MLT^{-2});
Q	discharge (LT^{-3});
r	radius of curvature (L);
Re	Reynolds number;
S	shear force on the interface between the two control volumes (MLT^{-2});
S_o	ground slope;
u_*	shear velocity (LT^{-1});
V	mean velocity (LT^{-1});
V_s	shear velocity along the separation zone interface (LT^{-1});
W	component of the weight of water in the control volume in the direction of the slope (MLT^{-2});
w	width of the control volume (L);
x	control volume length magnification factor;
y	water depth (L);
y_i	water depth along the interface between the two control volumes (L);
y_n	normal depth of flow (L);
y_s	water depth along the separation zone interface (L);
α	energy correction coefficient;
β	momentum correction coefficient;
δ	junction angle;
ϕ	Gurram's (1994) pressure coefficient;

γ	specific weight of water;
κ	Webber and Greated's (1966) empirical coefficient to extend their theory to different angles;
η	depth ratio (η_1) ratio of the main channel upstream depth to the main channel downstream depth and (η_2) ratio of the lateral channel depth to the main channel downstream depth;
ρ	density (ML^{-3});
τ_o	boundary shear stress ($\text{ML}^{-1}\text{T}^{-2}$);
ω	width ratio, (ω_1) ratio of the main channel upstream width to the main channel downstream width and (ω_2) ratio of the lateral channel width to the main channel downstream width;
ξ	discharge ratio, ratio of the lateral channel discharge to the total discharge.

Subscripts

1	main channel upstream section for section parameters (A, a, b, Fr, Q, y, V), main channel control volume for control volume parameters (L, dz, B, F_b, F_s);
2	lateral channel section for section parameters ($A, a, b, Fr, Q, y, V, K_c$), lateral channel control volume for control volume parameters (L, dz, B, F_b, F_s);
3	main channel downstream section;
l	left vertical side of rectangular channel section with respect to a viewer looking downstream;
r	right vertical side of rectangular channel section with respect to a viewer looking downstream.

Chapter 1

Introduction

1.1 General

Open channel networks are often encountered in water resources engineering. Typical examples include conveyance structures in urban water treatment plants, irrigation and drainage canals, and natural river systems. These networks are composed of channel segments and junctions where two or more channels intersect. The junctions are either combining streams (confluences) when two or more channels join to form a single channel or dividing flows (deltas) when one stream splits into two or more streams. The solution of the network problem involves determining the discharges and the water surface elevation at each cross section along the network. In addition to the external boundary conditions for the whole network and the interior conservation equations (St. Venant equations) for each computational channel segment, a set of compatibility relationships or interior boundary conditions is also required for each junction.

The difficulty of providing a set of interior equations to model junction flow is mainly due to the relatively large number of parameters involved and the complex flow features occurring at the junctions. The angles of intersection, the widths of the channels and the directions of flow can be combined in a multiplicity of ways so as to make a complete experimental investigation quite prohibitive. Further, the flow at the junctions is usually associated with regions of mean velocity gradients, depth-varying surfaces of flow division and separation, vortices, and recirculation zones.

In the case of a subcritical combining junction, considered in isolation, the boundary conditions specified are the inflow discharges and a downstream boundary condition that can be either a fixed depth or a rating curve. The problem is to predict the depth in each inflow channel just upstream of the junction. For subcritical dividing junctions, the inflow discharge is usually specified as the upstream boundary condition and either fixed depths or rating curves are specified for the downstream channels. The problem in this case is to determine the discharge split between the two outflow channels.

Currently, most numerical models of open channel networks provide the required equations by applying mass and energy conservation principles at the junctions (default method in HEC-RAS (US Army Corps of Engineers, 2001)). Since energy losses and differences in velocity heads are difficult to evaluate, the interior boundary conditions may simply diminish to the equality of water surface elevations and the conservation of mass, as in the One Dimensional Hydrodynamic Model (Environment Canada, 1988), Mike 11 model (Danish Hydraulic Institute) and Chaudhry (1993). Thus, physical effects such as gravity and bed friction, which are included in the channel reaches of these network models, are neglected when handling the junctions. These effects become relatively more important as horizontal scales increase relative to vertical scales. Further, equality of the water surface elevations may be unrealistic for dynamic unsteady flow applications such as ice jam release surges or dam break floods in tributary channels as well as abrupt gate closure in irrigation networks (Garcia Navarro (1992)).

Taylor (1944) presented the first study that addressed the problem of open channel junctions. He proposed a theoretical approach based on mass and momentum conservation for the combining junction problem. He performed experiments to verify his

theory. Taylor (1944) also presented a graphical solution for the dividing flow problem. Since then, a considerable amount of work on open channel junctions has been published. Most theories have relied on momentum. However, none of the existing momentum based theoretical approaches for solving the junction problem (e.g Taylor, 1944) is employed into the numerical models of open channel networks. This may be due to the inconsistency of these theories with the treatment of the channel segments in the network models and because of the assumptions associated with these theories that may be unrealistic for real world cases.

The purpose of this study is to provide a framework that leads to an improved set of internal boundary conditions, consistent with the level of approximation embodied in the St. Venant equations. Thus, it can be incorporated as an enhancement in the current open channel network models. A one-dimensional theoretical model for the case of steady subcritical open channel junction flows is introduced. The proposed model is based on applying the momentum conservation principle together with mass conservation through the junction. Two control volumes are considered: one for the main channel flow, and the other for the lateral channel flow. The control volumes are bounded by streamlines such that there are no lateral mass fluxes. Conservation of longitudinal momentum is applied to each control volume in the respective streamwise directions. An attempt to model all the interacting forces between the two control volumes and the separation zone shear forces for the combining and the dividing junctions is performed. The weight component in the direction of the slope and the boundary friction force are accounted for in the analysis. Including the boundary friction force in the model and applying the momentum in the streamwise direction allows the model to be scaled up to

real world applications and makes the handling of the junctions consistent with that of the channel reaches. Eventually, with the addition of terms for storage of mass and momentum, the model can be extended to unsteady dynamic junction flow situations.

1.2 Organization of the Thesis

In this thesis the development of two theoretical models, handling combining and dividing junctions respectively, is presented. Each model is introduced in a separate chapter. The implementation of the two models into an open channel network is presented in another chapter. Following is a brief introduction to each chapter.

Chapter 2 presents a review of the previous theoretical, experimental and numerical investigations related to open channel junctions. The chapter is divided into four sections. The first section reviews all previous work done on combining junctions. The second section includes all previous studies on dividing junctions. The third section presents some numerical studies on open channel networks and the approaches for handling junctions in these models. The last section presents a critique for all these previous studies.

Chapter 3 presents the theory upon which the combining junction model is based. The attempts to model all of the forces involved are explained. The final form of the governing equations and the solution procedure is presented. Calibration of the associated coefficients and validation of the results are discussed. Comparisons between the proposed theory and the current treatment for junctions in open channel network models that apply conservation of energy, as well as previous momentum based theoretical approaches, are presented.

Chapter 4 presents the development of the theoretical model providing the interior boundary conditions for dividing junctions. Modeling the different forces accounted for in the analysis is included. The dependence of the coefficients, associated with these forces, on the flow parameters is discussed. The model validation through comparison with the experimental measurements from previous studies is included. Comparison with previous momentum theories and the advantages of the proposed approach over these theories are presented. Further, the comparisons between the model results and the currently used energy approaches that handle dividing junctions in numerical network models are illustrated.

Chapter 5 presents two applications for the theoretical models developed in Chapters 3 and 4. The first application illustrates the use of the dividing junction flow model to determine the discharge split through a design chart. In the second application, the implementation of the two junctions' models into an open channel network is presented. Two examples are given: an irrigation network system and a river cutoff. The significance of including the different coefficients associated with the proposed models is assessed. Applications comparing the proposed momentum approach with the energy approaches are presented.

Chapter 6 presents a general discussion of the main contributions of the theoretical models presented in Chapters 3 and 4. A brief summary of each model and suggestions for future research are given.

References

- Environment Canada, Water Modeling Section. (1988). "*One dimensional hydrodynamic model.*" Water Planning And Management Branch, Environment Canada
- Chaudhry, M. H. (1993). *Open-Channel Flow*. Prentice Hall, Englewood Cliffs, New Jersey.
- Danish Hydraulic Institute, Denmark <http://www.dhi.dk>.
- Garcia-Navarro, P. (1992). "Numerical simulation of unsteady flow at open channel junctions." *J. Hydr. Research*, IAHR, 30 (5), 595-609.
- Taylor, E. H. (1944). "Flow characteristics at rectangular open channel junctions." *Trans.*, ASCE, 109, 893-912.
- US Army Corps of Engineers, Institute for Water Resources. (2001). "*HEC-RAS River Analysis System, Hydraulic Reference Manual.*" Hydrologic Engineering Center Version 3.0, January 2001. <http://www.hec.usace.army.mil>.

Chapter 2

Literature Review

2.1 Introduction

This chapter includes four sections. Section 2.2 discusses combining open channel junction flows. Previous theoretical and experimental studies are presented. The problem of dividing open channel junction flows is explained in section 2.3. Previous theoretical attempts to solve this problem and experimental investigations are illustrated. Section 2.4 presents the combination of the combining and the dividing flow problems into open channel network models. Previous numerical approaches for solving a whole network of open channels and their treatment for the junctions are discussed. Section 2.5 presents a brief summary of the critical comments made in the literature review and have inspired the present work.

2.2 Combining Open Channel Junctions

The problem of combining open channel junction flows occurs when two or more streams combine to form a single channel. For subcritical flow situations, the outflow depth of a junction, considered in isolation, is set by the backwater effects of the downstream channel or possibly by a critical condition. The inflow discharges must be known. The problem is to predict the depth just upstream of the junction in each of the inflow channels. This problem has a direct application in river confluences, irrigation and drainage systems and urban water treatment plants.

2.2.1 Subcritical Combining Flow Studies

Taylor (1944), Webber and Greated (1966), Gurram (1994) and Hsu et al. (1998) proposed theoretical models to solve for the upstream depths for subcritical open channel junction flows. They also performed experiments to verify their theories. The experimental work in each of these studies was performed on horizontal rectangular channels of equal width and turbulent flows. A detailed description of the work done in these four studies will be presented in the following discussion.

Fig. 2.1 shows the geometric configuration of the junctions considered in these studies where the subscripts 1 and 3 refer to the main channel upstream and downstream sections, respectively, and the subscript 2 refers to the lateral channel upstream section. Table 2.1 shows the experimental details for these studies where: b , y , Q , ξ , δ , Re , and Fr are the width, depth, discharge, discharge ratio ($\xi=Q_2/Q_3$), junction angle, Reynolds number and Froude number, respectively. Where the specified data was not explicitly mentioned in the published materials, N/A was indicated in the corresponding table cell.

Taylor (1944) performed the first study on open channel junction flows. In his theoretical analysis, Taylor (1944) applied the momentum equation in the main channel direction together with overall mass conservation to the junction. He assumed that: (1) the flow was parallel to the channel walls immediately upstream and downstream of the junction; (2) the wall friction was negligible; and (3) the inflow depths in the main and the lateral channels were equal immediately upstream of the junction. Taylor (1944) also assumed that the depths of the main and the branch channels at their junction are the same and thus compensated for the lateral channel wall pressure component by the

longitudinal hydrostatic pressure component in the lateral channel. Taylor (1944) developed the following dimensionless equation:

$$k_2 = \frac{\xi^2 (\eta^2 - 1)}{4\eta^2 [2\xi - \xi^2 (1 + \cos \delta) + \eta - 1]} \quad (2.1)$$

where k_2 is a kineticity coefficient which is equal to the ratio of the velocity head to the depth in the lateral channel, ($k_2 = V_2^2 / 2gy_2$, where V_2 is the mean velocity in the lateral channel and g is the gravitational acceleration), and η is the ratio of the depth upstream of the junction to that in the downstream channel.

Taylor (1944) conducted his experiments in a small rectangular flume with a width of 101.6 mm and a maximum depth of 101.6 mm. Point gauges were used to measure the water surface elevations and calibrated diaphragm orifices were used to measure the flow rates. The water surface elevation was controlled by adjustable gates at the downstream ends. The experimental details are presented in Table 2.1.

Taylor (1944) presented his results in the form of plots of the depth ratio, η , versus the lateral channel kineticity coefficient, k_2 , for different discharge ratios, $\xi = Q_2 / Q_3$, and different angles of intersection, δ . Taylor (1944) found that his theory was in agreement with his experimental data for the 45° intersection. However, poor agreement was noted for the 135° junction. He attributed this to the distortion of the velocity distribution downstream of the junction and to the fact that the flow was not parallel to the channel walls (as assumed in the theory).

In his discussion on Taylor's (1944) paper, Palmer (1944) suggested approaching the problem of combining open channel flows from the standpoint of loss of energy rather than the change of momentum. He recommended splitting the problem into two

parts, the first pertaining to the losses occurring in the main channel due to turbulence and contraction and the second pertaining to the lateral channel losses due to turbulence and deflection. Palmer (1944) mentioned that the constants used in his method could be determined experimentally. Hickox (1944) pointed out that the compensation of the pressure component in the lateral channel by the longitudinal component is of doubtful validity since it assumes that the pressure on the wall of the lateral channel is equal to the hydrostatic pressure of still water at the same depth. Hickox (1944) mentioned that at the junction the flow might not be parallel to the wall but rather curved and thus, the pressure might not be hydrostatic. He suggested that the unknown component of the pressure in the lateral channel might be evaluated from experimental data. Hickox (1944) also recommended the measurement of the pressures on the walls of the lateral channel by means of piezometers. Stevens (1944) declared that Taylor's (1944) assumptions that the upstream depths were equal and that the depth along the wall of the branch channel remained constant were incorrect as

“the water never had a uniform velocity distribution.”

Webber and Greated (1966) re-examined Taylor's (1944) theoretical approach. They employed Taylor's (1944) assumptions and developed their equation in terms of the lateral channel Froude number, Fr_2 , instead of the kineticity coefficient, k_2 . Webber and Greated (1966) also employed conformal mapping to design a 90° junction with a curved wall profile where there were little or no energy losses.

In their experimental work, Webber and Greated (1966) extended Taylor's (1944) investigation to include three additional angles of intersection (30°, 60°, and 90°) and two

additional discharge ratios (as shown in Table 2.1). They measured the flow depths and the velocity distributions at two cross sections in the main channel, upstream and downstream of the junction, respectively. These sections were chosen to be beyond the surface disturbances created at the junction. Then, Webber and Greated (1966) adjusted their depth measurements to eliminate the frictional resistance effect. They calculated a 'correction depth' by using the Blasius formula. This correction depth was subtracted from their measured upstream depths and was added to those depths in the downstream. Webber and Greated (1966) followed Hickox's (1944) suggestion and measured the pressure distribution by drilling piezometer tapings along the sidewalls of the junction at different depths above the bed.

Webber and Greated (1966) presented their results as plots of the non-frictional depth ratio, η , against the downstream Froude number, Fr_3 , for the different discharge ratios, ξ , and the different junction angles, δ , and compared their theory with their experiments. They noted that their observed values for the depth ratio, η , for a given downstream Froude number, Fr_3 , were less than their theoretical values, and that the discrepancy increased with the increase in discharge ratio. Webber and Greated (1966) noted that the discrepancies were too great to be accounted for by experimental error and thus they checked the assumptions made while developing the theoretical expressions. They found out that the assumption of equal depths in the approach channels and that of uniform velocity distributions were reasonable. However, the assumption of compensating the pressure on the lateral channel sidewalls by the longitudinal hydrostatic pressure in the lateral channel was less satisfactory. They attributed the agreement between the theory and the experiments for the 45° junction in Taylor's (1944) study to

“the fact that the two assumptions of negligible boundary friction and uniform hydrostatic pressure along the lateral channel had the effect of cancelling each other out”.

Webber and Greated (1966) used their wall pressure measurements to modify their theory and added an empirical coefficient in terms of the discharge ratio and the junction angle. This served to bring the theoretical curves into better conformity with the experimental curves.

Gurram (1994) developed another theory to compute the backwater effects in subcritical combining junctions. His assumptions were similar to Taylor's (1944) except for the first assumption of parallel streamlines downstream of the junction and the assumption that the pressure force on the lateral channel walls is equal to the hydrostatic pressure in the lateral channel. Gurram's (1944) equation included a downstream momentum correction coefficient and a lateral channel wall pressure ratio that were determined empirically.

In his experimental work Gurram (1994) examined junctions with angles similar to those of Webber and Greated's (1966) but for different discharge ratios. He measured the flow depths along the main and lateral channel walls and centerlines. He also took measurements in the transverse direction for four cross sections within the junction. Three of these sections were in the main channel: upstream of the junction, downstream of the junction, and at the vena contracta (Fig 2.1). The fourth section was at the entrance of the lateral channel. Point velocities and local flow directions at half flow depths were

also measured at these sections. Gurram (1994) also determined the shape and dimensions of the separation zone, by introducing dye on the water surface.

Gurram (1994) first determined the ratio of the lateral channel wall force in the downstream direction to the lateral channel static force by fitting his equations with his experiments and found it to be independent of the discharge ratio, ξ , and the downstream Froude number, Fr_3 , but varied mainly with the junction angle. Then he presented his semi-empirical results as plots of the depth ratio, η , against the downstream Froude number, Fr_3 , for the different discharge ratios, ξ , and the different angles, δ . He compared his theory with Taylor's (1944) and Webber and Greated's (1966) experimental data. Gurram (1994) found that his theory agreed fairly with their data. Further, Gurram (1994) noted that his theory agreed with Taylor's data for the 135° case better than Taylor's (1944) own theory.

Hsu et al. (1998) applied overall mass, energy, and momentum conservation to the junction to compute the upstream to downstream depth ratio as well as the energy loss coefficient through the junction. They divided the junction into two control volumes, one in the main channel and the second in the lateral channel. The momentum equation was then applied to each of these control volumes in the main and the lateral channel longitudinal directions, respectively. Energy and momentum correction coefficients for the different sections were included in the equations. Hydrostatic pressure distributions, negligible friction forces, equal upstream depths and equal upstream momentum and energy correction coefficients were assumed. Hsu et al. (1998) developed a third-degree

polynomial for calculating the backwater effects as well as a function for computing the energy loss coefficient through the junction.

Hsu et al. (1998) also performed experiments in a 155 mm wide flume. The downstream Froude number, Fr_3 , was kept approximately constant (0.59-0.62). They examined three junction angles (as shown in Table 2.1) with discharge ratios ranging between 0.092 and 0.918. Measurements of the flow depths and velocities were taken at four transverse sections in the junction. Each section had 15 equally spaced vertical profiles. For each profile the two components of the velocity were recorded at 8 equidistant points. Upstream depth measurements in the lateral channel were recorded. Hsu et al. (1998) used their main and lateral channel depth measurements to check and validate their assumption that these depths were equal. Then, they presented their results as plots of the main channel depth ratio, η_1 , versus the discharge ratio for the different angles of intersection, δ , and the limited range of the downstream Froude numbers, Fr_3 tested. They compared their theory with their experiments and found that their depth ratio measurements were slightly lower than their predictions.

Gurram and Karki (2000) argued that during the theoretical derivation, Hsu et al. (1998) cancelled out the flow deviation angle at the junction. This resulted in the usual momentum equation applied for the whole junction in the main channel direction. Gurram and Karki (2000) proved that the third degree polynomial developed by Hsu et al (1998) was the same as Taylor's (1944) equation if the momentum and energy correction coefficients were taken to unity. They included a wall pressure coefficient in the lateral channel and re-derived the polynomial. Gurram and Karki (2000) compared their

polynomial with the experimental data of Hsu et al. (1998) and found that it was giving better agreement than the theory of Hsu et al. (1998).

2.2.2 Flow Structure at Combining Open Channel Junctions

At combining open channel junctions two shear layers are formed: the first at the separation zone formed just downstream of the lateral channel entrance and the second shear layer at the interface between the converging flows (Fig. 2.1.). Many studies were performed to reveal the flow structure at confluences. Fujita and Komura (1988) applied visualization and image processing techniques to visualize the flow patterns and to obtain the instantaneous surface velocity distributions. They also measured the secondary flows by a hot wire anemometer. They found out that each converging flow yielded a three-dimensional separation before the confluence and created strong helicoidal flows along the interface between them. Weerakoon et al. (1991) investigated the three-dimensional flow structure in a rectangular channel confluence by measuring the two components of velocity at different water levels. They noted the following flow features: 1) two secondary flow cells that rotated at opposite directions due to streamline curvature existed at the confluence; 2) free surface super-elevation towards the opposite bank of the re-circulation zone and over the upstream corner region of the confluence occurred; 3) the size of the re-circulation zone became smaller with the distance from the free surface due to entrainment by the secondary flow; 4) unsteady upward swirling flow around the re-circulation zone that transferred momentum from the main stream to the re-circulation zone; and 5) larger velocities appear near bed as a consequence of secondary flows.

Rhoads and Kenworthy (1995) collected longitudinal and cross stream velocity data at the asymmetrical confluence of the Kaskaskia River and the Copper slough in east central Illinois, USA. They found that a large bar is formed along the inner bank of the downstream channel. They demonstrated that the flow conditions during low flow events are strongly influenced by the momentum ratio of the two incoming streams. Rhoads and Kenworthy (1995) concluded that a single large helical cell was formed when the momentum ratio of the lateral channel to the main channel exceeded one, and weak surface convergent helical cells were formed on opposite sides of the mixing interface when the momentum ratio was less than one. Mosley (1976) and Best (1988) studied bed morphology and sediment transport at river channel confluences. They suggested that the salient morphological features at channel confluences are: avalanche faces at the mouth of each confluent channel, a deep central scour due to the downward flow of the helical cells, and a bar within the separation zone at the downstream junction corner. Mamedov (1990) performed a field study for the characteristics and extent of channel deformations. He also conducted laboratory experiments in which the discharges, the time averaged longitudinal velocities at sections before and after the confluence and the water surface elevations and bed elevations were measured. The length and width of the separation zone were determined as functions of the momentum ratio and the confluence angle. Biron et al. (1996) performed a study to compare the turbulent flow structure at concordant and discordant open channel confluences. Shumate and Webber (1998) presented detailed measurements of three-dimensional velocities, turbulence, and water surface mapping in the immediate area of the channel junction in a large rectangular flume. These studies (Biron et al. (1996) and Shumate and Webber (1998)) were focused

on the two and three dimensional characteristics of the flow in the junction. They were not employed for the verification of the present study, as there were only a limited number of runs that do not give the variation of the depth ratios with the discharge ratio.

2.2.3 Energy Losses at Open Channel Junctions

Energy losses occur at the junction of combining open channel flows due to turbulent mixing and boundary friction. Lin and Soong (1979) presented an analysis to evaluate the energy loss in the junction. They applied the integral energy equation on a large control volume enclosing the junction. Manning's n was evaluated first and then used to compute the boundary friction loss. The losses due to turbulent mixing were evaluated by subtracting the boundary friction losses from the total energy losses.

2.2.4 Separation Zone Formation in Combining Junction Flows

One of the features that develop at open channel junctions is the separation zone occurring in the downstream channel. The momentum of the lateral channel ensures that the flow detaches itself from the side-wall as it enters the main channel leaving a separation of low pressure and recirculating fluid. Best and Reid (1984) presented experimental data to characterize the separation zone. They related the non-dimensional length and maximum width of the separation zone to the discharge ratio for the four junction angles of 15° , 45° , 70° , and 90° . Hager (1987) presented a theoretical analysis to determine the maximum width of the separation zone. He compared his theory with Best and Reid's (1984) data and found it to be in good agreement except for junctions with angle 90° . Hager (1987) attributed this to the fact that at the lateral channel inlet section

the flow angle did not coincide with the junction angle and that this effect was more pronounced for higher junction angle. Hager (1987) modified his equation to include the deviation in the flow angle and this improved the results for the 90° junction.

2.2.5 Unsteady Flow in Open Channel Junctions

Garcia-Navarro (1992) presented a discussion of the unsteady flow problem associated with numerical simulation of bore propagation through junctions and a statement of its main features from the point of view of a one-dimensional modelling approach. She showed that the usual technique of assuming the equality of the water levels at the junction as the internal boundary condition in network modeling was valid only for a few simplified cases of low Froude numbers and was inadequate when dealing with bore propagation and reflections through junctions. She suggested that a suitable general set of compatibility conditions related to conservation laws of momentum and energy should be used.

2.3. Dividing Flow in Open Channel Junctions

For dividing junction flows, the stream splits into two branches and the problem is to determine the flow division. For the subcritical case the inflow discharge is provided and the two downstream depths are set by the backwater effects of the two branch channels. The problem is to predict the discharges in the downstream channels. According to Taylor (1944)

“the analysis of the dividing flow problem is considerably more difficult than that of the combining flow, for the following reason: In the

combining flow case it was possible to assume that the depths in the tributary channels were equal immediately above the junction. No analogous assumption is permissible in the case of the dividing flow.”

Such assumption may be “*almost identical to assuming the solution to the problem.*”

Taylor (1944), Grace and Priest (1958) and Law (1965) presented experimental data for dividing junction flows. All of these studies were performed on rectangular channels with smooth boundaries, horizontal bottom slopes, and relatively small aspect ratios ($b/y=1.5 - 3.5$). Subcritical inflow conditions and Reynolds numbers ranging between 2,000 and 20,000 were achieved. Fig. 2.2 shows the experimental configuration for Taylor’s (1944), Grace and Priest’s (1958), and Law’s (1965) studies. In a similar manner to the combining flows, subscripts 1 and 3 indicate the upstream and the downstream sections of the main channel, respectively. Subscript 2 represents the branch channel out flow section. Table 2.2 presents the experimental parameters in these studies where Q , b , α , a_1 , ω_2 and Fr are the discharge, width, angle of intersection, aspect ratio (b_1/y_1 where y is the depth), width ratio (b_2/b_3) and Froude number, respectively. The work done in these studies will be described in the following section.

2.3.1 Subcritical Dividing Junction Flow Studies

Taylor (1944) presented the first experimental study on dividing junction flows. He used the same experimental setup that was used to study the combining flow case, and reversed the directions of flow. The intersection angle was set to 90° . Taylor (1944) presented his dividing flow results as plots of the discharge ratio, $\xi=Q_2/Q_1$, versus the

depth ratio, y_1/y_2 , for four values of a main channel upstream kineticity coefficient, $k_1=(V_1)^2/2gy_1$, (where V is the mean velocity and g is the gravitational acceleration). Taylor (1944) also plotted the relation between the ratio of the downstream depths, y_3/y_2 , and the depth ratio y_1/y_2 . Thus, given the downstream conditions of both channels (depths or rating curves) and the inflow discharge, the discharge split of a 90° junction could be determined graphically.

Grace and Priest (1958) presented a detailed experimental study for dividing open channel flows. They examined four junction angles, ($\theta=30^\circ, 60^\circ, 90^\circ$, and 120°) as shown in Table 2.2 with different discharge ratios and different upstream Froude numbers. For the 30° junction three lateral channel width ratios, ω_2 , were investigated. The inflow was passed through a grid and screen to improve the velocity distribution. Gates at the downstream ends of the channels were used for the regulation of flow. The outflow discharge from the main channel was measured by a 60° V-notch weir and that through the lateral channel was determined by dividing the collected volume by the accumulation time. The flow depths in the different channels were measured by point gauges.

Grace and Priest (1958) divided the results into two parts, one in which standing waves were evident and the other in which the surface was free of any disturbances. They presented their results as plots of the discharge ratio, ξ , versus the two depth ratios, y_2/y_1 and y_2/y_3 for the four junction angles and the three width ratios that they examined.

In his thesis, Law (1965) presented a detailed experimental study on a 90° junction to explore the performance of a horizontal dividing channel. Vertical sliding

gates were installed at the exit end of the channels to regulate the discharge and the depth of water. The mean depth in each channel was taken at a station 86.4 cm (34 in). from the center of the junction. These stations were checked to be away from hydraulic jumps and back water effects. Point gauges were used to measure the depths at a 2.54 cm (1-inch) grid spacing in the junction. Chalk powder traces were photographed with a time-calibrated camera. The length of the streaks of the chalk powder left on the pictures was used to determine the relative surface flow velocities. The depth measurements and the determined relative surface velocities were then used to compute the Froude numbers covering the junction and drawing contours of these Froude numbers. Law (1965) divided the results into two parts: one pertaining to flow in the main channel; and the second to that in the lateral channel. He presented his results as plots of the mean Froude numbers for the different discharge ratios.

Law (1965) was the first to attempt a theoretical analysis for dividing junction flows. He divided a 90° junction of two channels of equal width into two control volumes; one for the main channel flow and the second for the lateral channel flow. He applied the momentum principle to each control volume in the respective main and lateral channel directions together with the overall mass conservation. He also applied conservation of energy while neglecting losses in his analysis for the main channel extension. During his analysis for the branch channel flow, Law (1965) assumed that the upstream and downstream depths in the main channel were equal and included an empirical contraction coefficient to account for the flow separation in the branch channel. Friction losses were neglected. Law (1965) developed equations relating the mean upstream Froude number with that in each of the main channel extension and the branch

channel in terms of the discharge ratio. Further, he extended his theory to account for different angles of intersection.

Law (1965) compared his theory with his experiments and found them in good agreement except at high upstream Froude numbers. He found out that, for the main channel extension, at high Froude numbers, both the momentum and the energy theories were inaccurate. The flow in the junction was so complicated that for the momentum theory his estimate of the pressure force that acted on the dividing streamline was no longer accurate and the assumption of negligible energy losses in the energy consideration was no longer valid. Law (1965) examined the performance of the flow in the branch and found out that, for the cases of high upstream Froude number, Fr_1 the flow becomes critical either in the junction or in the branch. He also noted that a region of supercritical flow was developed in the junction when Fr_1 was about 0.6 and that this region expanded to fill the entire junction area when Fr_1 was higher than 0.7. Also hydraulic jumps were initiated in the main channel extension. Law (1965) mentioned that

“in both channels, when the discharge ratios were very small, large recirculation regions extending across the respective channels were formed.”

Based on Law's (1965) work, Law and Reynolds' (1965) published a paper. In their discussion of that paper, Lakshmana and Sridharan (1966) pointed out that there was an appreciable curvature in the dividing streamline that should result in a centrifugal force across this streamline. Law and Reynolds' (1965) formulation did not include this force. Because of the difficulty involved in estimating the component of this force in the main channel direction, Lakshmana and Sridharan (1966) preferred the use of the energy

consideration for the main channel analysis. They also recommended that the application of the momentum equation to the branch be at sections well upstream of the junction in the main channel and downstream of the junction in the branch to avoid the non-uniform flow reaches. In that case, the formulation should include friction losses.

Lakshamana and Sridharan (1967) conducted detailed experiments for five angles of off-take ranging between 30° and 90° and four width ratios between the branch channel and the main channel, ω_2 , ranging between 0.25 and 1.00. The flow condition in the main channel was varied by means of a tailgate fitted at the downstream end of the main channel. In all their experiments, the flow in the branch was free overfall type. They noted that for subcritical flow in the main channel, Fr_3 gave a better correlation than Fr_1 . This could be expected as the control section for subcritical flow was in the downstream channel. For supercritical flow in the main channel Fr_1 was to be taken as a reference parameter.

For the 90° off-take, Lakshamana and Sridharan (1967) found out that the separation zone width increased while the strength of the eddy decreased with the Froude numbers in the main channel channel. They compared the different flow features in the acute angled off-takes with those in the right angled off-take. They noted that the width of the separation zone, and the intensity of the eddy for the acute angled junctions were much less than those for the 90° junction. However, the length of the separation zone was larger for the acute angled junctions. A wave was formed in the branch originating at the downstream corner for the 45° off-take. This wave was not so clear for the 90° off-take. Lakshamana and Sridharan (1967) observed that the separation zone was absent for the

30° and the 45° junctions for Fr_1 values approaching critical. The water surface profile measurements indicated a drop in the water surface along the inner wall (the side from which the branch takes off) of the main channel. They explained this as the effect of the resultant centrifugal force as the flow changed its direction near the junction. They concluded that there were three types of flow that occurred in the main channel: In the first case, the flow was entirely subcritical and the surface was free from any waves; in the second case, Fr_1 was of the order of 0.75 and the flow became almost critical just upstream the inlet, the water surface profile across the inlet was of a falling nature and a wave formed in the main channel near the downstream edge of the inlet; and in the third case, the flow was supercritical in the entire reach of the main channel near the junction. Lakshamana and Sridharan (1967) presented a solution for the subcritical case based on a dimensional analysis and their experimental investigations. In their dimensional analysis they omitted the parameter y_2/y_1 for free flow in the branch. They presented an empirical equation relating the discharge split with Fr_3 with the coefficients depending on the junction angle, δ , and the width ratio, ω_2 . They also discussed the effects of the variation in ω_2 and δ on the discharge distribution.

Lakshamana et al. (1968) performed an experimental study for a 90° rectangular off-take with the branch channel width half that of the main channel. The flow in all of the channels away from the vicinity of the junction was subcritical and the majority of the observations were obtained by controlling both the main and the lateral channel flows. Flow characteristics such as surface profiles, dividing streamlines at the bed and on the surface, and return flow in the branch channel, were discussed. They correlated the

discharge split with Froude numbers in the main and the branch channels. They found that the flow in the main channel became free overfall type for $Fr_1 > 0.7$ and an oblique wave formed across the main channel. Streamline observations showed that while the surface streamlines entered the branch with a smooth curvature, the bed streamlines turned sharply (almost at 90° and in some cases at an obtuse angle) into the branch. They correlated the separation zone parameters with Fr_2 and Fr_3 .

Kasthuri and Pundarikanthan (1987), in their discussion of Best and Reid's (1984) paper, presented their experimental investigation for the separation zone dimensions in a 90° branching channel. Their results showed that the length and the width of the separation zone decreased with the increase in discharge ratio. They pointed out that the difference in the relationships between the separation zone dimensions and discharge ratio for a confluence and those for a branching channel could be attributed to the fact that the former was an addition of flow that would increase the inertial forces while in the latter it was the opposite case.

Ramamurthy and Satish (1987) presented a theoretical model for the discharge split in short branch channels when the flow in the branch was not submerged due to downstream controls. The model was developed for various width ratios of the branch to the main channel using the principles of momentum, energy and continuity. They made use of the similarity of flow configuration between the division of flow in a branch channel and in a two dimensional lateral outlet fitted with a barrier in estimating the contraction coefficient of the jet entering the branch channel. The discharge split was

related to Fr_3 and the model was validated by experimental data from that study and from previous ones. They found out that their model was in good agreement with the data. However the application of the model should be limited to cases where $\omega_2 \leq 1.0$, $Fr_3 < 0.7$ and $Fr_2 > 0.35$.

Tran (1989) presented a solution for the general case of dividing flow through right-angled junctions for all branch flow conditions. He first computed the momentum transferred from the main channel to the lateral channel then substituted for it in the main channel momentum equation. He expressed a discharge ratio, Q_3/Q_1 , in terms of Fr_1 and the depth ratio y_1/y_3 . He used his data and those from previous studies to check his estimate for the momentum transfer from the main channel to the lateral channel and then to verify his model. The model was validated for cases where $0 < Fr_1 < 0.75$. The model didn't require measurements of the flow depth in the lateral channel and there was no restriction to the nature of the flow in the branch channel.

Neary and Odgaard (1993) presented an experimental investigation for the flow structure at a 90° open channel diversion. Two different bed materials were used in the course of the experiments to simulate rough and smooth bed conditions in the main channel. For each roughness condition three different ratios of the diversion flow velocity to the main channel velocity were used. They found out that the width of the separation zone along the upstream wall of the diversion was smallest at the bottom and increased towards the water surface. Conversely, the dividing stream plane was closer to the wall at the surface than at the bottom. These differences over the depth increased when the

velocity ratio and the main channel bed roughness increased. The study showed that the flow at open channel diversions was three dimensional and exhibited similar characteristics to river bend flow. Neary and Odgaard (1993) indicated that for a given velocity ratio, an effective bend geometry was set up in which the dividing stream plane represented the outer bank and the shear layer delineating the separation zone represented the inner bank. Increasing the velocity ratio changed the geometry of the dividing stream plane and the separation zone thus inducing an effective radius of curvature.

Shettar and Murthy (1996) used a two dimensional numerical model which employs the depth averaged forms of the continuity and the momentum equations along with the k- ϵ turbulence closure scheme to simulate the flow at open channel divisions. A limited number of experiments were conducted to obtain data concerning velocity distribution and surface profiles at right-angled junctions, for the verification of the numerical model predictions. The numerical predictions of the discharge distribution and computed flow features, like water surface profile, depth averaged velocity distribution in the main channel and size of the separation zone, matched fairly well with the experimental observations. However, there was a certain amount of error in the prediction of velocity distribution in the branch channel.

Barkdoll et al. (1998) studied 90° junction flows. They presented experimental data of free-surface velocity and water surface elevation in an open channel and compared these to corresponding symmetry plane values in duct flows. They found that there was a difference in the near surface velocity. This was attributed to secondary

currents that were present in open channel flow but not in the duct flow. It was also found that as the flow turned to enter the branch, centrifugal forces caused a super-elevation of the water surface in the open channel flow. These observations suggested that caution should be taken when assuming that flow in an open channel cross section was equivalent to that in one half of a closed conduit.

Neary et al. (1999) developed and validated a three-dimensional numerical model for predicting time averaged turbulent flows through lateral intakes with rough walls. Calculations were carried out for flows through rectangular closed conduits and open channel 90° junctions. Comparisons of the predicted mean velocity field with laboratory experiments showed that the model captured most experimental trends with reasonable accuracy. The model reproduced known flow patterns and provided novel insights about the complex hydraulics and sediment transport processes encountered in lateral intakes at a level of detail that was not attainable by laboratory studies.

2.4 Numerical Modeling of Open Channel Networks

Networks of channel systems are frequently encountered in natural river basins and in man-made urban drainage systems. The channel network system is composed of channel segments connected at junctions to form loops, and tree-like dendritic structures (Barkau et al. (1989)). Many investigators in the past have simulated the flow in the channel segments using various numerical schemes to approximate the governing mass and momentum conservation flow equations and the boundary conditions specified for each channel. Kao (1980), Jolliffe (1984), Barkau et al. (1989) and Chao and Molinas

(1993) used implicit finite difference schemes to approximate the Saint-Venant equations for gradually varied unsteady flow in open channels. Instead of modeling the flow in channel reaches using the dynamic form of the equations, some researchers employed a simplified form of the equations by neglecting the inertial forces and used the diffusive wave equations (Akan and Yen (1981) and Blandford and Ormsbee (1993)). Blandford and Ormsbee (1993) used an implicit finite element scheme to represent the continuity equation. Finite element modeling is attractive as it is easier to use variable grid spacing and or higher-order elements in regions of rapid flow parameter variations (Blandford and Ormsbee (1993)).

At the junctions additional equations or interior boundary conditions are required. Chao and Molinas (1993) provided the required equations by applying conservation of mass and energy at the junctions. In the HEC-RAS (US Army Corps of Engineers), steady flow water surface profile calculations across the junctions can be performed in two different methods. The default method is an energy based method that includes frictional losses and models other losses as expansion or contraction losses. This method does not account for the angle of any of the tributary flows. The second method is a momentum based method. The manual recommends that the user switch to the momentum method when the angle of the tributary significantly affects the water surface. A one dimensional formulation of the momentum equation in the main channel direction is employed. The angles of the tributaries with respect to the main channel are used to evaluate the forces associated with tributary flows. The components of the frictional and the gravitational forces between the upstream and the downstream sections are included. Akan and Yen (1981), Jolliffe (1984), Schulte and Chaudhry (1987), Barkau et al. (1989),

Blandford and Ormsbee (1993), and Nguyen and Kawano (1995) neglected energy losses and changes in velocity heads that the interior boundary conditions simply diminished to the compatibility of water surface elevations and the continuity of discharge. The One Dimensional Hydrodynamic Model (Environment Canada, 1988), and Mike 11 model (Danish Hydraulic Institute) are also examples of network models applying the equal water surface elevations approach at the junctions.

Different algorithms to solve the resulting set of equations for the whole network were developed in order to reduce the computer storage requirements and computing time. Kao (1980) suggested a computational node numbering system that minimized the matrix bandwidth of the resulting system of equations. Akan and Yen (1981) applied an iterative successive overlapping segment technique in routing floods through dendritic channel networks so that the large network problem could be solved as a series of smaller problems. Jolliffe (1984) used a sparse matrix technique to store and solve the resulting set of linear equations. Schulte and Chaudhry (1987) used the Newton-Raphson method and then transformed the Jacobian matrix to a banded matrix. Chao and Molinas (1993) introduced an efficient solution algorithm transforming the off-diagonal terms of the solution matrix to diagonal terms through recursion equations. Nguyen and Kawano (1995) presented a double sweep algorithm for the simultaneous solution of implicit dynamic wave flood routing in non-looped channel networks.

2.5 Summary and Comments

In this section a critique for the previous works presented in the literature review is summarized:

- 1) Most of the momentum based theories (Taylor (1944), Webber and Greated (1966), Gurram (1994), Hsu et al. (1998), etc.) have adopted the assumption of negligible frictional and weight forces. Real world channels would have larger aspect ratios than the laboratory models. Gravity and bed friction become relatively more important as horizontal scales increase relative to vertical scales.
- 2) Existing momentum based approaches rely on the assumption of equal upstream depths in case of combining junctions (Taylor (1944), Webber and Greated (1966), Gurram (1994), Hsu et al. (1998)). This may limit extending the theories to real world application with more dynamic events. This assumption is *“valid only for a few simplified cases of low Froude numbers and is inadequate when dealing with bore propagation and reflections through junctions”* Garcia-Navarro (1992).
- 3) Most theories faced the difficulty of determining the contribution of longitudinal momentum from the lateral channel due to the deviation of the flow at the lateral channel entrance. Some researchers had to account for this component empirically (Webber and Greated (1966) and Gurram (1994)).
- 4) Although many studies revealed that the flow structure at confluences induces shear forces on the dividing stream plane (Fujita and Komura (1988) and Weerakoon et al. (1991)), no attempt has been made to include these forces in the previous theories.
- 5) Taylor (1944) pointed out that the difficulty of the dividing flow problem was due to the following:

“In the combining flow case it was possible to assume that the depths in the tributary channels were equal immediately above the junction. No analogous assumption is permissible in the case of the dividing flow.”

Such assumption may be *“almost identical to assuming the solution to the problem”*.

However, Law's (1965) analysis for the lateral channel was based on the assumption that the main channel depth ratio was equal to 1.

6) Although the observations of Lakshamana and Sridharan (1967), Neary and Odgaard (1993), and Barkdoll et al. (1998) indicated the presence of centrifugal forces as the flow changed its direction near the dividing junction, none of the theories accounted for the effect of these forces.

7) Most of the dividing flow studies reflected on the complexity of the flow structure at these junctions (Taylor (1944), Law (1965), Lakshamana and Sridharan (1967), Lakshamana et al. (1968)). Neary and Odgaard (1999) pointed out that *“The complex flow phenomena at dividing junctions are usually associated with considerable energy losses”*.

However, numerical models developed to solve open channel junction (Akan and Yen (1981), Jolliffe (1984), Schulte and Chaudhry (1987), Barkau et al. (1989), Blandford and Ormsbee (1993), and Nguyen and Kawano (1995)) apply the common energy approach of equal water surface elevations at the junctions. This approach neglects differences in velocity heads as well as energy losses.

8) The equal water surface approach when assumed at a combining junction implies that there is an energy gain. For a combining junction, the downstream velocity is

larger than that at the upstream due to the flow constriction. Comparing the energy levels upstream and downstream of the junction, it can be seen that the downstream section has larger energy (water head + velocity head) than the upstream.

- 9) Most of the dividing flow theories (Ramamurthy and Satish (1987), Tran (1989), and Lakshamana and Sridharan (1967)) were developed with limitations on the downstream flow conditions in the lateral channel or the upstream Froude number.
- 10) The only model that employs a momentum approach for handling junctions, HEC-RAS (US Army Corps of Engineers), employs the geometrical angles of the tributaries to evaluate the frictional and gravitational forces. However, these angles would give incorrect results for some cases such as the case of a tributary channel combining with a main channel at a 90° angle. This is attributed to the problem of estimating the contribution of the lateral channel momentum and the flow deviation angle. Further, this model does not account for the pressure forces on the longitudinal boundaries of the control volume due to its convergence or divergence.

The present investigation aims at overcoming the difficulties faced in previous studies for subcritical flow cases and offering enhanced solutions to the junction problems. The study attempts to account for more of the physical effects associated with open channel junctions.

References

- Akan, A. O. and Yen, B. C. (1981). "Diffusion wave flood routing in channel networks." *J. Hydr. Div.*, ASCE, 107 (6), 719-732.
- Barkau, R. L., Johnson, M. C., and Jackson, M. G. (1989). "UNET: a model of unsteady flow through a full network of open channels." *Proceedings of the 1989 National Conference on Hydraulic Engineering*, ASCE, New York.
- Barkdoll, B. D., Hagen, B. L. and Odgaard, A. J. (1998). "Experimental comparison of dividing open-channel with duct flow in T-junction." *J. Hydr. Engrg.*, ASCE, 124 (1), 92-95.
- Best, J. L. and Reid, I. (1984). "Separation zone at open channel junctions." *J. Hydr. Engrg.*, ASCE, 110 (11), 1588-1594.
- Best, J. L. (1988). "Sediment transport and bed morphology at river channel confluences." *Sedimentology*, 35, 481-498.
- Biron, P., Roy, A.G. and Best, J. L. (1996). "Turbulent flow structure at concordant and discordant open-channel confluences." *Experiments in Fluids*, 21, 437-446.
- Blandford, G. E. and Ormsbee, L. E. (1993). "A diffusion wave finite element model for channel networks." *Journal of Hydrology*, 142, 99-120.
- Chao, G. W. and Molinas, A. (1993). "Simultaneous solution algorithm for channel network modeling." *Water Resources Research*, 29, (2), 321-328.
- Danish Hydraulic Institute, Denmark @www.dhi.dk.
- Environment Canada, Water Modeling Section. (1988). "*One dimensional hydrodynamic model.*" Water Planning And Management Branch, Environment Canada

- Fujita, I. and Komura, S. (1988). "Visualization of the flow at a confluence." *Proc. of Third Int. Symposium on Refined Flow Modeling and Turbulence Measurements*, Tokyo, 691-698.
- Garcia-Navarro, P. (1992). "Numerical simulation of unsteady flow at open channel junctions." *J. Hydr. Research*, IAHR, 30 (5), 595-609.
- Grace, J. L., and Priest, M. S. (1958). "Division of flow in open channel junctions." *Bulletin No. 31*, Engineering Experiment Station, Alabama Polytechnic Institute.
- Gurram, S. K. (1994). "A study of subcritical and transitional combining flow in open channel junctions." PhD thesis, Banaras Hindu Univ., Varanasi, India.
- Gurram, S. K. and Kari, K. S. (2000). Discussion of "Subcritical open channel junction flow." *J. Hydr. Engrg.*, ASCE, 126 (1), 87-89.
- Hager, Willi H. (1987). Discussion of "Separation zone at open channel junctions." By J. L. Best and I. Reid, *J. Hydr. Engrg.*, ASCE, 113 (4), 539-543.
- Hsu, Chung-Chieh, Lee, Wen-Jung, and Chang, Cheng-Hsi (1998). "Subcritical open channel junction flow." *J. Hydr. Engrg.*, ASCE, 124 (8), 847-855.
- Joliffe, I. B. (1984). "Computation of dynamic waves in channel networks." *J. Hydr. Engrg.*, ASCE, 110 (10), 1358-1370.
- Kao, Kwang-Hong (1980). "Improved implicit procedure for multichannel surge computations." *Canadian Journal of Civil Engineering*, 7, 502-512.
- Kasthuri, B. and Pundarikanthan, N. V. (1987). Discussion of "Separation zone at open channel junctions." By J. L. Best and I. Reid, *J. Hydr. Engrg.*, ASCE, 113 (4), 543-544.

- Lakshamana, N. S., and Sridharan, K. (1966). Discussion of "Dividing flow in an open channel." By S. W. Law and A.J. Reynolds, *J. Hydr. Div.*, ASCE, 94 (HY6), 237-239.
- Lakshamana, N. S., and Sridharan, K. (1967). "Division of flow in open channels." *Irrigation and Power*, Vol. 24, No. 4, 393-407.
- Lakshamana, N. S., and Sridharan, K, and Baig, M. Y. A. (1968). "Experimental study of the division of flow in an open channel." *Proc., Third Australasian Conference on Hydraulics and Fluid Mechanics*, Sydney, Australia, Nov., 139-142.
- Law, S. W. (1965). "Dividing flow in an open channel." Thesis presented to McGill University, Montreal, Quebec, Canada, in partial fulfillment of the requirements for the degree of Master of Engineering.
- Law, S. W. and Reynolds, A. J. (1965). "Dividing flow in an open channel junction." *J. Hydr. Div.*, ASCE, 92 (HY2), 207-231.
- Lin, J. D. and Soong, H. K. (1979). "Junction losses in open channel flows." *Water Resour. Res.*, 15, 414-418.
- Mamedov, A. S. (1990). "Hydraulic calculation of a confluence." *Hydrotechnical Construction*, HYCOAR, 23: 553-556.
- Mosley, M. P. (1976). "An experimental study of channel confluences." *Geology*, 84, 535-562.
- Neary, V. S. and Odgaard, A. J. (1993). "Three dimensional flow structure at open channel diversions." *J. Hydr. Engrg.*, ASCE, 119 (11), 1223-1230.
- Neary, V. S., Sotiropoulos, F. and Odgaard, A. J. (1999). "Three dimensional numerical model of lateral intake inflows." *J. Hydr. Engrg.*, ASCE, 125 (2), 126-140.

- Nguyen, Quang K. and Kawano, H. (1995). "Simultaneous solution for flood routing in channel networks." *J. Hydr. Engrg.*, ASCE, 121 (10), 744-750.
- Palmer, H. K., Hickox, J. C. and Stevens, C. J. (1944). Discussion of "Flow characteristics at rectangular open channel junctions." *Trans.*, ASCE, 109, 903-912.
- Ramamurthy, A. S. and Satish, M. G. (1987) "Division of flow in short open channel branches." *J. Hydr. Engrg.*, ASCE, 114 (4), 428-438.
- Rhoads, B. L. and Kenworthy, S. T. (1995). "Flow structure at an asymmetrical stream confluence." *Geomorphology*, 11, 273-293.
- Shettar, A. S. and Murthy, K. K. (1996). "A numerical study of division of flow in open channels." *J. Hydr. Res.*, Delft, The Netherlands, 34(5), 651-675.
- Shulte, A. M. and Chaudhry, M. H. (1987). "Gradually varied flow in open channel networks." *J. Hydr. Res.*, 25(3), 357-371.
- Shumate, E. D. and Webber, L. J. (1998). "Experimental discription of combining flows at an open channel junction." *ASCE, Water Resources Eng.*, Memphis, Tennessee.
- Taylor, E. H. (1944). "Flow characteristics at rectangular open channel junctions." *Trans.*, ASCE, 109, 893-902.
- Tran, D. M. (1989). "Some characteristics of lateral flows in open channels." Thesis presented in partial fulfillment for the degree of Doctor of Philosophy to Concordia University Montreal Quebec, Canada.
- US Army Corps of Engineers, Institute for Water Resources. (2001). "*HEC-RAS River Analysis System Hydraulic Reference Manual*." Hydrologic Engineering Center Version 3.0, January 2001. <http://www.hec.usace.army.mil>.

Webber, N. B., and Greated, C. A. (1966). "An investigation of flow behavior at the junction of rectangular channels." *Proc., Inst. Civ. Engrs.*, London, England, 34, 321-334.

Weerakoon, S.B., Kawahara, Y. and Tamai, N. (1991). "Three-dimensional flow structure in channel confluences of rectangular section." *Proc XXIV Congress. Int. Assoc. Hyd. Res.* A373-380.

Author Date	Taylor [1944]	Webber and Greated [1966]	Kumar [1994]	Hsu et al. [1998]
b_1, b_2, b_3 (mm)	101.6	127	500	155
y_3 (mm)	N/A	N/A	60 - 100	80 - 91
Q_3 (m ³ /s)	N/A	N/A	0.037 - 0.125	0.058 - 0.071
ξ	0.40, 0.60, 0.80	0.20, 0.40, 0.50, 0.60, 0.80	0.25, 0.50, 0.75	0.092 - 0.918
δ	45°, 135°	30°, 60°, 90°	30°, 60°, 90°	30°, 45°, 60°
Re_3	N/A	>3000	24,000 - 74,000	37,000 - 46,000
Fr_3	0.20 - 0.75	0.20 - 0.60	0.25, 0.50, 0.75, 1.00	0.59 - 0.62

TABLE 2.1. Experimental Details for Previous Combining Flow Studies

Author [Date]	δ	ω_2	Fr_1	a_1	b_1 & b_3 (mm)	Q_1 (m ³ /s)
Taylor [1944]	90°	1.00	0.200, 0.374, 0.447, 0.635	~2.5	101.6	N/A
Grace & Priest [1958]	30°	0.40, 1.00, 1.40	0.051 - 0.670	-1.5	127.0	0.0009 - 0.0056
	60°, 90°, 120°	1.00	0.110 - 0.617			
Law [1965]	90°	1.00	0.130 - 0.823	2.0	203.2	0.0023 - 0.0062

TABLE 2.2. Experimental Details for Previous Dividing Flow Studies

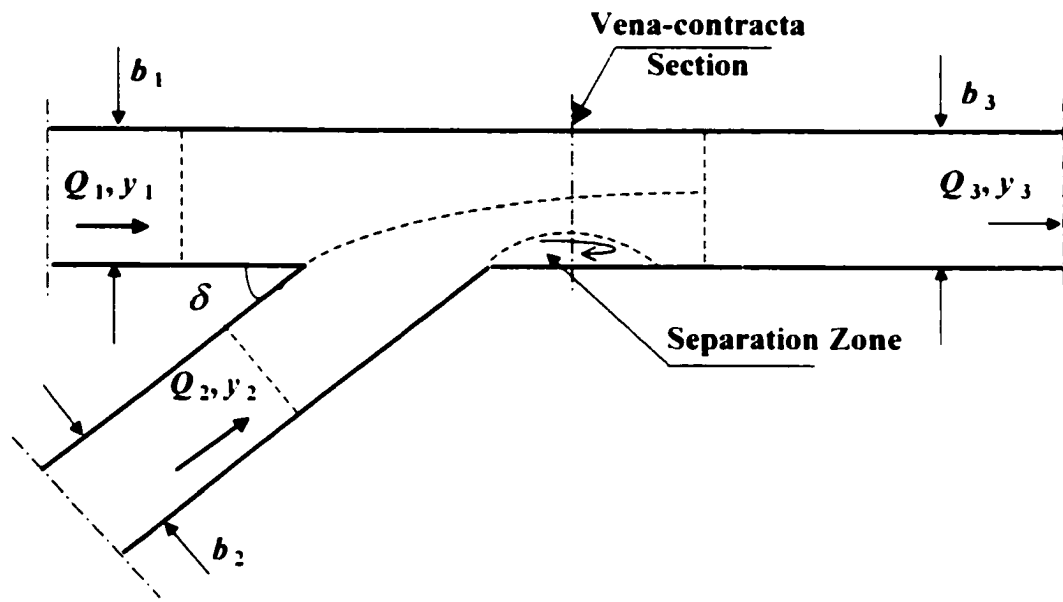


Fig. 2.1. Combining Junction Geometry and Notation

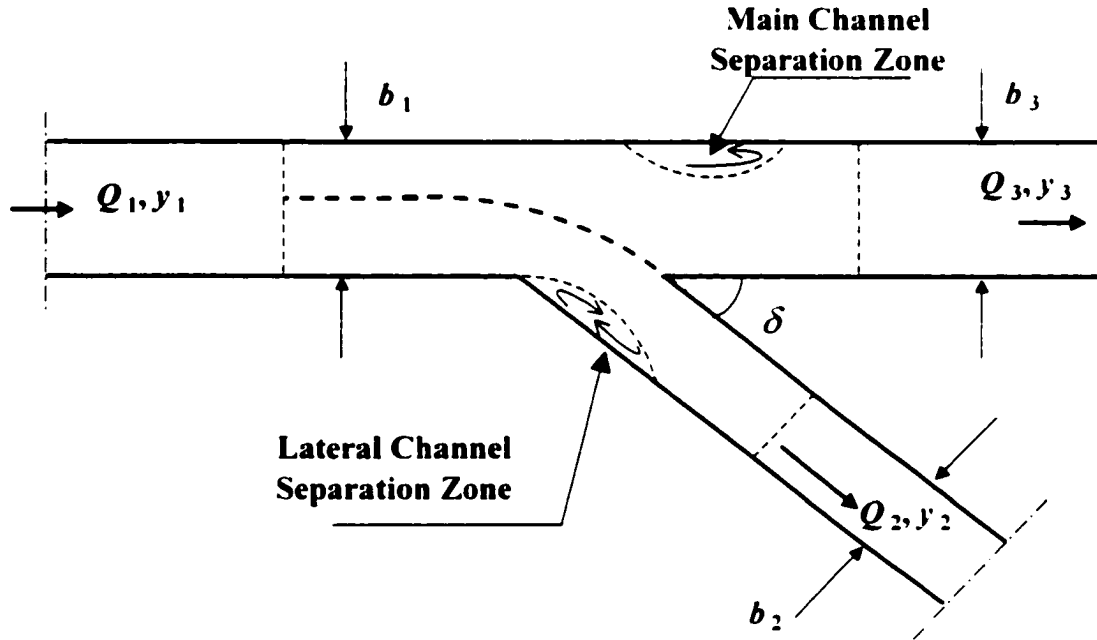


Fig. 2.2 Dividing Junction Geometry and Notation

Chapter 3

Theoretical Model for Combining Flows*

3.1 Introduction

Open channel networks are often encountered in water resources engineering. In addition to the external boundary conditions for the whole network and the interior conservation equations for each computational channel segment, a set of compatibility relationships or interior boundary conditions are also required for each junction. Currently, most numerical models of open channel networks provide the required equations by applying mass and energy conservation principles at the junctions (HEC-RAS (US Army Corps of Engineers)). Since energy losses and differences in velocity heads are difficult to evaluate, the interior boundary conditions may simply diminish to the equality of water surface elevations and the continuity of discharge, as in the One Dimensional Hydrodynamic Model (Environment Canada, 1988), Mike 11 model (Danish Hydraulic Institute) and Chaudhry (1993). Thus, physical effects considered significant enough to be included in the channel reaches of these network models are neglected when handling the junctions. Further, equality of the water surface elevations may be unrealistic for dynamic unsteady flow applications such as ice jam surges or dam break floods in tributary channels as well as abrupt gate closures in irrigation networks (Garcia Navarro (1992)). In this chapter, a one-dimensional theoretical model for the case of steady subcritical combining open channel junction flows is introduced. The purpose

* The main content of this chapter has been accepted in the Journal of Hydraulic Engineering of the American Society of Civil Engineers for publication.

of this model is to provide a framework that leads to an improved set of internal boundary conditions, consistent with the level of approximation embodied in the St. Venant equations. Thus, it can be incorporated as an enhancement in the current open channel network models.

3.2 Proposed Theoretical Approach

Fig. 3.1 shows the channel geometry to be considered in this analysis. The subscripts 1 and 3 refer to the main channel upstream and downstream sections, respectively, and the subscript 2 refers to the lateral channel upstream section. The six variables to be evaluated are the depths and discharges at the three sections enclosing the junction. In the case of subcritical flow, the boundary conditions are specified as the two inflow discharges, Q_1 and Q_2 , and a third downstream boundary condition that can be either a fixed depth or a rating curve. These boundary conditions define three of the six variables in the problem or two variables and one equation. Hence, three additional equations are required for closing the problem.

As illustrated in Fig. 3.1, two control volumes are considered: one for the main channel flow, C.V.₁, and the other for the lateral channel flow, C.V.₂. The control volumes are bounded by streamlines such that there are no lateral mass fluxes. The channels are all assumed to be of rectangular cross section. The streamline curvature is considered small and vertical accelerations negligible; hence the vertical pressure distribution is assumed hydrostatic. Uniform velocity distributions and parallel streamlines are also assumed at the inflow and outflow sections of the control volumes.

Applying overall mass conservation to the junction and conservation of streamwise momentum to each of the two control volumes provides the three necessary equations. Mass conservation gives:

$$Q_1 + Q_2 = Q_3 \quad (3.1)$$

Momentum conservation is applied to each control volume in the respective streamwise direction; however, direct curvilinear flow effects are neglected as the most important apparent forces due to curvature occur in the transverse direction. Transverse variations of velocity and depth due to curvature are assumed to be small compared to the section averaged values. This level of approximation is implicit when the usual one-dimensional momentum equation is applied to curved channel reaches. Then, conservation of momentum in the streamwise direction for the main channel control volume, C.V.₁, gives:

$$-\rho Q_1 V_1 + \rho Q_1 V_3 = P_1 - P_{31} + B_1 + W_1 - S - F_{b1} \quad (3.2)$$

and for the lateral channel control volume, C.V.₂:

$$-\rho Q_2 V_2 + \rho Q_2 V_3 = P_2 - P_{32} + B_2 + W_2 + S - F_{b2} - F_s \quad (3.3)$$

where: ρ is the water density, V is the mean velocity, P is the hydrostatic water pressure force acting on the control surface with the first subscript representing the section and the second subscript representing the control volume, B is the pressure force component due to the change in the control volume width, W is the component of the weight of water in the control volume in the down-slope direction, S is the shear force on the interface between the two control volumes, F_b is the friction force acting on the solid boundaries of the control volumes, and F_s is the shear force acting on the lateral channel control volume due to the separation zone forming downstream of the lateral channel entrance.

3.2.1 Hydrostatic Pressure Forces

The hydrostatic forces P_1 , P_2 , P_{31} , and P_{32} are due to the water pressure on the upstream and downstream boundaries of the two control volumes. These forces are given by:

$$P = \frac{1}{2} \gamma y^2 b \quad (3.4)$$

where: γ is the specific weight of water, y is the depth of water, and b is the width of the section under consideration.

3.2.2 Pressure Forces due to Convergence

The pressure force due to convergence acts on the longitudinal boundaries of each control volume. The momentum equation is applied to each control volume in the curvilinear streamwise direction. Fig. 3.2 shows a control volume for a meandering channel with the two longitudinal boundaries having different curvatures. The curvilinear coordinate, s , lies along the central streamline. All the forces acting on the control volume are resolved into two components one in the s direction (longitudinal) and the second perpendicular to the central streamline (transverse). Over a very small length, ds , the longitudinal component of the force acting on the left longitudinal boundary (for a viewer looking downstream) can be computed as the hydrostatic pressure force on the projected wall area normal to the s -direction. For a rectangular section this elemental component is equal to:

$$P_l = \frac{\gamma y^2}{2} \frac{\partial b_l}{\partial s} ds \quad (3.5)$$

where: y is the depth of water at the element ds . Integrating over the length of the control volume gives:

$$B_l = \int_n^m \frac{\gamma y^2}{2} \frac{\partial b_l}{\partial s} ds \quad (3.6)$$

where: n and m are the limits of the control volume in the s direction. Similarly the longitudinal component of the pressure force due to convergence acting on the right longitudinal boundary is given by:

$$B_r = \int_n^m \frac{\gamma y^2}{2} \frac{\partial b_r}{\partial s} ds \quad (3.7)$$

The total streamwise component of the pressure force due to convergence acting on the control volume will then be:

$$B = \int_n^m \frac{\gamma y^2}{2} \frac{\partial}{\partial s} (b_l + b_r) ds = \int_n^m \frac{\gamma y^2}{2} \frac{\partial b}{\partial s} ds \quad (3.8)$$

It can be concluded from equation (3.8) that the longitudinal component of this pressure force mainly depends on the net change in the total width and not on the individual curvatures of the longitudinal boundaries. This allows shifting the s coordinate from the central streamline to one of the control volume boundaries without affecting the magnitude of this component.

Fig.3.1 indicates that the width of the downstream section is divided between the two control volumes, C.V.₁ and C.V.₂, in terms of the discharge ratio. Therefore, the pressure forces, B_1 and B_2 are not equal because the amount of contraction experienced by the two control volumes may be different. Physically, the pressure on the interface between the two control volumes is equal and opposite. However the contribution to the

longitudinal momentum balance may differ due to the difference in the alignment of each control volume.

It should be noted that the super-elevation due to the curvature of the flow acts to increase the depth on the interface. It would also decrease the depth on the outer boundaries of each control volume. This might cause a change in this pressure force because of the depth parameter it includes. However, it may be reasonable to assume that, for each control volume, the increase in this force on the interface and the decrease at the outer boundary tend to counteract one another.

This pressure force can be approximated in terms of the average of the upstream and downstream depths of each control volume, and the difference between the corresponding widths, thus giving:

$$B_1 = \frac{1}{2} \gamma \left[\frac{y_1 + y_3}{2} \right]^2 (b_3 (1 - \xi) - b_1) \quad (3.9)$$

for C.V.₁ and for C.V.₂:

$$B_2 = \frac{1}{2} \gamma \left[\frac{y_2 + y_3}{2} \right]^2 (b_3 \xi - b_2) \quad (3.10)$$

This pressure force can be also approximated based on an average of the upstream and downstream pressures for each control volume, thus giving:

$$B_1 = \frac{1}{2} \left[\frac{\gamma y_1^2 + \gamma y_3^2}{2} \right] (b_3 (1 - \xi) - b_1) \quad (3.11)$$

for C.V.₁, and for C.V.₂:

$$B_2 = \frac{1}{2} \left[\frac{\gamma y_2^2 + \gamma y_3^2}{2} \right] (b_3 \xi - b_2) \quad (3.12)$$

Considering the curvature of the interface, it can be seen that this pressure force will attain a maximum value adjacent to the junction point I and will diminish in the downstream direction, as the streamlines become parallel. Thus, a third depth approximation based on the upstream depths of the control volumes will give:

$$B_1 = \frac{1}{2} \gamma y_1^2 (b_3 (1 - \xi) - b_1) \quad (3.13)$$

for C.V.₁, and for C.V.₂:

$$B_2 = \frac{1}{2} \gamma y_2^2 (b_3 \xi - b_2) \quad (3.14)$$

Since this pressure force is an internal force, it may be more reasonable to assume it to have the same depth approximation in both control volumes. Thus the downstream depth could be considered as the depth along the interface for both control volumes to give:

$$B_1 = \frac{1}{2} \gamma y_3^2 (b_3 (1 - \xi) - b_1) \quad (3.15)$$

for C.V.₁, and for C.V.₂:

$$B_2 = \frac{1}{2} \gamma y_3^2 (b_3 \xi - b_2) \quad (3.16)$$

Combining the third and fourth concepts for the depth term, the depth may be considered as the average of the upstream depths of the two control volumes and the difference in width for each of the two control volumes to give:

$$B_1 = \frac{1}{2} \gamma \left(\frac{y_1 + y_2}{2} \right)^2 (b_3 (1 - \xi) - b_1) \quad (3.17)$$

for C.V.₁, and for C.V.₂:

$$B_2 = \frac{1}{2} \gamma \left(\frac{y_1 + y_2}{2} \right)^2 (b_1 \xi - b_2) \quad (3.18)$$

All these approximations were tested with the available experimental data. Figs. 3.3 – 3.7 show the comparisons with Taylor's (1944), Webber and Greated's (1966) and Gurram's (1994) experimental data. In these figures the graphs' origin on the abscissa scale is shifted progressively to the right. Fig. 3.8(a-b) presents the comparisons with the data of Hsu et al. (1998). The measurements of Hsu et al. (1998) presented the variation of η_1 and η_2 with ξ at an approximately constant value of the downstream Froude number, Fr_3 . The reported range of Fr_3 of 0.59-0.62 mentioned in their study was computed including the energy correction coefficient for the main channel's downstream section. To be consistent with the present theoretical analysis, a set of downstream Froude numbers for the different runs of Hsu et al. (1998) was computed without including any correction coefficients. These values ranged between 0.52-0.54. Thus, an average value of $Fr_3=0.53$ was chosen to represent all of the flow cases of Hsu et al. (1998). The figures show that the first and the second approximations give similar results. The fourth approximation based on the downstream depth does not give good agreement with the experimental data. The third and fifth approximations alternately give good results. In addition, these two approximations give a net loss in the total energy between the upstream and the downstream sections of the junction. However, the fifth one proved to give the best results for the variations of the depth ratios with the discharge ratio (Fig. 3.8(a-b)) and is therefore used in the subsequent analysis.

3.2.3 Weight

W is the component of the weight of water in each control volume in the direction of the slope. These forces can be computed as:

$$W_1 = \gamma \left(\frac{A_1 + A_{31}}{2} \right) L_1 S_o \quad (3.19)$$

$$W_2 = \gamma \left(\frac{A_2 + A_{32}}{2} \right) L_2 S_o \quad (3.20)$$

where: A is the average cross sectional area of the control volume with the first subscript representing the section and the second subscript representing the control volume, and S_o is the longitudinal slope of the junction. L_1 and L_2 are the outer lengths of the two control volumes.

3.2.4 Boundary Friction Forces

F_{b1} and F_{b2} are the friction forces acting on the two control volumes due to the bed and the walls of the channels. These terms should be modeled in the same way as in channel control volumes and are computed as the average shear stress multiplied by the area of the solid boundary for each control volume. The nondimensional Chezy coefficient, C_* , was employed to compute the boundary shear stress where:

$$\tau_o = \rho u_*^2 \quad (3.21)$$

and

$$C_* = \frac{V}{u_*} \quad (3.22)$$

where: τ_o is the boundary shear stress, u_* is the shear velocity, and V is the cross sectionally averaged longitudinal velocity.

These boundary forces will have maximum values in the downstream section where the velocity is larger than that at the upstream. Hence, the wetted perimeters and the mean velocities at the downstream section were considered in the calculations. The outer lengths of the two control volumes were introduced into the equation as L_1 and L_2 , respectively giving:

$$F_{b1} = \rho \left(\frac{V_3}{C} \right)^2 \left(b_3 (1 - \xi) + y_3 \right) (L_1) \quad (3.23)$$

$$F_{b2} = \rho \left(\frac{V_3}{C} \right)^2 \left(b_3 \xi + y_3 \right) (L_2) \quad (3.24)$$

3.2.5 Interfacial Shear Force

S is the shear force on the interface. It acts on both control volumes, parallel to the interface, but in opposite directions in each. This force can be estimated as the average shear stress multiplied by the area of the interface giving:

$$S = C_f \frac{\rho (V_s)^2}{2} (y_i L_i) \quad (3.25)$$

where: C_f is the coefficient of friction, V_s is the shear velocity, y_i and L_i are the depth and the length of the dividing stream plane, respectively. The interfacial shear stress has a maximum value at point I (Fig. 3.1), where the difference in the control volumes' velocities is largest, and tends to decrease in the downstream direction. The depth of the interface is considered to be the average of the upstream depths similar to the pressure force due to convergence. Based on the linear lateral growth rate of plane compound shear layers (Rajaratnam, 1976) and the transverse distance to the nearest sidewall, the

length L_i may be approximated in terms of the downstream width b_3 . The shear velocity may be approximated as the difference between the incoming flows' velocities and this shear force can be written in the form:

$$S = C_f \frac{\rho (V_1 - V_2)^2}{2} \left(\frac{y_1 + y_2}{2} \right) b_3 \quad (3.26)$$

where: V_1 and V_2 are the cross sectionally averaged longitudinal velocities in the main and the lateral channels, respectively.

This form for the shear force gives a positive value for the force when V_1 is larger than V_2 , that is, when the shear stress is accelerating the flow in C.V.₂ and decelerating the flow in C.V.₁. For the force to change direction when V_1 becomes smaller than V_2 , an absolute value for the effective velocity is introduced and all the approximations and constants are combined into a single parameter, K^* , to give:

$$S = K^* \rho (V_1 - V_2) |V_1 - V_2| \left(\frac{y_1 + y_2}{2} \right) b_3 \quad (3.27)$$

The interfacial shear term should represent the momentum transfer between the two control volumes as well as the turbulence created on the interface. For the cases where $V_1 \approx V_2$ the interfacial shear term tends to zero. However, for these cases, there is turbulence created on the interface in the vertical direction and is transferred to the lateral direction for isotropy. This turbulence may be considered by including an average velocity in the shear velocity approximation to give the interfacial shear force in the form:

$$S = C_f \frac{\rho (V_1 - V_2) \left[\frac{V_1 + V_2}{2} \right]}{2} \left(\frac{y_1 + y_2}{2} \right) b_3 \quad (3.28)$$

Including the interfacial shear parameter K^* gives:

$$S = K^* \rho (V_1 - V_2) [V_1 + V_2] (y_1 + y_2) b_3 \quad (3.29)$$

The two interfacial shear models in equations (3.27) and (3.29) were tested with the available experimental data. Taylor's (1944), Webber and Greated's (1966), and Gurram's (1994) experimental data presented the variation of η_1 with Fr_3 at specific values of ξ . The value of K^* was calibrated for each set of experiments where the angle of intersection and the discharge ratio were held constant. The calibration for each data set was based on a least square error analysis between the measured and the predicted depth ratio, η_1 . Table 3.1 presents the calibrated values of K^* for each junction angle and each corresponding discharge ratio for each velocity model. These calibrated K^* values were then employed to compute the depth ratios η_1 for each flow case in the previous studies. Figs. 3.9-3.13 present the computed depth ratio, η_1 , for the different discharge ratios and the different junction angles. The figures also include the corresponding experimental data for each flow case and show the effect of including the interfacial shear term on the model equations' results. In these figures the graphs' origin on the abscissa scale is shifted progressively to the right. Including this term in the equations improves the model predictions to better agree with the experimental data. The figures indicate that the calibrated K^* is independent of the downstream Froude number. Both interfacial shear velocity models, equations (3.27) and (3.29), give the same predictions for the depth ratio. The difference between the two models is in the calibrated K^* values (Table 3.1). The table shows that the variation of K^* is mainly dependent on the junction angle and the discharge ratio. However, equation (3.29) gives less variation in K^* with the discharge

ratio. Consequently, the velocity model in equation (3.29) is chosen for the subsequent analysis.

Considering that the K^* was found to be independent of the downstream Froude number, further analysis was done to obtain K^* values that were only dependent on the junction geometry (δ) and not on the flow conditions (Fr_3 or ξ). Two extra models for the length of the interface, L_i , were tested. One of these models was based on the geometric mean of the downstream widths of the two control volumes and that gave:

$$S = K^* \rho (V_1 - V_2) [V_1 + V_2] (y_1 + y_2) \sqrt{(b_3 \xi) * b_3 (1 - \xi)} \quad (3.30)$$

and the other model was based on the harmonic mean of the downstream widths and that gave:

$$S = K^* \rho (V_1^2 - V_2^2) (y_1 + y_2) [2b_3 \xi (1 - \xi)] \quad (3.31)$$

A comparison between the three models for the length of the interface, L_i , was performed. The experimental data of Hsu et al. (1998) were employed in this comparison as they presented the variation of the depth ratios with the discharge ratio. Table 3.2 presents the calibrated values of K^* for each experimental run where the discharge ratio and the angle were held constant. The measured main channel depth ratio for each run was used for the calibration. The table also presents the average, the standard deviation, and the variance of the calibrated K^* values for each angle and for each length model as well as the overall values of the average, standard deviation, and variance for each of the three models. The values of the variance indicate that the third model, based on the harmonic mean of the downstream widths, gives the least variation with both the discharge ratio and the junction angle. The overall average values of K^* for the three

models were then employed to compute the main and lateral channel depth ratios, η_1 and η_2 . Fig 3.14 presents a comparison between the different models' predictions and the experimental data of Hsu et al. (1998). The figure shows that the harmonic mean model for the length L_i gives the best predictions for the depth ratios. Consequently, the harmonic mean of the downstream widths was used in the subsequent analysis as the model for the length L_i .

3.2.6 Separation Zone Shear Force*

F_s is the separation zone shear force. It acts only on the lateral channel control volume, C.V.₂, due to the recirculating flow downstream of the lateral channel entrance (Fig. 3.1). It decelerates the flow in C.V.₂, thus a negative sign precedes it in the momentum equation and a zero velocity is considered inside the separation zone. It is computed in a similar way as the interfacial shear force giving:

$$F_s = C_f \frac{\rho(V_2)^2}{2} y_s L_s \quad (3.32)$$

where: C_f is a coefficient of friction, y_s and L_s are the depth and the length of the separation zone interface, respectively.

In a manner analogous to the calculation of the interfacial shear force, the depth of the interface is approximated to be the lateral channel upstream depth and the length to be proportional to the lateral channel control volume downstream width (Best and Reid (1984)). Combining all the coefficients and approximations into one coefficient, the separation zone shear coefficient, K , the force can be written in the form:

-
- * The effect of the separation zone has been published in the 1st Minia International Conference for Advanced Trends in Engineering, MICATE'99, Minia, Egypt, pp 272-279.

$$F_s = K \rho V_2^2 y_2 b_3 \xi \quad (3.33)$$

3.2.7 Governing Equations

Substituting all the above forces into the momentum equations for the two control volumes, equations (3.2) and (3.3), the resulting equation for C.V.₁ is:

$$\begin{aligned} -\rho Q_1 V_1 + \rho Q_1 V_3 = \frac{\gamma y_1^2}{2} b_1 - \frac{\gamma y_3^2}{2} b_3 (1-\xi) + \frac{\gamma}{2} \left(\frac{y_1 + y_2}{2} \right)^2 (b_3 (1-\xi) - b_1) + \gamma \left(\frac{A_1 + A_{31}}{2} \right) L_1 S_o \\ - K^* \rho (V_1^2 - V_2^2) (y_1 + y_2) [2b_3 \xi (1-\xi)] - \rho \left(\frac{V_3}{C_*} \right)^2 [b_3 (1-\xi) + y_3] (L_1) \end{aligned} \quad (3.34)$$

For C.V.₂, this gives:

$$\begin{aligned} -\rho Q_2 V_2 + \rho Q_2 V_3 = \frac{\gamma y_2^2}{2} b_2 - \frac{\gamma y_3^2}{2} b_3 \xi + \frac{\gamma}{2} \left(\frac{y_1 + y_2}{2} \right)^2 (b_3 \xi - b_2) + \gamma \left(\frac{A_2 + A_{32}}{2} \right) L_2 S_o + \\ K^* \rho (V_1^2 - V_2^2) (y_1 + y_2) [2b_3 \xi (1-\xi)] - \rho \left(\frac{V_3}{C_*} \right)^2 [b_3 \xi + y_3] (L_2) - K \rho V_2^2 y_2 b_3 \xi \end{aligned} \quad (3.35)$$

It should be noted that equations (3.34) and (3.35) do not explicitly include the angle of the lateral channel. However, the angle may have an indirect influence through the magnitude of the separation zone shear coefficient, K , and the interfacial shear coefficient, K^* .

Non-dimensionalizing equations (3.34), and (3.35), using equation (3.1), in terms of the discharge ratio, $\xi = Q_2/Q_3$, the depth ratios, $\eta_1 = y_1/y_3$ and $\eta_2 = y_2/y_3$, the width ratios, $\omega_1 = b_1/b_3$ and $\omega_2 = b_2/b_3$, and the downstream Froude number, $Fr_3 = Q_3/(g b_3^2 y_3^3)^{0.5}$, results in the following equations:

$$\begin{aligned}
\underbrace{(1-\bar{\zeta}) - \frac{(1-\bar{\zeta})^2}{\omega_1 \eta_1}}_{\text{Momentum}} &= \underbrace{\frac{1}{2Fr_3^2} \left[\eta_1^2 \omega_1 - (1-\bar{\zeta}) + \frac{1}{4}(\eta_1 + \eta_2)^2 ((1-\bar{\zeta}) - \omega_1) \right]}_{\text{Net Pressure}} + \underbrace{\frac{1}{2Fr_3^2} \left(\frac{L_1 S_o}{y_3} \right) (\omega_1 \eta_1 + (1-\bar{\zeta}))}_{\text{Weight}} - \\
\underbrace{K^* \left(\left[\frac{(1-\bar{\zeta})}{\omega_1 \eta_1} \right]^2 - \left[\frac{\bar{\zeta}}{\omega_2 \eta_2} \right]^2 \right)}_{\text{Interfacial Shear}} &\underbrace{(\eta_1 + \eta_2) [2\bar{\zeta}(1-\bar{\zeta})]}_{\text{Frictional Shear}} - \frac{L_1}{b_3 C_*^2} \left(1 + \frac{b_3}{y_3} (1-\bar{\zeta}) \right) \quad (3.36)
\end{aligned}$$

$$\begin{aligned}
\underbrace{\bar{\zeta} - \frac{\bar{\zeta}^2}{\omega_2 \eta_2}}_{\text{Momentum}} &= \underbrace{\frac{1}{2Fr_3^2} \left[\eta_2^2 \omega_2 - \bar{\zeta} + \frac{1}{4}(\eta_1 + \eta_2)^2 (\bar{\zeta} - \omega_2) \right]}_{\text{Net Pressure}} + \underbrace{\frac{1}{2Fr_3^2} \left(\frac{L_2 S_o}{y_3} \right) (\omega_2 \eta_2 + \bar{\zeta})}_{\text{Weight}} + \\
\underbrace{K^* \left(\left[\frac{(1-\bar{\zeta})}{\omega_1 \eta_1} \right]^2 - \left[\frac{\bar{\zeta}}{\omega_2 \eta_2} \right]^2 \right)}_{\text{Interfacial Shear}} &\underbrace{(\eta_1 + \eta_2) [2\bar{\zeta}(1-\bar{\zeta})]}_{\text{Frictional Shear}} - \frac{L_2}{b_3 C_*^2} \left(1 + \frac{b_3}{y_3} \bar{\zeta} \right) - \underbrace{K \frac{\bar{\zeta}^3}{\omega_2^2 \eta_2}}_{\text{Separation Shear}} \quad (3.37)
\end{aligned}$$

Equations (3.36) and (3.37) are two non-linear equations that can be solved for the values of η_1 and η_2 , given $\bar{\zeta}$, and Fr_3 . Considering that $\bar{\zeta}$, η_1 , η_2 , ω_1 , and ω_2 are all of the order 1, an order of magnitude analysis can be performed on equations (3.36) and (3.37). It can be seen that the momentum term is of order 1 and the order of magnitude of the other terms can be determined by the parameter in each term. The order of the net pressure term depends upon the value of the downstream Froude number; thus for cases with low values of Fr_3 the net pressure and weight terms will dominate. In the limit of $Fr_3=0$, the solution can be shown to reduce to equality of water surface elevation. The magnitude of the weight and the frictional shear terms is determined by the parameters (LS_o/y_3) and $(L/y_3 C_*^2)$, respectively. These parameters will be significant for real world applications where the length to depth ratio is large. The orders of the interfacial shear and the separation shear terms are to be determined by the values of K^* and K , respectively.

3.3 Results and Discussion

The theoretical model equations (3.36) and (3.37) were solved using a Newton-Raphson procedure to calculate the depth ratios for the flow cases in the previous experimental studies. Since all these studies were performed on horizontal flumes, the weight term was not included in the analysis. In this investigation, experimental data from channels with smooth boundaries, low Reynolds numbers (3000-50,000) and small aspect ratios ($b/y=4 - 6$) were considered. For these cases, the bed friction effect should be very small. However, for real applications, the effect may be significant. This framework allows the use of a friction model consistent with that used in the channel reaches. Based on the physical model dimensions, the discharges, and the depths in each experiment, a value for the non-dimensional Chezy coefficient, C^* , was calculated. The lengths of the control volumes were estimated based on the location of the measurement sections or the flume dimensions in each study. The interfacial shear coefficient and the separation zone coefficient were calibrated using the available experimental data.

3.3.1 Calibration of the Interfacial Shear Coefficient, K^* , and the Separation Shear Coefficient K

For the case of equal upstream discharges, $\xi=0.5$, and equal widths, the approach velocities are equal, and thus the interfacial shear term vanishes from the equations. However for the general cases where $\xi \neq 0.5$ an interfacial shear coefficient is calibrated. As mentioned above, an average value of $Fr_3=0.53$ was chosen to represent all of the flow cases of Hsu et al. (1998). Taylor's (1944), Webber and Greated's (1966), and Gurram's (1994) experimental data presented the variation of η_1 with Fr_3 at specific

values of ζ . The values of K^* and K were calibrated for each set of experiments where the angle of intersection was held constant. The calibration for each data set was based on a least squares error analysis between the measured and the predicted depth ratios, η_1 and η_2 . Since Taylor (1944), Webber and Greated (1966) and Gurram (1994) did not provide measurements for the depth in the lateral channel and assumed the upstream depths to be equal, this assumption was employed while calibrating K^* and K for their data sets. Webber and Greated (1966) corrected their depth measurements to eliminate friction effects. Thus the boundary friction forces were not included during the calibration of K^* and K for their experiments.

Table 3.3 presents the calibrated values of the two coefficients K^* and K for each junction angle in each study. Figs. 3.15(a-b) show the variation of these calibrated coefficients with the junction angle. Fig. 3.15(a) shows that K^* appears to decrease linearly with the junction angle if the data of Gurram (1994) is excluded. Thus, a linear trend line was plotted for this variation. The equation of this line is:

$$K^* = -0.0015\delta + 0.30 \quad (3.38)$$

with a coefficient of determination of 0.92. Table 3.3 gives the empirical values of K^* computed using equation (3.38). The decrease in K^* with the junction angle may be attributed to the interaction between the forces acting on the dividing streamline (the pressure force due to convergence and the interfacial shear force). As the curvature of the dividing streamline increases, with the increase in angle, the pressure force B becomes more pronounced and the interfacial shear is less significant. As the angle decreases it is the opposite case and the interfacial shear force becomes more significant. Including Gurram's (1994) calibrated K^* data points, the variation of K^* with the junction angle

may be also considered constant. Thus, a mean value of $K^* = 0.21$ was computed from all the calibrated values. The two approaches for determining the values of K^* were employed in the model verification and both gave equally good agreement with the experimental measurements.

Fig. 3.15(b) indicates that K is more sensitive than K^* to the variation in the junction angle especially for angles between 30° and 90° . The figure shows a linear increase in the K with the junction angle. This is expected since the separation zone effects, such as the constriction to the flow, increase with the increase in angle. Gurrani's (1994) are excluded and a second trend line was plotted for the variation of K with δ . The equation of the trend line is:

$$K = 0.0092\delta - 0.1855 \quad (3.39)$$

with a coefficient of determination of 0.91. Equation (3.39) was used to compute the empirical values of K for the angles considered in the subsequent analysis. These empirical values are presented in Table 3.3.

3.3.2 The Final Model Results

Figs. 3.16(a-b) present the variation of the measured and the computed depth ratios, η_1 , and η_2 , with ξ , for the three angles of intersection (30° , 45° and 60°) that Hsu et al. (1998) investigated. The computations for the proposed momentum approach are presented for two cases: the first where the interfacial or separation shear forces are not included and the second where they are included. Equations (3.38) and (3.39) are used to determine K^* and K for the second case. The figure shows a good agreement between the

computations and the measurements. This indicates that K^* and K are independent of the discharge ratio.

Figs. 3.16(a-b) also present a comparison between the proposed momentum approach and two energy approaches: the common approach of the equality of the water surface elevations ($\eta_1 = \eta_2 = 1$) (neglecting velocity heads and losses); and the simple energy approach (conservation of energy while neglecting losses). The comparison shows that assuming all three water surface elevations are equal, represented by the x-axis in Figs 3.16(a-b), does not reflect the actual experimental observations. Including the velocity heads improves the predictions, but still underestimates both upstream depths for most discharge ratios. The proposed momentum approach, without including the interfacial shear or the separation zone shear terms ($K^* = 0, K = 0$), shows an improvement in the predictions over these energy approaches for most discharge ratios, though some discrepancy in both η_1 and η_2 is still evident. Including the two shear terms in the analysis has a very small effect at a discharge ratio, ξ , of 0.5, due to the equal velocities in the two control volumes. However, at the higher and lower discharge ratios these terms have a more significant effect in that the interfacial shear tends to further equalize the depth ratios while the separation shear term captures the increased upstream depths with larger lateral channel discharges and angles.

Figs. 3.17-3.25 present plots of the computed depth ratios η_1 and η_2 against Fr_3 . In Figs 3.17-3.19 comparisons with Webber and Greated's (1966) experimental data are presented for junction angles of 30° , 60° , and 90° , respectively. Fig. 3.20(a-c) presents comparisons with Webber and Greated's (1966) data for a discharge ratio of 0.5 and for the three junction angles investigated. Figs. 3.21-3.22 present the comparisons with

Taylor's (1944) data for junction angles of 45° and 135° , respectively. Figs. 3.23-3.25 present the comparisons with Gurram's (1994) data for junction angles of 30° , 60° , and 90° , respectively. The calculated depth ratios are presented in each plot for two cases, the first not including the interfacial or the separation shear terms ($K^* = 0$, $K = 0$) and the second while including them. In the latter, the empirical values (Table 3.3) of both coefficients for each case were used in the calculations. The good agreement between the proposed model predictions and the measurements for the different angles indicate that the interfacial and separation coefficients are independent of the downstream Froude number. For the cases where the discharge ratio is 0.5, the interfacial shear term vanishes from the equations, as the upstream velocities are equal. Therefore, the model predictions for η_1 and η_2 are independent of the K^* values. When no interfacial shear or separation shear are included ($K^* = 0$, $K = 0$) in the computations and the discharge ratio is 0.5 the model equations give $\eta_1 = \eta_2$ for different values of Fr_3 .

The validity of the assumption of equal upstream depths ($\eta_1 = \eta_2$) adopted in all of the previous theories was checked by comparing the computed depth ratios while including the interfacial shear and separation shear in each of the Figs. 3.17-3.25. The figures indicate that the assumption is valid for most of the cases observed. However, this assumption cannot be generalized for different width ratios, aspect ratios or unsteady flow situations due to the limitation in the available verification data.

In practice both K^* and K should be treated as calibration coefficients. In this study, these coefficients were found to be independent of the discharge ratios and the downstream Froude number but were found to be dependent on geometry. For practical

cases, once they have been calibrated for a specific geometry at known flow conditions, it may be possible to use the same values for different flow situations.

3.4 Comparison with Previous Theories

Comparisons between the proposed momentum approach and the theories of Taylor (1944), Webber and Greated (1966), Gurram (1994), and Hsu et al. (1998) were performed. Taylor (1944) presented a theory based on applying mass and momentum conservation to the junction. He simplified his equation by assuming that the depth at the lateral channel entrance was everywhere equal and was equal to the upstream depth in the lateral channel. Taylor (1944) introduced a dimensionless factor, the kineticity coefficient, $k_2 = V_2^2 / 2gy_2$, and his resulting equation was:

$$k_2 = \frac{\xi^2 [\eta^2 - 1]}{4\eta^2 (2\xi - \xi^2 (1 + \cos \delta) + \eta - 1)} \quad (3.40)$$

where η is either of the depth ratios η_1 or η_2 as they were assumed to be equal in Taylor's (1944) study.

Webber and Greated (1966) presented a theory similar to Taylor's (1944) but in terms of the downstream Froude number instead of the lateral channel kineticity coefficient where:

$$Fr_3 = \frac{Q_3}{(gb_3^2 y_3^3)^{0.5}} = \frac{(2K_2 \eta_2^3)^{0.5} \omega_2}{\xi} \quad (3.41)$$

and their equation was in the form:

$$Fr_3 = \left\{ \frac{\eta(\eta^2 - 1)}{2(\eta - (1 - \xi)^2 - \xi^2 \cos \delta)} \right\}^{1/2} \quad (3.42)$$

When Webber and Greated (1966) checked the validity of Taylor's (1944) assumption regarding the force component imposed by the lateral channel they found it to be unsatisfactory. Thus they sought an empirical correction, κ , that would bring the theoretical curves in better conformity with the experimental ones. They obtained the following equation:

$$Fr_3 = \left\{ \frac{\eta(\eta^2 - 1)(1 + \kappa)}{2(\eta - (1 - \xi)^2 - \xi^2 \cos \delta)} \right\}^{2/3} \quad (3.43)$$

where: $\kappa = 0.3(\xi + \sin \delta - 1)$ (3.44)

Gurram (1994) presented a theory based on conservation of momentum and continuity of discharge in the junction. He included the momentum correction coefficient for the downstream section, β_3 , in his analysis. Gurram (1994) introduced a pressure coefficient, ϕ , in his theory to account for the lateral channel wall pressure component. His theory resulted in the following equation:

$$\eta^3(1 + \cos \delta - \phi) - \eta(1 + 2\beta_3 Fr_3^2) + 2Fr_3^2[(1 - \xi)^2 + \xi^2 \cos \delta] = 0 \quad (3.45)$$

where ϕ and β_3 were determined from the following empirical equations:

$$\beta_3 = [1 + 0.12(\xi \sin^2 \delta)^2] Fr_3^{-0.02} \quad (3.46)$$

$$\phi = 0.251\xi^2 - 0.287\xi + 0.89 \quad (3.47)$$

for 30° junctions and $\phi = 0.218\xi^2 - 0.251\xi + 0.521$ (3.48)

for 60° junctions and $\phi = -0.108\xi^2 + 0.072\xi + 0.0433$ (3.49)

for the 90° junctions.

Hsu et al. (1998) presented another theory based on applying the momentum principle to two control volumes in the junction: one in the main channel and the second

in the lateral channel together with overall mass and energy conservation. They assumed the depth ratios η_1 and η_2 to be equal and derived the following third degree polynomial to compute the depth ratio, η .

$$\eta^3 - \left(1 + 2\frac{\beta}{\alpha} Fr_3^2\right)\eta + 2\frac{\beta}{\alpha} Fr_3^2 \left[(1 - \zeta)^2 + \cos \delta \zeta^2\right] = 0 \quad (3.50)$$

where: α is the energy correction coefficient and β is the momentum correction coefficient.

Figs. 3.26-3.30 present the comparisons with Taylor's (1944), Webber and Greated's (1966) and Gurram's (1994) theories. The figures also include the available data for each angle and each discharge ratio. In these figures the graphs' origin on the abscissa scale is shifted progressively to the right. Each figure presents the comparisons for the case of a constant junction angle and different discharge ratios (0.2, 0.25, 0.4, 0.5, 0.6, 0.75, and 0.8). For each angle, the empirical values of K^* and K are used in the computations of the present theory. Equations (3.42), (3.43), and (3.45) are used for plotting Taylor's (1944), Webber and Greated's (1966), and Gurram's (1994) theories, respectively. The empirical coefficients β_3 and ϕ used in the predictions for the 45° and the 135° junctions are based on Gurram's experimental measurements of junction angles up to 90°. Taylor's (1944), Webber and Greated's (1966) and Gurram's (1994) experimental data are shown for validation.

The comparisons with the theory of Hsu et al. (1998) are presented in Figs. 3.31(a-b). These figures present the case of a constant downstream Froude number $Fr_3=0.53$ and different discharge ratios. Equation (3.50) is used for plotting the theory of

Hsu et al. (1998) while keeping $\alpha=\beta=1$. The present theory is plotted using the empirical values of K^* and K for each of the three junction angles investigated.

On comparing the model equations with the different theories it can be seen that the model predictions for both depth ratios are generally as good as the other theories for most discharge ratios and slightly superior for high discharge ratios. The advantage of the proposed approach over these other theories is in its capability to be scaled up to prototype applications, since it includes most of the physical effects neglected in other theories. The boundary friction force has been neglected in all of the other theories and although this works well at model scales, it is significant in real world cases. For example, consider two cases: the first, a real river with an aspect ratio of 100 and a Chezy C of 10 and the second, an experimental flume with an aspect ratio of 3 and a Chezy C of 17. Keeping the discharge ratio, the width ratios, and the downstream Froude number the same and performing an order of magnitude analysis for the different terms in equations (3.36) and (3.37) for the two cases, we find that in the first case the friction term is almost of the same magnitude as the net pressure term. However, in the second case the friction term is negligible. The second advantage of the proposed model is that it does not rely on the assumption of equality of the upstream depths in both the main and the lateral channels. For general situations, this assumption may not be applicable.

3.5 Summary and Conclusions

A one-dimensional theoretical model providing the necessary interior boundary equations governing subcritical combining open channel junction flow was developed. The momentum principle was applied to two control volumes in the junction, in the

respective streamwise directions. Given the inflow discharges and a downstream boundary condition, the model calculates the upstream depths for each of the incoming channels.

The interfacial shear force between the two control volumes and the separation zone shear force in the lateral channel control volume were included in the analysis. Two shear coefficients were calibrated, using the available experimental data, for the different junction angles. It was found that the variation in these coefficients was independent of the discharge ratio and the downstream Froude number but was dependent on the angle of intersection. From this we tentatively conclude that, in general, the coefficients are dependent on junction geometry, but not on flow. The latter conclusion requires further experimental verification, but may be acceptable as a working hypothesis in practical cases.

A comparison between the current treatment for junctions in open channel network models that apply conservation of energy and the proposed model was performed. This showed that the proposed model gave better predictions, for both depth ratios, than the energy approach.

A comparison between the proposed theory and previous momentum based theoretical approaches was performed. The comparison showed that the proposed model predictions were about as good as the other theories and somewhat superior at high discharge ratios. The advantage of the proposed theory is that it models almost all of the physical effects involved, such as the boundary friction forces which were neglected in all of the other theories, and thus it can be scaled up to real world applications. Further, the application of the momentum principle in the streamwise direction to two control

volumes in the junction allows the model to be easily implemented in network models and makes handling of the junctions consistent with that of the channel reaches.

References

- Best, J.L., and Reid, I (1984). "Separation zone at open-channel junctions." *J. Hydr. Engrg.*, ASCE, 110 (11), 1588-1594.
- Danish Hydraulic Institute, Denmark @www.dhi.dk.
- Environment Canada, Water Modeling Section. (1988). "*One dimensional hydrodynamic model.*" Water Planning And Management Branch, Environment Canada
- Chaudhry, M. H. (1993). *Open-Channel Flow*. Prentice Hall, Englewood Cliffs, NJ.
- Garcia-Navarro, P. (1992). "Numerical simulation of unsteady flow at open channel junctions." *J. Hydr. Research*, IAHR, 30 (5), 595-609.
- Gurram, S. K. (1994). "A study of subcritical and transitional combining flow in open channel junctions." PhD thesis, Banaras Hindu Univ., Varanasi, India.
- Hsu, Chung-Chieh, Lee, Wen-Jung, and Chang, Cheng-Hsi (1998). "Subcritical open channel junction flow." *J. Hydr. Engrg.*, ASCE, 124 (8), 847-855.
- Rajaratnam, N. (1976). *Turbulent Jets*. Elsevier Publishing Co., The Netherlands, 304 p.
- Taylor, E. H. (1944). "Flow characteristics at rectangular open channel junctions." *Trans.*, ASCE, 109, 893-902.
- US Army Corps of Engineers, Institute for Water Resources. (2001). "*HEC-RAS River Analysis System Hydraulic Reference Manual.*" Hydrologic Engineering Center Version 3.0, January 2001. <http://www.hec.usace.army.mil>.

Webber, N. B., and Greated, C. A. (1966). "An investigation of flow behavior at the junction of rectangular channels." *Proc., Inst. Civ. Engrs.*, London, England, 34, 321-334.

APPENDIX

Alternate Control Volume Configurations

Alternate control volume configurations were examined in order to better model the separation zone effects in the theory. Figs. 3.32 and 3.33 show three and four control volumes' configurations, respectively. For the three control volumes, the depth at the maximum contracted section and the width of the separation zone are added to the variables. The number of equations also increases as an extra equation is formulated for C.V.₃ and an empirical equation (Best and Ried (1984)) for the separation zone width is included. For the four control volumes' approach, two depths are added at the maximum contracted section and the separation zone width. However, comparisons between the computed depth ratios using the two, three, and four control volumes' approaches and the experimental data proved that the two control volume approach gave the best agreement and the most stable results.

Author	δ	ξ	Calibrated K^*	
			$S=K^*(V_1-V_2)*abs(V_1-V_2)*(y_1+y_2)*b_3$	$S=K^*(V_1-V_2)*(V_1+V_2)*(y_1+y_2)*b_3$
Webber and Greated (1966)	30°	0.20	0.19	0.11
Gurram (1994)		0.25	0.00	0.00
Webber and Greated (1966)		0.40	0.69	0.14
Webber and Greated (1966)		0.60	0.65	0.13
Gurram (1994)		0.75	0.70	0.32
Webber and Greated (1966)		0.80	0.14	0.09
Taylor (1944)	45°	0.40	1.58	0.30
Taylor (1944)		0.60	0.00	0.00
Taylor (1944)		0.80	0.00	0.00
Webber and Greated (1966)	60°	0.20	0.17	0.10
Gurram (1994)		0.25	0.00	0.00
Webber and Greated (1966)		0.40	1.51	0.29
Webber and Greated (1966)		0.60	0.00	0.00
Gurram (1994)		0.75	0.00	0.00
Webber and Greated (1966)		0.80	0.00	0.00
Webber and Greated (1966)	90°	0.20	0.20	0.12
Gurram (1994)		0.25	0.26	0.13
Webber and Greated (1966)		0.40	2.53	0.46
Webber and Greated (1966)		0.60	0.00	0.00
Gurram (1994)		0.75	0.00	0.00
Webber and Greated (1966)		0.80	0.00	0.00
Taylor (1944)	135°	0.40	0.61	0.12
Taylor (1944)		0.60	0.00	0.00
Taylor (1944)		0.80	0.00	0.00

Table 3.1 Comparing the Interfacial Shear Coefficient, K^* , for the Two Interfacial Shear Velocity Models

L_1 Model		b_3	$\text{SQRT}(b_3\xi * b_3(1-\xi))$	$2*b_3\xi * b_3(1-\xi)$	
	δ	ξ	Calibrated K^*		
	30°		0.918	0.05	0.19
		0.811	0.10	0.25	0.32
		0.708	0.12	0.26	0.29
		0.609	0.13	0.26	0.26
		0.518			
		0.42	0.04	0.09	0.09
		0.321	0.12	0.26	0.28
		0.205	0.07	0.18	0.22
		0.097	0.05	0.17	0.28
Average			0.085	0.206	0.261
Standard Deviation			0.035	0.064	0.080
Variance			0.416	0.308	0.307
45°		0.904	0.05	0.17	0.29
		0.809	0.08	0.20	0.26
		0.7	0.10	0.22	0.24
		0.611	0.12	0.24	0.25
		0.5			
		0.42	0.11	0.23	0.23
		0.313	0.09	0.20	0.22
		0.203	0.10	0.25	0.31
		0.092	0.05	0.18	0.31
Average			0.089	0.212	0.264
Standard Deviation			0.026	0.028	0.036
Variance			0.290	0.131	0.135
60°		0.91	0.02	0.07	0.13
		0.824	0.02	0.06	0.08
		0.697	0.03	0.07	0.08
		0.62			
		0.511			
		0.425	0.28	0.56	0.56
		0.3201	0.18	0.39	0.41
		0.212	0.11	0.27	0.32
		0.097	0.05	0.17	0.28
Average			0.099	0.226	0.267
Standard Deviation			0.097	0.189	0.184
Variance			0.984	0.838	0.689
Overall Average			0.090	0.214	0.264
Overall Std. Deviation			0.057	0.106	0.108
Overall Variance			0.626	0.497	0.409

Table 3.2 Comparing the Interfacial Length Models Using the Data of Hsu et al. (1998)

Author	δ	Calibrated Values		Mean	Empirical Values		
		K^*	K	K^*	K^*	K	
Webber and Greated (1966)	30°	0.26	0.00	0.21	0.26	0.09	
Gurram (1994)		0.18	0.00				
Hsu et al. (1998)		0.28	0.06				
Taylor (1944)	45°	0.20	0.33		0.23	0.23	
Hsu et al. (1998)		0.24	0.21				
Webber and Greated (1966)	60°	0.22	0.30		0.21	0.21	0.37
Gurram (1994)		0.15	0.26				
Hsu et al. (1998)		0.20	0.38				
Webber and Greated (1966)	90°	0.17	0.84		0.17	0.64	
Gurram (1994)		0.26	1.61				
Taylor (1944)	135°	0.10	0.95	0.10	1.06		

Table 3.3 Calibrated and Empirical Values of K^* and K

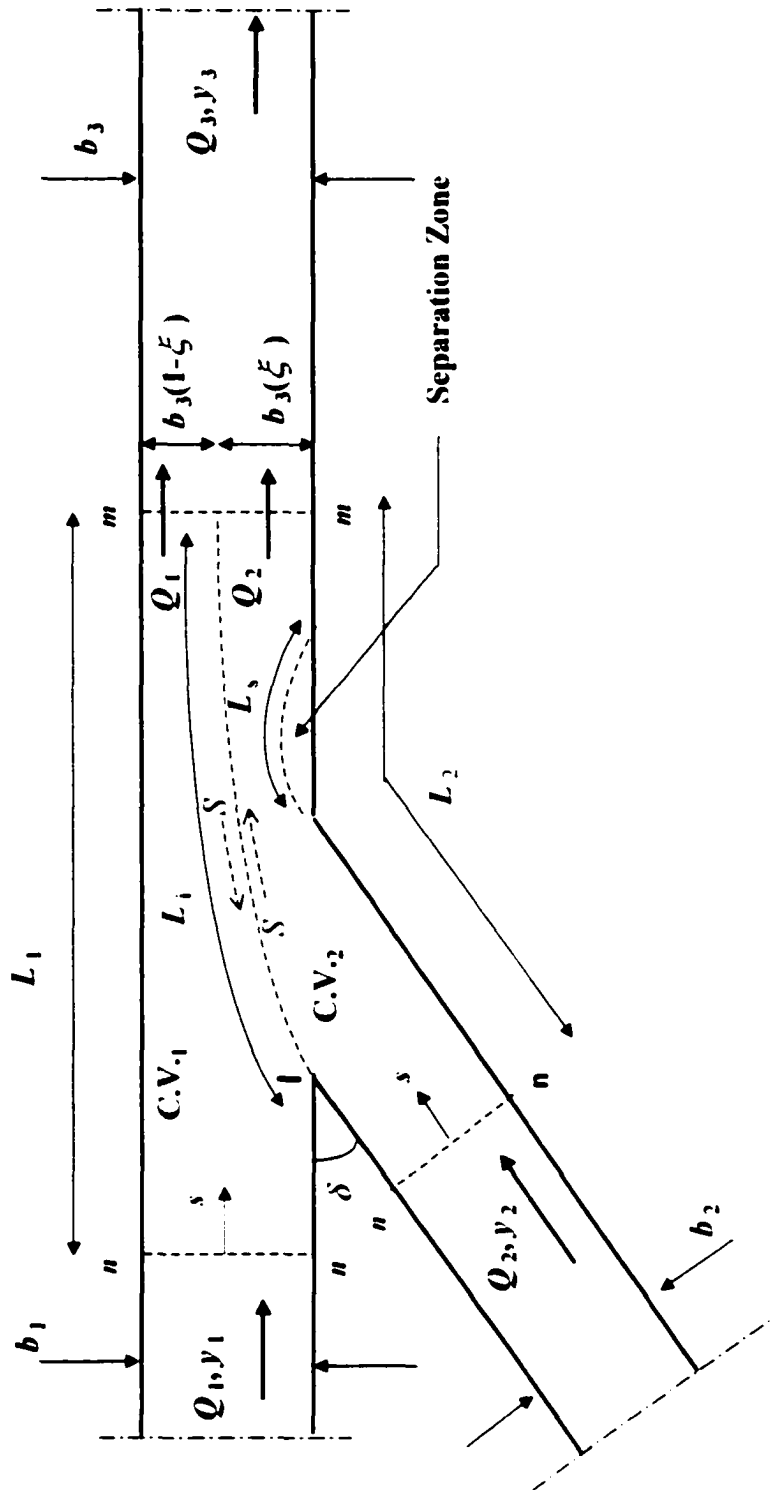


Fig. 3.1. Combining Open Channel Junction with the Control Volumes and Notation

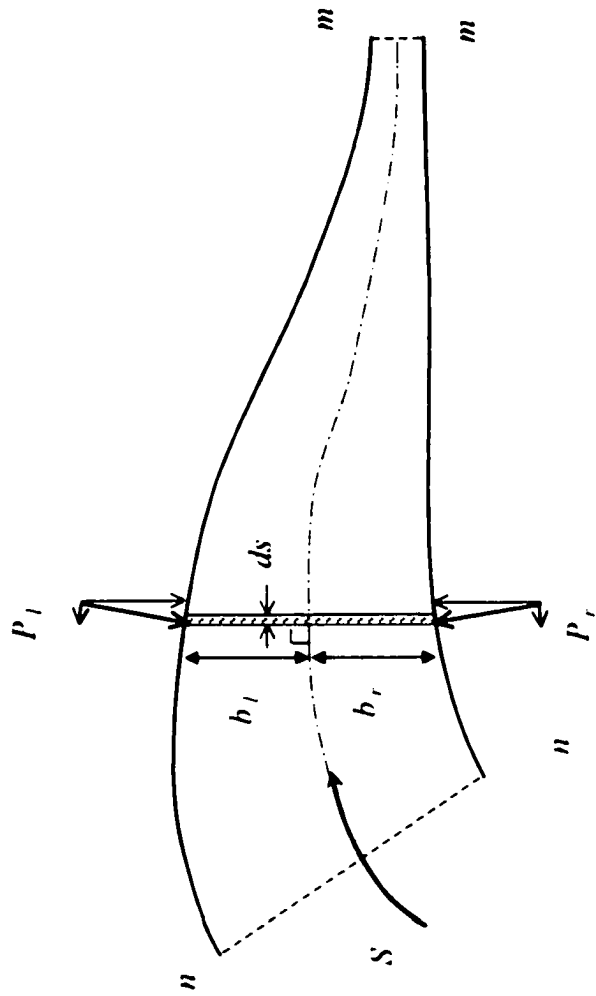


Fig. 3.2 Curvilinear Coordinate System and the Pressure Force due to Convergence

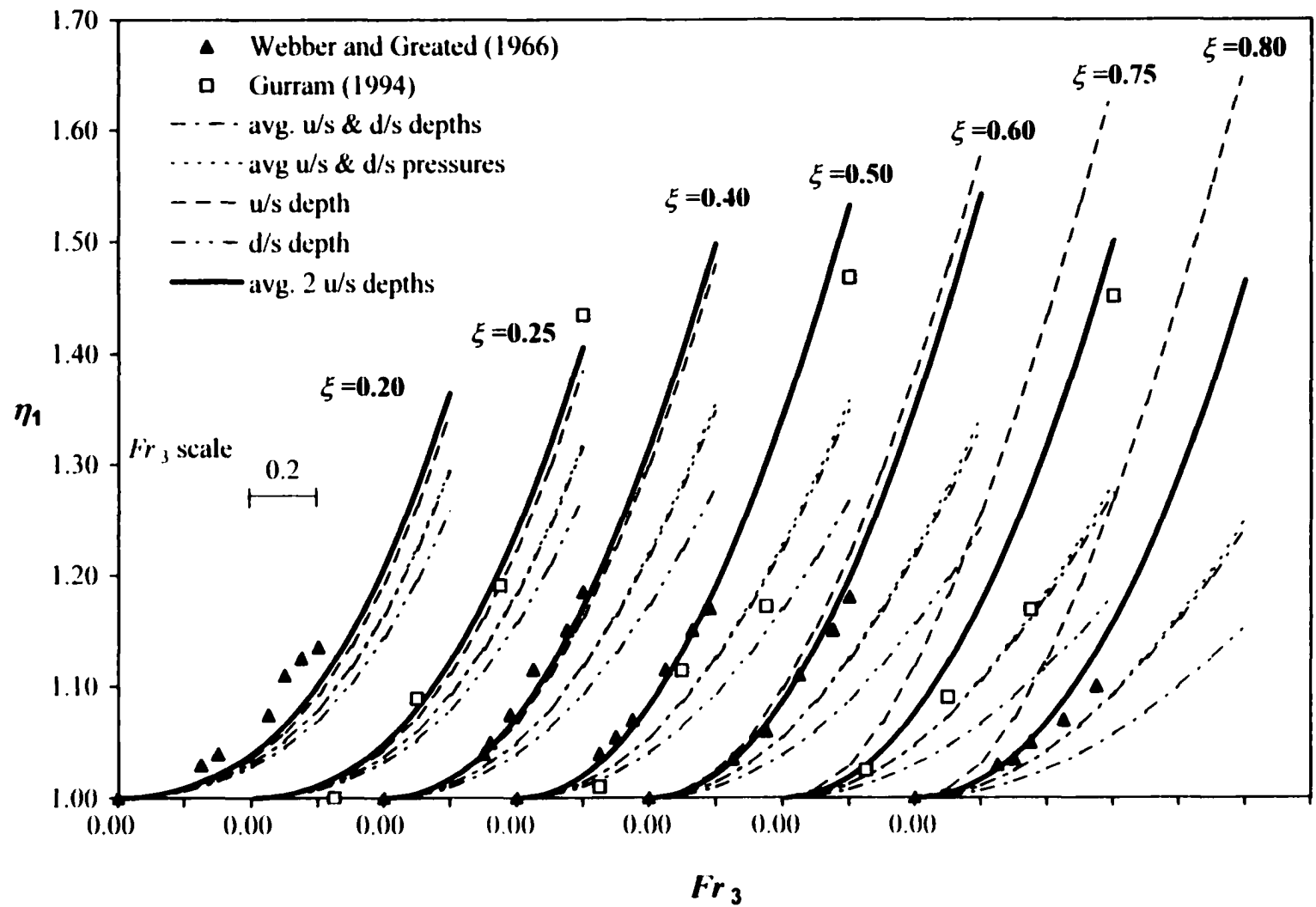


Fig. 3.3 Comparing the Different Theories for Pressure Force B ($\delta = 30^\circ$)

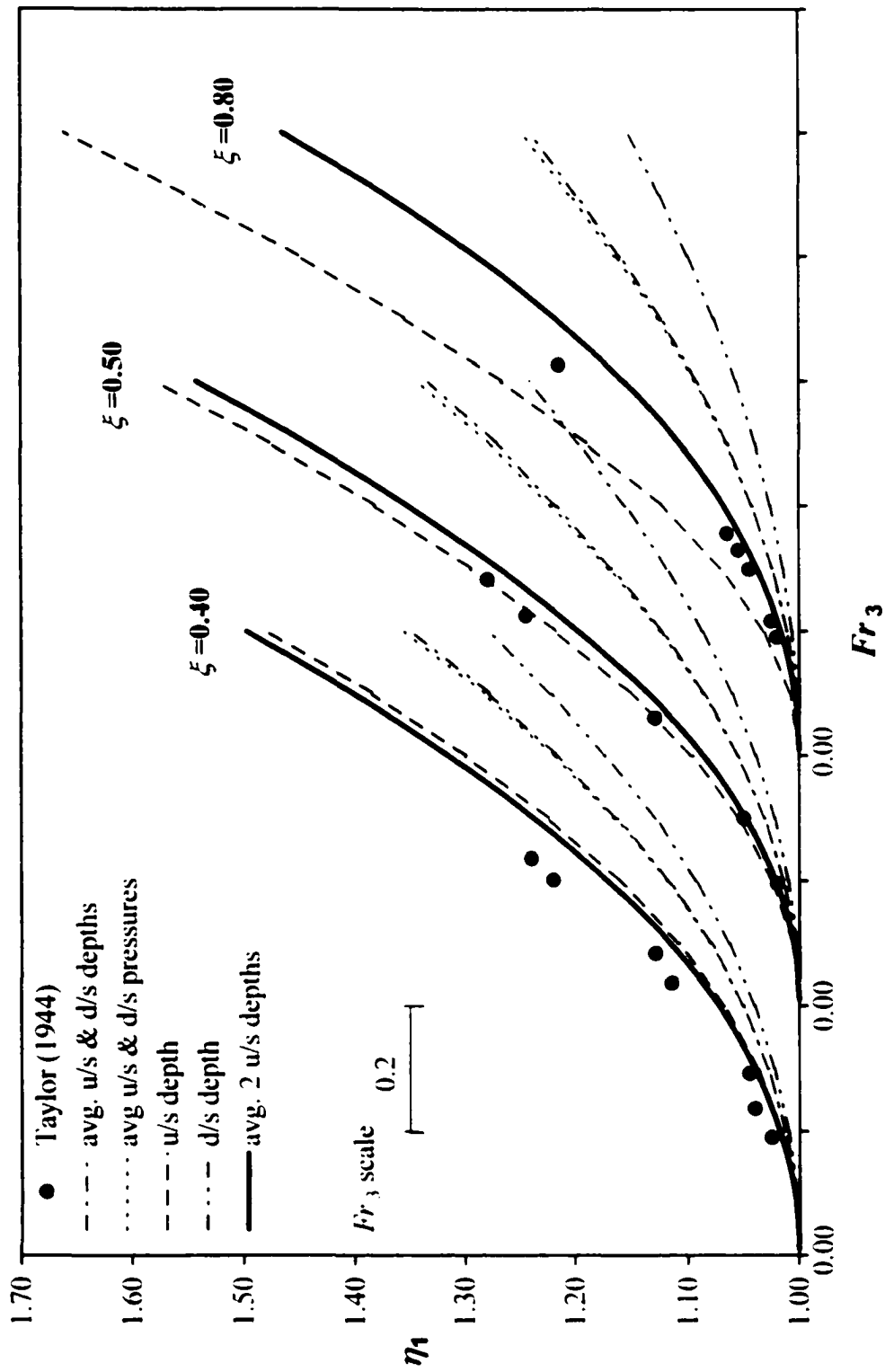


Fig. 3.4 Comparing the Different Theories for Pressure Force B ($\delta = 45^\circ$)

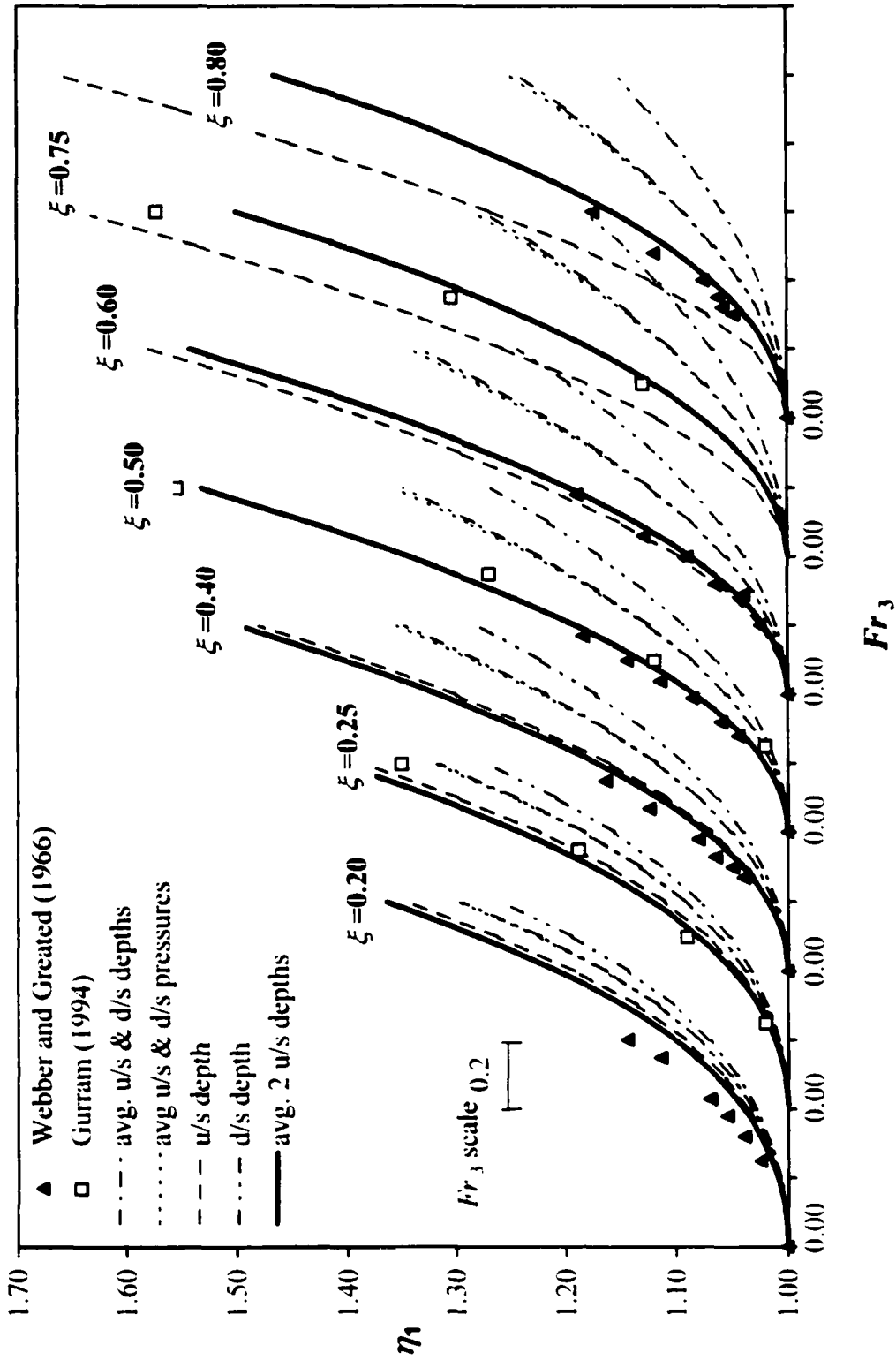


Fig. 3.5 Comparing the Different Theories for Pressure Force B ($\delta = 60^\circ$)

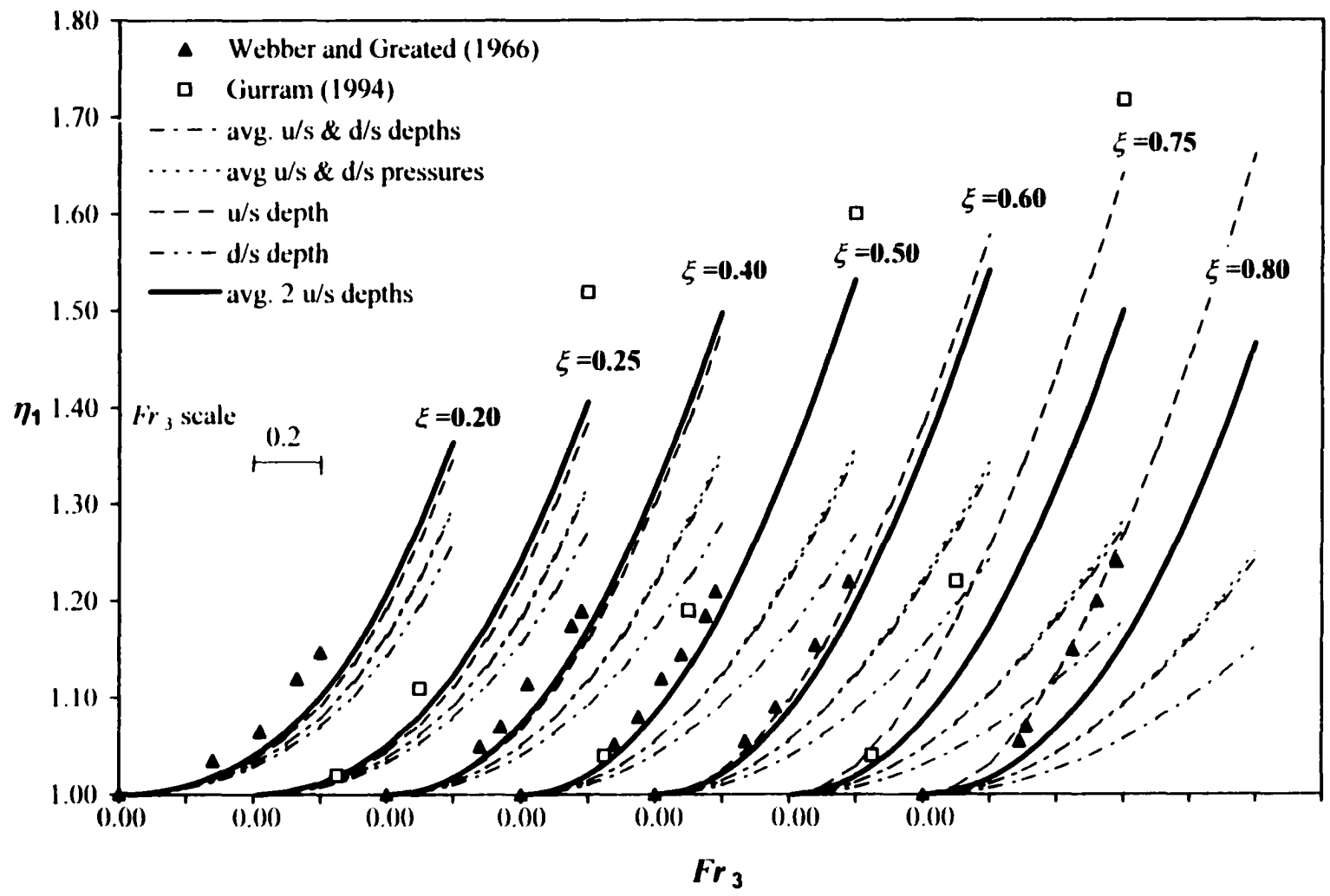


Fig. 3.6 Comparing the Different Theories for Pressure Force B ($\delta = 90^\circ$)

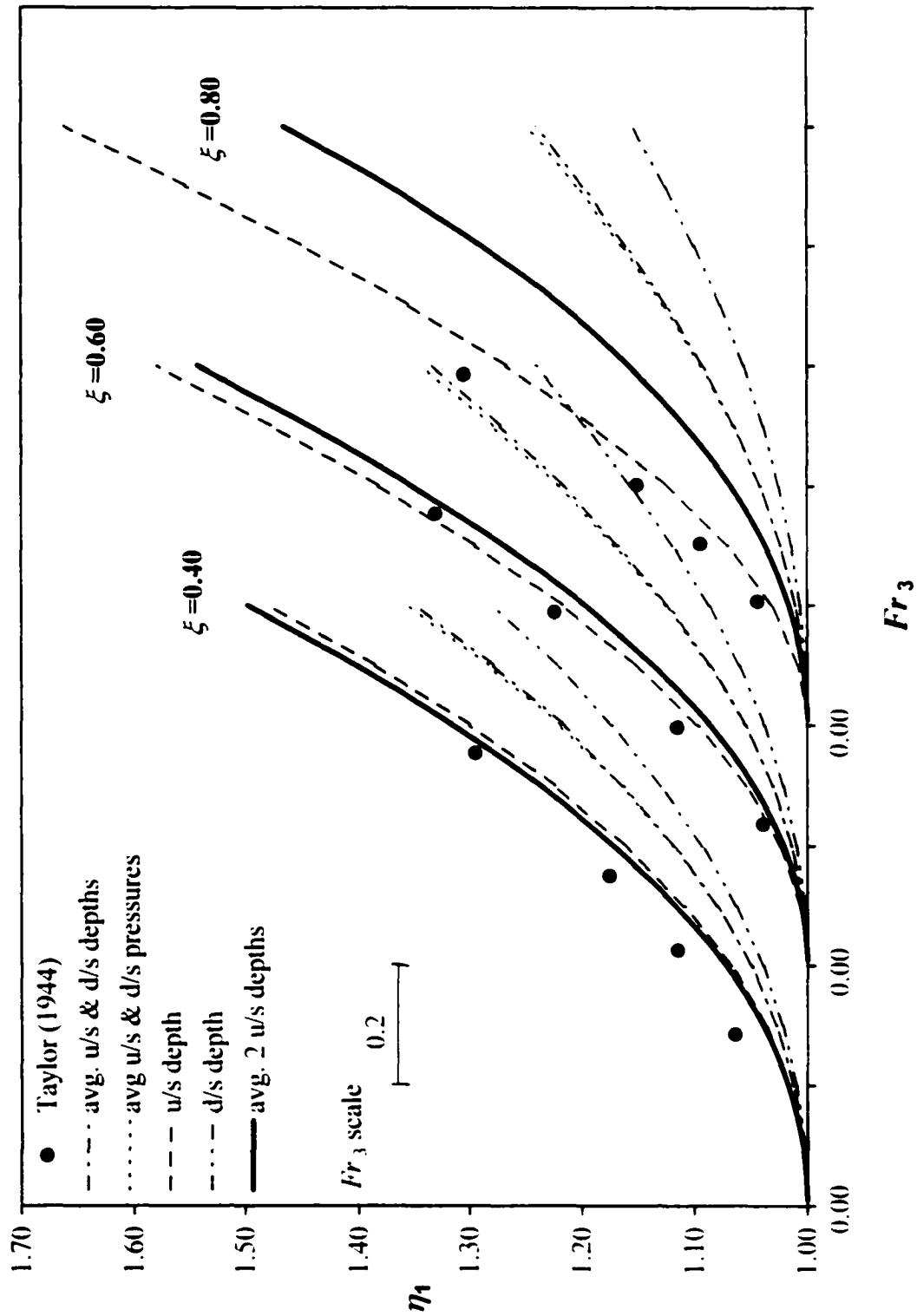


Fig. 3.7 Comparing the Different Theories for Pressure Force B ($\delta = 135^\circ$)

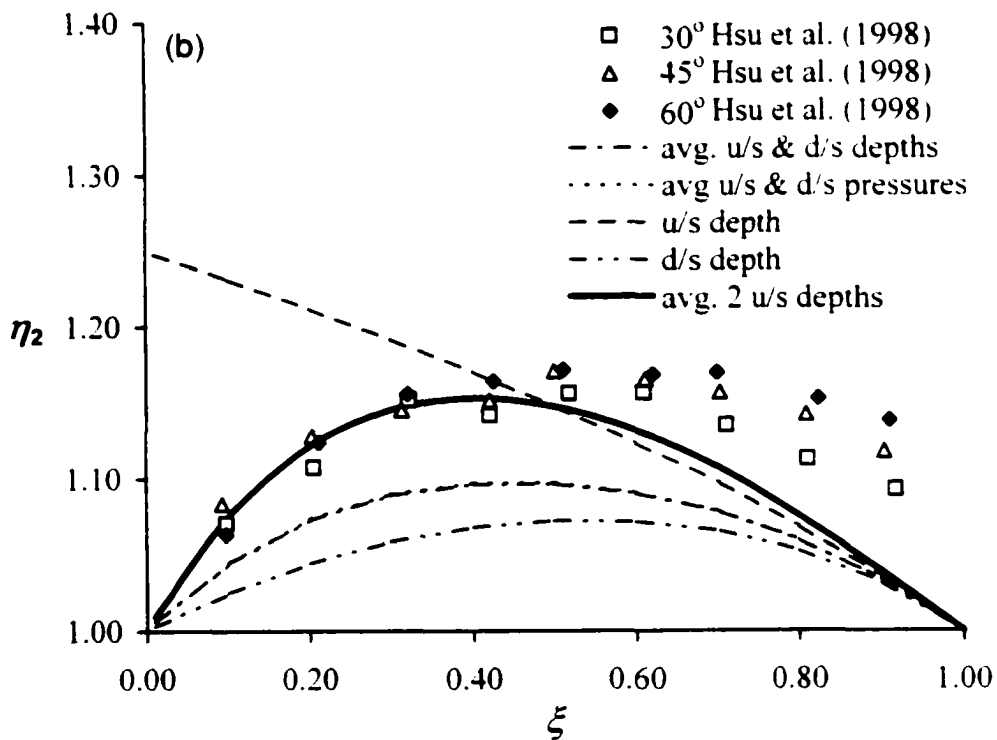
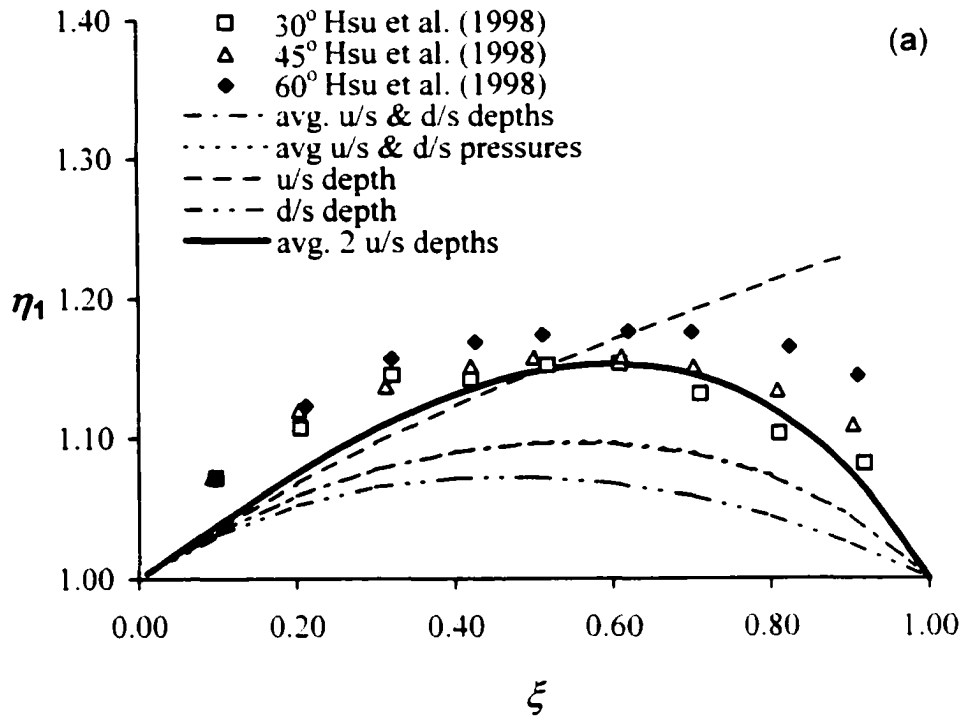


Fig. 3.8(a-b) Comparing the Different Theories for Pressure Force B
(a) The Main Channel Depth Ratio η_1
(b) The Lateral Channel Depth Ratio η_2

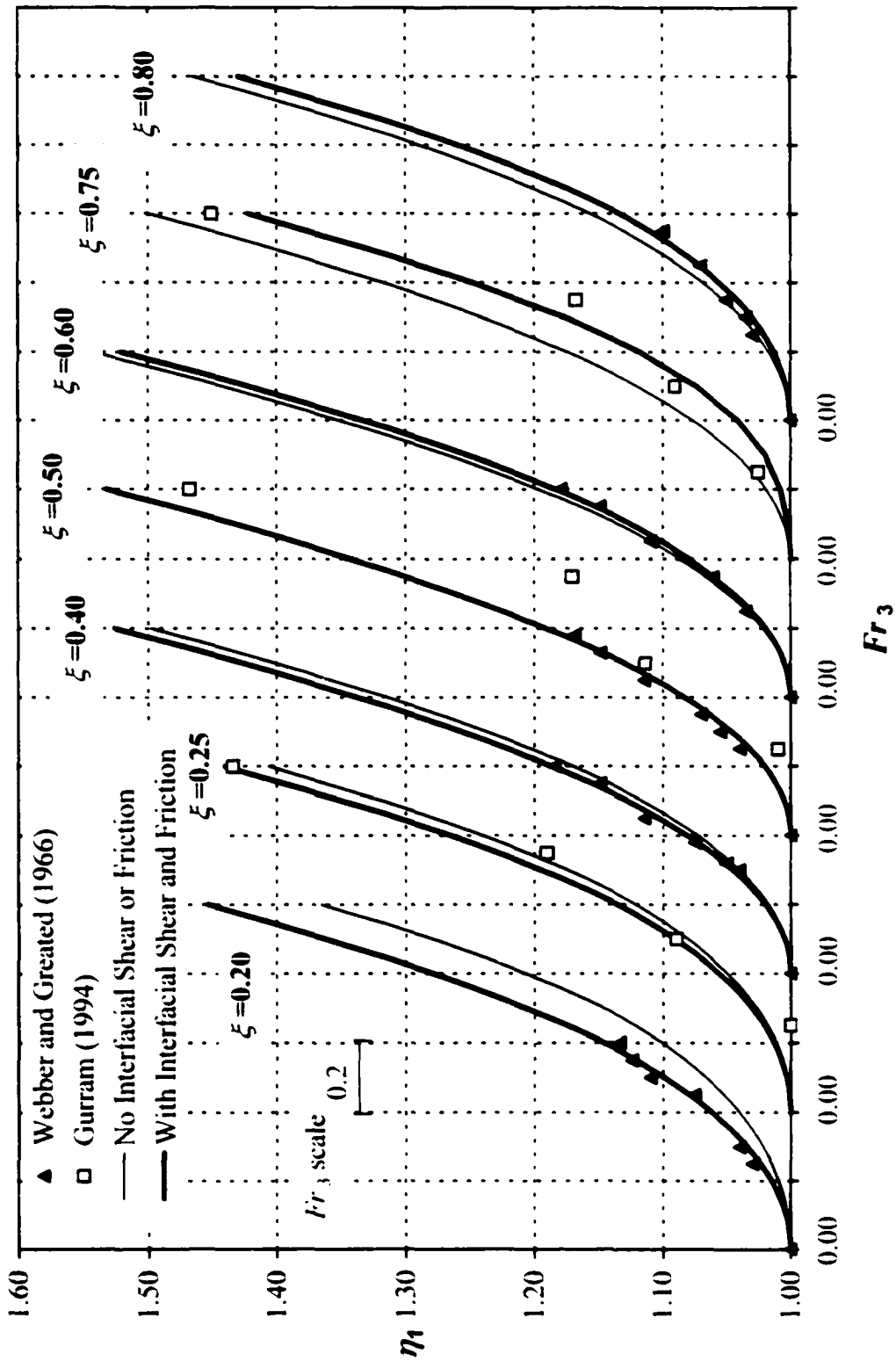


Fig. 3.9 Including the Effects of Interfacial Shear and Friction ($\delta=30^\circ$)

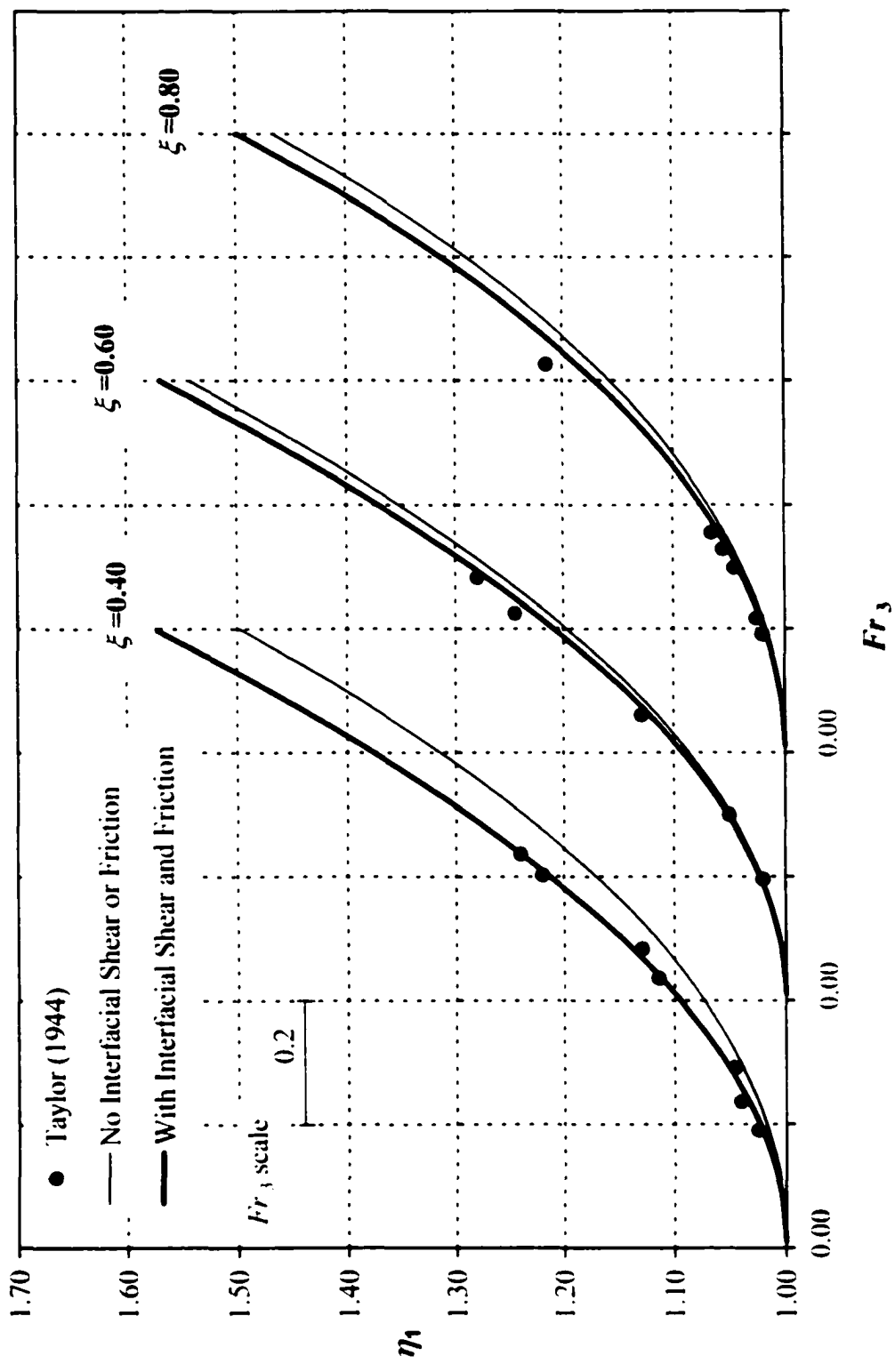


Fig. 3.10 Including the Effects of Interfacial Shear and Friction ($\delta=45^\circ$)

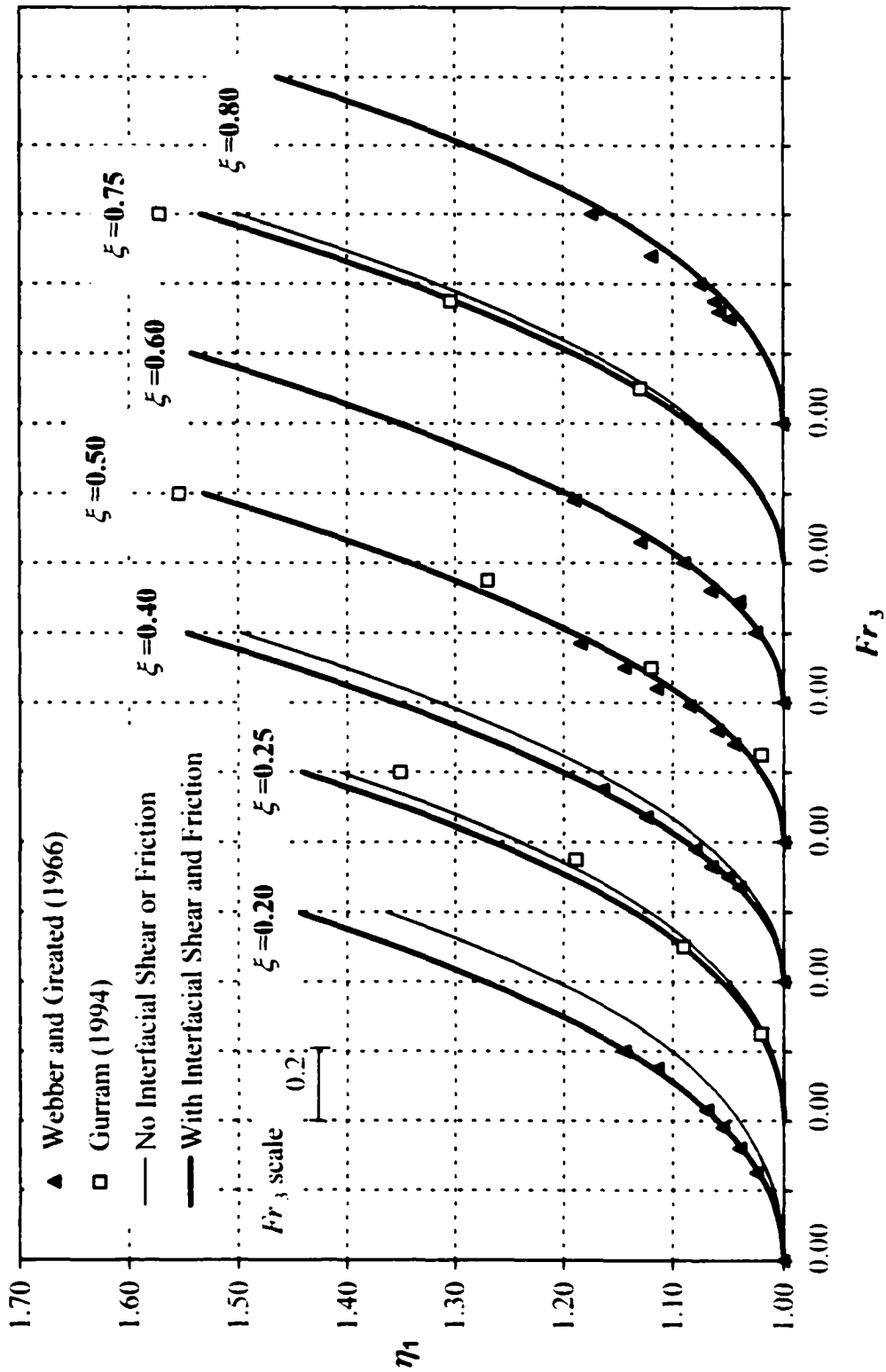


Fig. 3.11 Including the Effects of Interfacial Shear and Friction ($\delta = 60^\circ$)

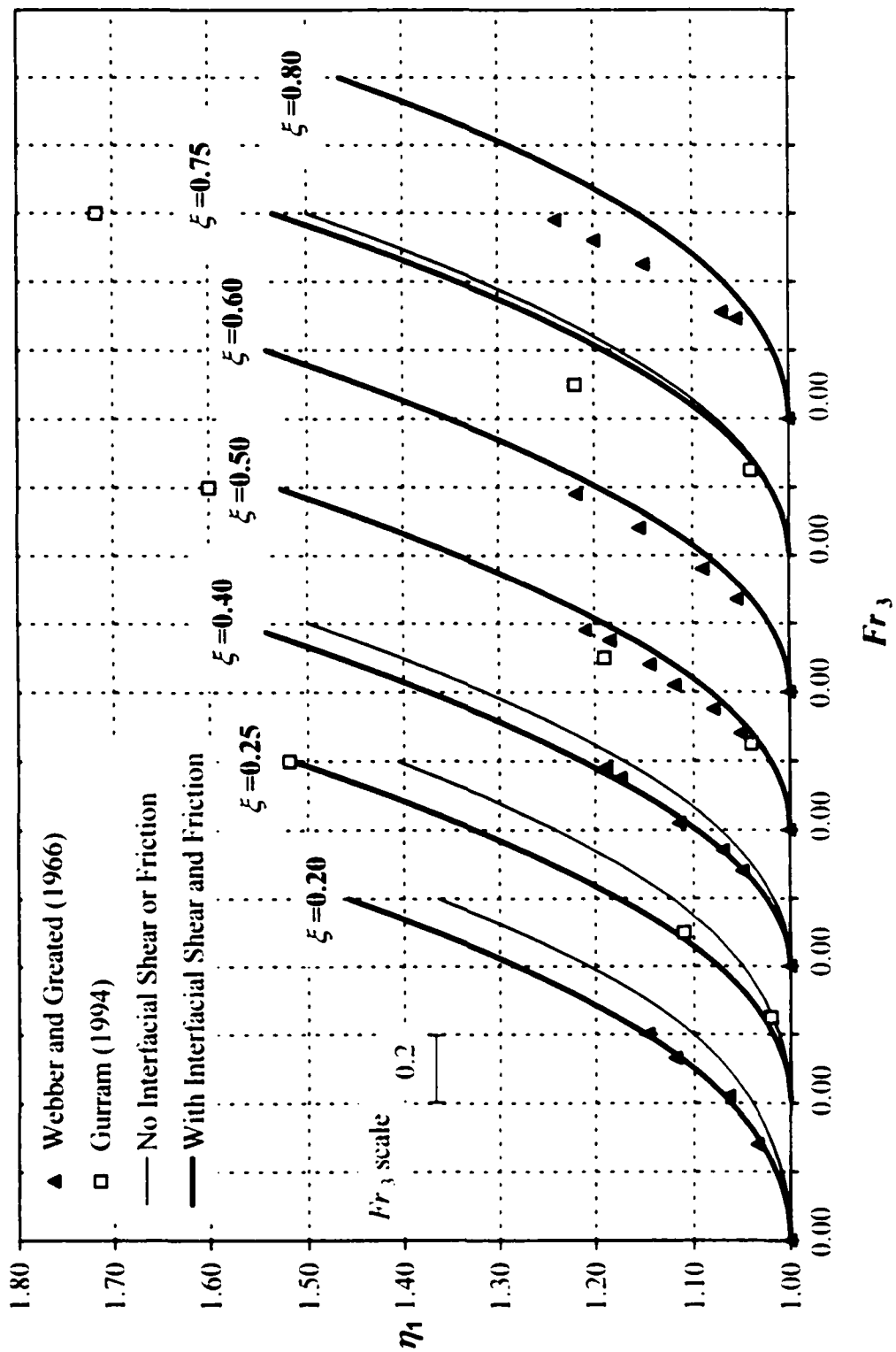


Fig. 3.12 Including the Effects of Interfacial Shear and Friction ($\delta = 90^\circ$)

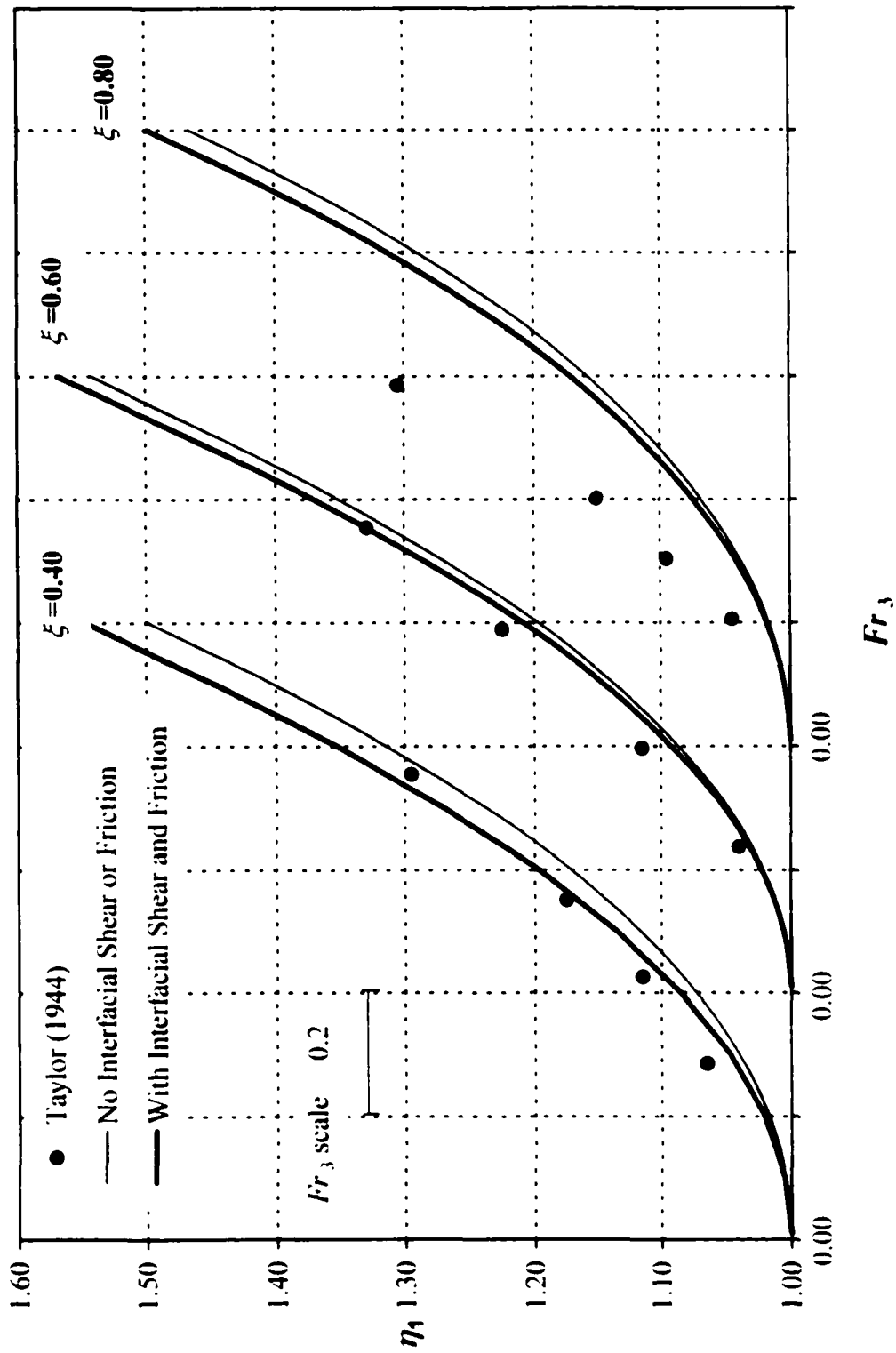


Fig. 3.13 Including the Effects of Interfacial Shear and Friction ($\delta = 135^\circ$)

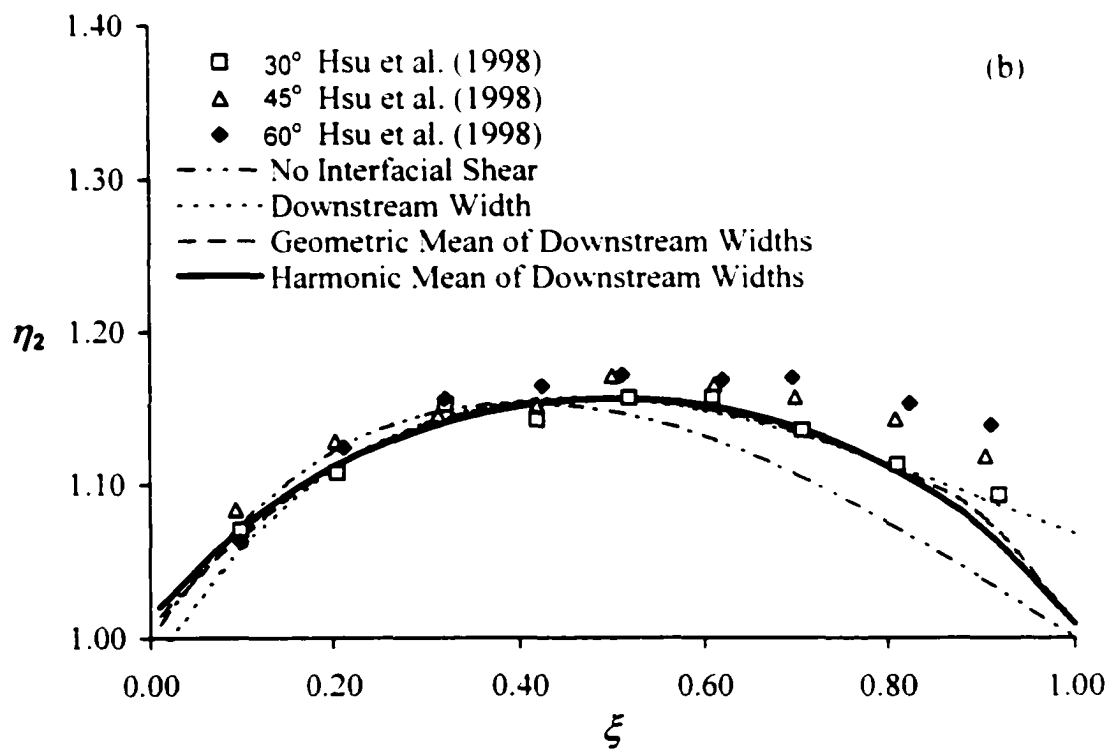
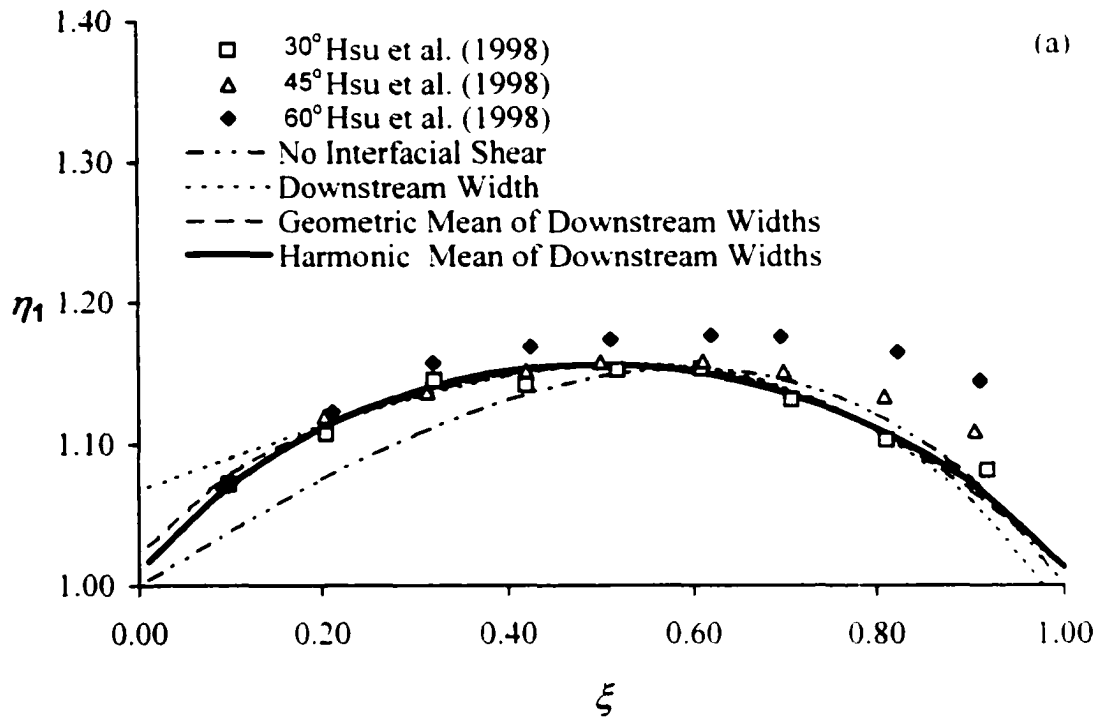
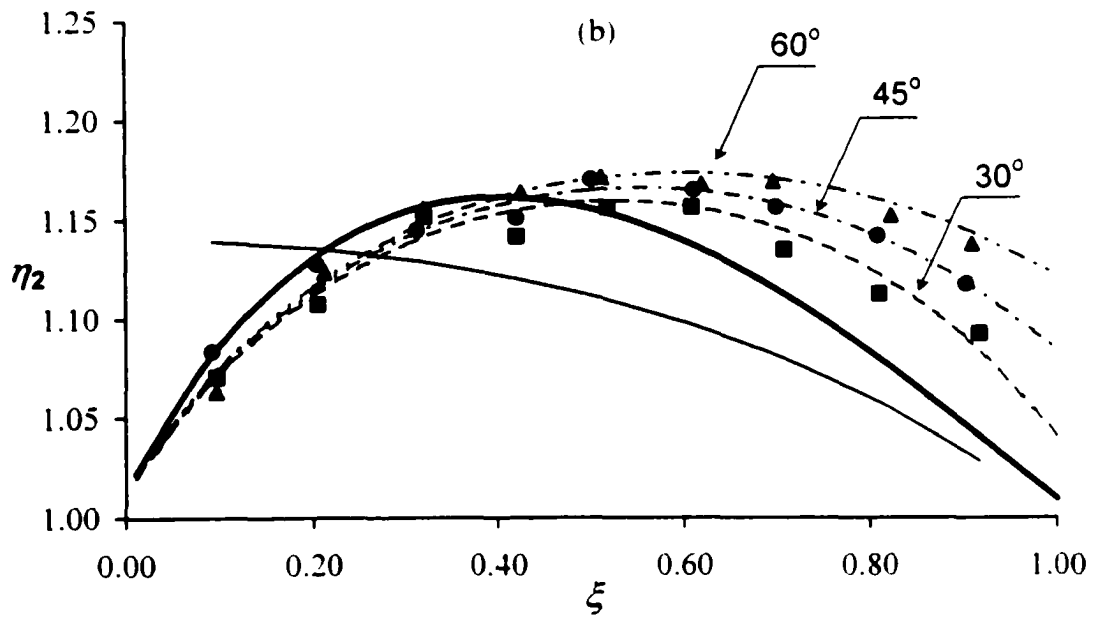
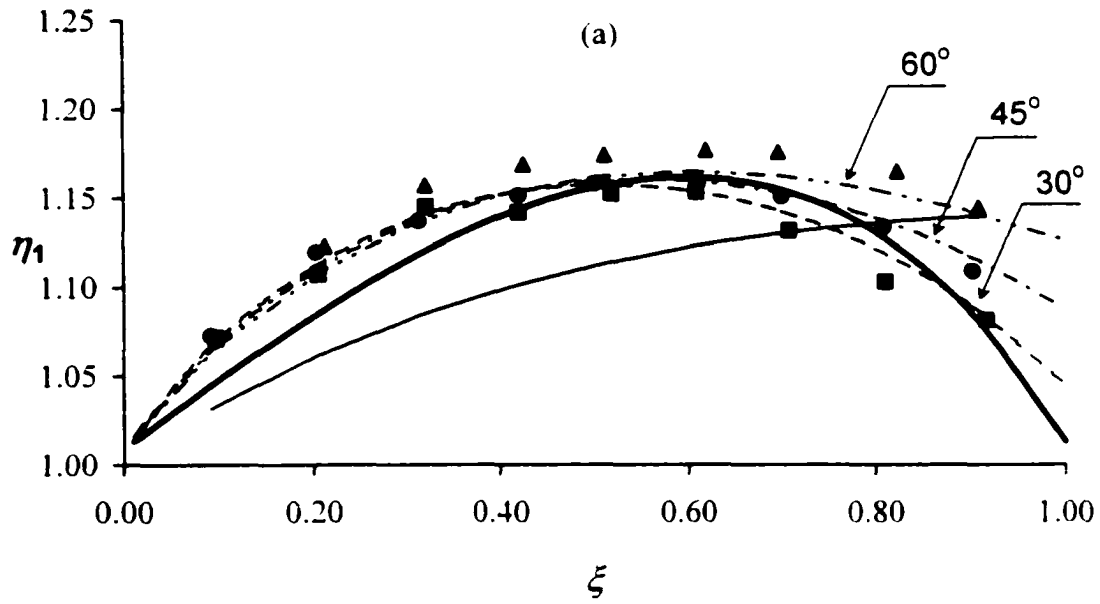


Fig. 3.14 Comparing the Theories for Interfacial Shear Length, L_s
(a) The Main Channel Depth Ratio η_1
(b) The Lateral Channel Depth Ratio η_2



**Fig. 3.16(a-b) The Final Model Results.
Comparison with Hsu et al. (1998)**

- | | |
|---------------------------------------|---------------------------------------|
| ■ 30° Hsu et al. (1998) | ● 45° Hsu et al. (1998) |
| ▲ 60° Hsu et al. (1998) | — Energy Approach |
| — Momentum $K^*=0, K=0$ | - - - Momentum $K^*=0.26, K=0.09$ |
| - · - · - Momentum $K^*=0.23, K=0.23$ | - · - · - Momentum $K^*=0.21, K=0.37$ |

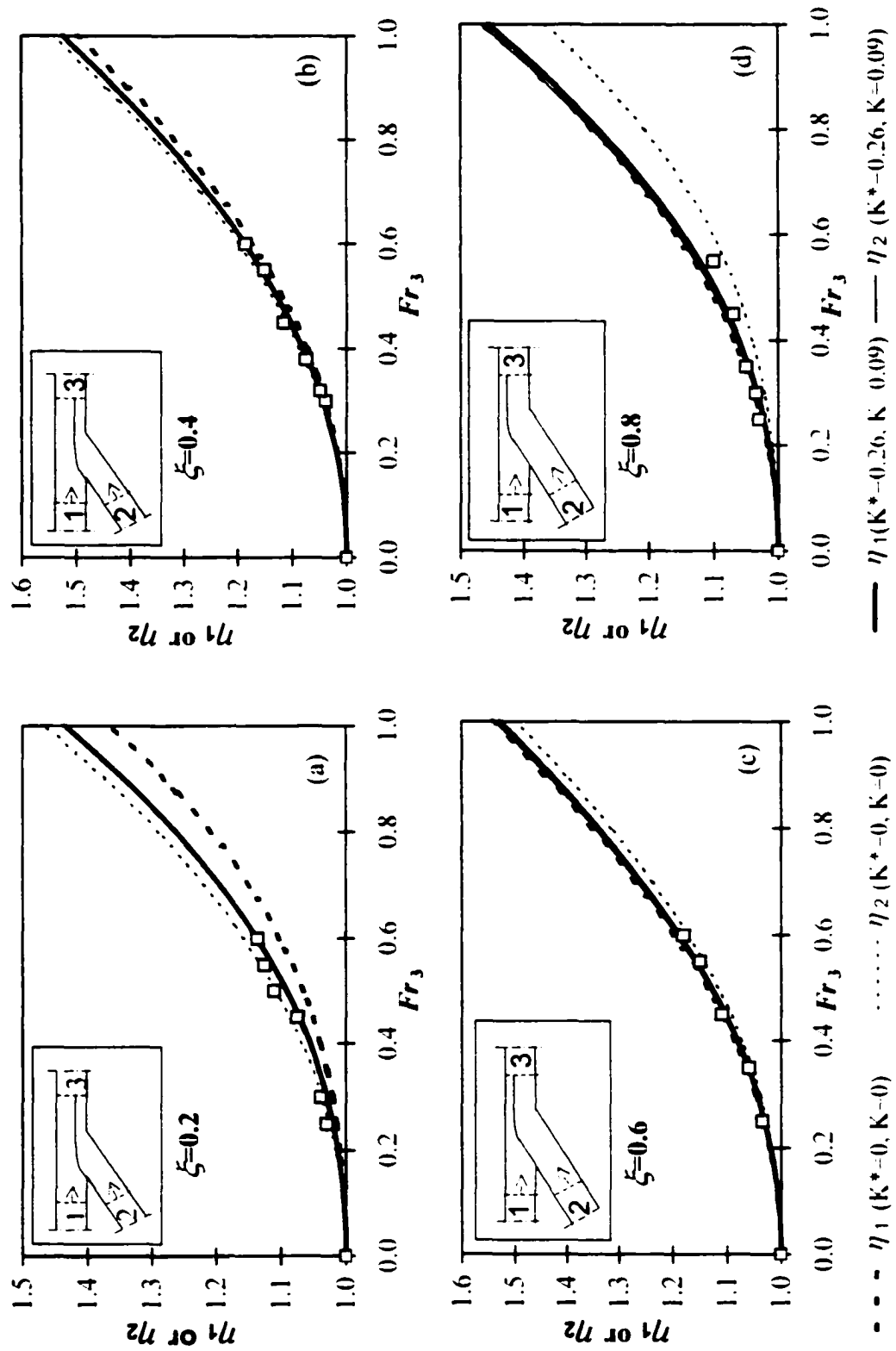


Fig. 3.17(a-d) The Final Model Results. Comparison with Webber and Greated (1966) $\delta=30^\circ$

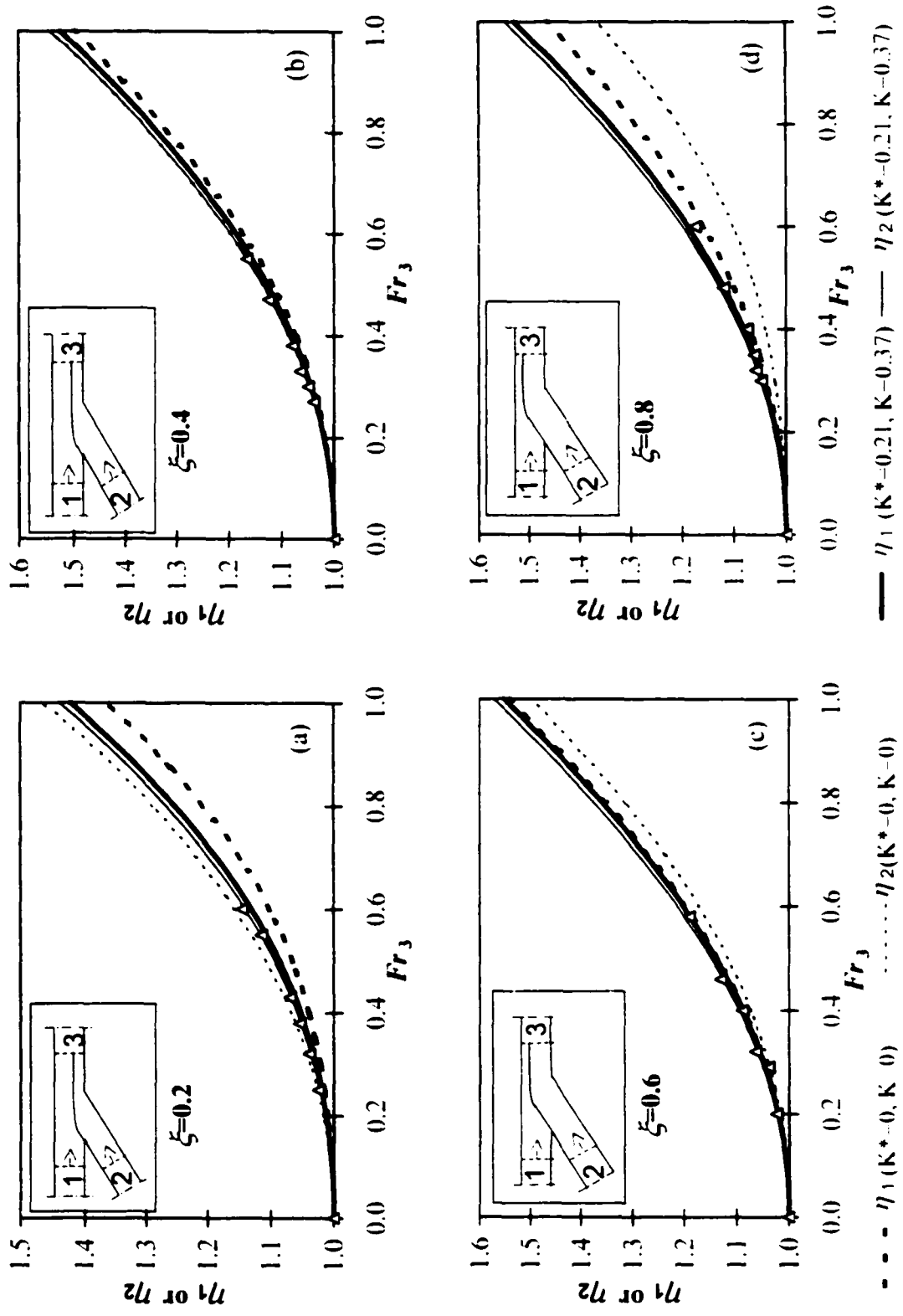


Fig. 3.18(a-d) The Final Model Results. Comparison with Webber and Greated (1966) $\delta=60^\circ$

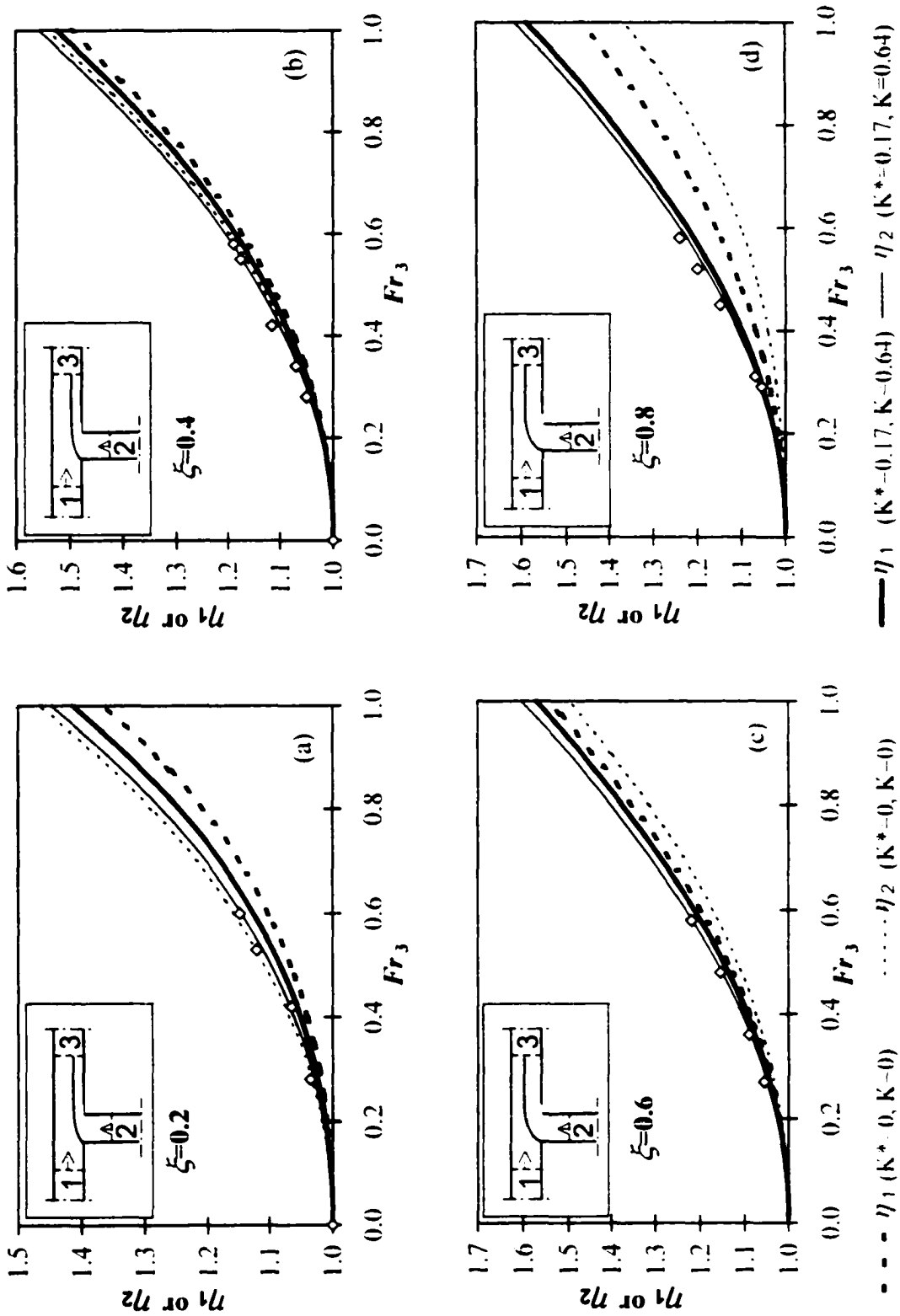
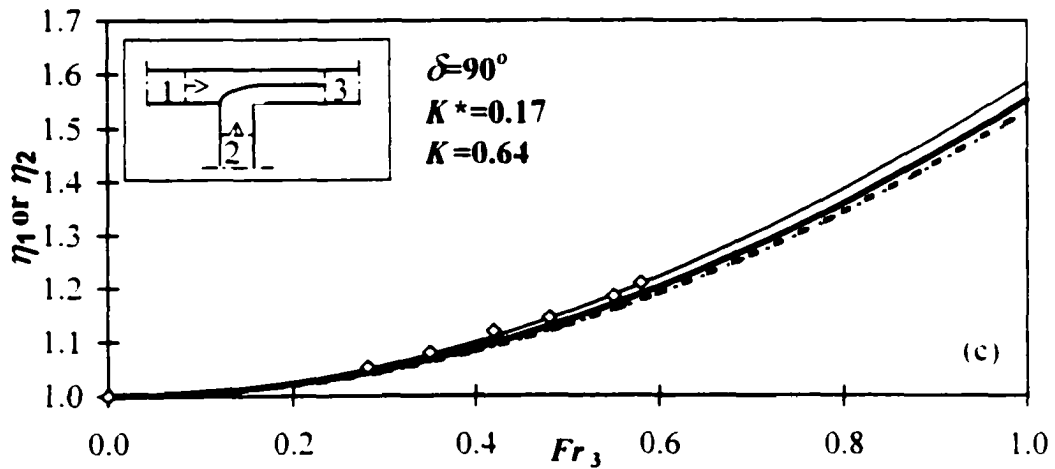
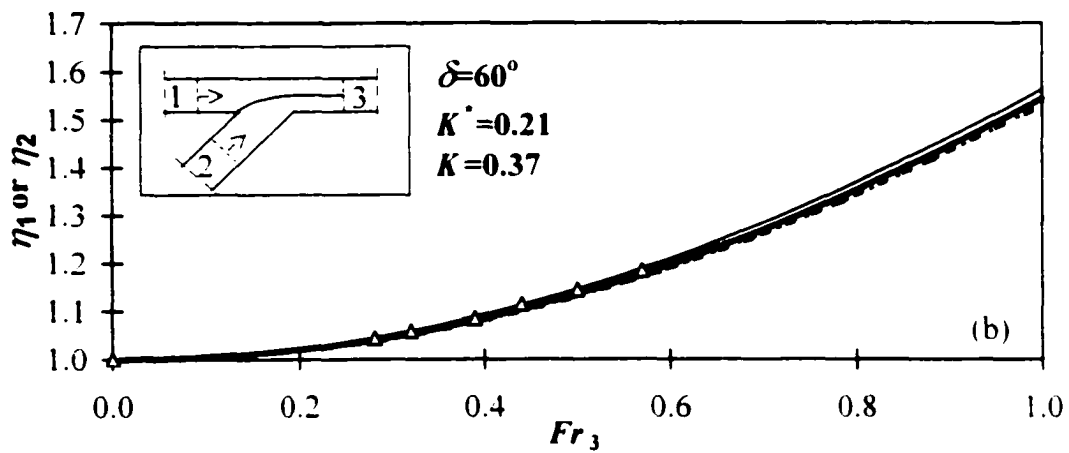
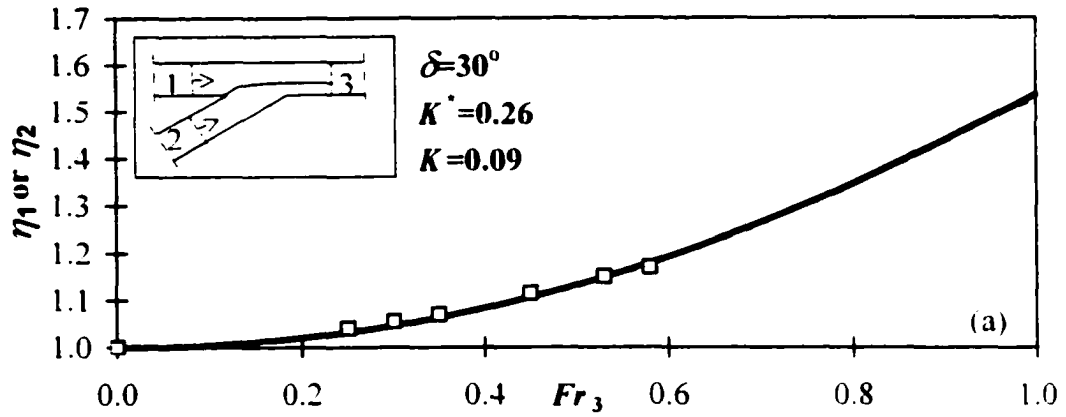
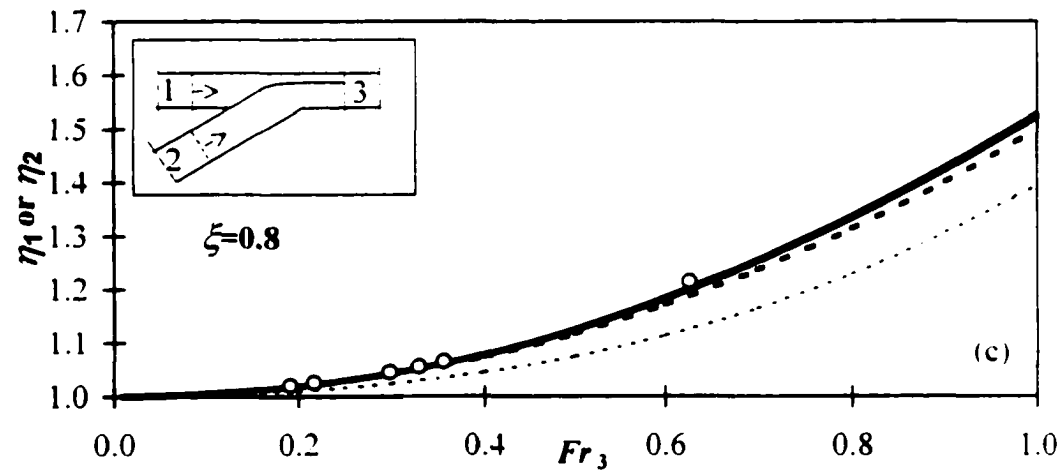
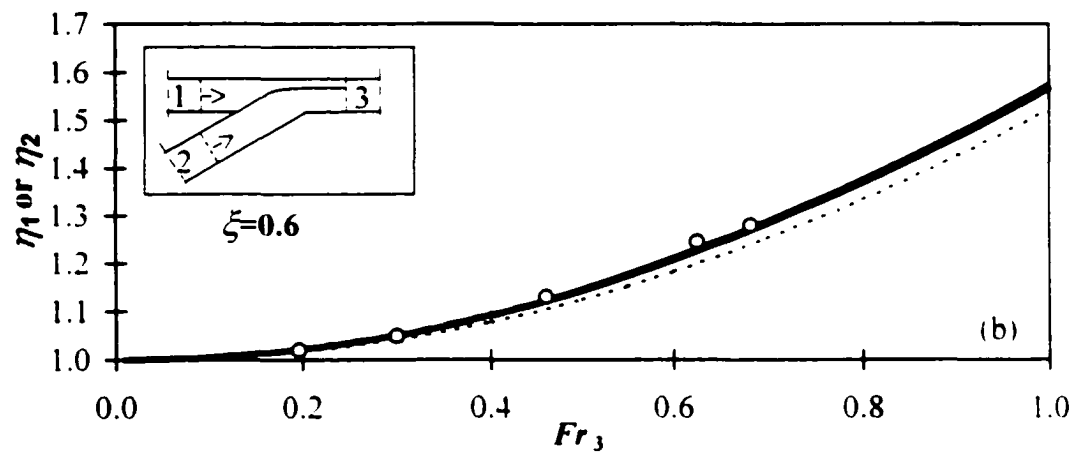
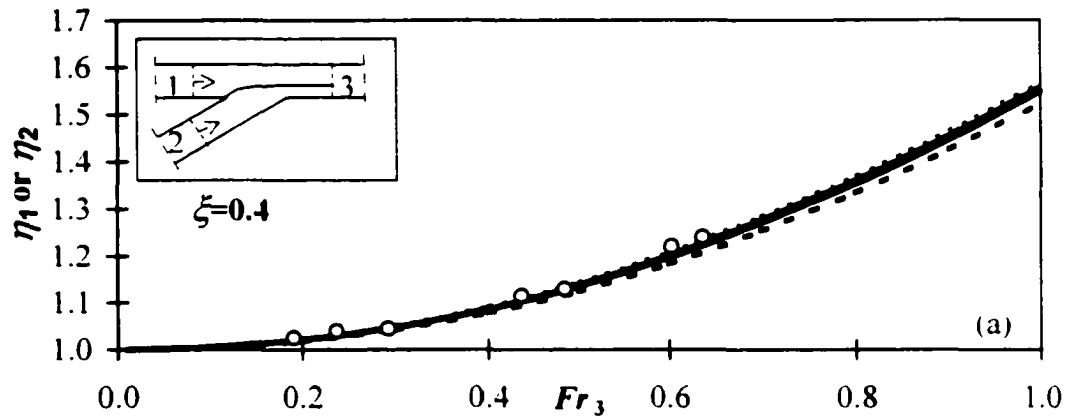


Fig. 3.19(a-d) The Final Model Results. Comparison with Webber and Greated (1966) $\delta=90^\circ$



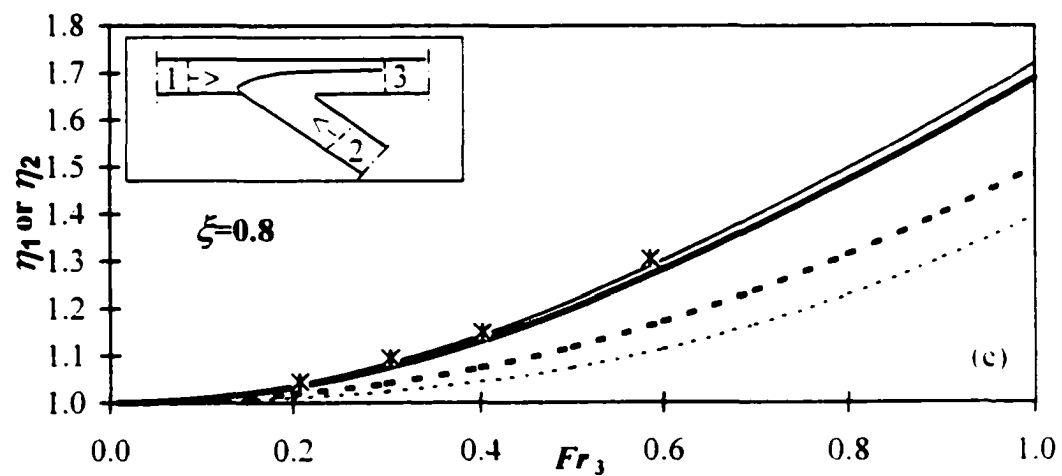
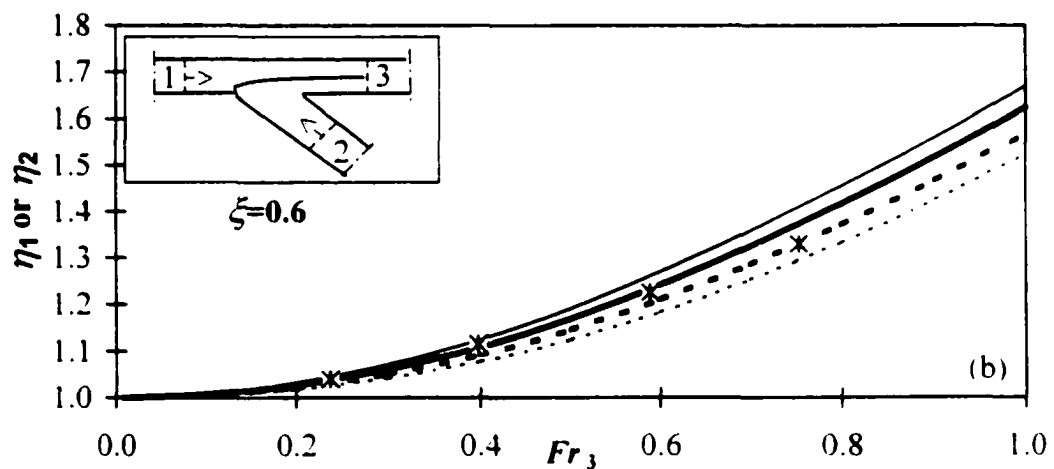
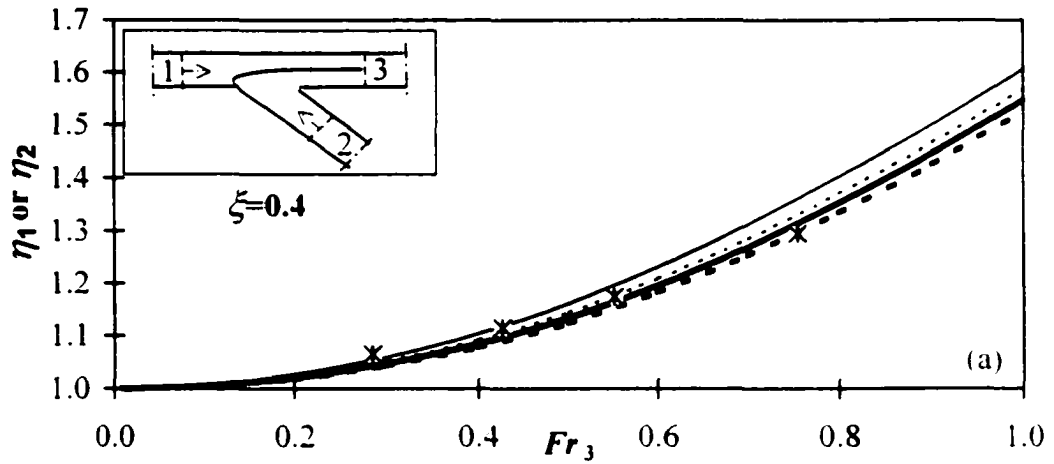
- - - η_1 No Shear Forces ······ η_2 No Shear Forces
 ——— η_1 With Shear Forces ——— η_2 With Shear Forces

**Fig. 3.20(a-c) The Final Model Results.
Comparison with Webber and Greated (1966) $\xi=0.5$**



- - - η_1 ($K^*=0, K=0$) ······ η_2 ($K^*=0, K=0$)
 ——— η_1 ($K^*=0.23, K=0.23$) ——— η_2 ($K^*=0.23, K=0.23$)

**Fig. 3.21(a-c) The Final Model Results.
Comparison with Taylor (1944) $\delta=45^\circ$**



- - - $\eta_1(K^*=0, K=0)$ ······ $\eta_2(K^*=0, K=0)$
 ——— $\eta_1(K^*=0.10, K=1.06)$ ——— $\eta_2(K^*=0.10, K=1.06)$

**Fig. 3.22(a-c) The Final Model Results.
Comparison with Taylor (1944) $\delta=135^\circ$**

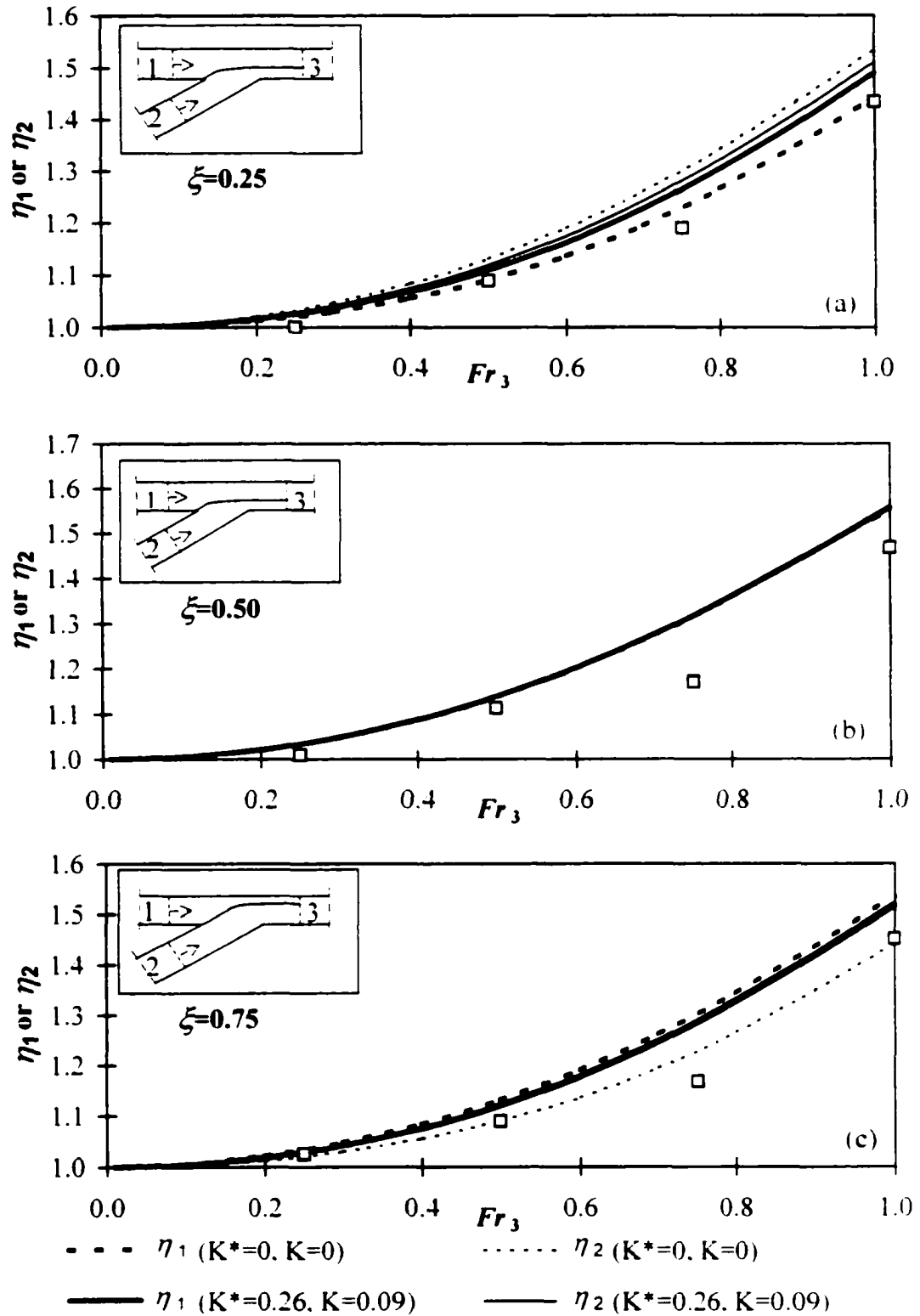


**Fig. 3.23(a-c) The Final Model Results.
Comparison with Gurram (1994) $\delta=30^\circ$**

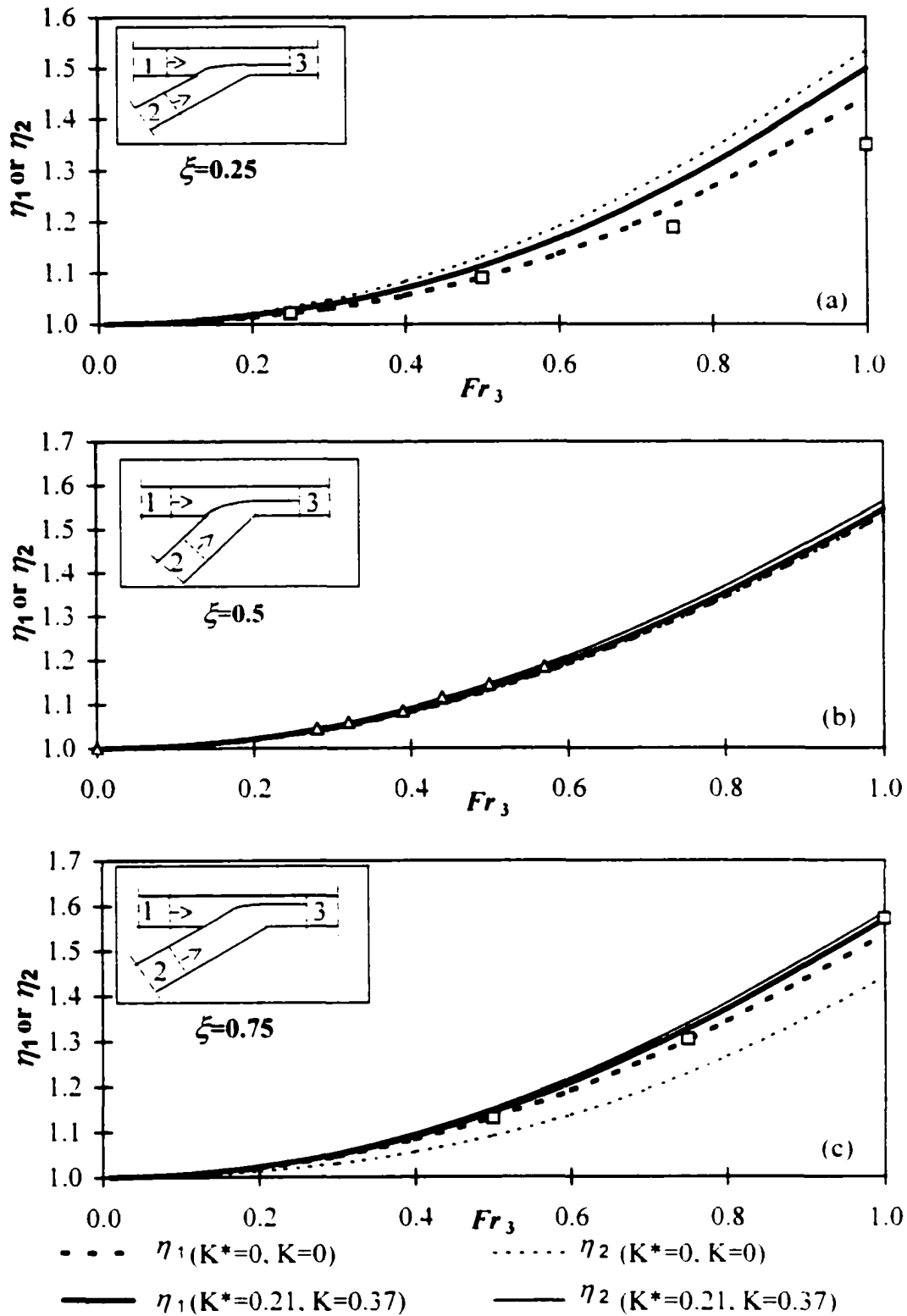


**Fig. 3.24(a-c) The Final Model Results.
Comparison with Gurram (1994) $\delta=60^\circ$**

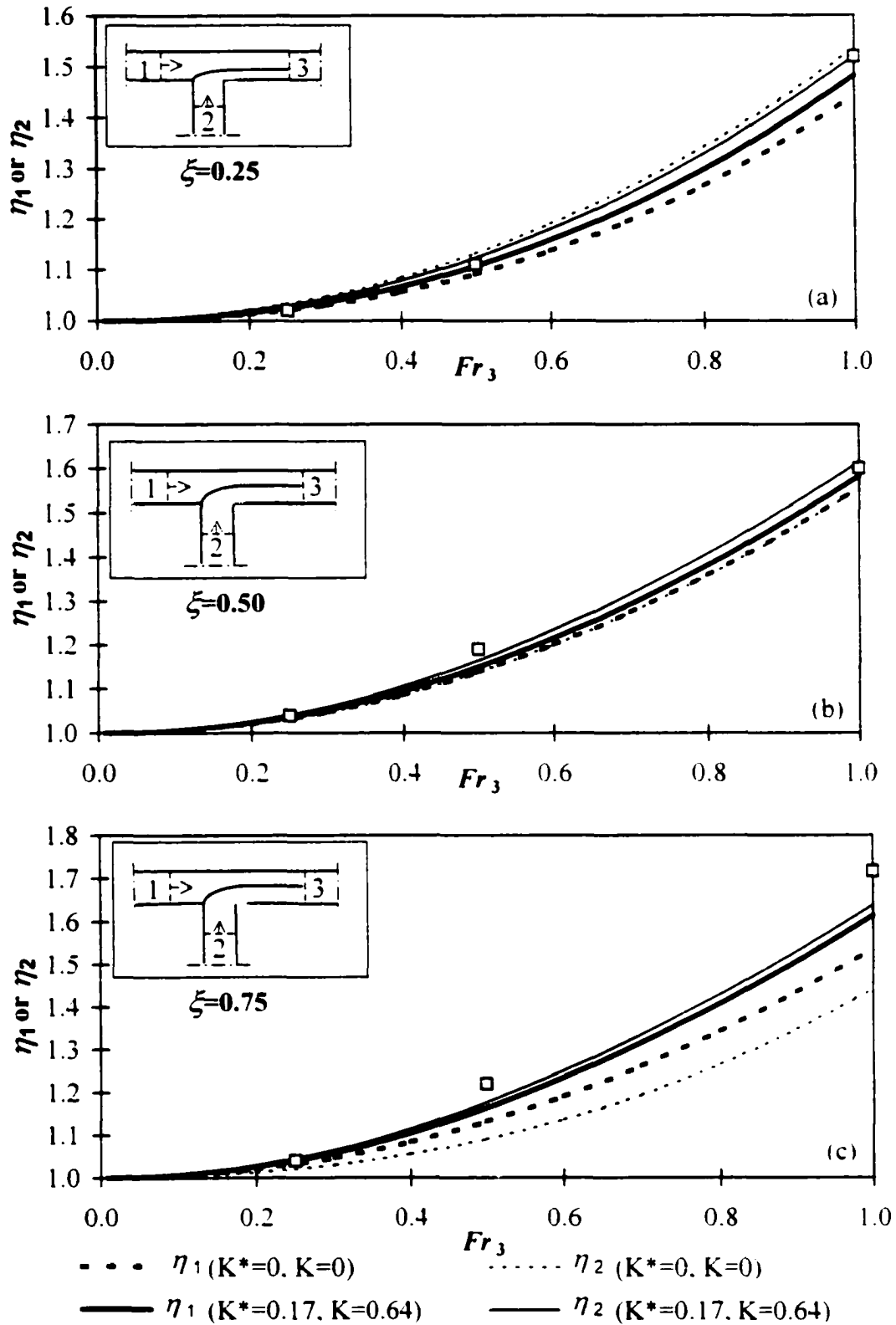


**Fig. 3.25(a-c) The Final Model Results.
Comparison with Gurram (1994) $\delta=90^\circ$**

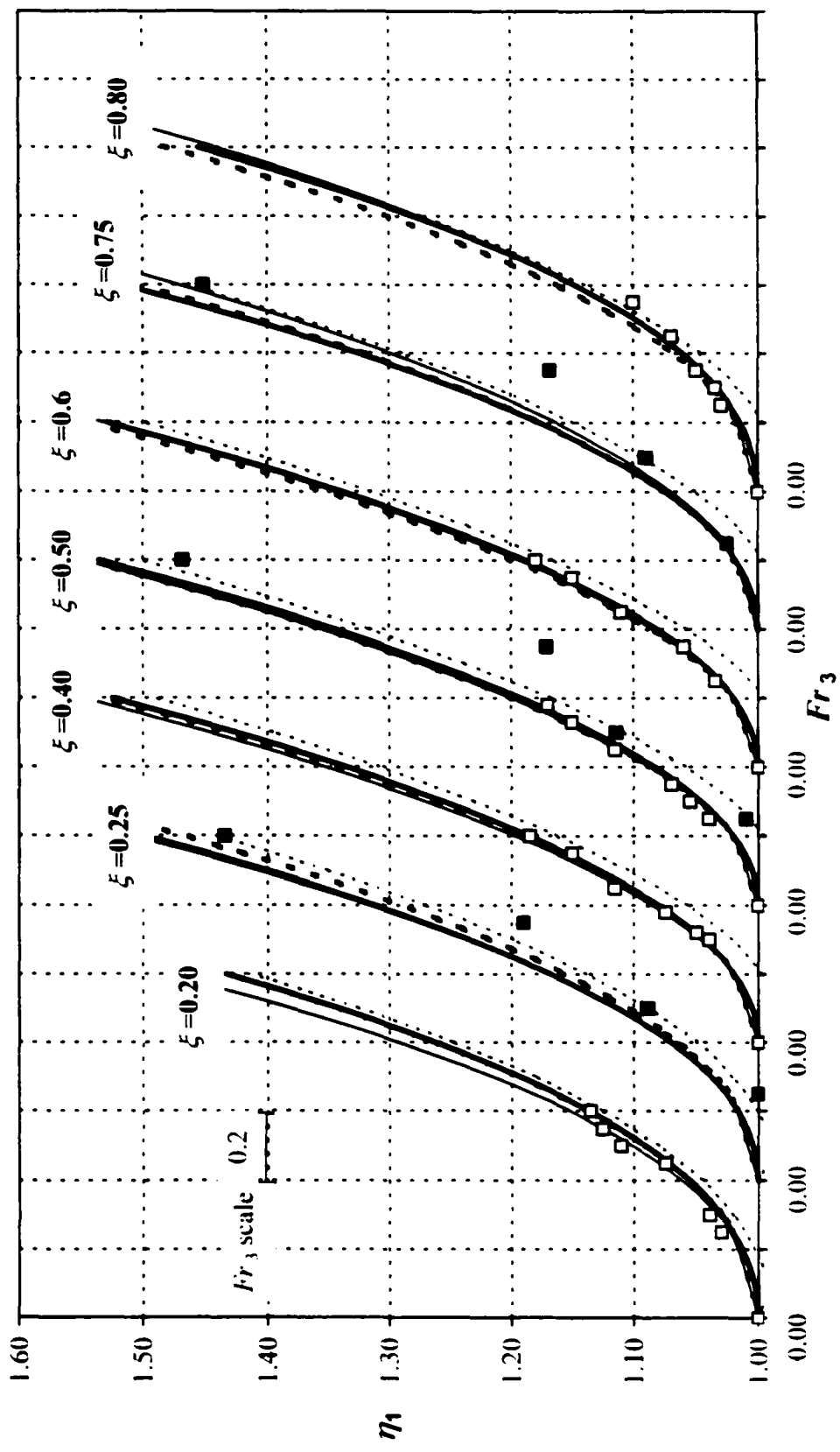


Fig. 3.26 Comparing the Different Theories ($\delta=30^\circ, K^*=0.26, K=0.09$)

- \square Webber and Greated's (1966) Data
- \blacksquare Gurram's (1994) Data
- Present Theory
- - - Taylor's (1944) Theory
- Gurram's (1994) Theory
- Webber and Greated's (1966) Theory

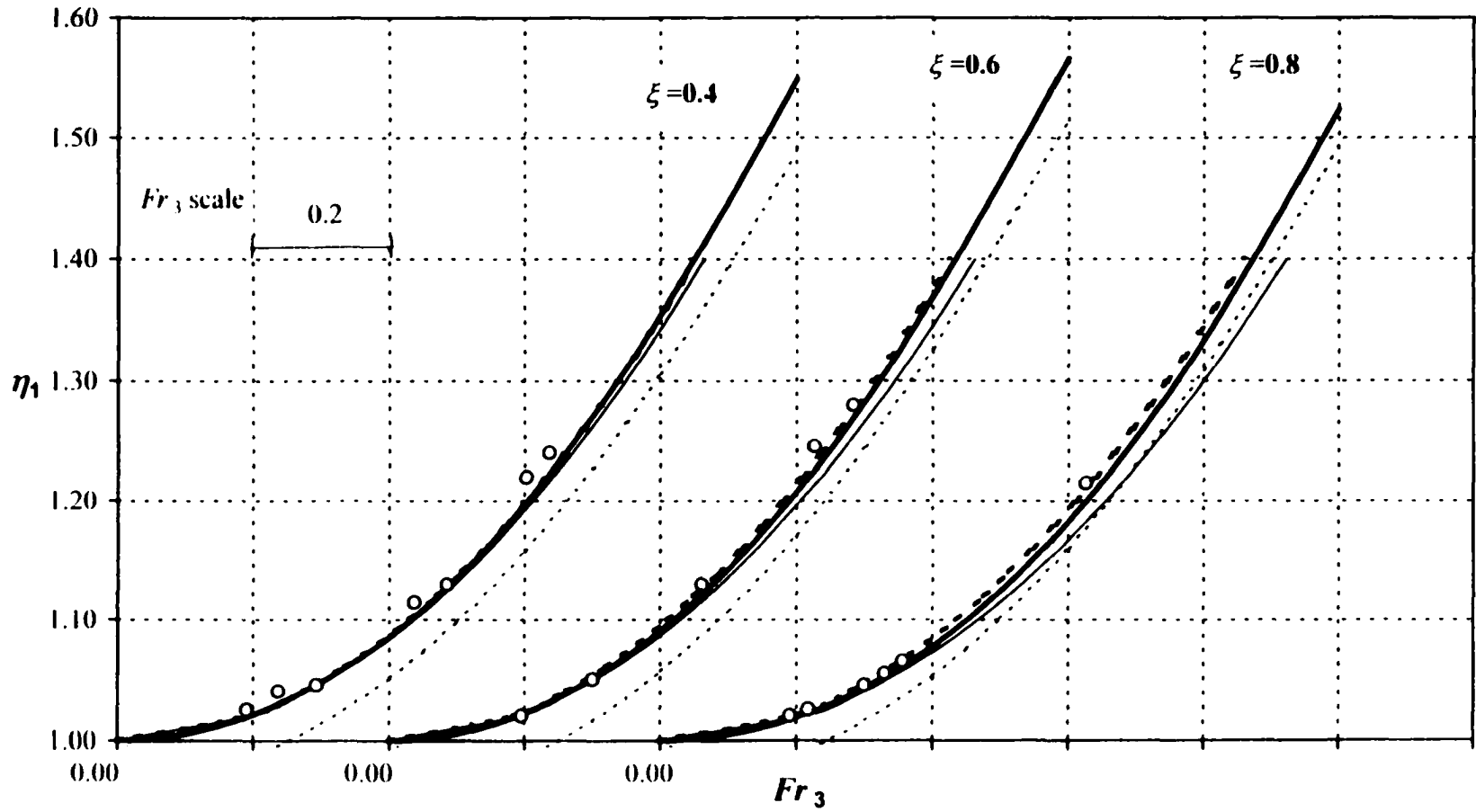


Fig. 3.27 Comparing the Different Theories ($\delta=45^\circ$, $K^+=0.23$, $K=0.23$)

- | | |
|------------------------------|--------------------------------------|
| ○ Taylor's (1944) Data | — Present Theory |
| - - - Taylor's (1944) Theory | — Webber and Greated's (1966) Theory |
| Gurram's (1994) Theory | |

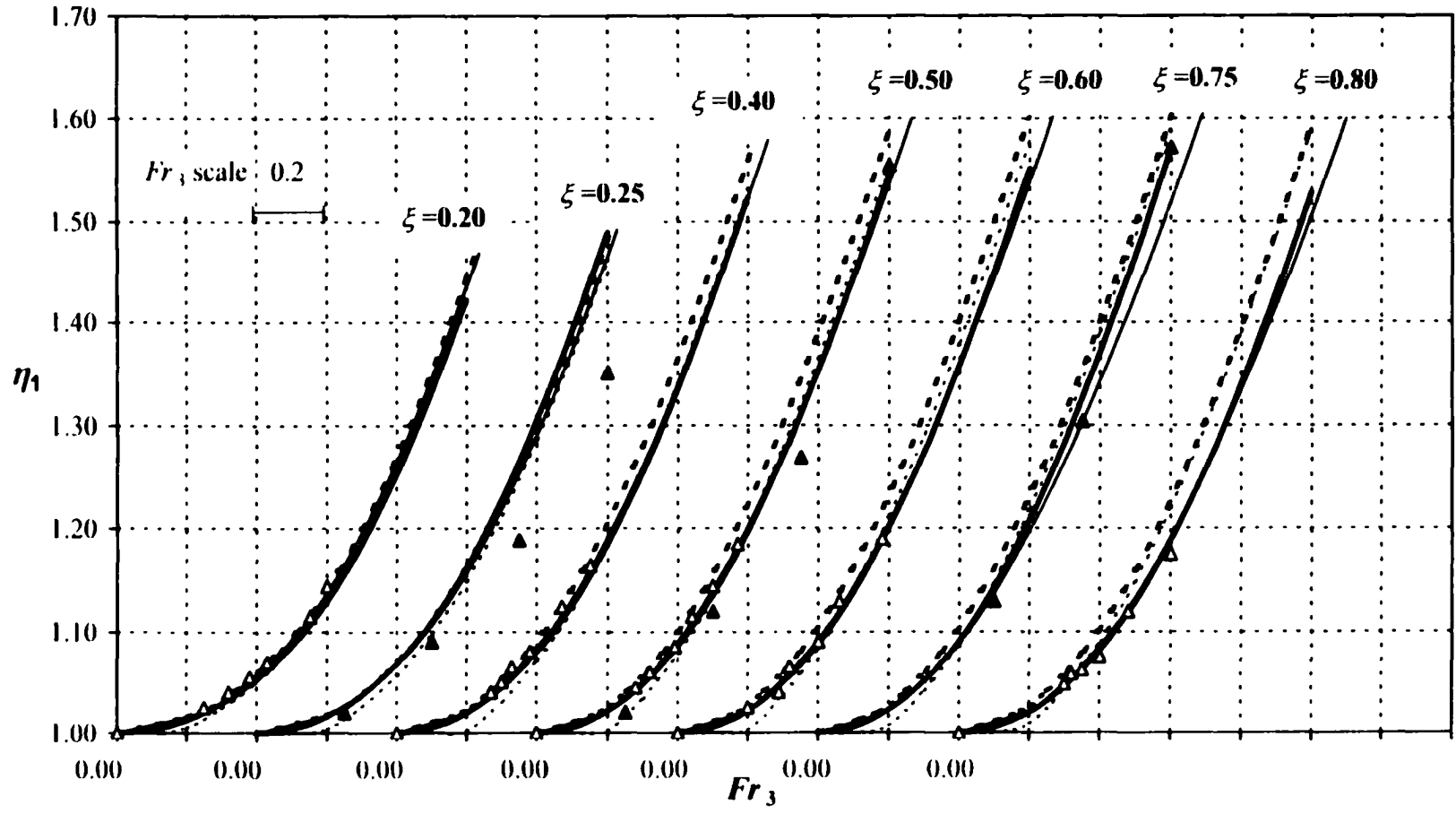


Fig. 3.28 Comparing the Different Theories ($\delta=60^\circ$, $K^+=0.21$, $K=0.37$)

- | | |
|---|---------------------------------------|
| Δ Webber and Greated's (1966) Data | \blacktriangle Gurram's (1994) Data |
| — Present Theory | - - - Taylor's (1944) Theory |
| — Webber and Greated's (1966) Theory | ⋯ Gurram's (1994) Theory |

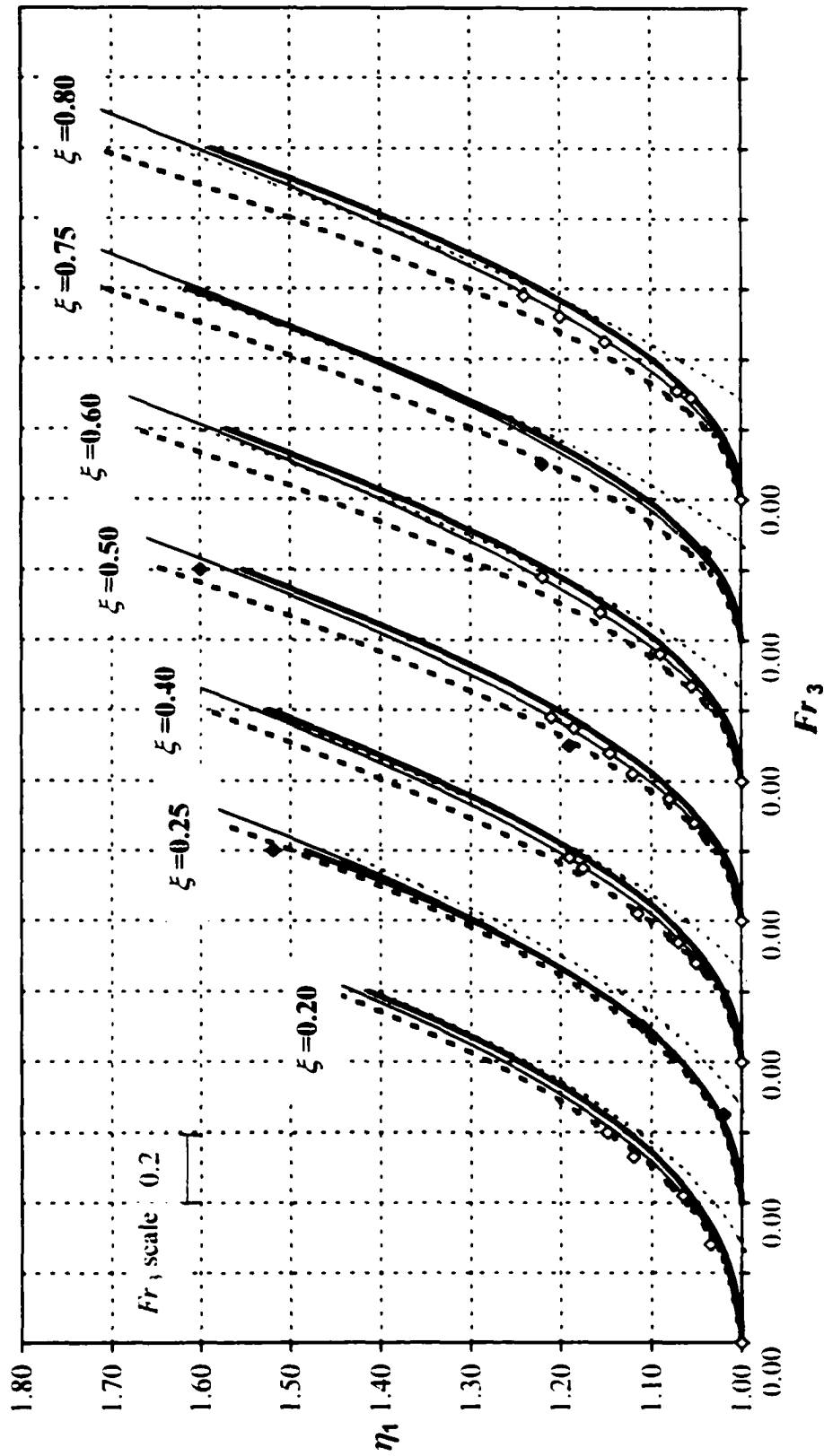


Fig. 3.29 Comparing the Different Theories ($\delta=90^\circ, K=0.17, K=0.64$)

- \diamond Webber and Greated's (1966) Data
- \bullet Gurram's (1994) Data
- Present Theory
- - - Taylor's (1944) theory
- Gurram's (1994) Theory

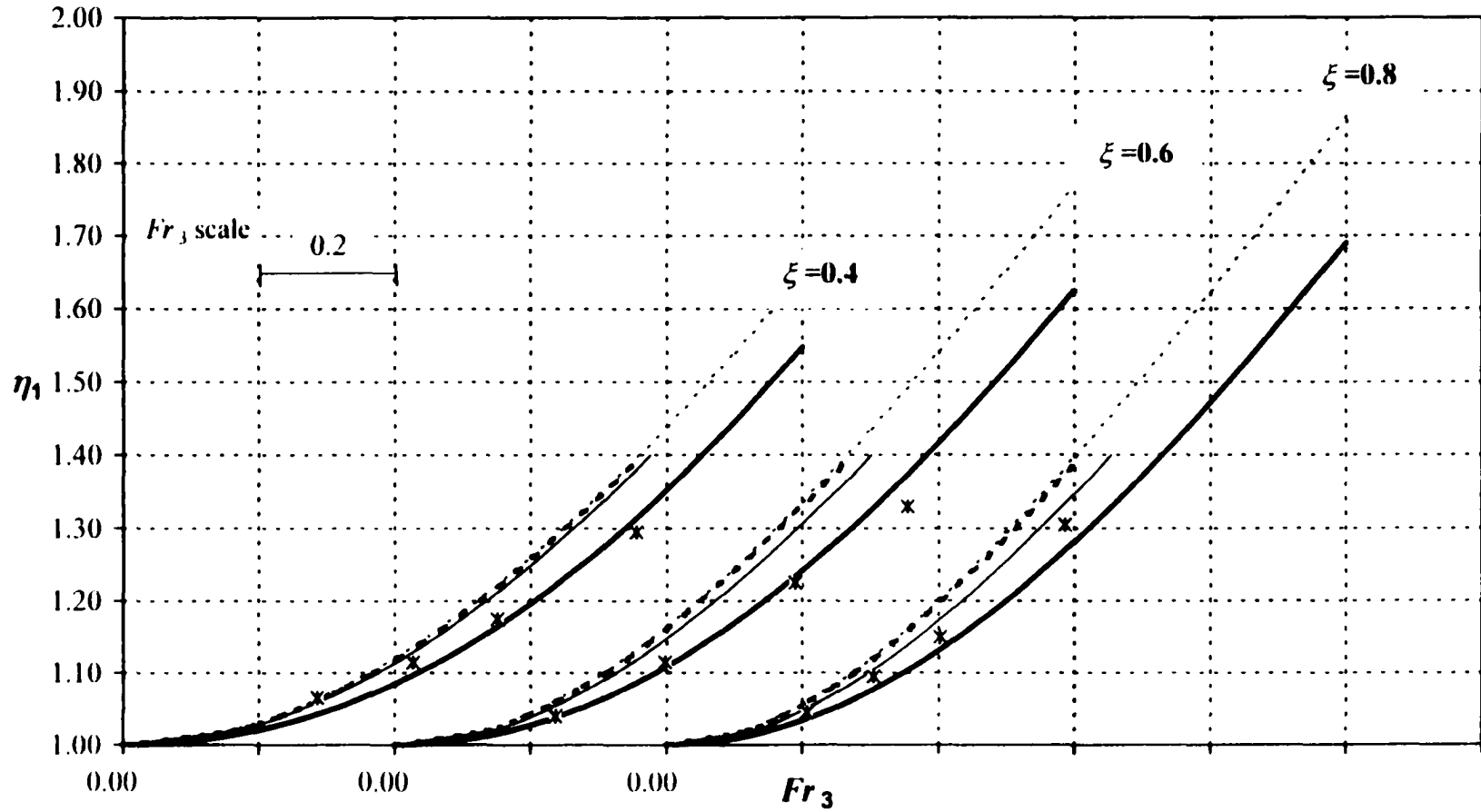


Fig. 3.30 Comparing the Different Theories ($\delta=135^\circ$, $K^*=0.1$, $K=1.06$)

- × Taylor's (1944) Data
 - - - Taylor's (1944) Theory
 - Gurram's (1994) Theory
- Present Theory
 - Webber and Greated's (1966) Theory

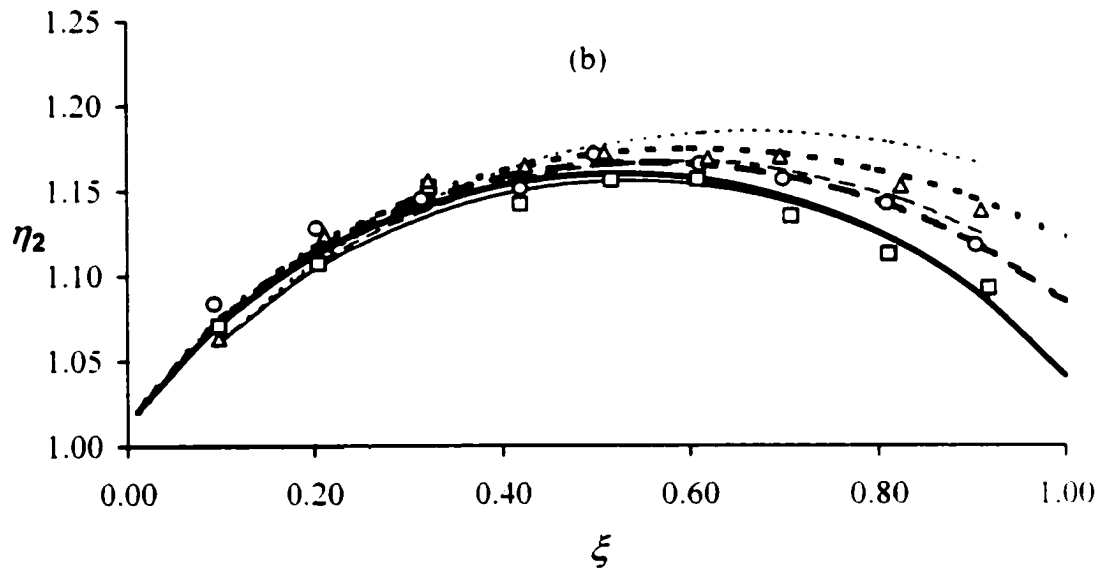
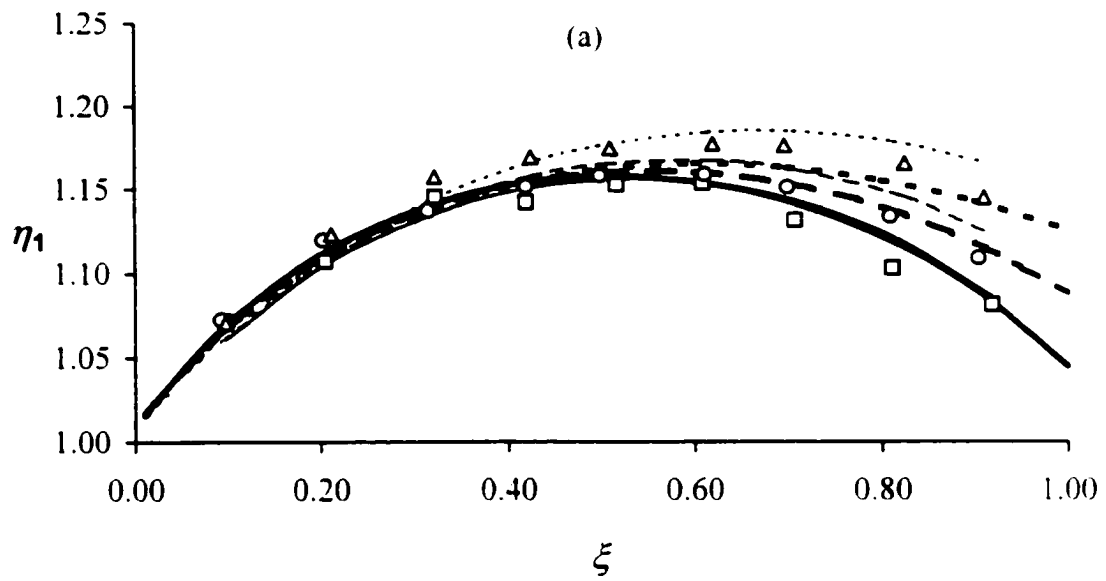


Fig 3.31 Comparison with The Theory of Hsu et al. (1998)

(a) The Main Channel Depth Ratio η_1

(b) The Lateral Channel Depth Ratio η_2

- | | |
|------------------------------------|------------------------------------|
| □ 30° Hsu et al. (1998) | ○ 45° Hsu et al. (1998) |
| △ 60° Hsu et al. (1998) | — 30° Present Theory |
| — — 45° Present Theory | - - - 60° Present Theory |
| — 30° Hsu et al. (1998) Theory | - - - 45° Hsu et al. (1998) Theory |
| 60° Hsu et al. (1998) Theory | |

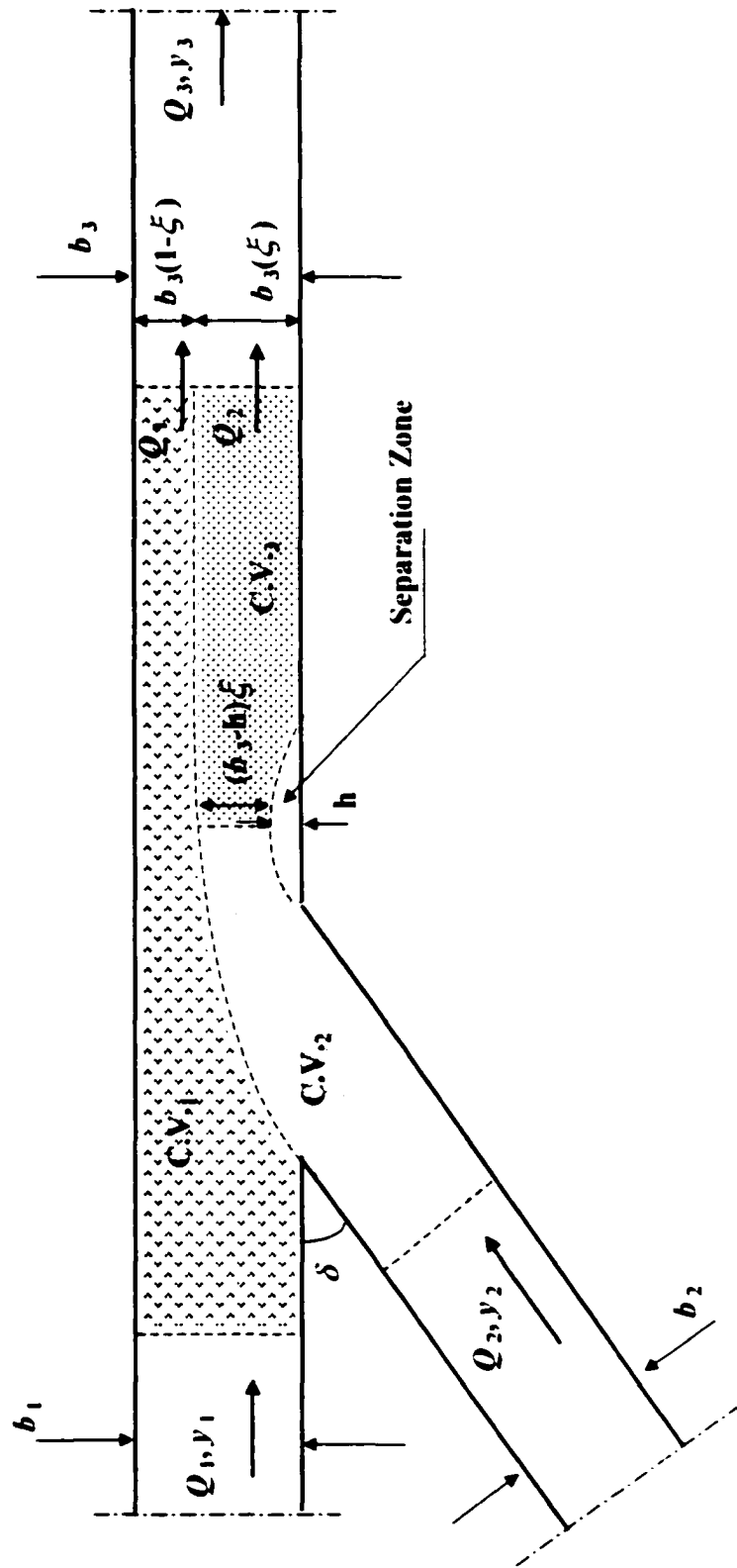


Fig. 3.32 Combining Junction with Three Control Volumes Configuration

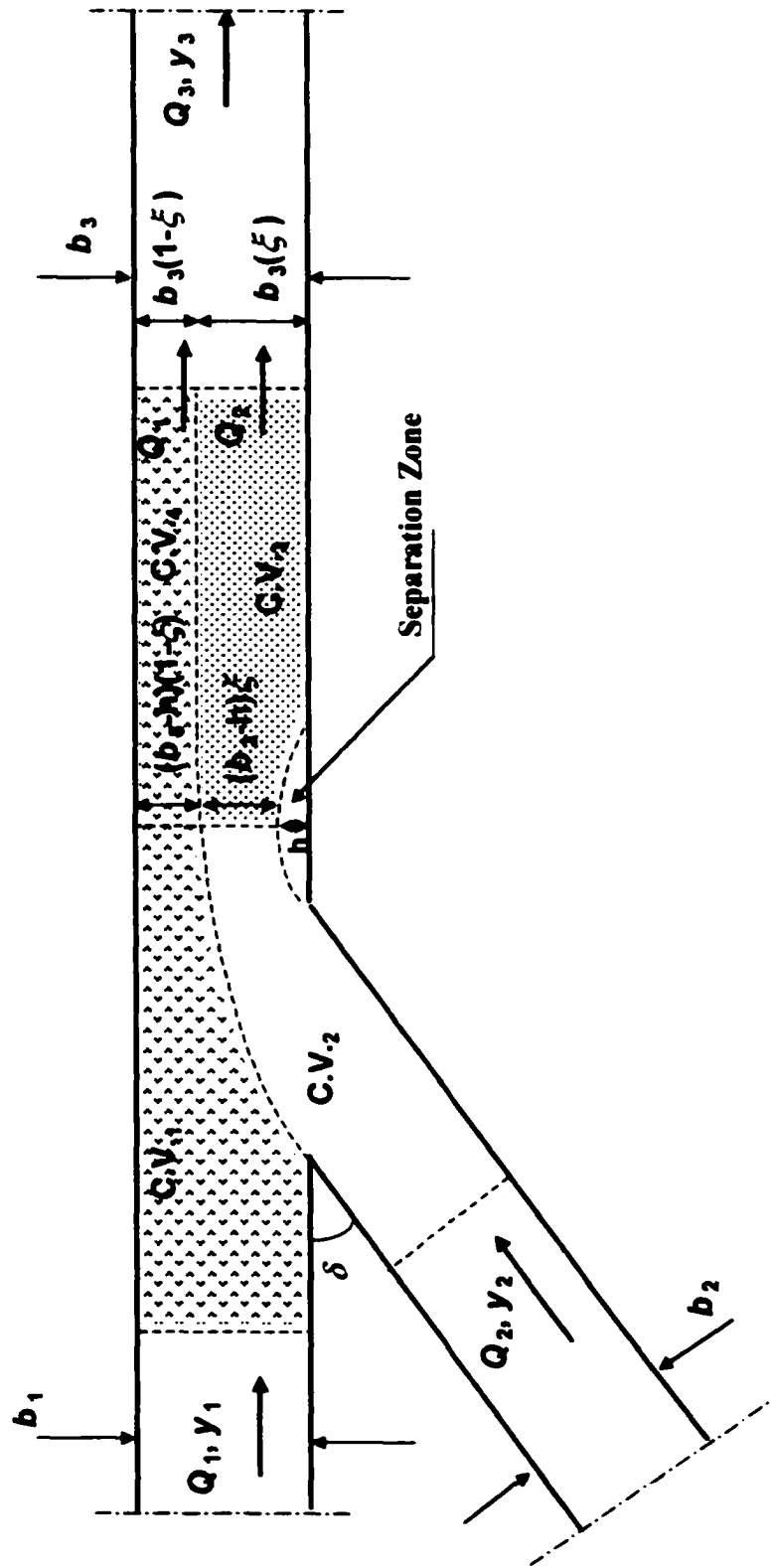


Fig. 3.33 Combining Junction with Four Control Volumes Configuration

Chapter 4

Theoretical Model for Subcritical Dividing Flows*

4.1 Introduction

The study of dividing junction flows in open channels is considered the complementary part to that of the combining flows presented in the previous chapter. Together they have a direct application in the design of water and waste water treatment plants, irrigation and drainage canals, and in the analysis of natural river network systems. The problem of the dividing flows is different from that of the combining ones.

“It can be stated as: when a given stream splits into two branches, what is the flow division?” (Taylor 1944). The analysis of the dividing flow problem *“is considerably more difficult than that of the combining flow for the following reason: In the combining flow case it was possible to assume that the depths in the tributary channels were equal immediately above the junction. No analogous assumption is permissible in the case of the dividing flow.”* such an assumption may be *“almost identical to assuming the solution to the problem”* (Taylor 1944).

“The complex flow phenomena at dividing junctions are usually associated with considerable energy losses. The transverse pressure gradients in the vicinity of the lateral channel entrance induce regions of

* Preliminary results for the content of this chapter were published in the 1999 Canadian Society of Civil Engineers Annual Conference, Hydrotechnical Engineering Speciality Conference, Regina, Saskatchewan, pp. 11-20.

* The main content of this chapter is under review in the Journal of Hydraulic Engineering, ASCE, for possible publication.

mean velocity gradients, depth varying surfaces of flow division and separation, vortices, and zones of flow reversal” (Neary and Odgaard 1999).

However, most numerical models of open channel networks currently neglect energy losses and differences in velocity heads and assume the equality of the water surface elevations at the junctions. The purpose of this study is to provide a set of internal boundary conditions based on momentum conservation to enhance the handling of dividing junctions in open channel network models especially for dynamic flow situations where the assumption of equal water surface is not applicable. This set of interior equations is consistent with those presented in the previous chapter for combining flows as well as the St. Venant equations handling the channel reaches. This is achieved by trying to model most of the physical effects in the problem, thereby avoiding the assumption of the equality of the water surface elevations at these junctions. Meanwhile, this study investigates the significance of the various flow phenomena occurring at these junctions.

4.2 Proposed Theoretical Approach

Fig. 4.1 shows the junction geometry to be considered in the analysis. Subscripts 1, 2, and 3 indicate the upstream section of the main channel, the branch channel outflow section and the downstream section of the main channel, respectively. The variables of the problem are the three flow depths, y_1 , y_2 , and y_3 and the three discharges Q_1 , Q_2 and Q_3 , at the end points of all the intersecting channels. For the steady subcritical flow case, the boundary conditions supply three of these variables; the inflow discharge, Q_1 , and

two downstream conditions; those can be either fixed depths or depth discharge relationships. Thus, three equations are required to close the problem.

Analogous to the combining flow theory, the junction is divided into two control volumes one for the main channel flow and the other for the lateral channel flow. The control volumes are bounded by streamlines such that there are no lateral mass fluxes. The channels are all assumed to be of rectangular cross section. The streamline curvature is considered to be small and vertical accelerations to be negligible, hence the vertical pressure distribution is hydrostatic. Uniform velocity distributions and parallel streamlines are assumed at the inflow and outflow sections of the control volumes. Thus, the inflow width is divided between the two control volumes in terms of the discharge ratio, $\xi = Q_2/Q_1$.

Applying overall mass and momentum conservation in the streamwise direction to each of the two control volumes in the junction provides the three interior equations required to close problem. Overall mass conservation gives:

$$Q_1 = Q_2 + Q_3 \quad (4.1)$$

Conservation of momentum in the streamwise direction for the main channel control volume, C.V.₁, gives:

$$-\rho Q_3 V_1 + \rho Q_3 V_3 = P_{11} - P_3 + B_1 + W_1 - F_{b1} + F_c - F_{s1} \quad (4.2)$$

Considering that the geometric effects that are occurring on opposite sides of the central streamline of the lateral channel control volume, due to curvature, tend to compensate, then conservation of momentum for the lateral channel control volume, C.V.₂, is:

$$-\rho Q_2 V_1 + \rho Q_2 V_2 = P_{12} - P_2 + B_2 + W_2 - F_{b2} - F_{s2} \quad (4.3)$$

where: ρ is the water density, V is the mean velocity, P is the hydrostatic water pressure force acting on the control surface, W is the weight component in the direction of the slope, B is the pressure force component due to the change in the control volume width, F_b is the friction force acting on the solid boundaries of the control volumes, F_s is the shear force due to the separation zone, and F_c is the centrifugal force acting on the main channel control volume due to the flow curvature in the lateral channel control volume. F_c is not included in the analysis of the lateral channel control volume as it is acting in the transverse direction.

4.2.1 Hydrostatic Pressure Forces

The hydrostatic forces: P_{11} ; P_3 ; P_{12} ; and P_2 , are due to the water pressure on the upstream and downstream boundaries of the two control volumes with the first subscript representing the section and the second subscript representing the control volume. These forces are given by:

$$P = \frac{1}{2} \gamma y^2 b \quad (4.4)$$

where: y is the depth of water, γ is the specific weight of water, and b is the width of the channel at the section under consideration.

4.2.2 Pressure Force due to Divergence

The pressure force due to divergence, B , acts on the longitudinal boundaries of each control volume. It can be written in a general form as:

$$B = \int_n^n \frac{\gamma y^2}{2} \frac{db}{ds} ds \quad (4.5)$$

where: s is the spatial coordinate along the streamwise direction, and n and m are the limits of the control volume in the s direction (Fig. 4.1).

The variation in width with distance, db/ds , is the difference between the upstream and downstream widths for each control volume. Analogous to the combining flow analysis, the depth along the longitudinal boundaries may be approximated as the average of the downstream depths and the force takes the form:

$$B_1 = \frac{1}{2} \gamma \left(\frac{y_2 + y_3}{2} \right)^2 (b_3 - b_1 (1 - \xi)) \quad (4.6)$$

for C.V.₁ and for C.V.₂:
$$B_2 = \frac{1}{2} \gamma \left(\frac{y_2 + y_3}{2} \right)^2 (b_2 - b_1 \xi) \quad (4.7)$$

Another approximation based on the upstream depth can be used where:

$$B_1 = \frac{1}{2} \gamma y_1^2 (b_3 - b_1 (1 - \xi)) \quad (4.8)$$

for C.V.₁ and for C.V.₂:
$$B_2 = \frac{1}{2} \gamma y_1^2 (b_2 - b_1 \xi) \quad (4.9)$$

An average form of the above two approaches can be used where the average of the upstream depth and the two downstream depths in the junction is used thus giving:

$$B_1 = \frac{1}{2} \gamma \left[\frac{y_1 + \left(\frac{y_2 + y_3}{2} \right)}{2} \right]^2 (b_3 - b_1 (1 - \xi)) \quad (4.10)$$

for C.V.₁ and for C.V.₂:
$$B_2 = \frac{1}{2} \gamma \left[\frac{y_1 + \left(\frac{y_2 + y_3}{2} \right)}{2} \right]^2 (b_2 - b_1 \xi) \quad (4.11)$$

In the dividing flow case the boundary conditions generally provide the two downstream depths, y_2 and y_3 , and the inflow discharge, Q_1 . The three model equations, with the pressure forces only, can be used to compute the outflow discharges, Q_2 and Q_3 , and the upstream depth, y_1 . The three formulations for the pressure due to divergence are tested with a sample of the experimental data (Taylor (1944)). Fig. 4.2 presents the variation of the discharge ratio, ξ , with the downstream depth ratio $\eta_2=y_2/y_3$. The figure shows a comparison between the model computations and Taylor's (1944) dividing flow experimental data for the four upstream Froude numbers that he investigated. The comparisons indicate that the model does not give good agreement with the data for any of the formulations tested. This may be due to the significance of the other forces that are not included at this stage of the analysis. Consequently, the choice of the best formulation for the divergence pressure will be postponed until more physical effects are included.

4.2.3 Weight

W_1 and W_2 are the weight components in the direction of the slope for C.V.₁ and C.V.₂, respectively. These forces are computed as:

$$W_1 = \gamma \left(\frac{A_{11} + A_3}{2} \right) L_1 S_o \quad (4.12)$$

$$W_2 = \gamma \left(\frac{A_{12} + A_2}{2} \right) L_2 S_o \quad (4.13)$$

where: A is the average cross sectional area at the section under consideration with the first subscript representing the section and the second subscript representing the control volume, S_o is the longitudinal slope of the junction and L_1 and L_2 are the lengths of C.V.₁ and C.V.₂, respectively.

4.2.4 Boundary Friction Forces

F_{b1} and F_{b2} are the friction forces acting on the two control volumes due to the bed and the walls of the channels. These forces are equal to the average bed shear stress multiplied by the area of the solid boundary of each control volume giving:

$$F_{b1} = \rho \left(\frac{V_1}{C_*} \right)^2 (b_1(1 - \xi) + y_1)(L_1) \quad (4.14)$$

$$F_{b2} = \rho \left(\frac{V_1}{C_*} \right)^2 (b_1\xi + y_1)(L_2) \quad (4.15)$$

where: C_* is the non dimensional Chezy coefficient. The shear velocity and the cross sectional area are approximated to be in terms of the inflow section parameters of each control volume.

4.2.5 Lateral Channel Separation Zone Shear Force

F_{s2} is the shear force which acts on the lateral channel control volume due to the separation zone that form as the flow turns to enter the lateral channel as shown in Fig. 4.1. This force is computed as the average shear stress due to the difference between the flow velocity in the lateral channel control volume and that inside the separation zone, multiplied by the area of the shear interface. It may be approximated as:

$$F_{s2} = C_{f2} \frac{\rho(V_{s2})^2}{2} (y_{s2})(L_{s2}) \quad (4.16)$$

where: C_{f2} is the shear coefficient, V_{s2} is the shear velocity on the interface of the separation zone, y_{s2} and L_{s2} are the depth and the length of the separation interface, respectively. In a manner analogous to the calculation of the separation zone shear force

for the combining flows, the depth of the interface is approximated to be the upstream depth and the length of the interface is approximated to be the upstream width of the lateral channel control volume. Further, $V_{s,2}$ is approximated to be the cross sectionally averaged longitudinal velocity at the inflow section, V_1 . Putting all of the coefficients and approximations into one coefficient, K_{d2} , this shear force can be written in the form:

$$F_{s,2} = K_{d2} \rho V_1^2 (y_1 b_1 \xi) \quad (4.17)$$

This force can be also approximated based on the parameters of the outflow section of the lateral channel control volume to give:

$$F_{s,2} = K_{d2} \rho V_2^2 (y_2 b_2) \quad (4.18)$$

For the dividing flow case, the lateral channel separation shear force is more significant than that for the combining flow case. Including this force in the computations considerably improves the ability of the model to predict discharge ratios. Consequently, the choice of the best formulation for the divergence pressure as well as that for the lateral channel separation can be now pursued. Figs. 4.3-4.8 present the comparisons between the model predictions for the discharge ratio and Taylor's (1944) experimental data. The computations for the proposed momentum approach are presented for two cases: the first where the lateral channel separation shear force is not included and the second where it is included. Different combinations for the formulations of the divergence pressure and the lateral channel separation shear forces are tested. The value of the lateral channel separation shear coefficient, K_{d2} , is calibrated first for each set of experiments with a constant upstream Froude number, Fr_1 , and for each model formulation. The calibration is based on a least squares error analysis between the computed and the measured upstream depth ratio, $\eta_1 = y_1/y_3$ and discharge ratio, $\xi = Q_2/Q_1$.

The computations in Figs. 4.3-4.5 employ Eq. (4.17) while those in Figs. 4.6-4.8 employ Eq. (4.18) to model the lateral channel separation shear force. For modeling the divergence pressures, the upstream depth, Eq. (4.8) and (4.9), the average of the downstream depths, Eq. (4.6) and (4.7), and the average of the three depths, Eq. (4.10) and (4.11), are respectively employed in both sets of figures, 4.3-4.5 and 4.6-4.8. Figs. 4.3-4.8 indicate the significance of including the lateral channel separation shear force in the computations of the discharge ratios. The figures also show that the best model formulation is the one that employs the upstream depth for the divergence pressure forces and the upstream parameters for the lateral channel separation shear, Fig. 4.3. Consequently, Eqs. (4.8) and (4.9) for the divergence pressure and Eq. (4.17) for the lateral channel separation zone shear are chosen for the subsequent analysis.

Fig. 4.9 shows the comparisons between the model predictions for the upstream depth ratio η_1 and Taylor's (1944) data. It should be noted that Taylor (1944) presented a plot that gave the relationship between the two depth ratios η_1 and η_2 . Therefore, in Fig. 4.9 Taylor's (1944) data are not presented as discrete points. These comparisons indicate that the model predictions for the depth ratio are not as good as those for the discharge ratio. The computations are less than the observations for the high Fr_1 values and as Fr_1 decreases the predictions become greater than the measurements. This may be attributed to the significance of the other forces that have not been included in the model yet. The figure shows that the best predictions are obtained as η_2 tends to 1.

4.2.6 Centrifugal Force

F_c is the centrifugal force acting on the dividing streamline due to the flow curvature in the lateral channel control volume. Lakshamana and Sridharan (1966) pointed out that there was an appreciable curvature in the dividing streamline that should result in a centrifugal force across this streamline. Therefore, this force is included in the analysis of the main channel control volume. However, this force is not included in the lateral channel analysis as it is acting in the transverse direction. Two approaches are attempted to model this force. In the first approach, the centrifugal force is considered to be exerted by the water mass in the lateral channel stream tube, M , when flowing by a velocity, V , due to the flow curvature by radius, r . Thus the force will take the general form:

$$\text{Centrifugal Force} = \frac{MV^2}{r} \quad (4.19)$$

For this approach, F_c will be the component of the centrifugal force in the streamwise direction of the main channel control volume. The mass can be computed as the density of water multiplied by the volume of water in the lateral channel stream tube. The volume is the average cross sectional area multiplied by the length of the lateral channel control volume. The area and the radius of curvature are assumed to be proportional to the upstream area and the upstream width of the lateral channel control volume, respectively. The velocity is approximated by the lateral channel downstream velocity. Including a centrifugal coefficient, C , to account for all these approximations and to consider the component of the force in the streamwise direction, F_c will take the form:

$$F_c = \rho C \frac{b_1 \xi y_1 V_2^2}{b_1 \xi} L_2 \quad (4.20)$$

The second approach for modeling the centrifugal force is to consider the centrifugal effect in increasing the depth along the dividing streamline by an increment dy . This extra depth is then included in the formulation of the pressure force, B_1 as follows:

$$B_1 + F_c = \frac{1}{2} \gamma (y_1 + dy)^2 (b_3 - b_1 (1 - \xi)) \quad (4.21)$$

where dy is computed as:

$$dy = \frac{V^2}{gr} w \quad (4.22)$$

where: V is the velocity in the lateral channel control volume along the dividing streamline, w and r are the width and the radius of curvature of the lateral channel control volume stream tube, respectively, and g is the gravitational acceleration. The right hand side in Eq. (4.21) is expanded and the second order term of the depth increment, dy , is neglected. Substituting Eq. (4.22) in Eq (4.21) and separating the centrifugal force gives:

$$F_c = \rho y_1 V^2 \frac{b}{r} (b_3 - b_1 (1 - \xi)) \quad (4.23)$$

Different approximations for the velocity, the width and the radius of curvature are tested. The velocity can be approximated as the upstream velocity, V_1 , the lateral channel downstream velocity, V_2 , or the average of the two velocities V_1 and V_2 . The width and the radius of curvature may be approximated to be the upstream width or the downstream width of the lateral channel control volume. Different combinations of these approximations for the three parameters are formulated and the force is included in the model. The approximations and the constants in each formulation are all combined into

one coefficient, the centrifugal coefficient, C . Taylor's (1944) data sets are then employed for the calibration of the lateral channel separation zone coefficient, K_{d2} , and the centrifugal coefficient, C , for each formulation. The calibration is performed for each data set where the upstream Froude number is kept constant. The calibration is based on a least squares error analysis between the measured and the computed discharge ratio and main channel depth ratio.

Table 4.1 presents the calibrated values of the lateral channel separation coefficient and the centrifugal coefficient and the least squares error resulting from the calibration for each of the upstream Froude numbers that Taylor (1944) investigated. The table presents these values for each of the two, above mentioned, approaches for computing the centrifugal force. For the depth increment approach, the formulations resulting from the alternate combinations of the approximations for the velocity, the width and the radius of curvature are all included in the table.

Table 4.1 shows that the different formulations give similar least squares error for each data set with the same upstream Froude number. Consequently, the choice of the best approach and the formulation to be used to model the centrifugal force is based on the values and the trend of variation of K_{d2} and C , with Fr_1 and not on the resulting error. The table indicates that formulations number 4, 5, and 7 give zero centrifugal coefficients. That is, for these formulations the effect of the centrifugal force will not be considered in the analysis and therefore these formulations are excluded from the comparison. Using the first approach for computing this force has a significant effect on the variation of K_{d2} with the upstream Froude number. Considering the significance of the lateral channel separation shear force in the dividing flow analysis and that the

independence of the flow generalizes the model application to more flow situations, the first approach is excluded from the analysis. Formulations number 2 and 3 are also excluded as no trend for the variation of C with Fr_1 can be deduced. Comparing formulations 6, 8, 9, and 10, it can be seen that they give similar trends for the variation of K_{d2} and C with Fr_1 . However, formulations 6 and 10 are less complicated than 8 and 9 and therefore the latter ones are excluded. Since formulation 10 shows less variation in K_{d2} and C with Fr_1 , it is therefore chosen for the subsequent analysis where:

$$F_c = \rho C y_1 V_2^2 \frac{b_2}{b_1 \xi} (b_3 - b_1 (1 - \xi)) \quad (4.24)$$

For flow divisions where the two downstream channels take off at an angle (Fig 4.10), the centrifugal effects should be included in the two control volumes. Two centrifugal coefficients should be calibrated for these cases.

4.2.7 Main Channel Separation Zone Shear Force

Neary et al. (1999) mentioned that a separation zone might form along the outer wall of the main channel depending on the cross sectional aspect ratio and the discharge ratio. They noted that this rarely occurred at lateral intakes with relatively low discharge ratios, but it was quite common in natural river bifurcations. F_{s1} is the separation zone shear force that acts on the main channel control volume. This force may be evaluated in a similar manner to that for the lateral channel, and it is written in the form:

$$F_{s1} = C_{f1} \rho \frac{(V_{s1})^2}{2} y_{s1} L_{s1} \quad (4.25)$$

where: C_{f1} is the separation shear coefficient, y_{s1} and L_{s1} are the depth and the length of the separation interface, respectively, and V_{s1} is the shear velocity along the separation

interface. The depth and the length of the interface, y_{s1} and L_{s1} can be approximated, similar to the lateral channel separation shear parameters, to be the upstream depth and the upstream width of the main channel control volume, respectively.

Different approximations for the shear velocity, V_{s1} , are tested. Analogous to the lateral channel separation, the shear velocity can be approximated to be the upstream velocity, V_1 . Separation zones and flow recirculation were observed in the main channel for cases with high discharge ratios (Law; 1965). Fig. 4.11 shows the configuration of the control volumes for these cases. The figure indicates that, for the most part of the main channel separation zone, the lateral channel velocity, V_2 , may accelerate the main channel control volume flow velocity. Consequently, the shear velocity may be approximated in terms of both V_1 and V_2 and the separation shear coefficient, C_{η} , can be considered proportional to the discharge ratio, ξ . Fig. 4.11 also indicates that the mechanism of the flow separation in the main channel may be different from that in the lateral channel. The former is due to the flow expansion while the latter occurs due to the flow deviation around the sharp edged corner of the junction. Thus the shear velocity, V_{s1} , may be also approximated as the expansion loss velocity between V_1 and V_3 . For each velocity approximation, the coefficients and constants are all combined into one coefficient, the main channel separation zone coefficient, K_{d1} , and the force is included in the model. Taylor's (1944) data is then used to calibrate the three coefficients, K_{d2} , C , and K_{d1} for each formulation of the main channel separation shear. The calibration is based on a least squares error analysis between the measured and the computed discharge ratio and main channel depth ratio. The three coefficients are calibrated for each data set where the upstream Froude number is kept constant.

Table 4.2 presents the calibrated coefficients and the least squares error for the different formulations of the main channel separation shear. In the first five formulations, the proportionality of C_{f1} with ξ is employed in the derivation while in the last five formulations it is not. The table indicates that including the main channel separation shear in the model reduces the variation of K_{d2} with the upstream Froude number. The approach employing the proportionality of C_{f1} with ξ , formulations (1) to (5), gives more significance to the main channel separation shear force. However, the least squares error for all the formulations are very similar. The choice of the shear velocity approximation and the separation shear approach is therefore based on the simplicity of the resulting formulation and consistency with the lateral channel separation analysis. Thus, formulation (6) that states:

$$F_{s1} = \rho K_{d1} V_1^2 (b_1(1-\xi)y_1) \quad (4.26)$$

is chosen for the main channel separation and is used in the subsequent analysis.

4.2.8 Governing Equations

Substituting all the forces into the momentum equations of the two control volumes, Eqs. (4.2) and (4.3), the resulting equation for C.V.₁ is:

$$\begin{aligned} \rho Q_3 V_3 - \rho Q_3 V_1 = \frac{\gamma y_1^2}{2} b_1(1-\xi) - \frac{\gamma y_3^2}{2} b_3 + \frac{1}{2} \gamma y_1^2 (b_3 - b_1(1-\xi)) + \gamma \left(\frac{A_{11} + A_3}{2} \right) L_1 S_o \\ - \frac{\rho V_1^2}{C_s^2} (b_1(1-\xi) + y_1)(L_1) + \rho C_{y1} V_2^2 \frac{b_2}{b_1 \xi} (b_3 - b_1(1-\xi)) - \rho K_{d1} V_1^2 y_1 b_1(1-\xi) \end{aligned} \quad (4.27)$$

For C.V.₂, this gives:

$$\rho Q_2 V_2 - \rho Q_1 V_1 = \frac{\gamma y_1^2}{2} b_1 \bar{\xi} - \frac{\gamma y_2^2}{2} b_2 + \frac{1}{2} \gamma y_1^2 (b_2 - b_1 \bar{\xi}) + \gamma \left(\frac{A_{12} + A_2}{2} \right) L_2 S_o - \frac{\rho V_1^2}{C^2} (b_1 \bar{\xi} + y_1) (L_2) - \rho K_{d2} (V_1^2) (y_1 b_1 \bar{\xi}) \quad (4.28)$$

It should be noted that the model equations, (4.27) and (4.28), do not explicitly include the junction angle due to applying conservation of momentum in the curvilinear direction. However, the angle may have an indirect effect through the different coefficients included in the equations, specifically C , K_{d1} , and K_{d2} .

Equations (4.27) and (4.28) are non-dimensionalized, using Eq. (4.1), in terms of the discharge ratio, $\bar{\xi} = Q_2/Q_1$, the depth ratios, $\eta_1 = y_1/y_3$ and $\eta_2 = y_2/y_3$, the width ratios, $\omega_1 = b_1/b_3$ and $\omega_2 = b_2/b_3$, and the upstream Froude number, $Fr_1 = Q_1 / (g b_1^2 y_1^3)^{0.5}$ to give the following equations:

$$\underbrace{(1 - \bar{\xi})^2 - \frac{(1 - \bar{\xi})}{\eta_1 \omega_1}}_{\text{Momentum}} = \underbrace{\frac{1}{2 Fr_1^2} \frac{(\eta_1^2 - 1)}{\omega_1^2 \eta_1^3}}_{\text{Net Pressure}} + \underbrace{\frac{1}{2 Fr_1^2} \left(\frac{L_1 S_o}{y_1} \right) \left[\frac{(\eta_1 \omega_1 (1 - \bar{\xi}) + 1)}{\eta_1^2 \omega_1^2} \right]}_{\text{Weight}} - \underbrace{\frac{L_1}{C^2 b_1} \left[\frac{b_1}{y_1} (1 - \bar{\xi}) + 1 \right] \frac{1}{\eta_1 \omega_1}}_{\text{Friction}} + \underbrace{C \bar{\xi} \frac{\eta_1 (1 - \omega_1 (1 - \bar{\xi}))}{\omega_1 \omega_2 \eta_2^2}}_{\text{Centrifugal Pressure}} - \underbrace{K_{d1} \frac{(1 - \bar{\xi})}{\omega_1 \eta_1}}_{\text{Separation Shear}} \quad (4.29)$$

$$\underbrace{\frac{\bar{\xi}^2}{\eta_2 \omega_2} - \frac{\bar{\xi}}{\eta_1 \omega_1}}_{\text{Momentum}} = \underbrace{\frac{1}{2 Fr_1^2} \frac{\omega_2 (\eta_1^2 - \eta_2^2)}{\omega_1^2 \eta_1^3}}_{\text{Net Pressure}} + \underbrace{\frac{1}{2 Fr_1^2} \left(\frac{L_2 S_o}{y_1} \right) \left[\frac{(\eta_1 \omega_1 \bar{\xi} + \eta_2 \omega_2)}{\eta_1^2 \omega_1^2} \right]}_{\text{Weight}} - \underbrace{\frac{L_2}{C^2 b_1} \left(\frac{b_1}{y_1} \bar{\xi} + 1 \right) \frac{1}{\omega_1 \eta_1}}_{\text{Friction}} - \underbrace{K_{d2} \frac{\bar{\xi}}{\omega_1 \eta_1}}_{\text{Separation Shear}} \quad (4.30)$$

Equations (4.29) and (4.30) are two non-linear equations that can be solved for $\bar{\xi}$ and η_1 given η_2 and Fr_1 . The magnitude of the different terms in the equations can be

determined by performing an order of magnitude analysis, noting that all the ratios, ξ , η_1 , η_2 , ω_1 , and ω_2 are all of order 1. It can also be noted that the momentum terms are of order 1 and the order of the net pressure term is determined by the magnitude of Fr_1 . Thus, for cases with low Fr_1 values the net pressure and the weight terms will be significant in the analysis. The order of the friction and the weight terms is determined by the parameters $(L/C \cdot y_1)$ and (LS_0/y_1) , respectively. These parameters are significant in real world applications where the length to depth ratio is large. The orders of the other terms are to be determined by the magnitudes of the different coefficients, C , K_{d1} , and K_{d2} .

4.3 Results and Discussion

The model equations, (4.29) and (4.30), are solved by the Microsoft Excel solver, which employs the Generalized Reduced Gradient (GRG2) nonlinear optimization code developed by Lasdon and Warren (1982). Since all of the experimental studies were performed on horizontal flumes, the weight term is not included in the following analysis. The non-dimensional Chezy coefficient, the aspect ratio and the width ratios are determined for each set of experimental data according to the flume dimensions, and the measured values of the discharges and the depths. The lengths of the control volumes are determined from the location of the measurement sections in each study. Where these locations are not mentioned, the lengths are estimated based on the experimental flume dimensions. The values of K_{d2} , K_{d1} , and C are calibrated using the available experimental data.

4.3.1 Calibration of the Separation Coefficients, K_{d1} and K_{d2} , and the Centrifugal Coefficient, C

The procedure to calculate ξ and η_1 for the flow cases presented in the previous experimental studies is performed by calibrating a set of coefficients, K_{d2} , K_{d1} , and C , for each data set where Fr_1 is held constant. The calibration is based on minimizing the sum of the least squares error between the measured and the computed discharge ratios and upstream depth ratios that is given by:

$$\sum_{i=1}^{i=N} \left[(\eta_{1i \text{ computed}} - \eta_{1i \text{ measured}})^2 + (\xi_{i \text{ computed}} - \xi_{i \text{ measured}})^2 \right] \quad (4.31)$$

where N is the number of data points in the set in each study with a constant Fr_1 value.

Taylor's (1944) experimental data presented the variation of ξ with η_2 for a 90° junction at four particular values of Fr_1 . Fig. 4.12 (a) shows a comparison between Taylor's (1944) experimental data and the proposed model results while including the calibrated coefficients. The good agreement obtained between the computations and the data, using one set of coefficients for each Fr_1 value, indicates that the values of K_{d2} , K_{d1} , and C are independent of the discharge ratio. However, the variation in these coefficients may be dependent on the junction angle, the width ratio, and the upstream Froude number.

Grace's (1958) and Law's (1965) experimental data included the variation of ξ with η_2 for different values of Fr_1 . Grace's (1958) data included this variation for different junction angles and for different width ratios. Since K_{d2} , K_{d1} , and C have been found to be independent of the discharge ratio, each of these data sets, for which the

junction angle and width ratio were held constant, was divided into ranges of Fr_1 values. For each range the values of the three coefficients were then calibrated.

Table 4.3 presents the values of the calibrated coefficients for each experimental setup and Fr_1 value or range. The comparison between the K_{d1} and K_{d2} values indicate that, for these experimental setups, the separation in the main channel is less significant than that in the lateral channel. For Taylor's (1944) data, the calibrated coefficients indicate that K_{d2} can be considered independent of the upstream Froude number. The values also indicate that K_{d1} may be also considered constant for different values of Fr_1 , if for $Fr_1=0.374$ the calibrated K_{d1} is considered anomalous (with Taylor's (1944) Grace's (1958) and Law's (1965) calibrated K_{d1} for 90° junction angles). Thus, an average value of $K_{d1}=0.01$ can be used for all Fr_1 values. The centrifugal coefficient is the only coefficient that seems to vary with Fr_1 for Taylor's (1944) data. The value of C decreases as the upstream Froude number increases. This may be attributed to the hydraulic jumps that are initiated in the main channel extension at high upstream Froude numbers. These jumps disturb the flow at the junction such that the centrifugal effects may no longer be significant.

For Law's (1965) experiments, Table 4.3 indicates that the separation shear in the lateral channel is the only significant force and K_{d2} can be considered constant for the different values of Fr_1 . Grace's (1958) experimental data show the effect of the junction angle and the width ratio on the coefficients. An increase in K_{d2} with the junction angle can be noted from the table. However the change in the width ratio does not seem to have a significant effect on the K_{d2} values. No trend for the variation of K_{d1} or C with the junction angle, or the width ratio, can be deduced.

In practice K_{d2} , K_{d1} , and C should be treated as calibration coefficients. These coefficients were found to be independent of the discharge ratio and may be considered constant over narrow ranges of Fr_1 values but were dependent on geometry. For irrigation channel systems, the variations in the depth and the velocity cause small changes in the Fr_1 values, thus the coefficients can be calibrated for certain geometry at known flow conditions and then the same values can be applied for different flow situations.

4.3.2 The Final Model Results

Figs. 4.12-4.18 present the comparisons of the proposed momentum approach with Taylor's (1944), Grace's (1958) and Law's (1965) data for their different experimental setups. For each setup in Grace's (1958) and Law's (1965) experiments, the data is divided into ranges of Fr_1 values and the coefficients are calibrated for each range. Then an average Fr_1 value is computed for each range and is used, with the calibrated coefficients and the measured lateral channel depth ratios, to compute the discharge ratios. In each of these figures three plots are presented: the first shows the variations of ξ with η_2 ; the second presents the computed discharge ratios versus the measured ones; and the third presents the computed main channel depth ratios versus the measured ones. In the first plot the computations are presented for the average Fr_1 values while the experimental data are presented for the corresponding ranges of Fr_1 values. For the second and third plots of each figure, the computations are presented at the actual Fr_1 values and a 45° line is plotted for comparisons. The figures show fair agreement between the computations and the measurements.

4.4 Comparison with Previous Theories and Energy Approaches

Law (1965) presented a theoretical approach to the problem of dividing open channel flows for a 90° junction of channels of equal width. He divided the junction into two control volumes; one for the main channel flow and the other for the lateral channel flow. For the main channel analysis, Law (1965) applied the momentum equation in the main channel direction and included the component of the hydrostatic pressure force acting on the dividing streamline. He also applied the continuity equation and put it in terms of the Froude numbers Fr_1 and Fr_3 . Combining the two equations, momentum and continuity, Law (1965) was able to relate the discharge ratio to the Froude numbers in the following equation:

$$(1 - \xi)^2 \left(\frac{Fr_1}{Fr_3} \right)^2 = \left[\frac{\frac{2 - \xi}{2} + 2(1 - \xi)Fr_1^2}{\frac{2 - \xi}{2} + 2Fr_3^2} \right]^{\frac{3}{2}} \quad (4.32)$$

Law (1965) simplified Eq. (4.32) and obtained a linear approximation between the discharge ratio and the Froude numbers ratio where:

$$\left(\frac{Fr_3}{Fr_1} \right) \cong (1 - \xi) \quad (4.33)$$

Law (1965) also applied the conservation of energy neglecting losses to the main channel control volume. After simplification he obtained the same linear approximation, Eq. (4.33). However, the error term resulting from the energy simplification was larger than that resulting from the momentum equation. Consequently, Law (1965) recommended the use of the momentum approach for the main channel analysis.

The analysis of the lateral channel was based on applying the momentum equation in the lateral channel direction. Law (1965) included a contraction coefficient, c , to

account for the effect of the separation zone in the lateral channel and he assumed that $\eta_1=1$. He obtained the following equation for the lateral channel control volume:

$$\frac{\eta_2}{\eta_1} - \left(\frac{\eta_2}{\eta_1}\right)^3 = \frac{2Fr_1^2 \xi^2}{c} \quad (4.34)$$

Law (1965) attempted to extend his theory to include divisions with different angles. The equation for the main channel extension remained the same as Eq. (4.32). However, the lateral channel equation included the component of the momentum flux in the main channel and was modified to:

$$\frac{\eta_2}{\eta_1} \left[1 + 2Fr_1^2 \xi \cos \delta\right] - \left(\frac{\eta_2}{\eta_1}\right)^3 = \frac{2Fr_1^2 \xi^2}{c} \quad (4.35)$$

Nevertheless, the contraction coefficient, c , needed to be determined for each particular combination of Fr_1 , ξ , δ and η_2 .

Tran (1989) presented another theoretical approach for the 90° flow divisions. He divided the junction into two control volumes: the first was for the main channel flow and the second was for the lateral channel flow and ended at the lateral channel entrance section. He applied the momentum equation to the lateral channel control volume to compute the component of the momentum transfer between the two channels in the main channel direction. Then, by applying the momentum conservation to the main channel control volume and including the momentum transfer, Tran (1989) was able to express the discharge ratio in terms of Fr_1 and η_1 through the equation:

$$\frac{\xi}{40} Fr_1^4 + \left(\frac{1}{6} + \frac{5}{6}(1-\xi) - (1-\xi)\eta_1\right) Fr_1^2 + \frac{\eta_1^2 - 1}{2\eta_1} = 0 \quad (4.36)$$

It should be noted that Tran's (1989) equation does not include any lateral channel variables. Therefore, Tran (1989) pointed out that it could be used for any branch channel flow conditions and its verification did not need lateral channel depth measurements.

Figs. 4.19-4.31 present the comparisons between the proposed momentum approach and each of Law's (1965) theory and Tran's (1989) theory. For this comparison, Taylor's (1944) experimental data is employed in Figs. 4.19-4.22. Figs. 4.23-4.29 employ Law's (1965) data, while Figs. 4.30-4.31 employ Grace's (1958) experimental data for the 90° junction. Equations (4.32) and (4.34) are used to compute ξ and η_2 to plot Law's (1965) theory. Tran's (1989) equation, Eq. (4.36), for the main channel extension is used twice. First, to compute ξ , when Fr_1 and η_1 are employed as inputs, and second, to compute η_1 , when Fr_1 and ξ are the inputs. In Figs. 4.19-4.31, plots (a) present the measurements at the actual Fr_1 values and all the theoretical computations are carried out at the average Fr_1 value printed on each plot. In plots (b) and (c) of each figure, the computations are carried out at the actual Fr_1 values.

The comparisons with Law's (1965) theory show that the model predictions are in better agreement with the experimental data especially as η_2 increases. The proposed approach does not rely on the assumption that $\eta_1=1$. This assumption may be unreasonable in flow division problems due to the considerable energy losses associated with these problems. The comparisons with Tran's (1989) theory indicate the superiority of the proposed theory. For most of the data sets, Tran's (1989) theory does not accurately compute the discharge ratio and does not reflect the correct variation of ξ with η_2 . Further, The present model directly solves the flow division problem, using the

boundary conditions provided, Fr_1 and η_2 , for the required discharge split and upstream depth.

Figs. 4.19 to 4.31 also present a comparison between the proposed theory and the two energy approaches. The first is the common approach of the equality of the water surface elevations, $\eta_1 = \eta_2 = 1$, which neglects the differences in velocity heads and energy losses. The second is the simple approach that neglects energy losses. The figures indicate that the first approach, represented by the vertical line at $\eta_2 = 1$, does not reflect the experimental data and the discrepancy increases as the inflow Froude number increases. Including the differences in velocity heads, in the second approach, improves the energy predictions by reflecting the trend of the data. However, the predictions of the discharge ratio are still not accurate. This can be attributed to the significant losses that are occurring in the lateral channel that cannot be neglected.

The advantage of the proposed momentum approach is that it includes all the physical effects such as the boundary friction forces and the separation and centrifugal effects and thus may be scaled to real world situations without affecting the accuracy of the predictions. Further, the momentum is applied in the streamwise direction and thus the model can handle different junction geometries whereas the previous theories are all limited to the 90° junctions and channels of equal width. In addition, the proposed model can be easily implemented in open channel network problems since the handling the dividing junctions will be consistent with that of combining junctions and that of channel reaches.

4.5 Summary and Conclusions

A one-dimensional theoretical model providing the interior boundary conditions for subcritical dividing junction flows was developed. The junction was divided into two control volumes. The conservation of momentum was applied to each of the two control volumes in the respective streamwise direction together with overall mass conservation. Given the upstream Froude number and each of the main and the lateral channel downstream depths, the model could be solved for the discharge ratio and the upstream depth. The model was validated through comparison with the experimental measurements from previous studies.

The boundary friction forces, the separation zone shear forces in the main and the lateral channels, and the centrifugal pressure force were included in the analysis. Two separation shear coefficients and a centrifugal coefficient were introduced to compute these forces. Experimental measurements from the technical literature were used to explore the variations in these coefficients with the different parameters governing the flow such as the upstream Froude number, the discharge ratio, the junction angle and the width ratio between the lateral channel and the main channel.

It was found that the predictions of the proposed momentum approach gave good agreement with the available experimental measurements. Including the lateral channel separation zone was found to be significant in the analysis of dividing junction flows. The three coefficients were found to be independent of the discharge ratio and for limited ranges of the upstream Froude number. They mainly varied with geometry. However, no trend for this variation could be deduced.

A comparison between the proposed theory and previous momentum theories proved the superiority of the proposed approach especially for large downstream depth ratios. The advantage of the proposed approach is that it does not rely on any simplifying assumptions and it can handle any junction angle and any width ratios while the previous theories are limited to a junction angle of 90° and channels of equal width. Further, the proposed approach models all the physical effects such as the boundary friction and thus may be scaled up to real world applications. Applying the momentum in the streamwise direction makes handling of the dividing junctions consistent with that for the channel reaches. This facilitates incorporating the theory into open channel network models to provide the interior boundary conditions governing dividing junction flows.

A comparison between the currently used energy approaches which handle junctions in network models and the proposed momentum approach was performed. It was found that the predictions of the momentum approach for the discharge ratio and the main channel depth ratio were better than these energy approaches.

References

- Grace, J. L., and Priest, M. S. (1958). "Division of flow in open channel junctions." *Bulletin No. 31*, Engineering Experiment Station, Alabama Polytechnic Institute.
- Neary, F. S. and Odgaard, A. J. (1999). "Three dimensional theoretical model of lateral-intake inflows" *J. Hydr. Div.*, ASCE, 125(2), 126-140.
- Lasdon, L. S. and Waren A. D. (1982). GRG2 User's Guide. Department of General Business. School of Business Administration. University of Texas. Austin, TX 78712.

- Lakshamana, N. S., and Sridharan, K. (1966). Discussion of "Dividing flow in an open channel." By S. W. Law and A.J. Reynolds, *J. Hydr. Div.*, ASCE, 94 (HY6), 237-239.
- Law, S. W. (1965). "Dividing flow in an open channel." Thesis presented to McGill University, Montreal, Quebec, Canada, in partial fulfillment of the requirements for the degree of Master of Engineering.
- Neary, V. S., Sotiropoulos, F. and Odgaard, A. J. (1999). "Three dimensional numerical model of lateral intake inflows." *J. Hydr. Engrg.*, ASCE, 125 (2), 126-140.
- Taylor, E. H. (1944). "Flow characteristics at rectangular open channel junctions." *Trans.*, ASCE, 109, 893-912.
- Tran, D. M. (1989). "Some characteristics of lateral flows in open channels." Thesis presented in partial fulfillment for the degree of Doctor of Philosophy to Concordia University Montreal Quebec, Canada.

	Fr_1	K_{02}	C	Least Square Error	Centrifugal Formulation
1	0.632 0.447 0.374 0.200	0.00 0.25 0.77 0.84	0.70 0.61 0.35 0.56	0.0078 0.0117 0.0352 0.0050	$\text{Centrifugal Force} = \frac{mV^2}{r} \implies F_c = \rho C \frac{b_1^\xi y_1 V_2^2}{b_1^\xi} L_2$
2	0.632 0.447 0.374 0.200	0.70 0.64 0.29 0.80	0.00 0.28 1.02 0.64	0.0078 0.0104 0.0293 0.0049	$B_1 + F_c = \frac{1}{2} \gamma (y_1 + dy)^2 (b_3 - b_1(1 - \xi)) \quad dy = \frac{V^2}{gr} w$ $V = V_2, b = b_2, r = b_2 \implies F_c = \rho C y_1 V_2^2 (b_3 - b_1(1 - \xi))$ <p>or $b = b_1^\xi, r = b_1^\xi$</p>
3	0.632 0.447 0.374 0.200	0.70 0.66 0.32 0.88	0.00 0.30 1.14 0.64	0.0078 0.0109 0.0333 0.0051	$B_1 + F_c = \frac{1}{2} \gamma (y_1 + dy)^2 (b_3 - b_1(1 - \xi)) \quad dy = \frac{V^2}{gr} w$ $V = V_2, b = b_1^\xi, r = b_2 \implies F_c = \rho C y_1 V_2^2 \frac{b_1^\xi}{b_2} (b_3 - b_1(1 - \xi))$
4	0.632 0.447 0.374 0.200	0.70 0.74 0.83 1.11	0.00 0.00 0.00 0.00	0.0078 0.0186 0.0633 0.0234	$B_1 + F_c = \frac{1}{2} \gamma (y_1 + dy)^2 (b_3 - b_1(1 - \xi)) \quad dy = \frac{V^2}{gr} w$ $V = V_1, b = b_2, r = b_1^\xi \implies F_c = \rho C y_1 V_1^2 \frac{b_2}{b_1^\xi} (b_3 - b_1(1 - \xi))$
5	0.632 0.447 0.374 0.200	0.70 0.74 0.82 1.08	0.00 0.00 0.01 0.00	0.0078 0.0186 0.0633 0.0207	$B_1 + F_c = \frac{1}{2} \gamma (y_1 + dy)^2 (b_3 - b_1(1 - \xi)) \quad dy = \frac{V^2}{gr} w$ $V = V_1, b = b_2, r = b_2 \implies F_c = \rho C y_1 V_1^2 (b_3 - b_1(1 - \xi))$ <p>or $b = b_1^\xi, r = b_1^\xi$</p>

Table 4.1 Calibrated Coefficients and Least Square Error for the Different Centrifugal Formulations

	Fr_1	K_{a2}	C	Least Square Error	Centrifugal Formulation
6	0.632	0.70	0.00	0.0078	$B_1 + F_i = \frac{1}{2} \gamma (y_1 + dy)^2 (b_3 - b_1(1 - \xi)) \quad dy = \frac{V^2}{gr} w$ $V = V_1, b = b_1 \xi, r = b_2 \implies F_i = \rho C y_1 V_1^2 \frac{b_1 \xi}{b_2} (b_3 - b_1(1 - \xi))$
	0.447	0.60	0.30	0.0125	
	0.374	0.33	0.86	0.0364	
	0.200	0.53	0.89	0.0051	
7	0.632	0.70	0.00	0.0078	$B_1 + F_i = \frac{1}{2} \gamma (y_1 + dy)^2 (b_3 - b_1(1 - \xi)) \quad dy = \frac{V^2}{gr} w$ $V = \frac{V_1 + V_2}{2}, b = b_2, r = b_1 \xi \implies F_i = \rho C y_1 [V_1 + V_2]^2 \frac{b_2}{b_1 \xi} (b_3 - b_1(1 - \xi))$
	0.447	0.74	0.00	0.0186	
	0.374	0.83	0.00	0.0633	
	0.200	1.11	0.00	0.0234	
8	0.632	0.70	0.00	0.0078	$B_1 + F_i = \frac{1}{2} \gamma (y_1 + dy)^2 (b_3 - b_1(1 - \xi)) \quad dy = \frac{V^2}{gr} w$ $V = \frac{V_1 + V_2}{2}, b = b_2, r = b_2 \implies F_i = \rho C y_1 [V_1 + V_2]^2 (b_3 - b_1(1 - \xi))$ <p style="text-align: center;"><i>or</i> $b = b_1 \xi, r = b_1 \xi$</p>
	0.447	0.62	0.06	0.0143	
	0.374	0.47	0.15	0.0453	
	0.200	0.40	0.26	0.0053	
9	0.632	0.70	0.00	0.0078	$B_1 + F_i = \frac{1}{2} \gamma (y_1 + dy)^2 (b_3 - b_1(1 - \xi)) \quad dy = \frac{V^2}{gr} w$ $V = \frac{V_1 + V_2}{2}, b = b_1 \xi, r = b_3 \implies F_i = \rho C y_1 [V_1 + V_2]^2 \frac{b_1 \xi}{b_3} (b_3 - b_1(1 - \xi))$
	0.447	0.63	0.08	0.0106	
	0.374	0.31	0.25	0.0307	
	0.200	0.77	0.18	0.0049	
10	0.632	0.70	0.00	0.0078	$B_1 + F_i = \frac{1}{2} \gamma (y_1 + dy)^2 (b_3 - b_1(1 - \xi)) \quad dy = \frac{V^2}{gr} w$ $V = V_2, b = b_2, r = b_1 \xi \implies F_i = \rho C y_1 V_2^2 \frac{b_2}{b_1 \xi} (b_3 - b_1(1 - \xi))$
	0.447	0.61	0.25	0.0117	
	0.374	0.35	0.77	0.0352	
	0.200	0.56	0.84	0.0050	

Table 4.1 Calibrated Coefficients and Least Square Error for the Different Centrifugal Formulations (Cont.)

	F_{r1}	K_{d2}	C	K_{d1}	Least Square Error	Main Channel Separation Formulation
1	0.632	0.74	0.00	0.13	0.0059	$V_{s1}^2 = V_1^2, C_{r1} \propto \xi \implies F_{s1} = \rho \xi K_{d1} V_1^2 (b_1(1-\xi)y_1)$
	0.447	0.69	0.18	0.18	0.0085	
	0.374	0.63	0.43	0.70	0.0070	
	0.200	0.67	0.72	0.12	0.0050	
2	0.632	0.79	0.00	0.11	0.0033	$V_{s1}^2 = \left[\frac{V_1 + V_2}{2} \right]^2, C_{r1} \propto \xi \implies F_{s1} = \rho \xi K_{d1} \left[\frac{V_1 + V_2}{2} \right]^2 (b_1(1-\xi)y_1)$
	0.447	0.69	0.24	0.10	0.0091	
	0.374	0.58	0.65	0.43	0.0134	
	0.200	0.69	0.71	0.08	0.0049	
3	0.632	0.76	0.00	0.13	0.0047	$V_{s1}^2 = V_1 \left[\frac{V_1 + V_2}{2} \right], C_{r1} \propto \xi \implies F_{s1} = \rho \xi K_{d1} V_1 \left[\frac{V_1 + V_2}{2} \right] (b_1(1-\xi)y_1)$
	0.447	0.69	0.21	0.14	0.0087	
	0.374	0.62	0.51	0.55	0.0095	
	0.200	0.69	0.71	0.10	0.0049	
4	0.632	0.79	0.06	0.44	0.0025	$V_{s1}^2 = V_2 \left[\frac{V_1 + V_2}{2} \right], C_{r1} \propto \xi \implies F_{s1} = \rho \xi K_{d1} V_2 \left[\frac{V_1 + V_2}{2} \right] (b_1(1-\xi)y_1)$
	0.447	0.65	0.30	0.25	0.0108	
	0.374	0.36	0.91	0.58	0.0327	
	0.200	0.70	0.75	0.29	0.0049	
5	0.632	0.79	0.00	0.51	0.0032	$V_{s1}^2 = (V_1^2 - V_2^2), C_{r1} \propto \xi \implies F_{s1} = \rho \xi K_{d1} (V_1^2 - V_2^2) (b_1(1-\xi)y_1)$
	0.447	0.67	0.35	0.62	0.0084	
	0.374	0.53	0.83	2.41	0.0201	
	0.200	0.72	0.70	0.40	0.0049	

Table 4.2 Calibrated Coefficients and Least Square Error for the Different Main Channel Separation Formulations

	Fr_1	K_{d2}	C	K_{d1}	Least Square Error	Main Channel Separation Formulation
6	0.632	0.70	0.00	0.00	0.0078	$V_{d1}^2 = V_1^2 \Rightarrow F_{d1} = \rho K_{d1} V_1^2 (b_1(1-\xi)y_1)$
	0.447	0.67	0.17	0.03	0.0093	
	0.374	0.64	0.36	0.21	0.0050	
	0.200	0.59	0.80	0.01	0.0050	
7	0.632	0.71	0.00	0.01	0.0073	$V_{d1}^2 = \left[\frac{V_1 + V_2}{2} \right]^2 \Rightarrow F_{d1} = \rho K_{d1} \left[\frac{V_1 + V_2}{2} \right]^2 (b_1(1-\xi)y_1)$
	0.447	0.68	0.18	0.02	0.0089	
	0.374	0.64	0.40	0.12	0.0057	
	0.200	0.63	0.75	0.02	0.0050	
8	0.632	0.70	0.00	0.01	0.0076	$V_{d1}^2 = V_1^2 \left[\frac{V_1 + V_2}{2} \right] \Rightarrow F_{d1} = \rho K_{d1} V_1 \left[\frac{V_1 + V_2}{2} \right] (b_1(1-\xi)y_1)$
	0.447	0.68	0.17	0.03	0.0091	
	0.374	0.64	0.37	0.16	0.0052	
	0.200	0.61	0.78	0.02	0.0050	
9	0.632	0.77	0.14	0.00	0.0041	$V_{d1}^2 = V_2^2 \left[\frac{V_1 + V_2}{2} \right] \Rightarrow F_{d1} = \rho K_{d1} V_2 \left[\frac{V_1 + V_2}{2} \right] (b_1(1-\xi)y_1)$
	0.447	0.69	0.14	0.21	0.0087	
	0.374	0.61	0.55	0.53	0.0099	
	0.200	0.69	0.10	0.71	0.0049	
10	0.632	0.73	0.00	0.08	0.0064	$V_{d1}^2 = (V_1^2 - V_2^2) \Rightarrow F_{d1} = \rho K_{d1} (V_1^2 - V_2^2) (b_1(1-\xi)y_1)$
	0.447	0.69	0.18	0.15	0.0084	
	0.374	0.63	0.43	0.66	0.0069	
	0.200	0.67	0.72	0.11	0.0050	

Table 4.2 Calibrated Coefficients and Least Square Error for the Different Main Channel Separation Formulations (Cont.)

Author	δ	ω_2	Fr_1	K_{d2}	K_{d1}	C
Taylor (1944)	90°	1.0	0.632	0.700	0.003	0.000
			0.447	0.669	0.029	0.174
			0.374	0.635	0.206	0.360
			0.200	0.586	0.014	0.805
Law (1965)	90°	1.0	0.70-0.83	1.632	0.025	0.000
			0.61-0.69	1.140	0.000	0.000
			0.52-0.60	0.966	0.000	0.048
			0.40-0.50	0.957	0.000	0.080
			0.30-0.40	1.211	0.000	0.000
			0.22-0.29	1.003	0.000	0.000
Grace (1958)	30°	1.0	0.50-0.67	0.588	0.016	0.196
			0.40-0.49	0.419	0.033	0.554
			0.31-0.40	0.324	0.017	0.532
			0.20-0.30	0.468	0.000	0.294
			0.12-0.19	1.171	0.157	0.000
Grace (1958)	60°	1.0	0.30-0.40	1.295	0.008	0.243
			0.20-0.30	0.538	0.157	0.344
			0.13-0.20	0.121	0.095	0.857
Grace (1958)	90°	1.0	0.20-0.28	1.270	0.000	0.308
			0.11-0.20	0.946	0.000	2.015
Grace (1958)	120°	1.0	0.20-0.30	1.508	0.000	0.157
			0.16-0.18	1.872	0.000	0.000
Grace (1958)	30°	0.4	0.20-0.28	0.524	0.033	0.205
			0.10-0.20	0.381	0.034	0.491
			0.05-0.10	0.904	0.000	0.000

TABLE 4.3. The Calibrated Coefficients for Previous Studies

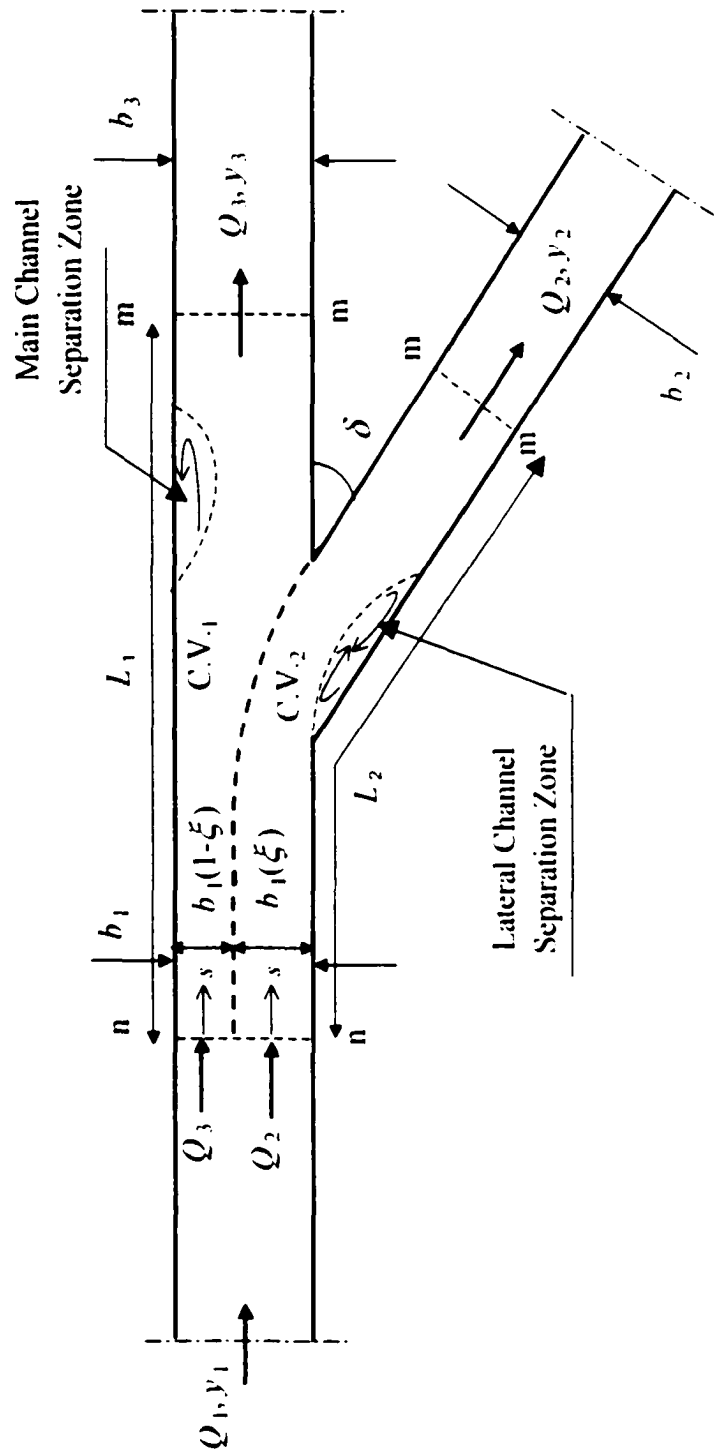
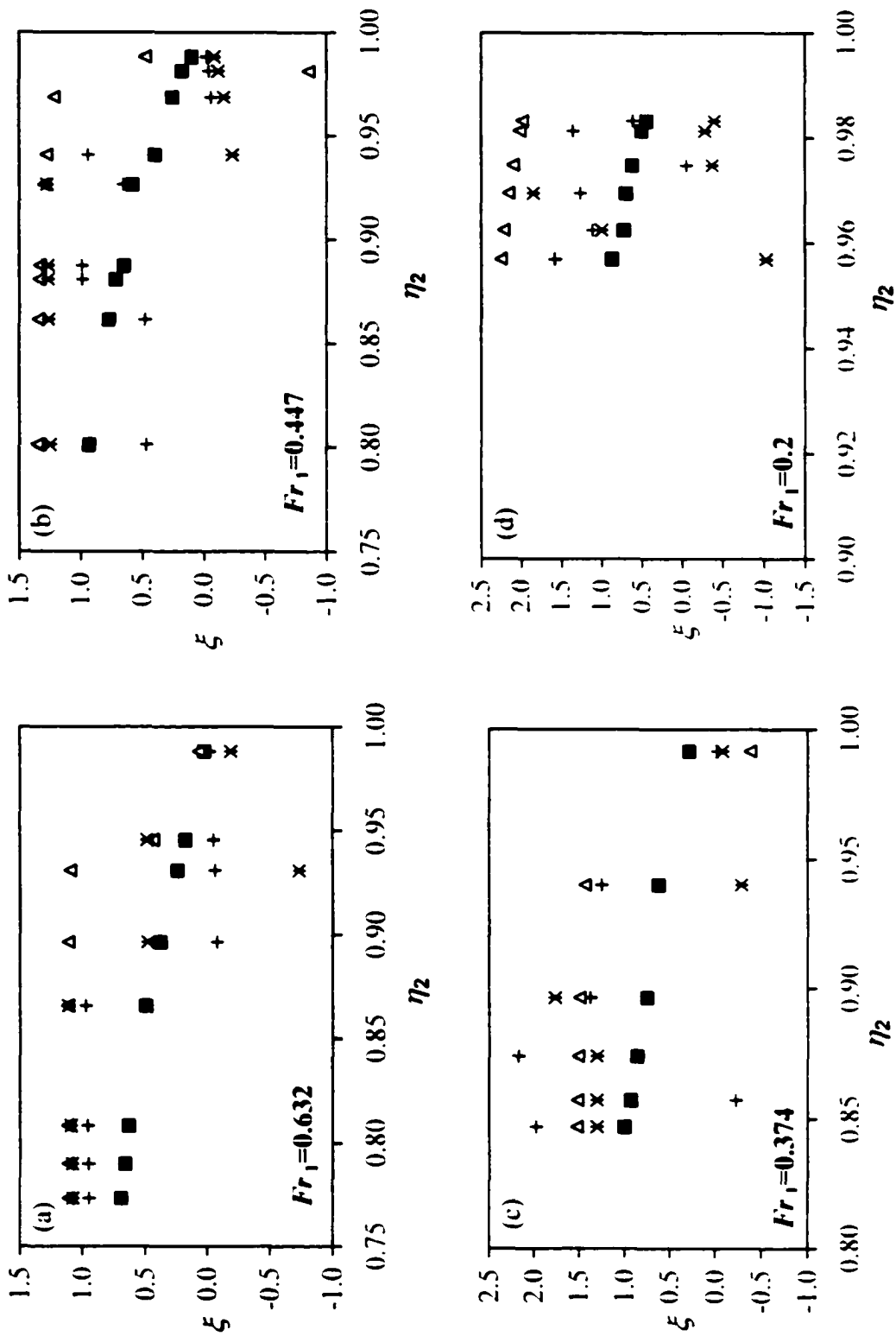


Fig. 4.1 Dividing Open Channel Junction with the Control Volumes and Notation



Taylor's (1944)
 + Eqs. (4.6) and (4.7)
 Δ Eqs. (4.8) and (4.9)
 \times Eqs. (4.10) and (4.11)

Fig. 4.2 Comparing the Different Formulations for the Divergence Pressure

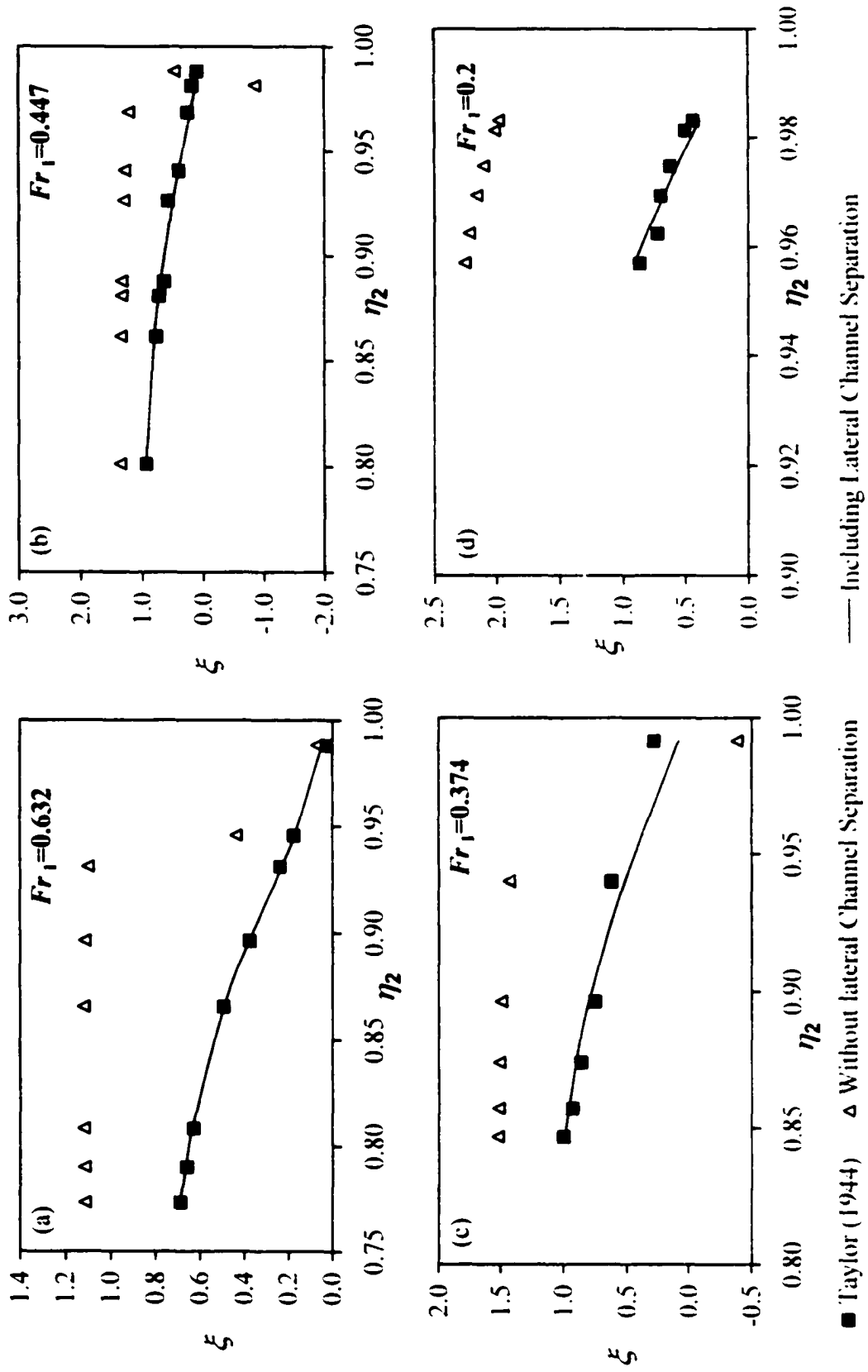


Fig. 4.3 Comparisons Between Taylor's (1944) Data and the Model Predictions Using Eqs. (4.8) and (4.9) for the Pressure and Eq. (4.17) for the Lateral Channel Separation Shear

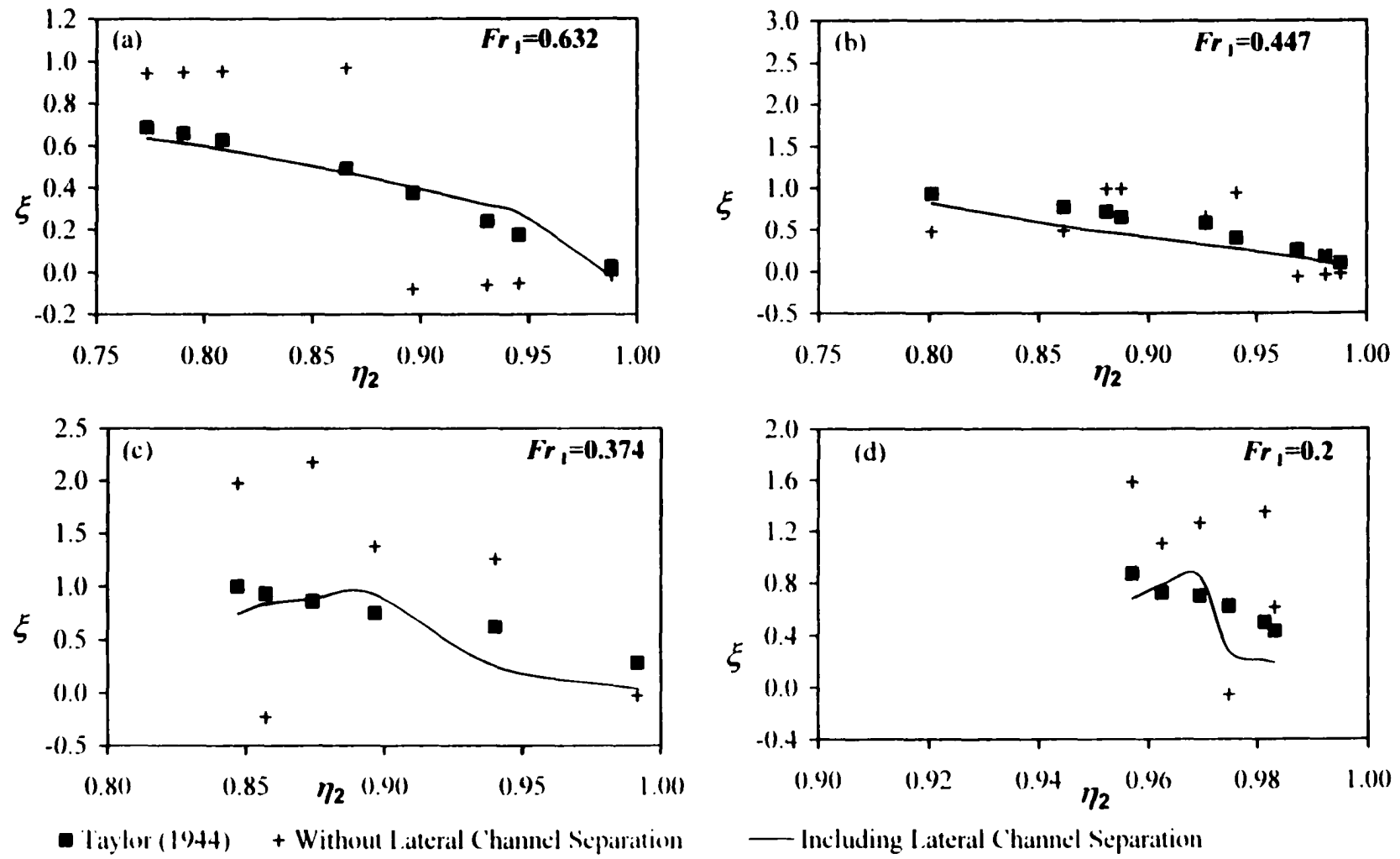


Fig. 4.4 Comparisons Between Taylor's (1944) Data and the Model Predictions Using Eqs. (4.6) and (4.7) for the Pressure and Eq. (4.17) for the Lateral Channel Separation Shear

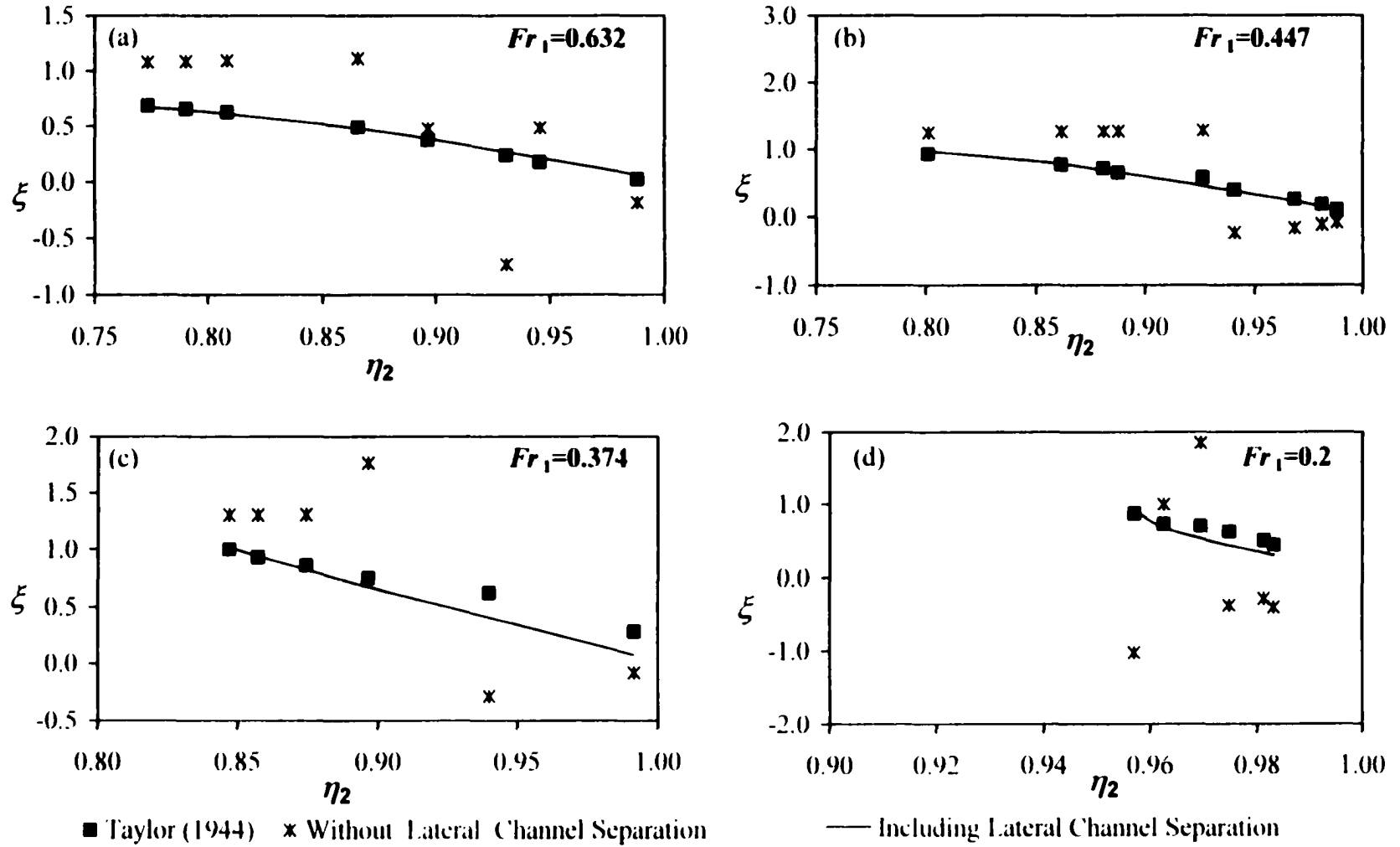


Fig. 4.5 Comparisons Between Taylor's (1944) Data and the Model Predictions Using Eqs. (4.10) and (4.11) for the Pressure and Eq. (4.17) for the Lateral Channel Separation Shear

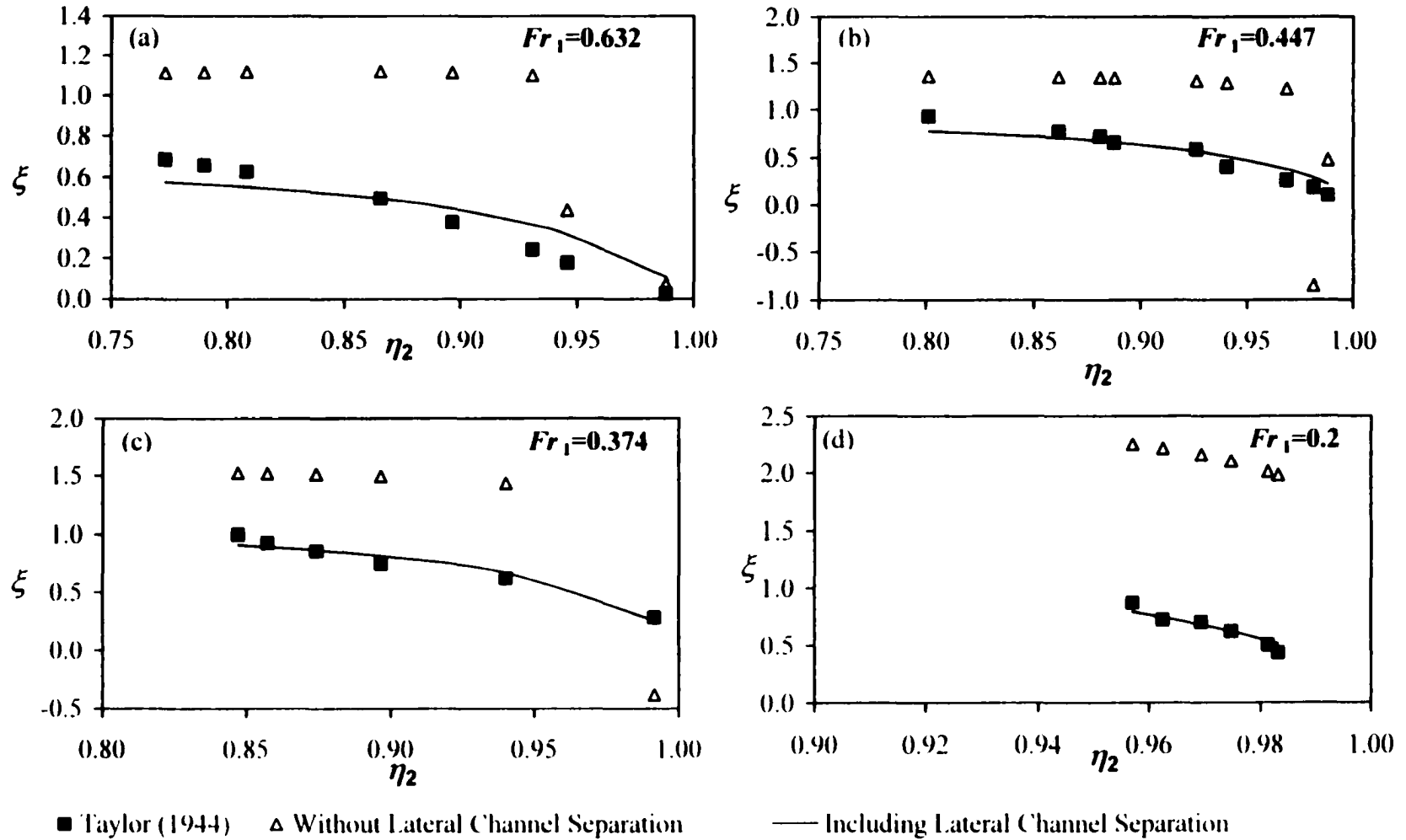


Fig. 4.6 Comparisons Between Taylor's (1944) Data and the Model Predictions Using Eqs. (4.8) and (4.9) for the Pressure and Eq. (4.18) for the Lateral Channel Separation Shear

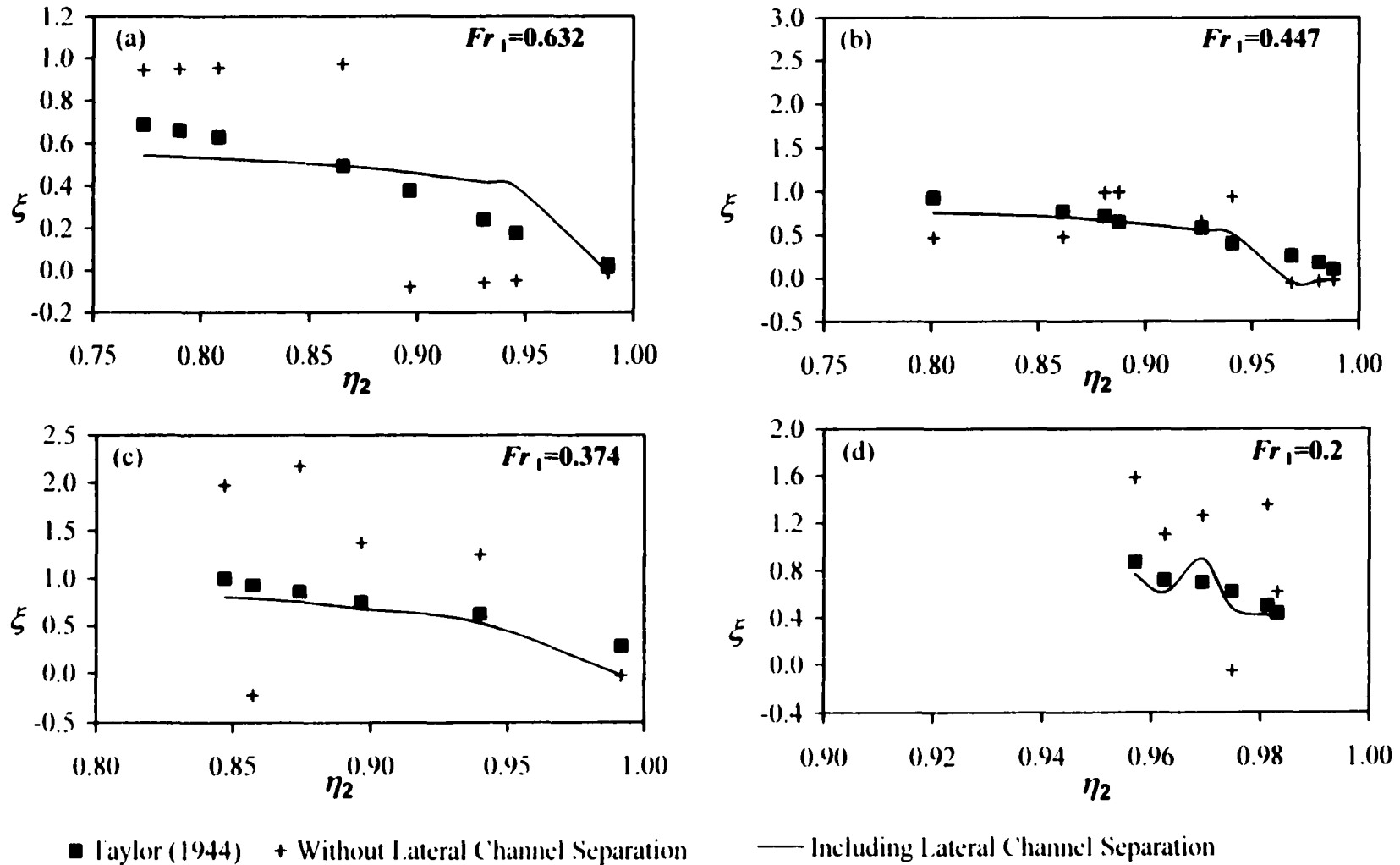


Fig. 4.7 Comparisons Between Taylor's (1944) Data and the Model Predictions Using Eqs. (4.6) and (4.7) for the Pressure and Eq. (4.18) for the Lateral Channel Separation Shear

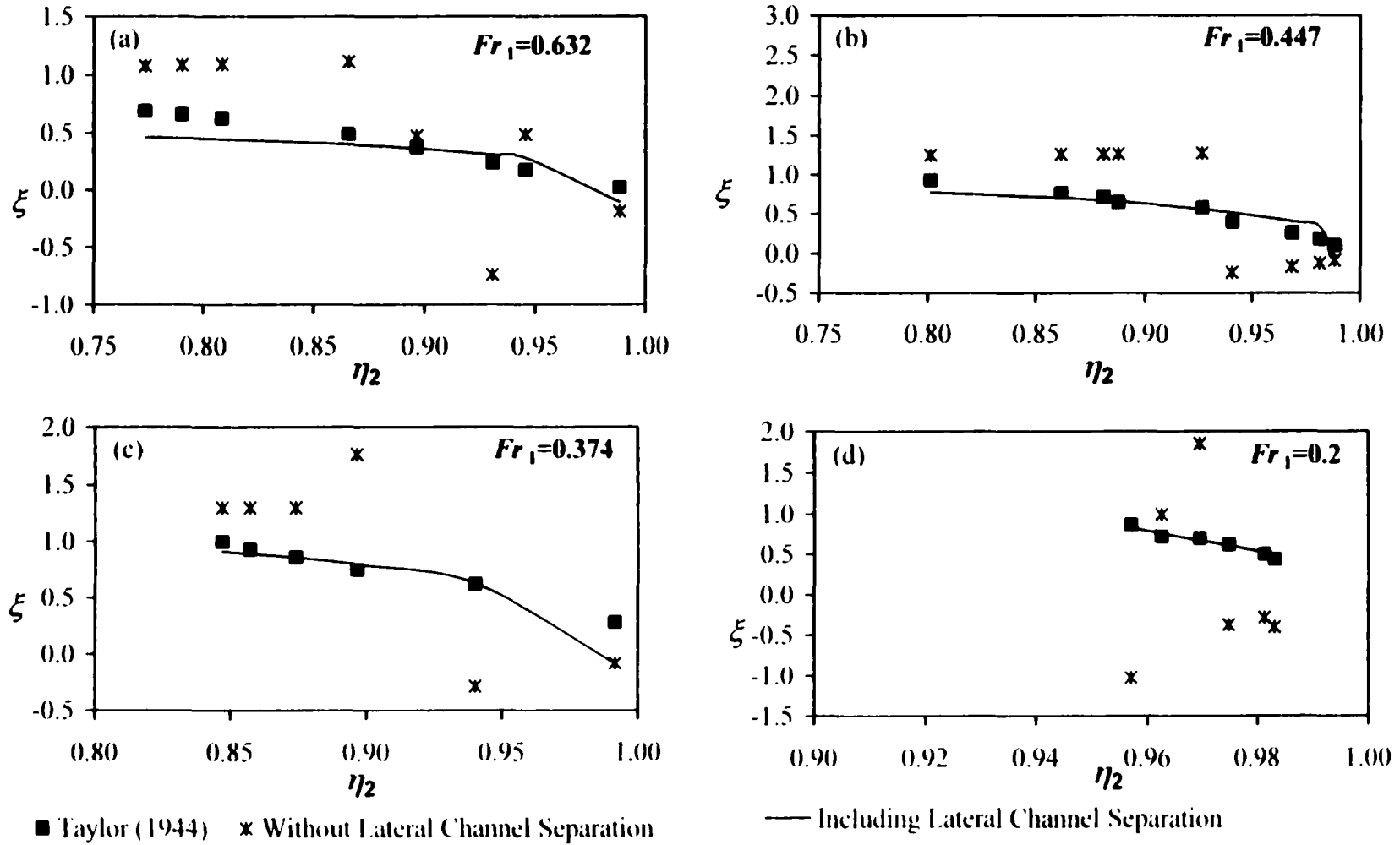


Fig. 4.8 Comparisons Between Taylor's (1944) Data and the Model Predictions Using Eqs. (4.10) and (4.11) for the Pressure and Eq. (4.18) for the Lateral Channel Separation Shear

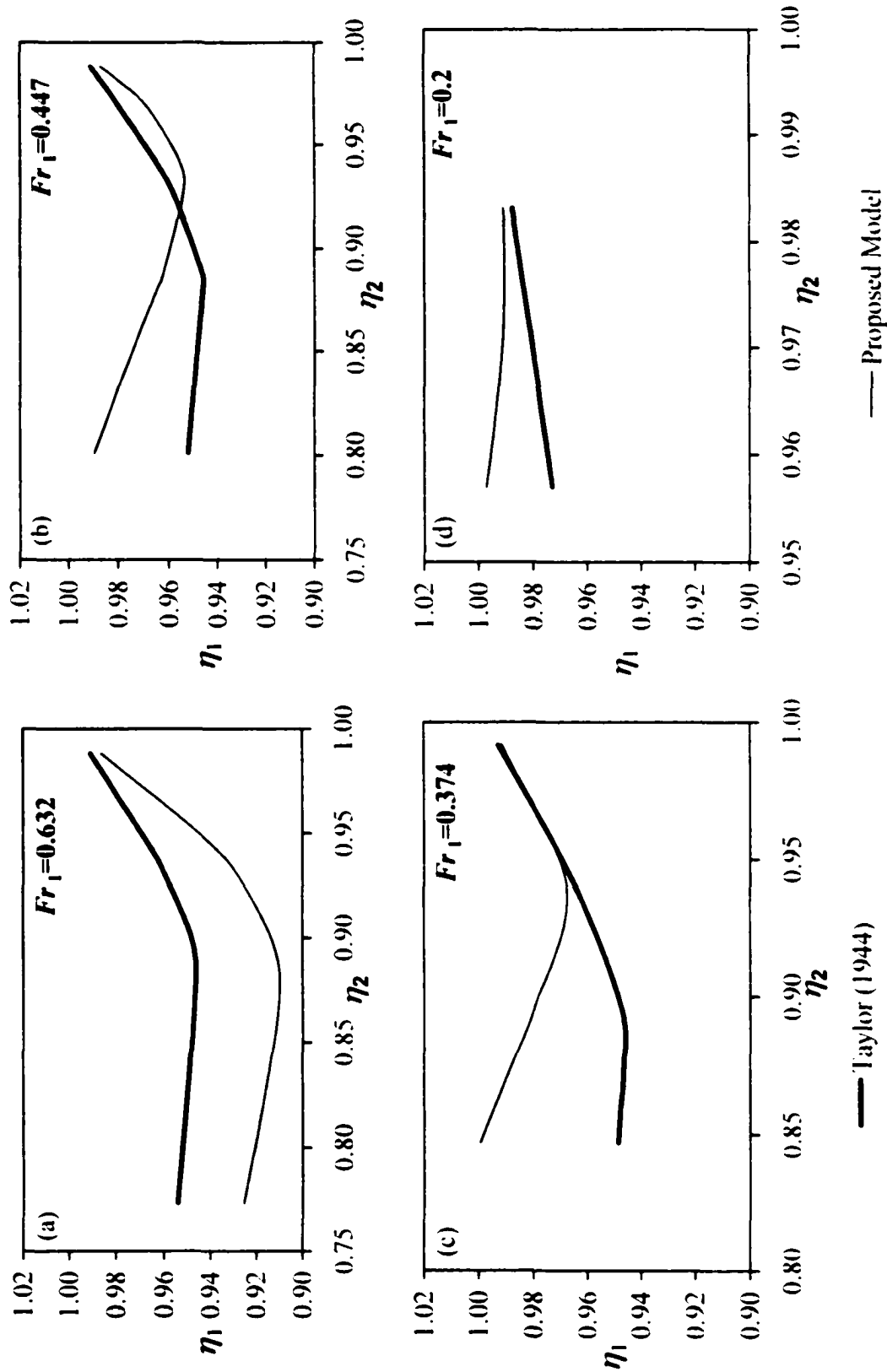


Fig. 4.9 The Model Predictions for the Main Channel Depth Ratio, η_1 , Using Eqs. (4.8) and (4.9) for the Pressure and Eq. (4.17) for the Lateral Channel Separation Shear

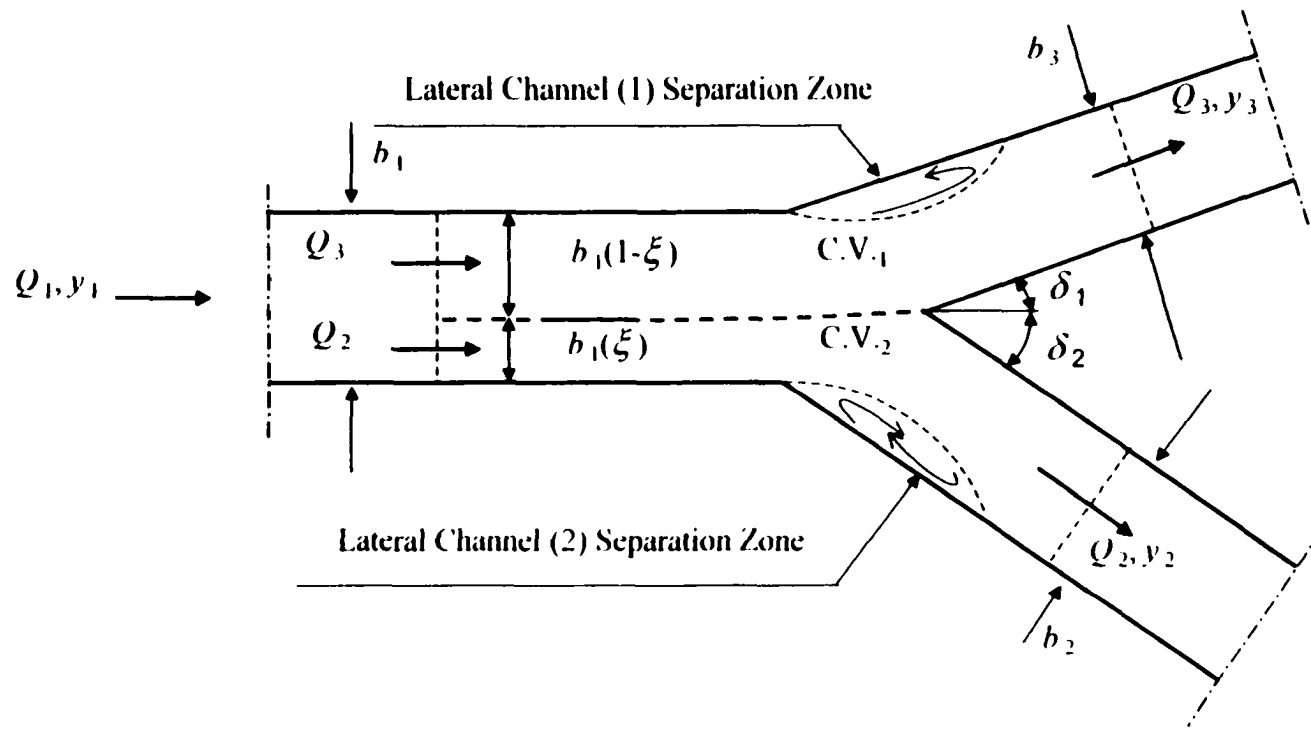


Fig. 4.10 Junction Geometry for Two Lateral Channels' Take-off (Symmetrical Junction)

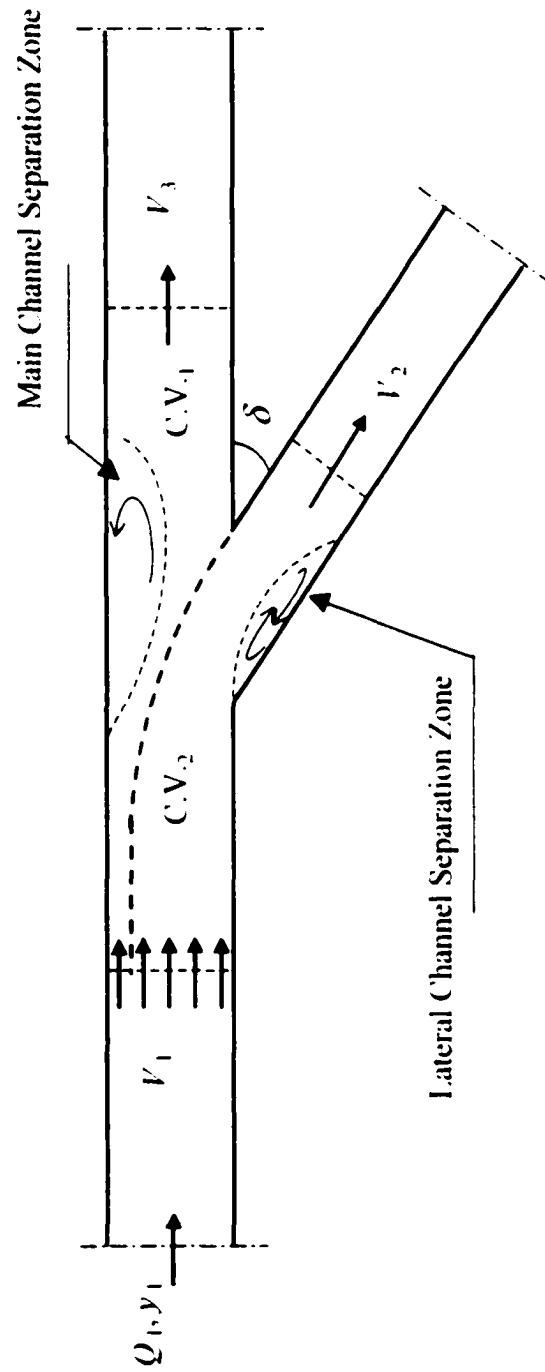


Fig. 4.11 Junction Geometry and Control Volumes Configuration for High Discharge Ratios

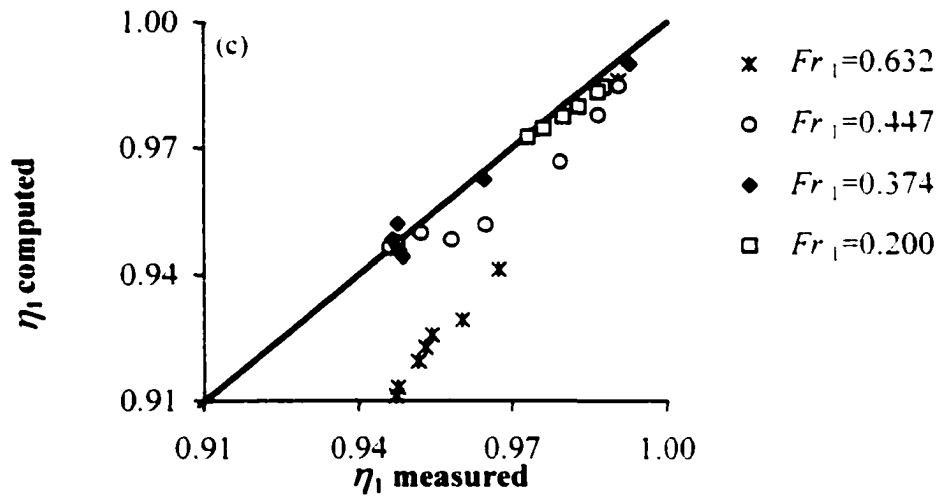
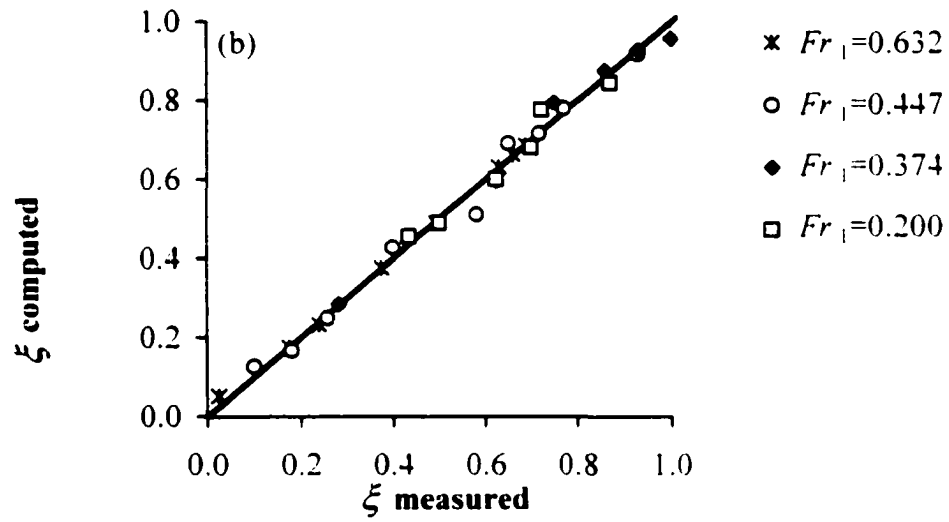
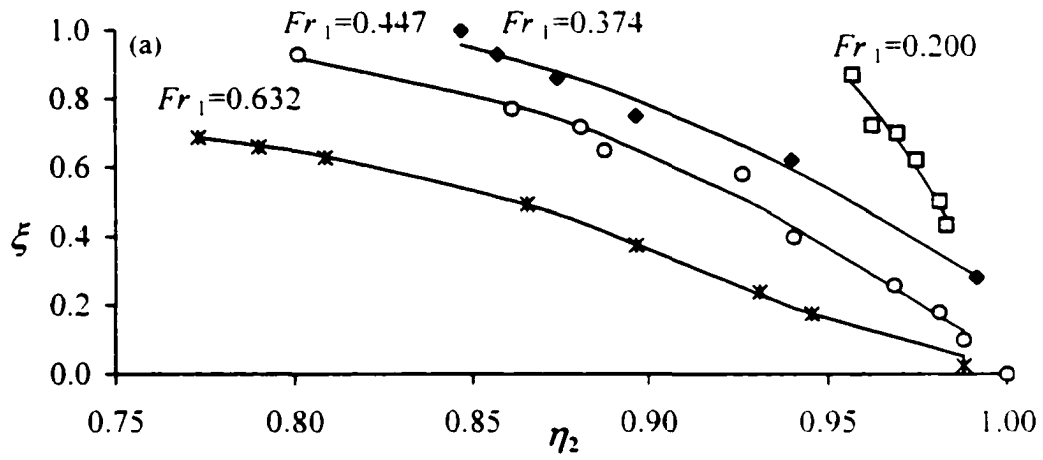
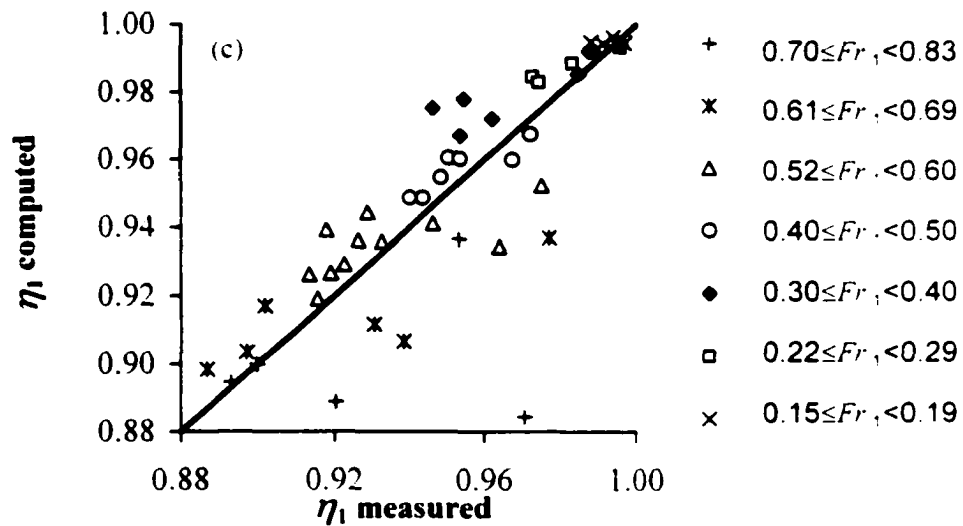
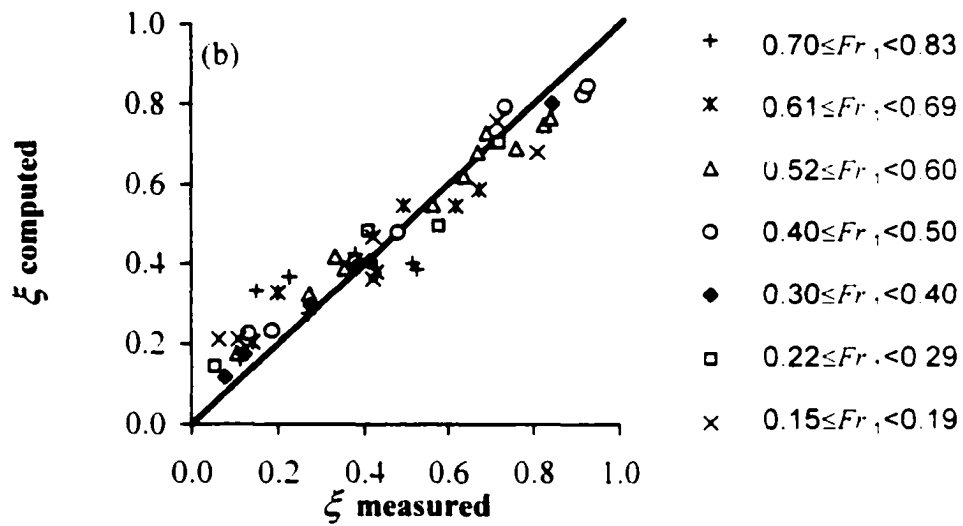
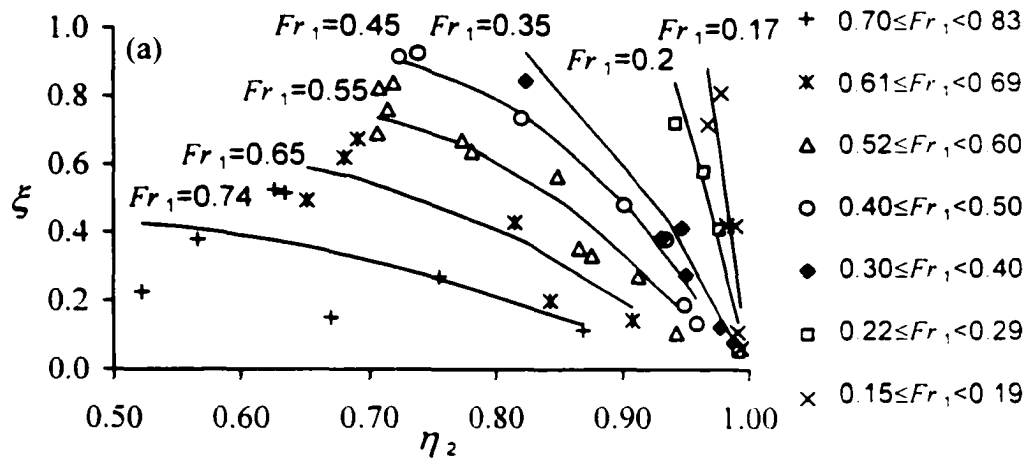
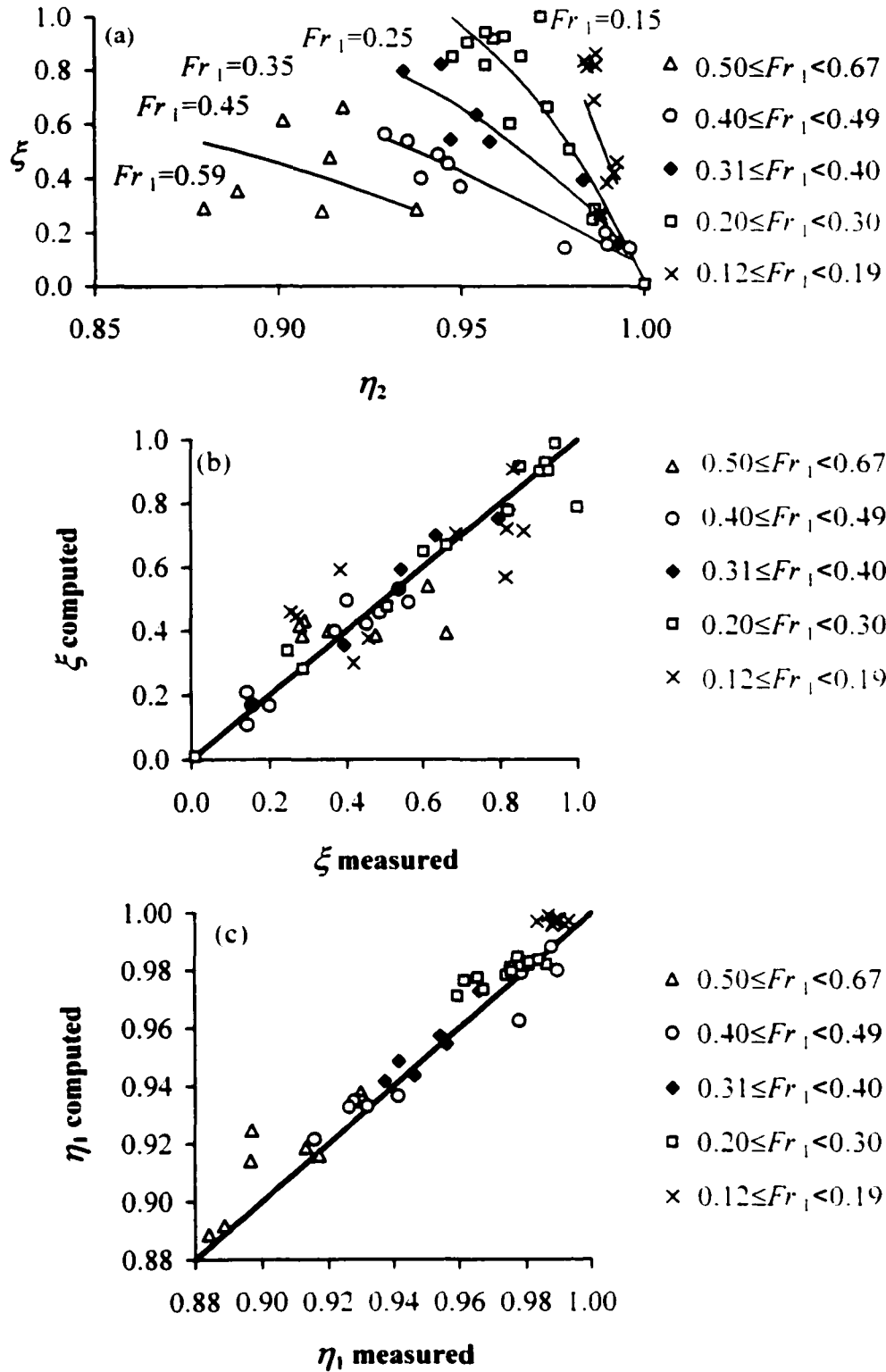


Fig. 4.12 (a-c) The Final Model Results. Comparison with Taylor's (1944) Data



**Fig. 4.13 (a-c) The Final Model Results.
Comparison with Law's (1965) Data**



**Fig. 4.14 (a-c) The Final Model Results.
Comparison with Grace's (1958) Data for $\delta=30^\circ$ and $\omega_2=1.0$**

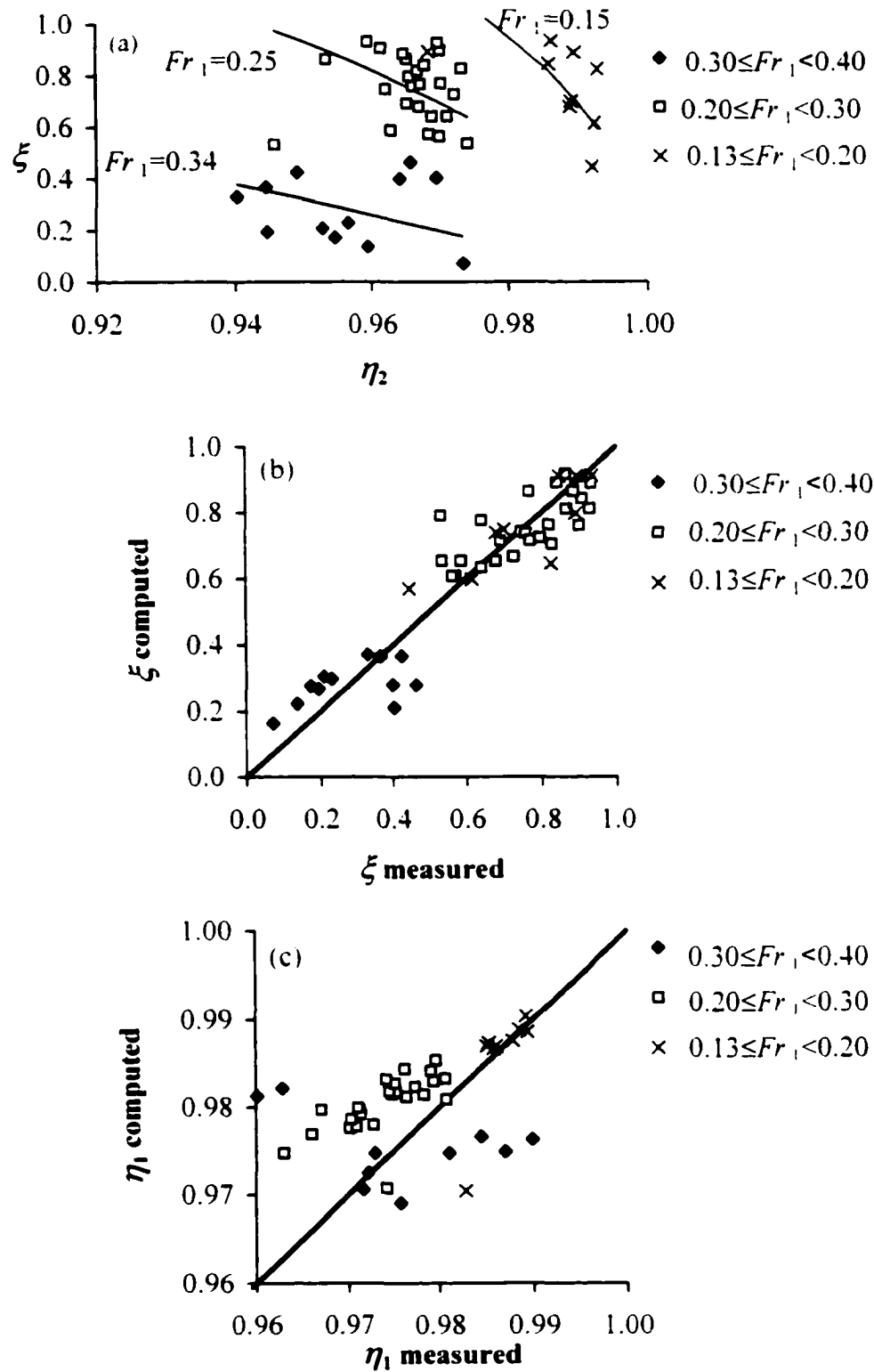
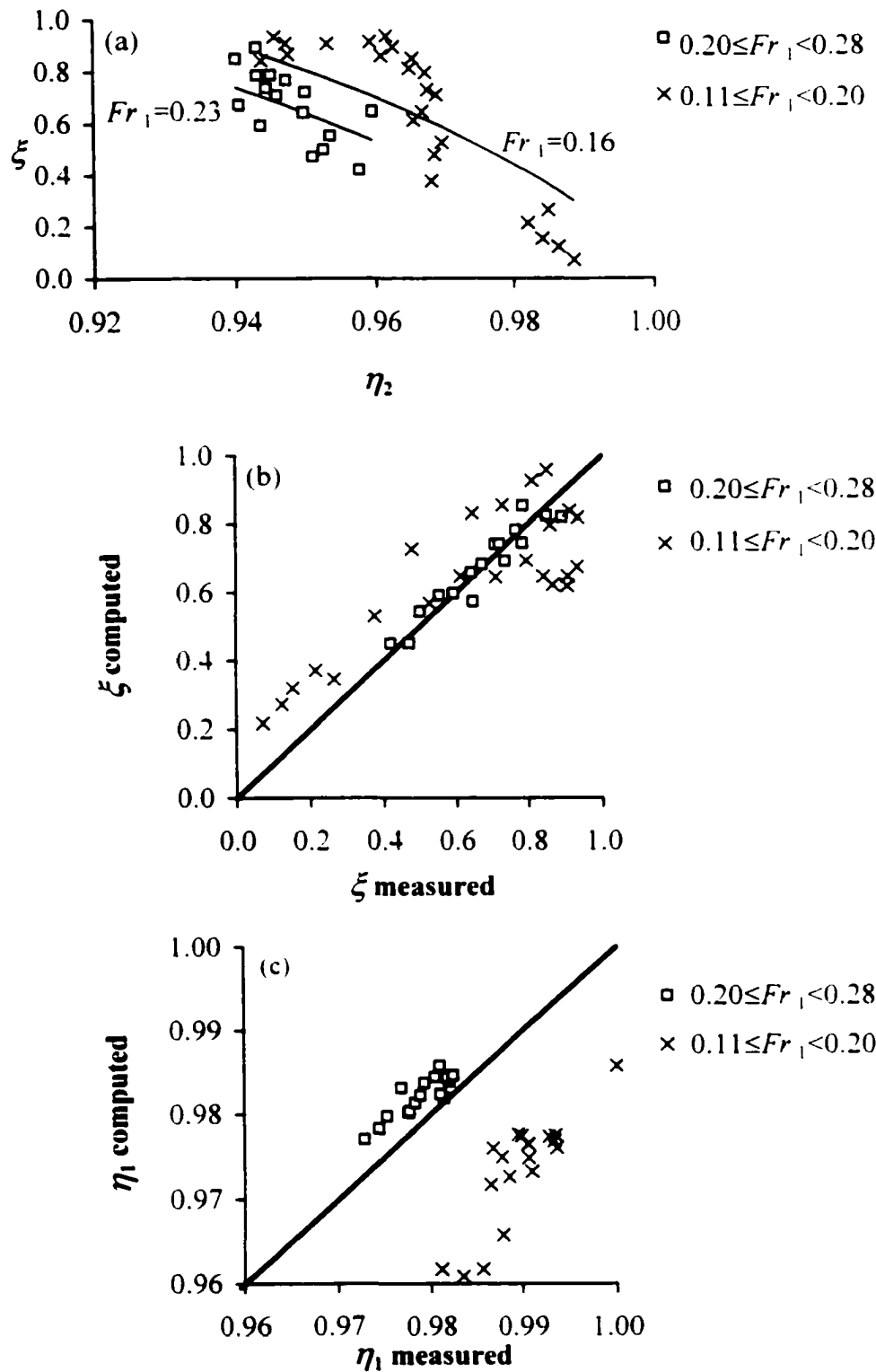
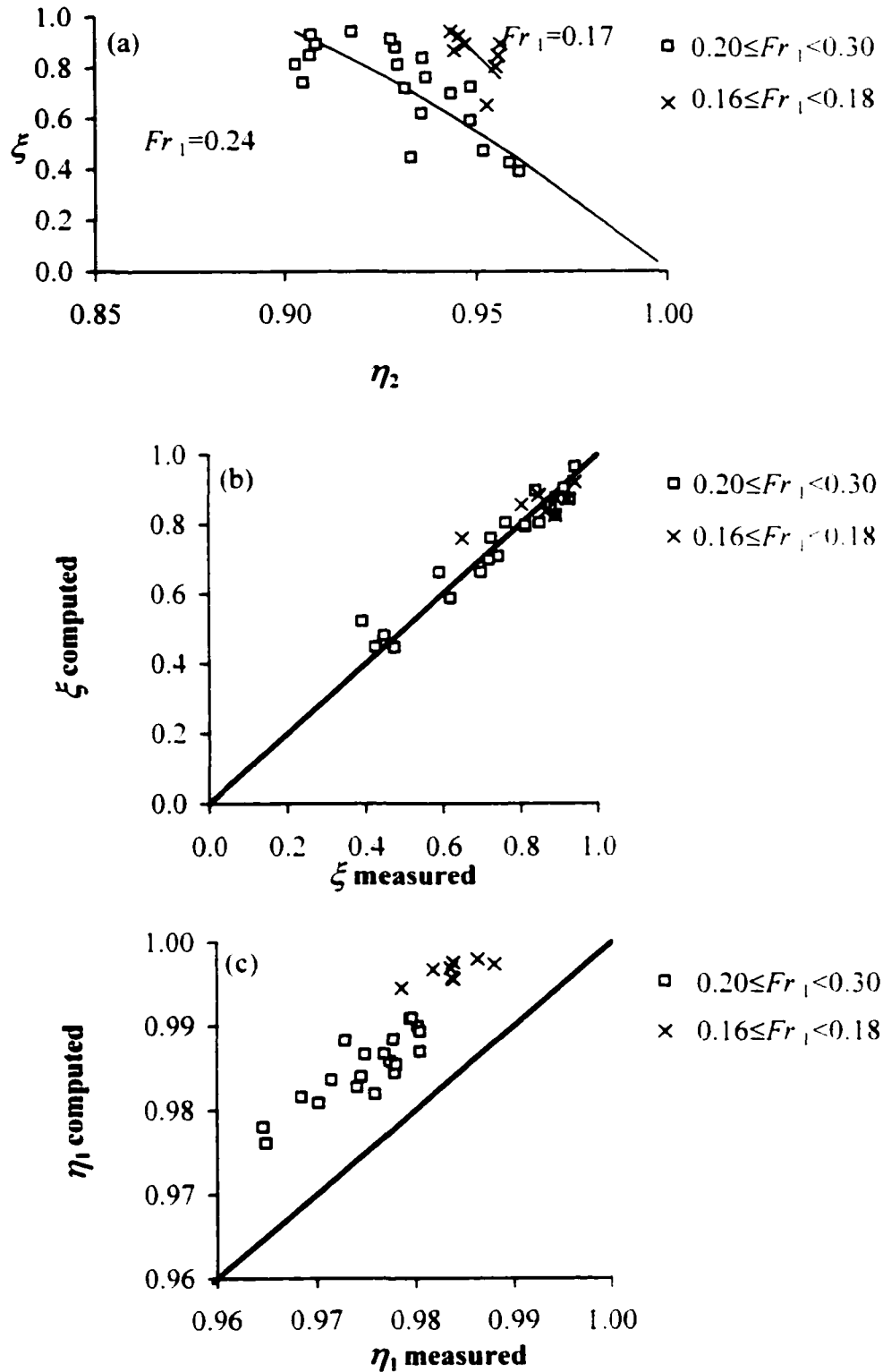


Fig. 4.15 (a-c) The Final Model Results.
Comparison with Grace's (1958) Data for $\delta=60^\circ$ and $\omega_2=1.0$



**Fig. 4.16 (a-c) The Final Model Results.
Comparison with Grace's (1958) Data for $\delta=90^\circ$ and $\omega_2=1.0$**



**Fig. 4.17 (a-c) The Final Model Results.
Comparison with Grace's (1958) Data for $\delta=120^\circ$ and $\omega_2=1.0$**

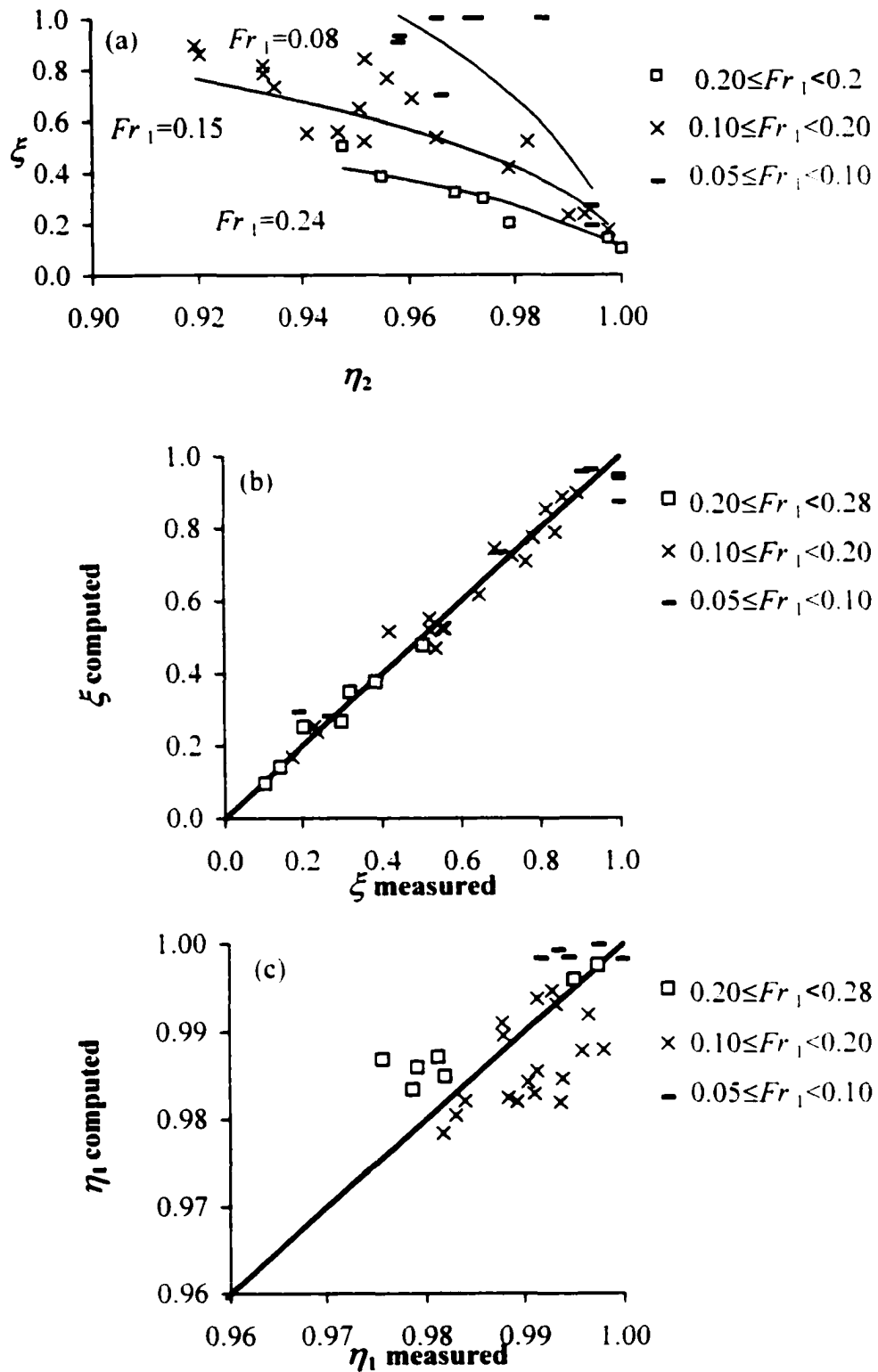


Fig. 4.18 (a-c) The Final Model Results.
Comparison with Grace's (1958) Data for $\delta=30^\circ$ and $\omega_2=0.4$

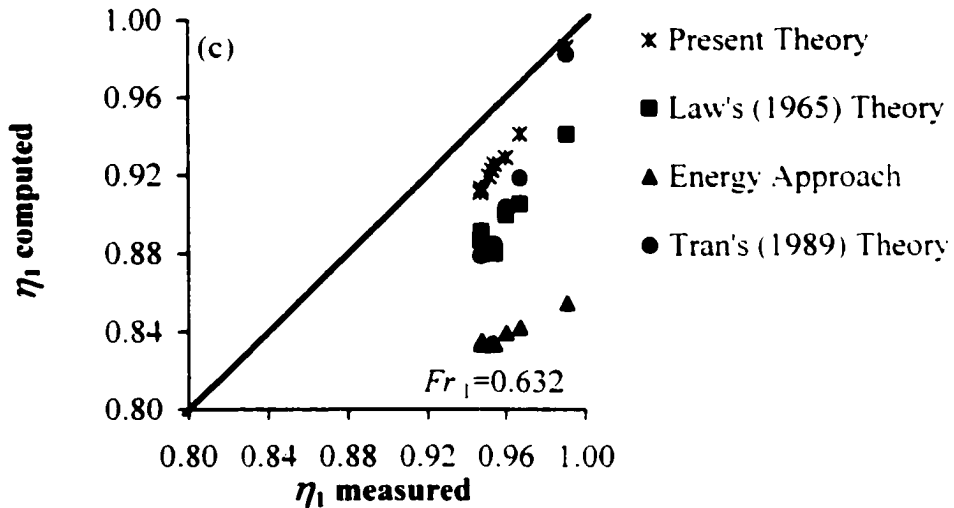
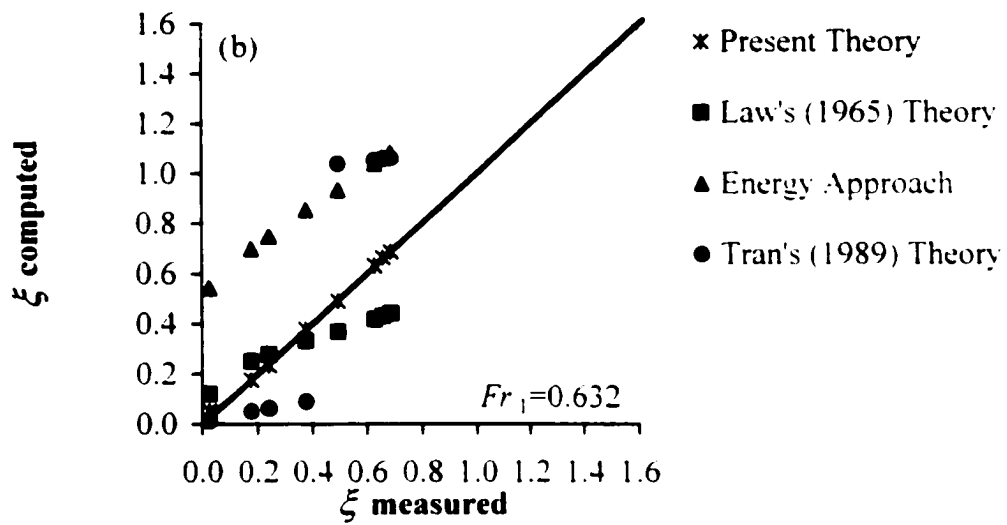
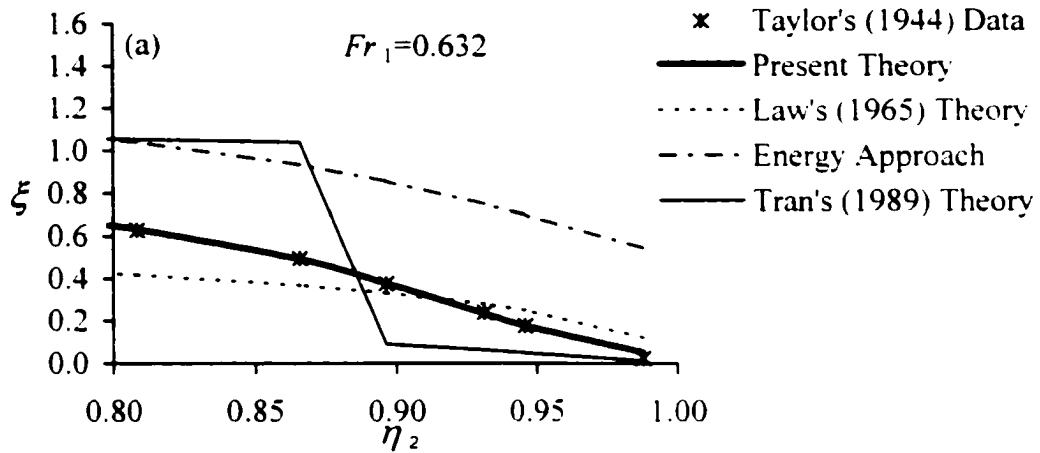


Fig. 4.19(a-c) Comparing the Proposed Theory with Law's (1965) Theory, Tran's (1989) Theory and the Energy Approach Using Taylor's (1944) Data $Fr_1=0.632$

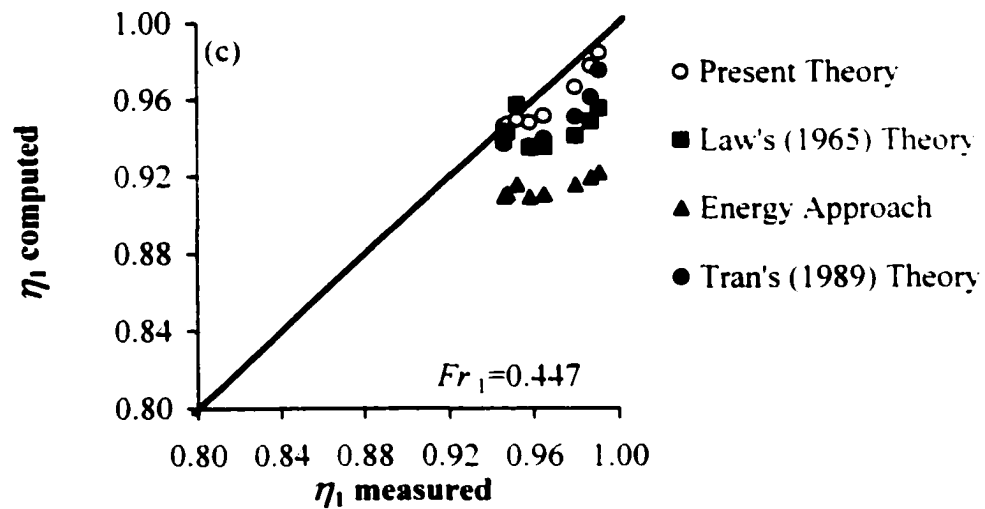
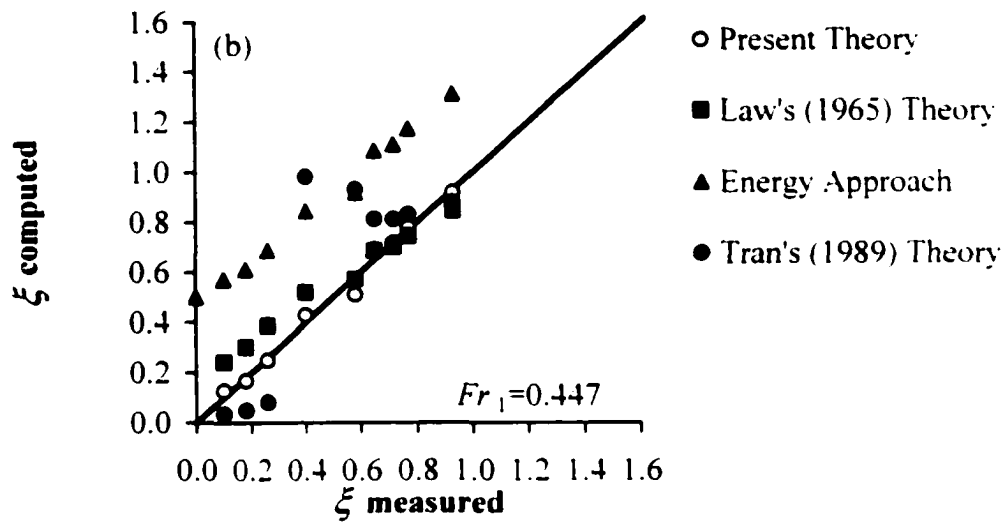
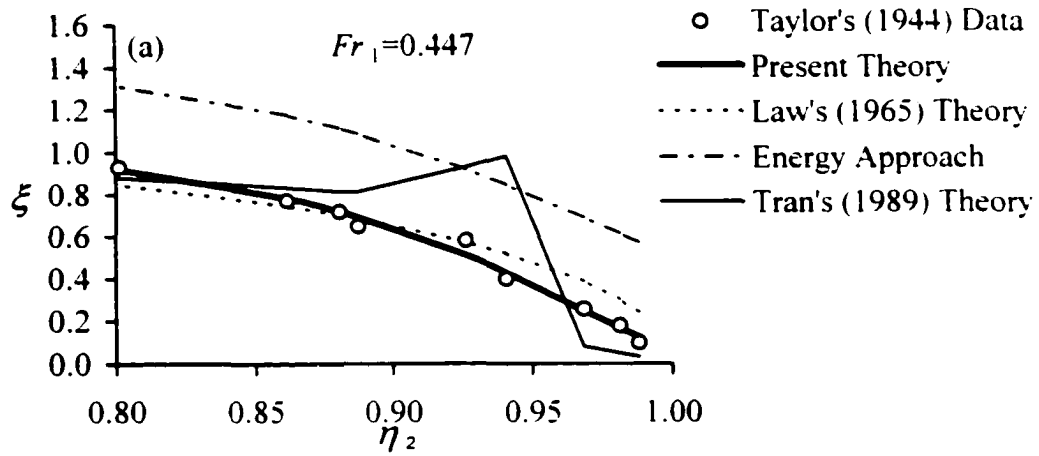


Fig. 4.20(a-c) Comparing the Proposed Theory with Law's (1965) Theory, Tran's (1989) Theory and the Energy Approach Using Taylor's (1944) Data $Fr_1=0.447$

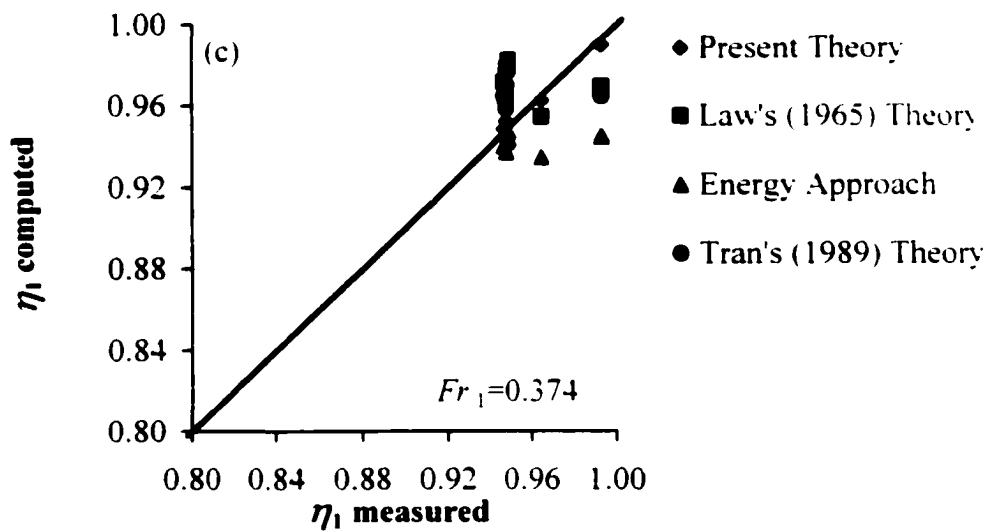
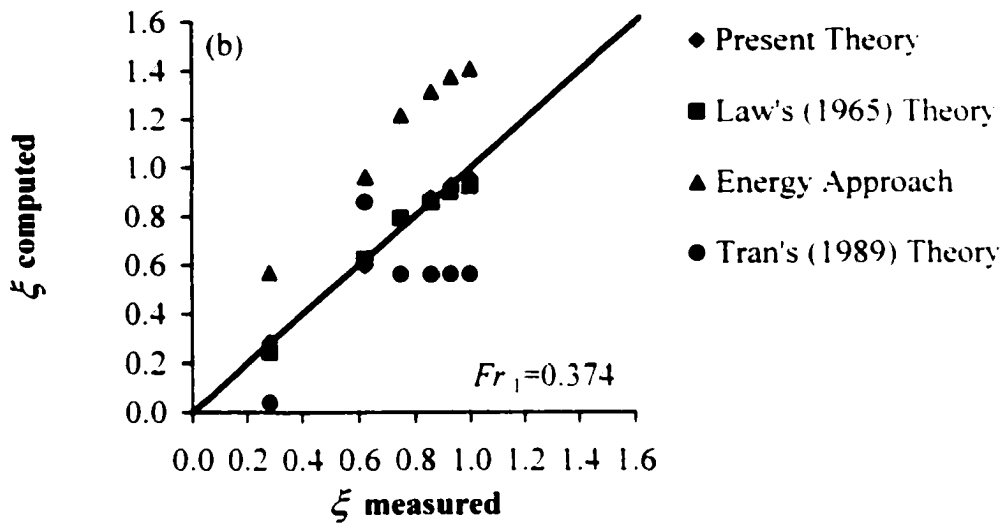
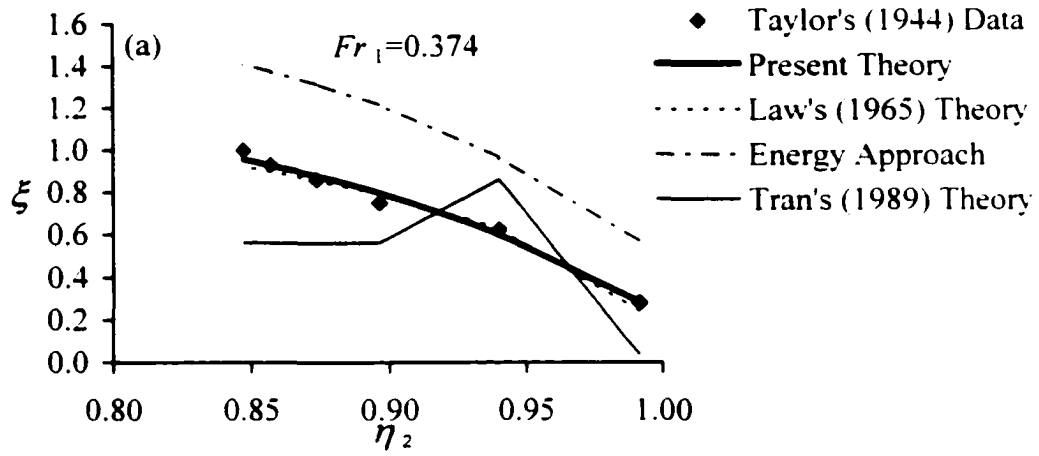


Fig. 4.21(a-c) Comparing the Proposed Theory with Law's (1965) Theory, Tran's (1989) Theory and the Energy Approach Using Taylor's (1944) Data $Fr_1 = 0.374$

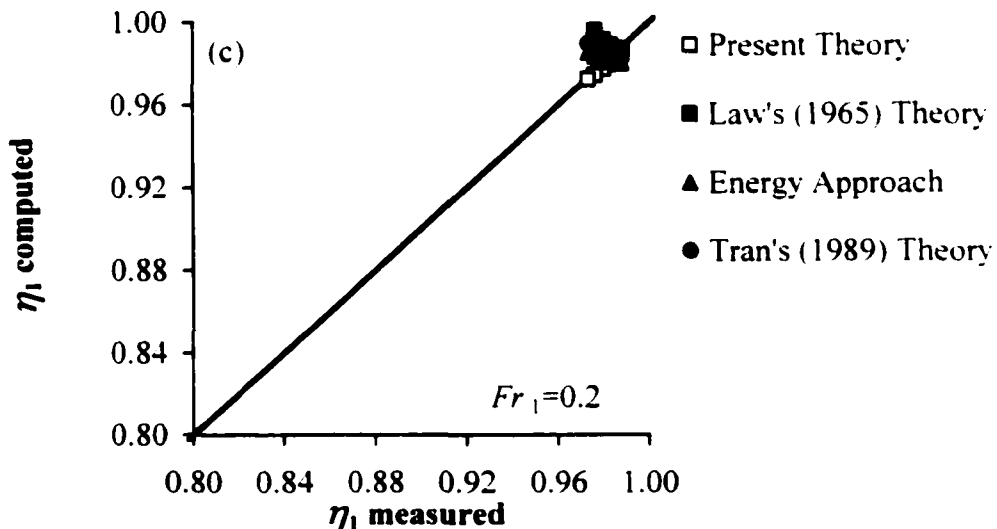
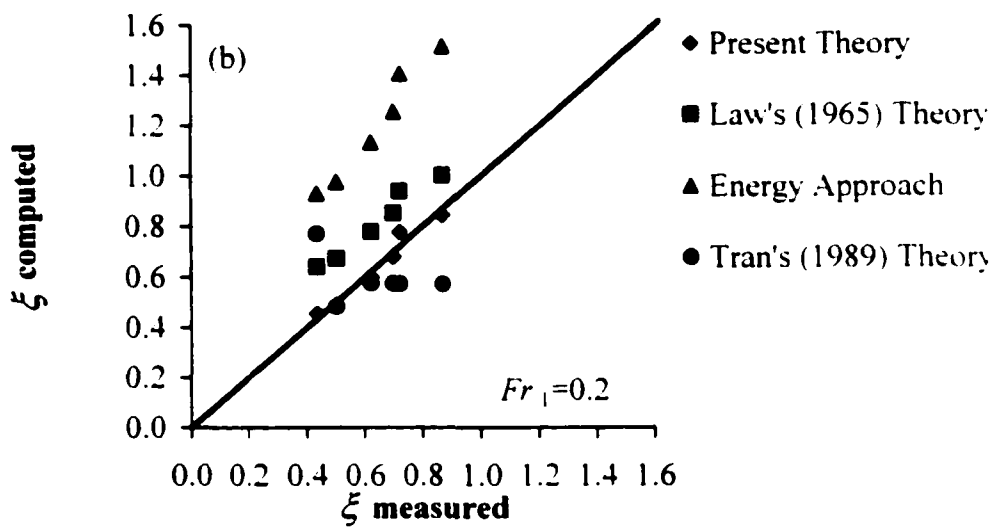
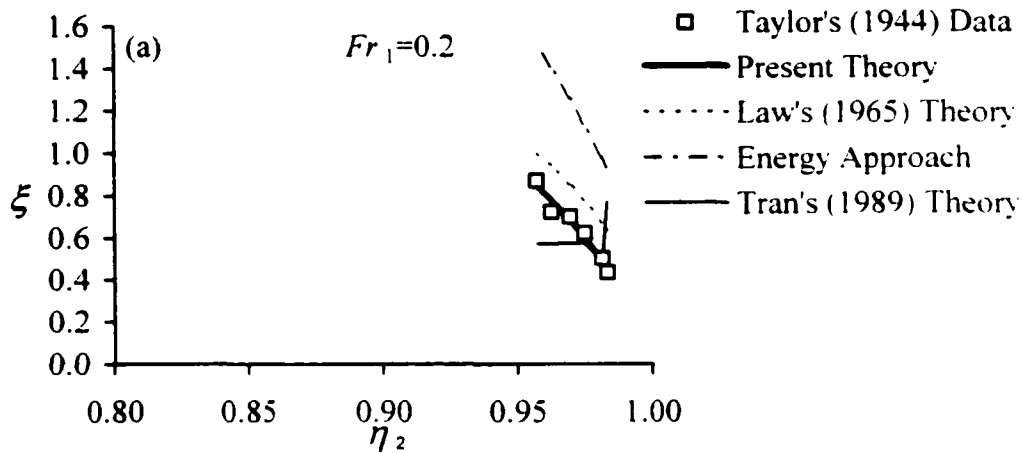


Fig. 4.22(a-c) Comparing the Proposed Theory with Law's (1965) Theory, Tran's (1989) Theory and the Energy Approach Using Taylor's (1944) Data $Fr_1=0.2$

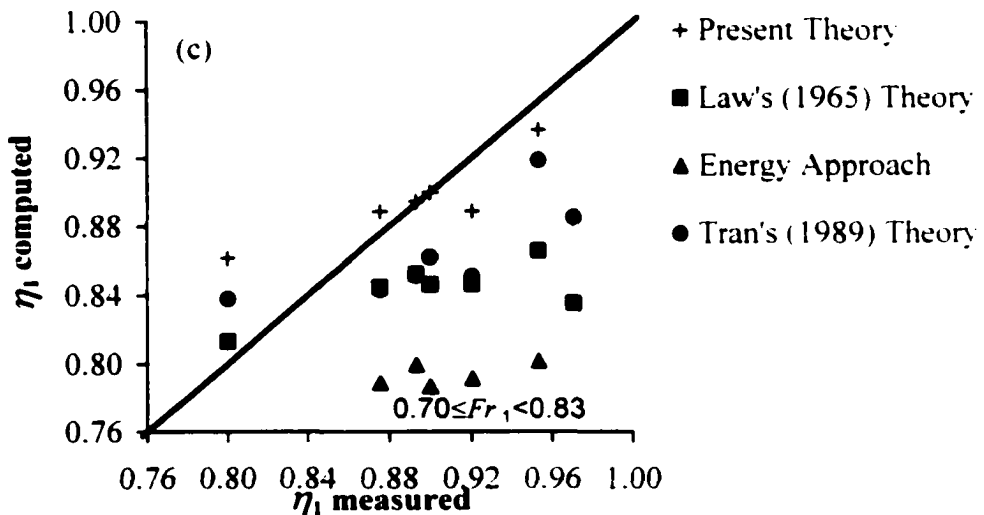
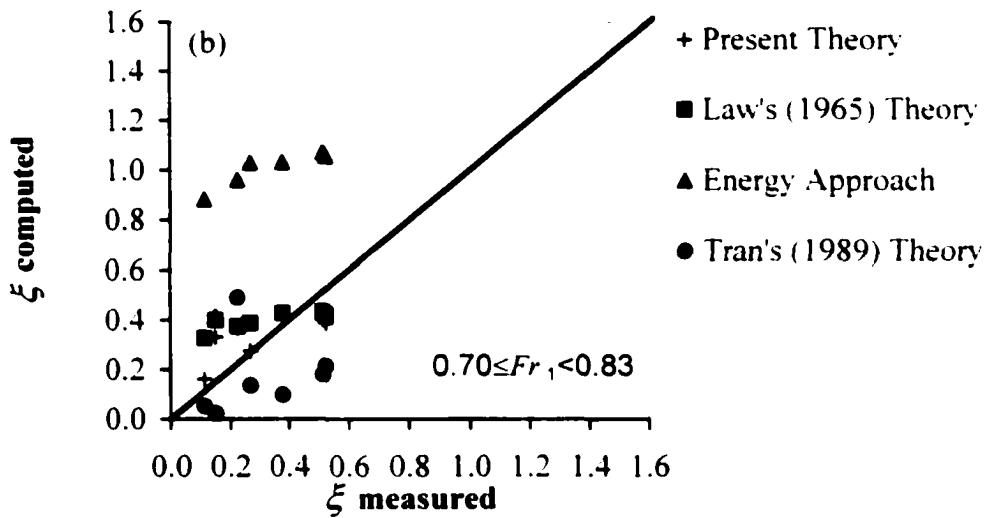
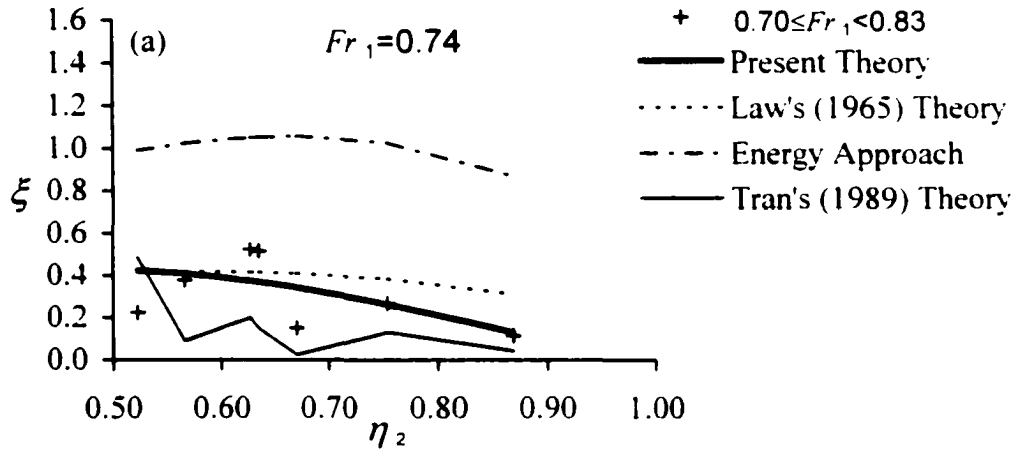


Fig. 4.23(a-c) Comparing the Proposed Theory with Law's (1965) Theory, Tran's (1989) Theory and the Energy Approach Using Law's (1965) Data $0.70 \leq Fr_1 < 0.83$

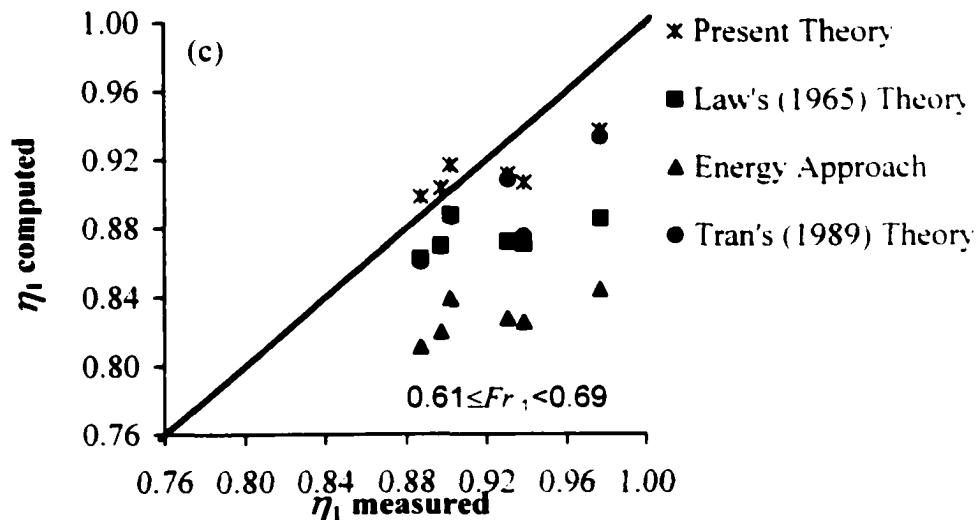
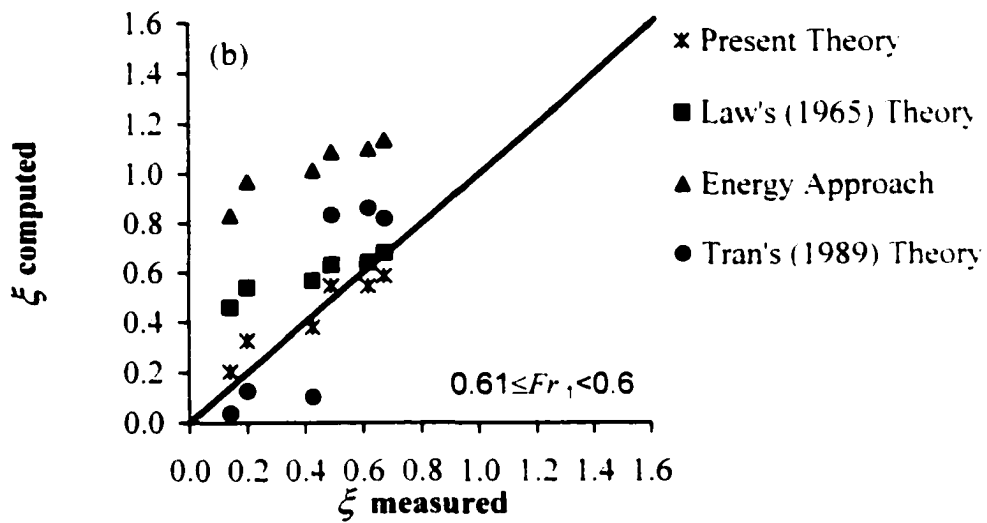
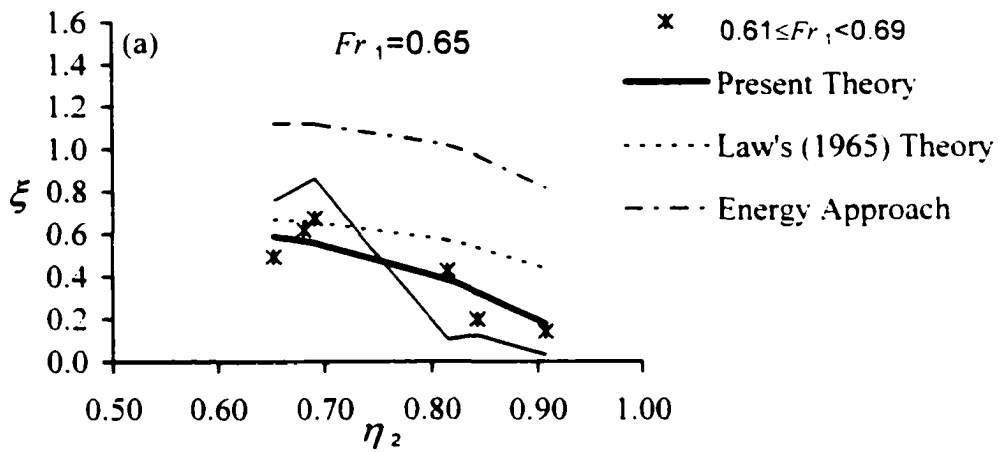


Fig. 4.24(a-c) Comparing the Proposed Theory with Law's (1965) Theory, Tran's (1989) Theory and the Energy Approach Using Law's (1965) Data $0.61 \leq Fr_1 < 0.69$

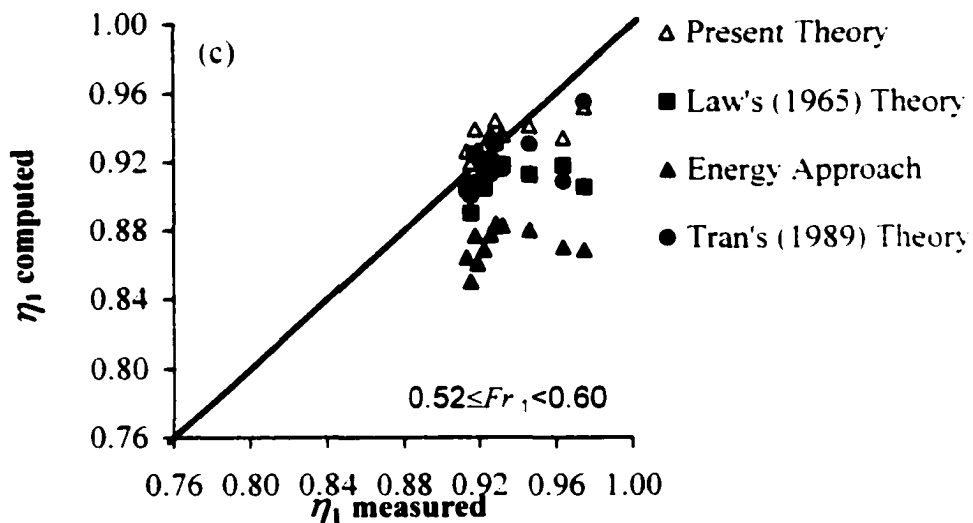
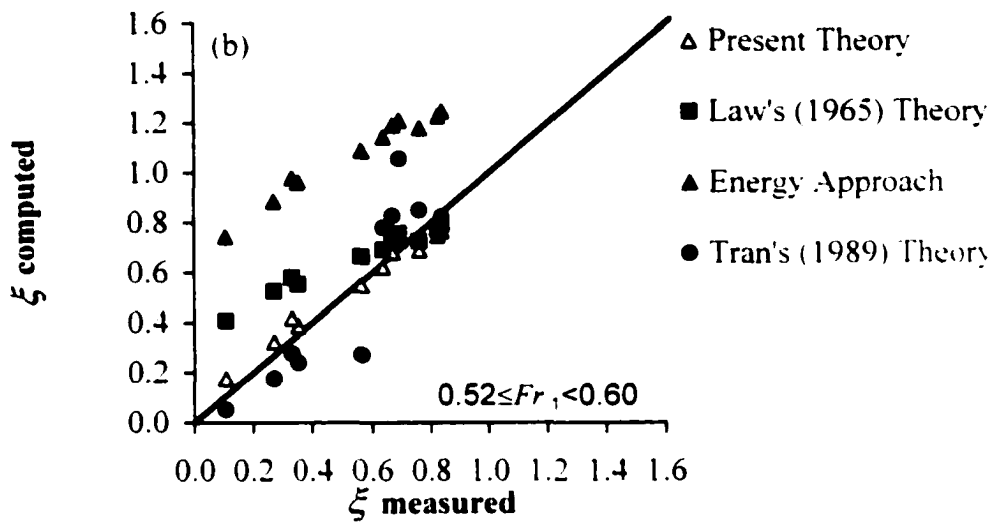
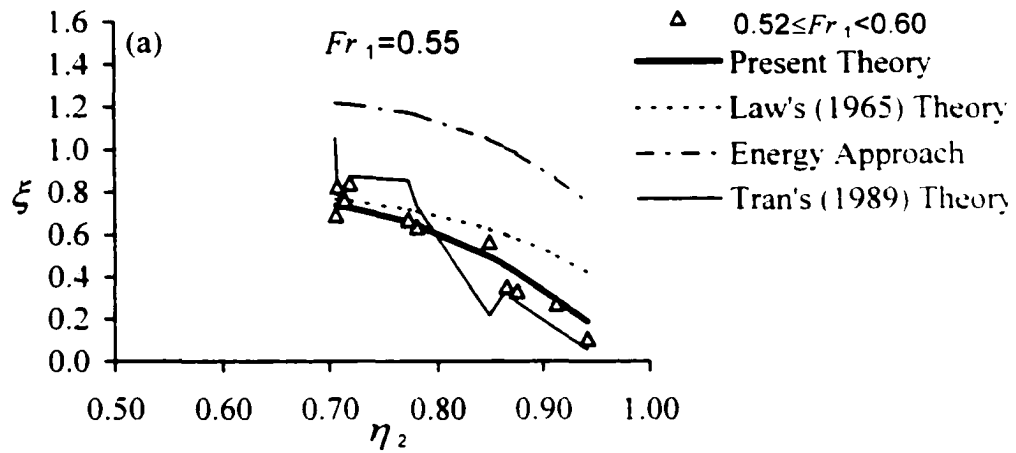


Fig. 4.25(a-c) Comparing the Proposed Theory with Law's (1965) Theory, Tran's (1989) Theory and the Energy Approach Using Law's (1965) Data $0.52 \leq Fr_1 < 0.60$

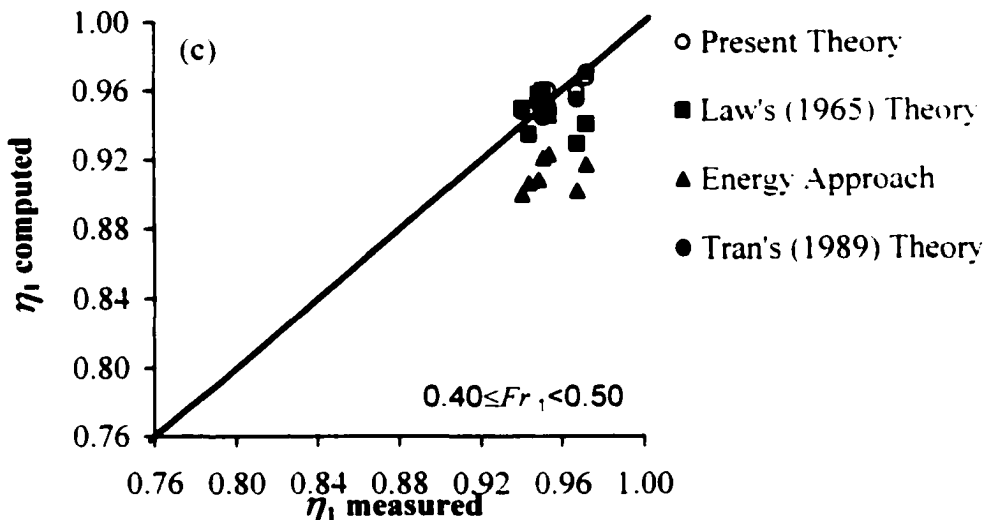
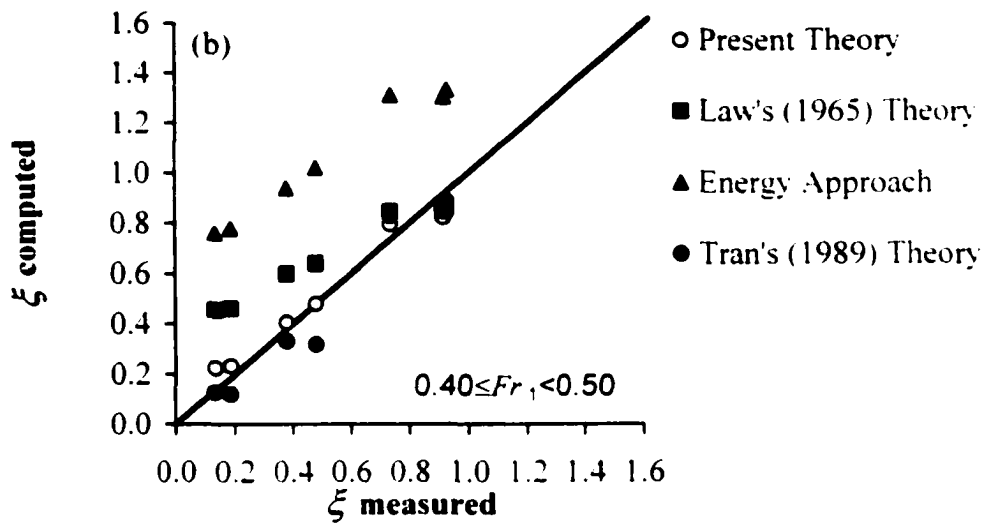
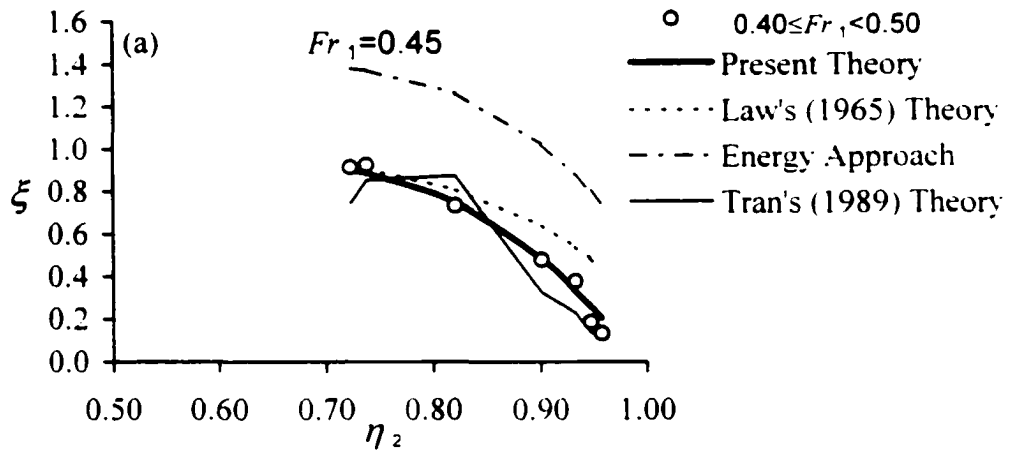


Fig. 4.26(a-c) Comparing the Proposed Theory with Law's (1965) Theory, Tran's (1989) Theory and the Energy Approach Using Law's (1965) Data $0.40 \leq Fr_1 < 0.50$

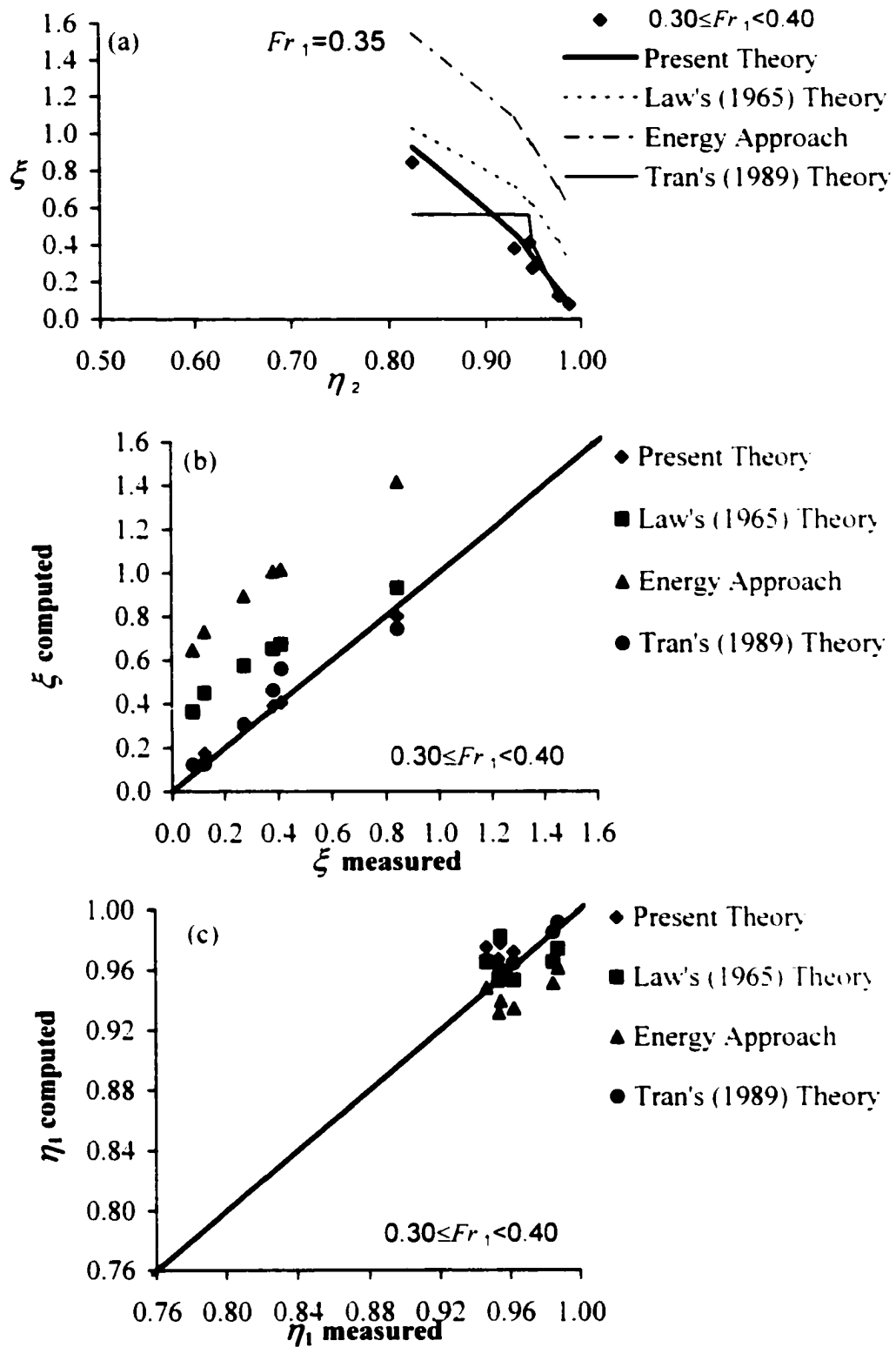


Fig. 4.27(a-c) Comparing the Proposed Theory with Law's (1965) Theory, Tran's (1989) Theory and the Energy Approach Using Law's (1965) Data $0.30 \leq Fr_1 < 0.40$

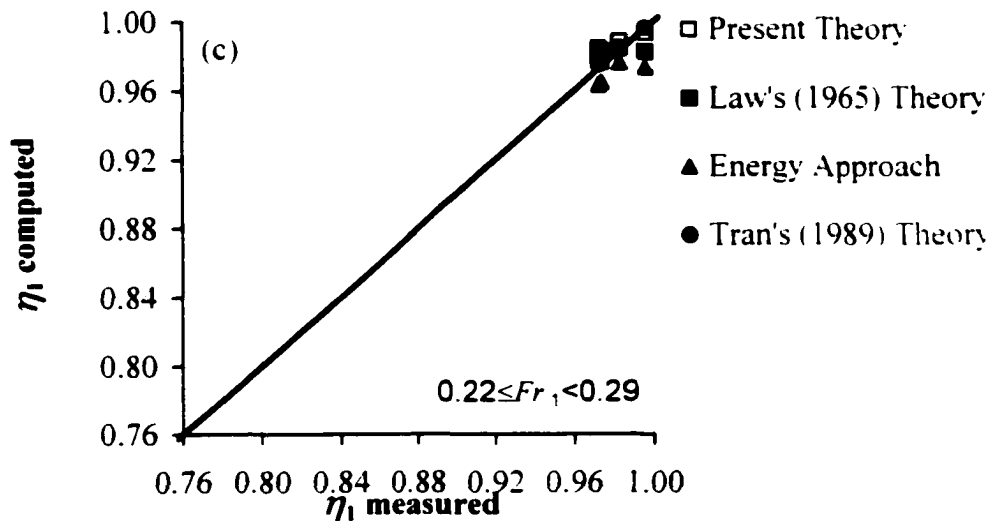
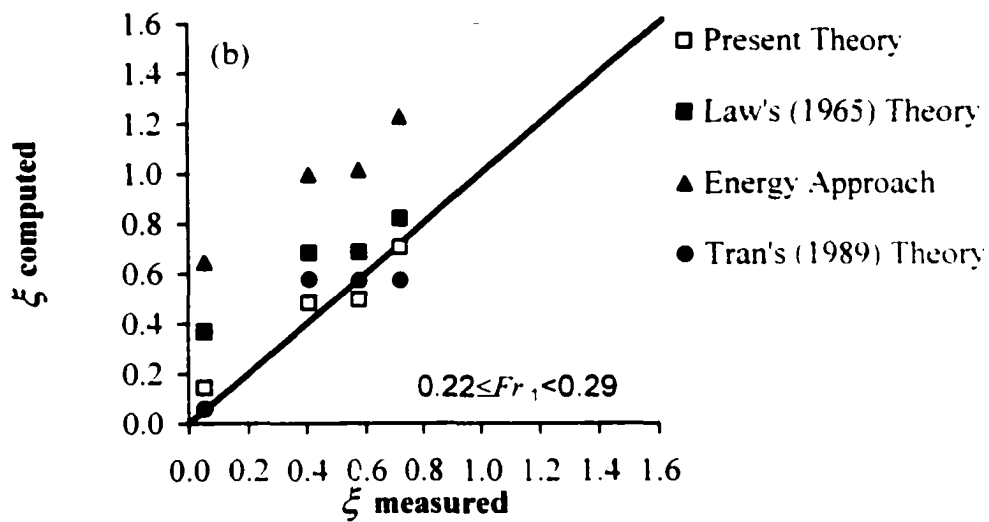
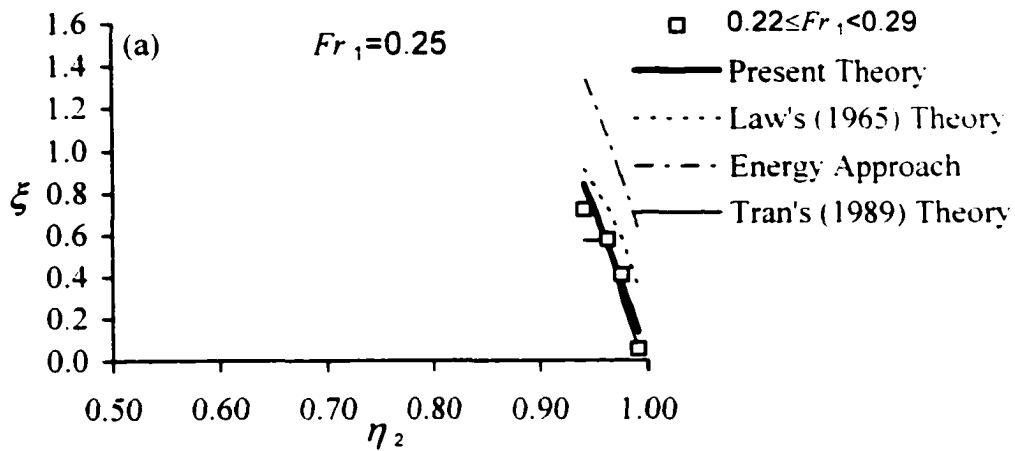


Fig. 4.28(a-c) Comparing the Proposed Theory with Law's (1965) Theory, Tran's (1989) Theory and the Energy Approach Using Law's (1965) Data $0.22 \leq Fr_1 < 0.29$

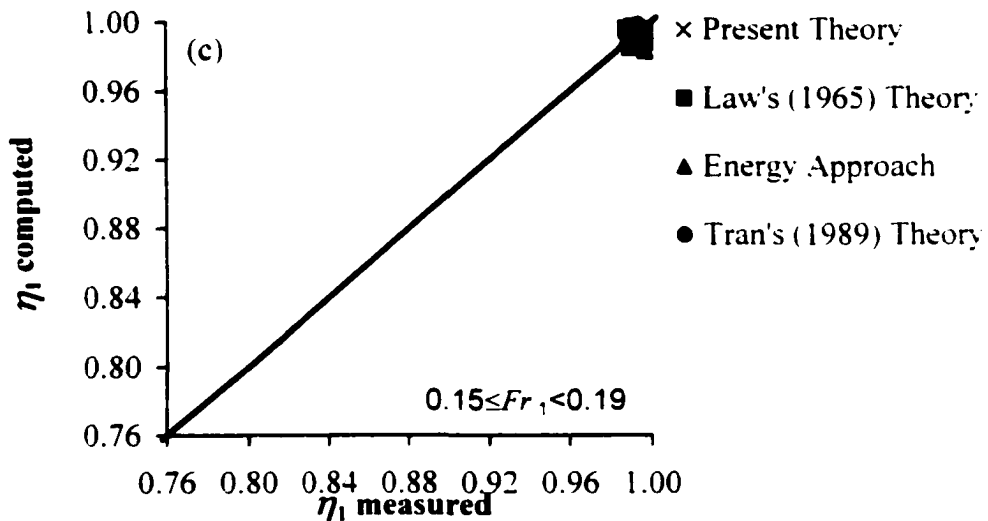
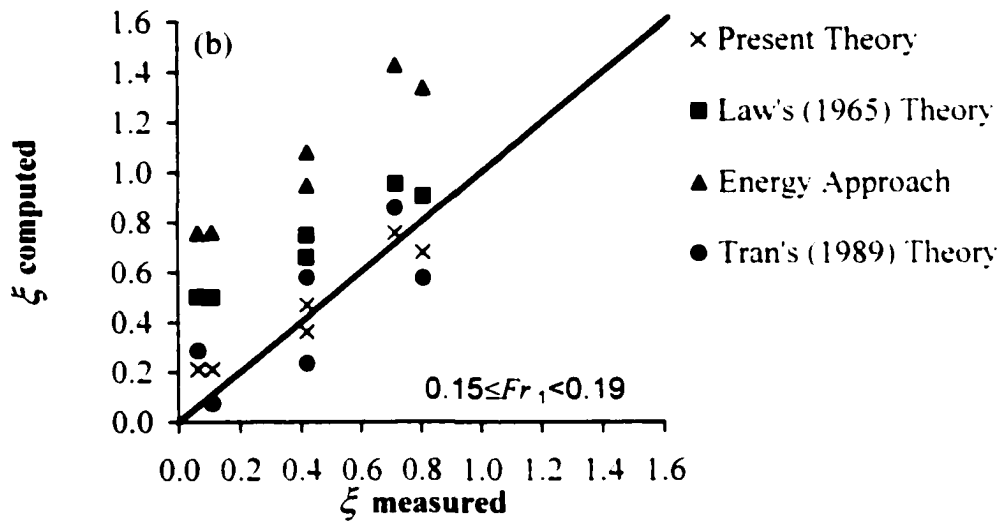
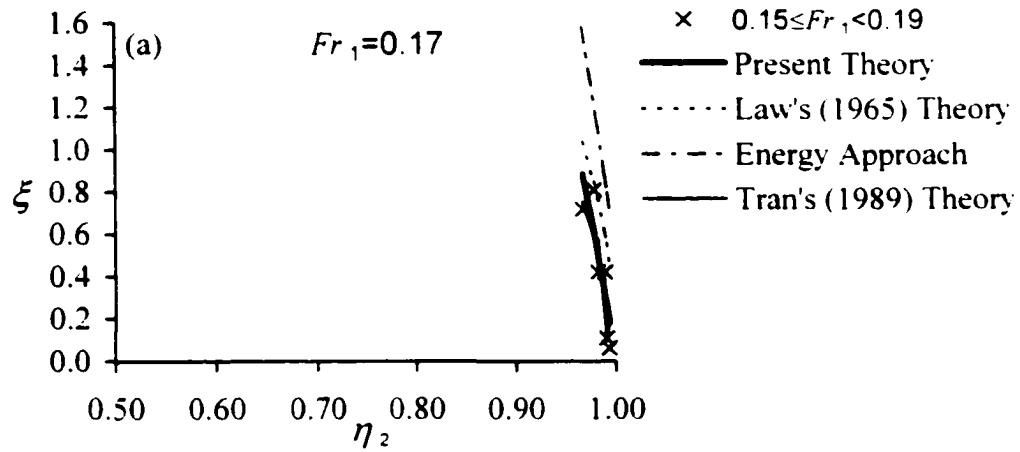


Fig. 4.29(a-c) Comparing the Proposed Theory with Law's (1965) Theory, Tran's (1989) Theory and the Energy Approach Using Law's (1965) Data $0.15 \leq Fr_1 < 0.19$

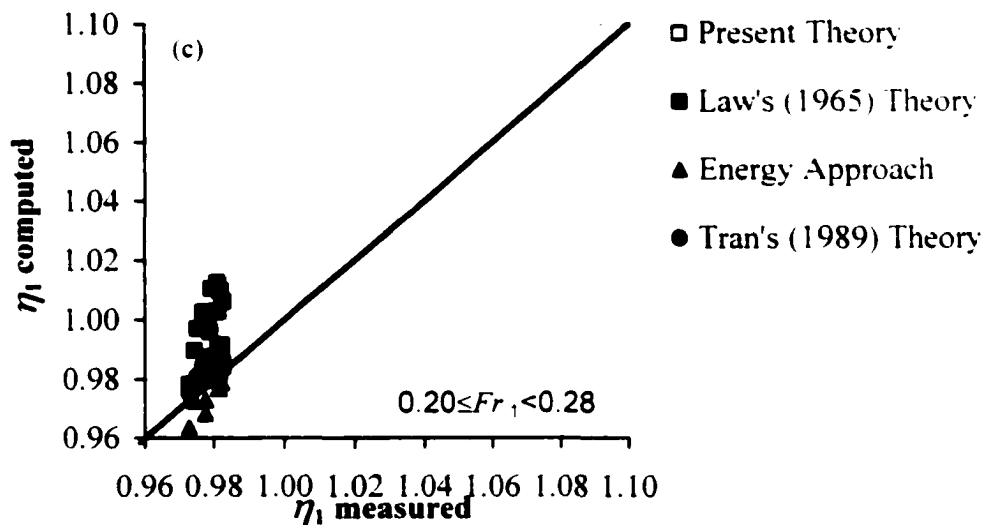
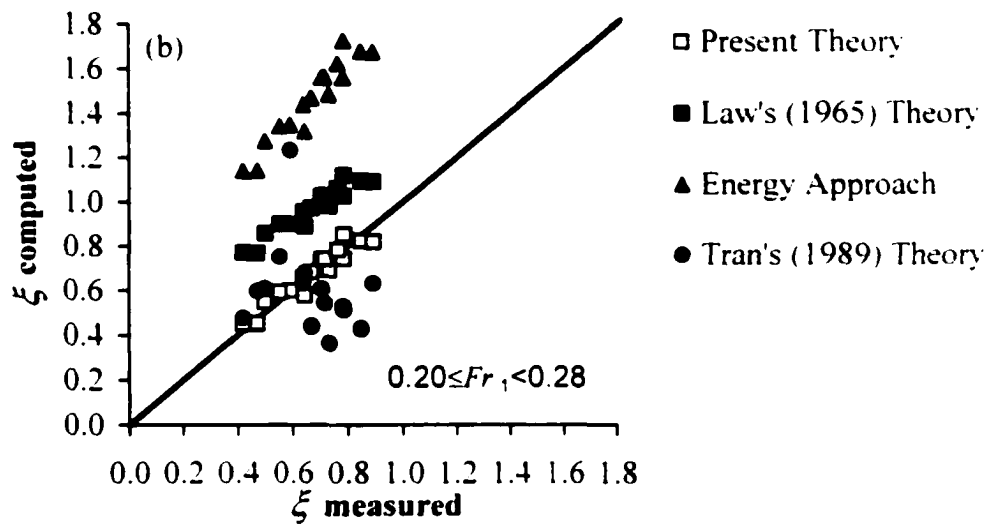
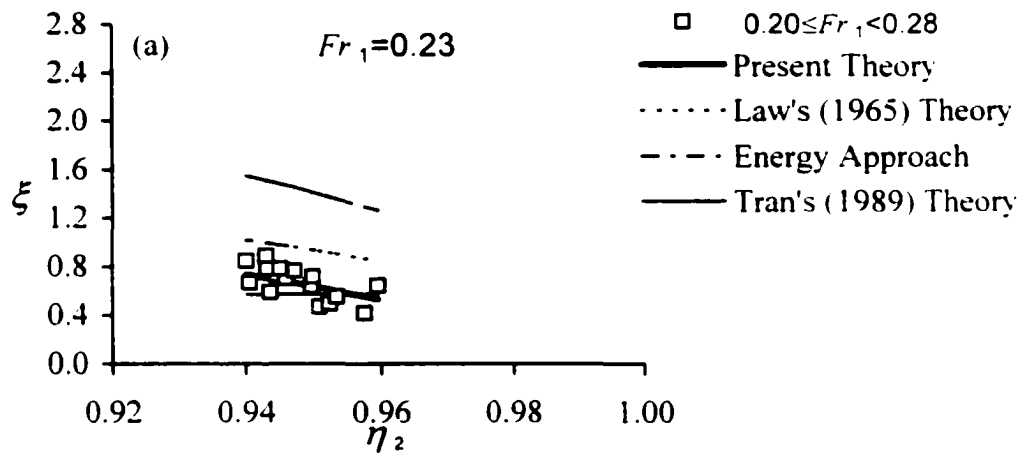


Fig. 4.30(a-c) Comparing the Proposed Theory with Law's (1965) Theory, Tran's (1989) Theory and the Energy Approach Using Grace's (1944) Data $0.20 \leq Fr_1 < 0.28$

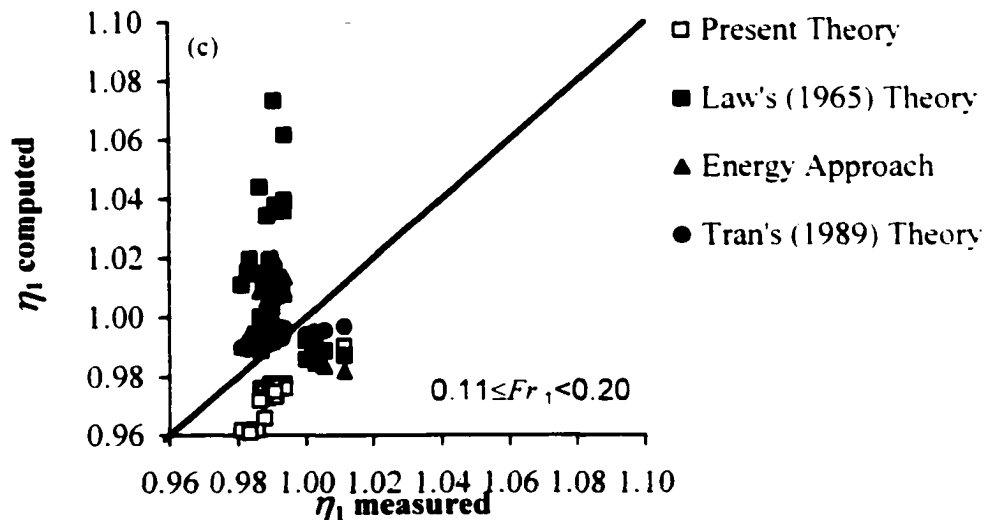
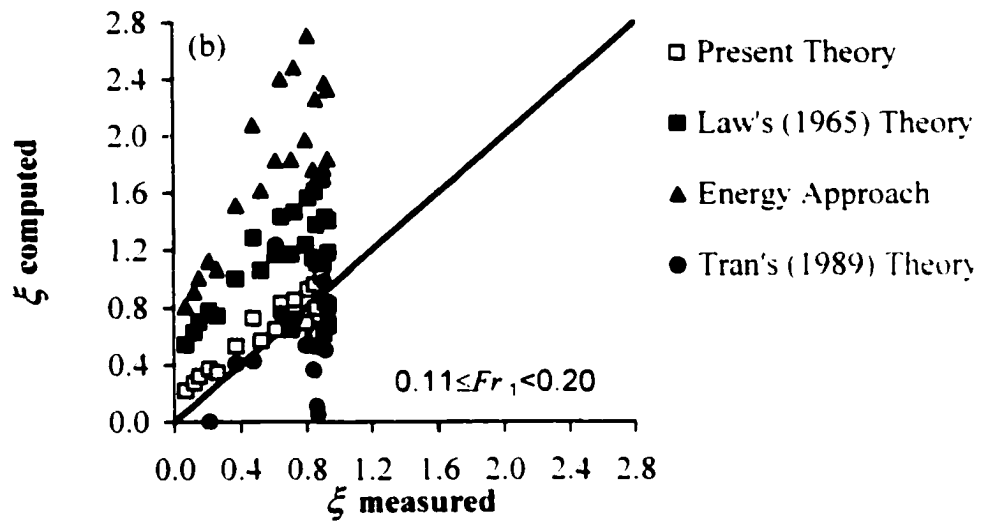
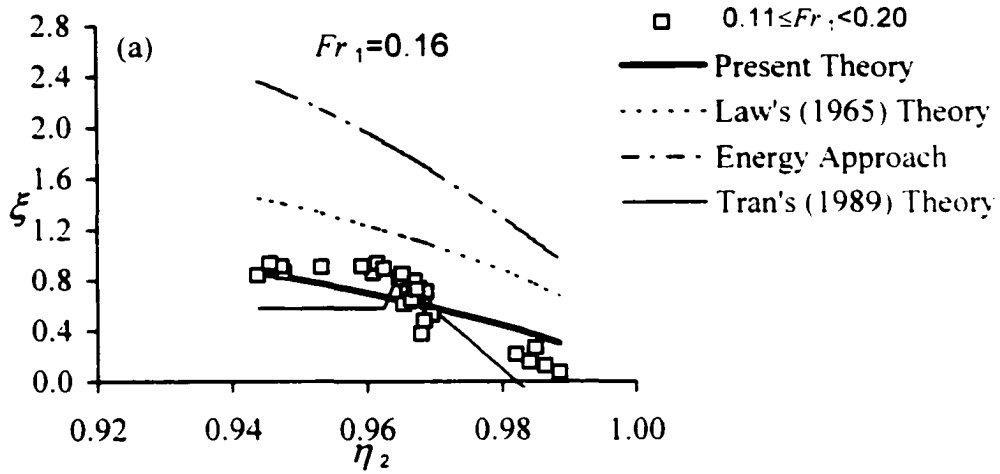


Fig. 4.31(a-c) Comparing the Proposed Theory with Law's (1965) Theory, Tran's (1989) Theory and the Energy Approach Using Grace's (1944) Data: $0.11 \leq Fr_1 < 0.20$

Chapter 5

Applications

5.1 Introduction

In this chapter two applications for the models developed in Chapters 3 and 4 are presented. The first application is based on the dividing junction model. A sample design chart for computing the discharge split for different combinations of downstream boundary conditions is presented. The chart can be developed after calibrating the coefficients, K_{d2} , K_{d1} , and C , for the range of upstream Froude numbers occurring at this junction. In the second application, the implementation of the combining and the dividing junction models into an open channel network is presented. Two simple networks analogies are considered; an irrigation system or a water treatment system, and a river cut off. The significance of the combining and the dividing flow models' coefficients on the discharge split computation is assessed. Comparisons between the results of applying the present model and the currently used energy approaches at the junctions are presented.

5.2 Design Charts*

Based on the dividing flow equations derived in chapter 4, a set of design curves is developed for a hypothetical dividing junction (Fig. 5.1). A similar chart can be developed for any junction after calibrating the dividing flow coefficients. As mentioned in the previous chapter the variations in the upstream Froude number are limited for cases such as irrigation networks. Since the dividing flow coefficients were found constant for limited ranges of upstream Froude number, they can be calibrated for the range of Froude

* The main content of this section is included in the article (under review) referred to in chapter 4.

numbers occurring at this junction. Each curve gives the variation of the discharge split with the upstream Froude number for a specific conveyance ratio for the downstream channels.

The downstream boundary conditions are usually specified as rating curves that can be put in the general forms:

$$y_2 = \frac{1}{K_{c2}} (Q_2)^{n_2} \quad (5.1)$$

for the lateral channel and for the main channel extension:

$$y_3 = \frac{1}{K_{c3}} (Q_3)^{n_3} \quad (5.2)$$

where: K_{c2} and K_{c3} represent the conveyances of sections 2 and 3, respectively, and n_2 and n_3 depend on the type of resistance equation used. For simplicity, it is assumed that $n_2=n_3=n$. Dividing Eq. (5.1) by Eq. (5.2) gives the non dimensional form for the downstream boundary condition:

$$\eta_2 = K_c \left(\frac{\xi}{(1-\xi)} \right)^n \quad (5.3)$$

where the variation in the conveyance ratio, $K_c=K_{c3}/K_{c2}$, reflects the combined effect of the various boundary conditions in the downstream channels. Employing the calibrated values of K_{d2} , K_{d1} , and C , the three equations, (4.29), (4.30) and (5.3), can then be solved for the values of ξ , η_1 and η_2 for the different values of the upstream Froude number Fr_1 and the conveyance ratio K_c .

Fig. 5.2 presents the design curves for a junction of two rectangular channels with equal widths, a Chezy coefficient of 12, an upstream aspect ratio, $a_1=8$, $n=0.6$; K_{d2} , K_{d1} , and C are chosen based on Table 4.3. The figure indicates that for the hypothetical case

where $Fr_1 \rightarrow 0$ and both downstream channels have the same conveyance, that is $K_c=1$, the inflow discharge splits equally between the two downstream channels, $\xi=0.5$. For $K_c=1$, the discharge ratio decreases as the upstream Froude number increases. This can be attributed to the effect of the asymmetrical forces at the junction where the lateral channel separation shear is considered to be more significant than that of the main and thus less flow goes to the lateral channel. The figure also shows the limiting curves for the flow in each downstream channel in this junction. For these cases, the flow in the downstream channel becomes critical and any increase in the upstream Froude number causes the discharge ratio to follow the limiting curve. It can be concluded from the trend of the curves that for low values of the upstream Froude number and as the conveyance ratios increases the discharge ratio becomes independent of Fr_1 .

Fig. 5.3 shows the discharge split for a symmetrical junction geometry (Fig. 4.10) where the two downstream channels have the same width and take off at equal angles, $\delta_1=\delta_2$. For this case the separation shear coefficients are considered to be equal, $K_{d1}=K_{d2}=0.4$, and the centrifugal forces go to zero, $C=0$. The figure shows that the discharge splits equally between the downstream channels when they have the same conveyance, $K_c=1$, for all values of the upstream Froude number. Further, the alternate conveyance ratios, $K_c=0.8$ and $K_c=1/0.8$, give symmetric discharge splits between the two downstream channels.

Fig. 5.4 shows the design chart for an asymmetrical junction geometry where the lateral channel takes off the main channel with a width ratio $\omega_2=0.5$. The figure indicates that the lateral channel reaches the critical limiting curve at lower values of Fr_1 than those causing the flow in the main channel to become critical. Fig. 5.5 shows the

complementary case to that in Fig. 5.4 where the lateral channel takes off at a width that is 1.5 times that of the main channel.

Fig. 5.6 shows a sample design chart for a large scale river junction where the aspect ratio is 100. For this case, the high aspect ratio causes an increase in the magnitude of the frictional resistance to become of the same magnitude as the pressure forces. This causes a decrease in the downstream depths in such a way that they reach their critical states at low values of Fr_1 . This is verified through the case plotted in Fig. 5.7 where the frictional resistance is highly reduced by increasing the non dimensional Chezy coefficient to be 20 (and keeping the large aspect ratio). The figure shows that the upstream Froude number required to cause the downstream channel to reach their critical state increases to values comparable to those of the original asymmetrical junction geometry (Fig. 5.2) with equal widths, $C^*=12$, $a_1=8$, and $n=0.6$.

5.3 Junction Formulation in an Open Channel Network Model

5.3.1 Setup

In this section two open channel networks are considered. The networks are hypothetical cases set up to show the implementation of the junction models into a network model. The first application is an idealization for an irrigation network or a water treatment system and is schematically shown in Fig. 5.8. The second application is a river cutoff as shown in Fig. 5.9. The two applications are set up to have different conveyance ratios: in Fig. 5.8 the main channel conveyance is larger than that of the lateral channel and in Fig. 5.9 it is the opposite case. This is achieved by the choice of the direction of the land slope at the site and the lengths of the channels downstream of the

dividing junction for each case. Therefore, two discharge splits, $\zeta < 0.5$ and $\zeta > 0.5$, are created for the irrigation system and the river cutoff, respectively.

In each of the two applications, rectangular sections of equal widths and subcritical flow are maintained throughout the network. The downstream boundary is specified for each network such that uniform flow is achieved at section 9. For the irrigation network, an average slope, S_{o2} , is determined for the lateral channel based on the bed slope chosen for the main channel, S_{o1} , where:

$$S_{o2} = \frac{L_{1(A-B)} S_{o1}}{L_{2(A-B)}} \quad (5.4)$$

where: $L_{1(A-B)}$ is the distance along the centerline of the main channel between the two cross sections at points A and B, and $L_{2(A-B)}$ is the distance along the centerline of the lateral channel from the section at A to that at B. In case of the river cutoff, the slope of the main meandering channel, S_{o1} , is determined, based on the bed slope in the lateral channel direction, in the same manner.

For subcritical flow in each network, the exterior boundary conditions are specified as the inflow discharge and the downstream depth or rating curve (depth discharge relationship). The flow computation is carried out from the downstream of the network towards the upstream to obtain the discharge and the flow area at each cross section. The equations required are divided into 3 types: channel segment equations, combining junction equations and dividing junction equations. The continuity and the one-dimensional momentum equations (Saint Venant Equations) used for the channel reaches can be written in a discrete form as follows:

$$Q_i - Q_{i+1} = 0 \quad (5.5)$$

$$\underbrace{\frac{Q_{i+1}^2}{A_{i+1}} - \frac{Q_i^2}{A_i}}_{\text{Momentum}} = \underbrace{\frac{g}{2} b_{i+1} \left[\left(\frac{A_i}{b_i} \right)^2 - \left(\frac{A_{i+1}}{b_{i+1}} \right)^2 \right]}_{\text{Pressure}} - \underbrace{\frac{Q_{i+1}^2}{A_{i+1}^2 C_*^2} \left(b_{i+1} + 2 \frac{A_{i+1}}{b_{i+1}} \right)}_{\text{Friction}} ds_i + \underbrace{\frac{g}{2} (A_i + A_{i+1}) dz_i}_{\text{Weight}} \quad (5.6)$$

where: subscript i indicates the upstream cross section of the channel control volume and subscript $i+1$ indicates the downstream section of the control volume, ds represents the curvilinear length of the control volume along its centerline and dz is the difference in bed elevation between the upstream and the downstream sections of the control volume.

At the junctions, the conservation of mass is applied together with either of: the momentum conservation equations presented in chapters 3 and 4; the conservation of energy while neglecting losses; or the common energy approach of neglecting losses and velocity heads and assuming equal water surface elevations. The continuity and momentum equations used at the combining junctions in the discrete form can be given as follows:

$$Q_1 + Q_2 - Q_3 = 0 \quad (5.7)$$

$$\underbrace{\frac{Q_1 Q_3}{A_3} - \frac{Q_1^2}{A_1}}_{\text{Momentum}} = \underbrace{\frac{g}{2} \left[\frac{A_1^2}{b_1} - \frac{A_3^2}{b_3} \left(\frac{Q_1}{Q_3} \right) \right]}_{\text{Hydrostatic Pressure}} + \underbrace{\frac{g}{8} \left[\frac{A_1}{b_1} + \frac{A_2}{b_2} \right]^2 \left[b_3 \left(\frac{Q_1}{Q_3} \right) - b_1 \right]}_{\text{Convergence Pressure}} - \underbrace{\frac{Q_3^2 L_1}{A_3^2 C_*^2} \left[b_3 \left(\frac{Q_1}{Q_3} \right) + \frac{A_3}{b_3} \right]}_{\text{Friction}} - \underbrace{K_* \left[\left(\frac{Q_1}{A_1} \right)^2 - \left(\frac{Q_2}{A_2} \right)^2 \right] \left[\frac{A_1}{b_1} + \frac{A_2}{b_2} \right] \left[\frac{2b_3 Q_1 Q_2}{Q_3^2} \right]}_{\text{Interfacial Shear}} + \underbrace{\frac{g}{2} \left[A_1 + A_3 \left(\frac{Q_1}{Q_3} \right) \right]}_{\text{Weight}} dz_1 \quad (5.8)$$

for the main channel control volume and for the lateral channel control volume:

$$\begin{aligned}
\frac{Q_2 Q_3}{A_3} - \frac{Q_2^2}{A_2} &= \underbrace{\frac{g}{2} \left[\frac{A_2^2}{b_2} - \frac{A_3^2}{b_3} \left(\frac{Q_2}{Q_3} \right) \right]}_{\text{Hydrostatic Pressure}} + \underbrace{\frac{g}{8} \left[\frac{A_1}{b_1} + \frac{A_2}{b_2} \right]^2 \left[b_3 \left(\frac{Q_2}{Q_3} \right) - b_2 \right]}_{\text{Convergence Pressure}} - \\
\frac{Q_3^2 L_2}{A_3^2 C^2} \left[b_3 \left(\frac{Q_2}{Q_3} \right) + \frac{A_3}{b_3} \right] &+ \underbrace{K \cdot \left[\left(\frac{Q_1}{A_1} \right)^2 - \left(\frac{Q_2}{A_2} \right)^2 \right] \left[\frac{A_1}{b_1} + \frac{A_2}{b_2} \right] \left[\frac{2b_3 Q_1 Q_2}{Q_3^2} \right]}_{\text{Interfacial Shear}} \\
&+ \underbrace{\frac{g}{2} \left[A_2 + A_3 \left(\frac{Q_2}{Q_3} \right) \right]}_{\text{Weight}} dz_2 - \underbrace{\frac{K \frac{Q_2^3 b_3}{b_2 Q_3 A_2}}{}}_{\text{Separation Shear}}
\end{aligned} \tag{5.9}$$

where: subscript 1 and 2 represent the main channel and the lateral channel upstream sections and subscript 3 represent the main channel downstream section. For the dividing junctions, the mass and momentum conservation formulations used can be given in the dimensional form as follows:

$$Q_1 = Q_2 + Q_3 \tag{5.10}$$

$$\begin{aligned}
\frac{Q_3^2}{A_3} - \frac{Q_3 Q_1}{A_1} &= \underbrace{\frac{g}{2} b_3 \left[\frac{A_1^2}{b_1^2} - \frac{A_3^2}{b_3^2} \right]}_{\text{Net Pressure}} + \underbrace{\frac{g}{2} \left[A_3 + A_1 \left(\frac{Q_3}{Q_1} \right) \right]}_{\text{Weight}} dz_1 - \\
\frac{Q_1^2 L_1}{A_1^2 C^2} \left[b_1 \left(\frac{Q_3}{Q_1} \right) + \frac{A_1}{b_1} \right] &+ \underbrace{C \frac{Q_2 Q_1 A_1 b_2}{(A_2 b_1)^2} \left[b_3 - b_1 \left(\frac{Q_3}{Q_1} \right) \right]}_{\text{Centrifugal Effect}} - \underbrace{\frac{K_{d1} Q_1 Q_3}{A_1}}_{\text{Separation}}
\end{aligned} \tag{5.11}$$

$$\begin{aligned}
\frac{Q_2^2}{A_2} - \frac{Q_2 Q_1}{A_1} &= \underbrace{\frac{g}{2} b_2 \left[\frac{A_1^2}{b_1^2} - \frac{A_2^2}{b_2^2} \right]}_{\text{Net Pressure}} + \underbrace{\frac{g}{2} \left[A_2 + A_1 \left(\frac{Q_2}{Q_1} \right) \right]}_{\text{Weight}} dz_2 - \\
\frac{Q_1^2 L_2}{A_1^2 C^2} \left[b_1 \left(\frac{Q_2}{Q_1} \right) + \frac{A_1}{b_1} \right] &- \underbrace{\frac{K_{d2} Q_1 Q_2}{A_1}}_{\text{Separation}}
\end{aligned} \tag{5.12}$$

Numerical models of open channel networks currently employ conservation of energy or assume equal water surface elevation at the end points of the intersecting channels for treatment of junctions. Comparisons between the momentum model and these approaches are performed. The energy conservation equations used at the combining and dividing junctions are:

$$\frac{Q_1^2}{2gA_1^2} - \frac{Q_3^2}{2gA_3^2} + dz_1 + \left[\frac{A_1}{b_1} - \frac{A_3}{b_3} \right] = 0 \quad (5.13)$$

$$\frac{Q_2^2}{2gA_2^2} - \frac{Q_3^2}{2gA_3^2} + dz_2 + \left[\frac{A_2}{b_2} - \frac{A_3}{b_3} \right] = 0 \quad (5.14)$$

with the same subscript notation as the momentum equations. The equal water surface elevation employ the same equations, (5.13) and (5.14), but without the velocity head terms.

An inflow discharge of 34 m³/s and a non-dimensional Chezy *C* of 11 are specified for the two networks considered. The cross section width throughout the irrigation network is taken to be 15m and that throughout the river cutoff is 20m. The lengths of the control volumes, *ds_i* are presented in Table 5.1 and Table 5.2 for the irrigation network and the river cutoff, respectively.

5.3.2 Results

The set of non linear equations for each network is solved, using the TK Solver that employs the Newton Raphson procedure, for the discharges and the areas of the cross sections. Tables 5.3-5.11 present the results of the implementation of the three junction models (momentum, energy conservation and equal water surface elevation) into the two

networks considered. In Tables 5.3-5.7 the results for the irrigation system are presented and those for the river cutoff are presented in Tables 5.8-5.11.

Table 5.3 shows the results of applying the momentum equations at the two junctions. The values for the combining and the dividing junction coefficients are chosen based on Figs. 3.14(a-b) and Table 4.3. A factor, x , is added to the model in order to increase or decrease the lengths of the control volumes. Table 5.3 includes 7 runs for the model through the network where the main channel slope and the lengths of the control volumes are varied to create different Froude numbers upstream of the dividing junction, Fr_2 . The variation of the computed discharge ratio with Fr_2 is compared to the design chart in Fig. 5.2. Since the design chart is developed with uniform flow depths downstream the junction, the normal depths at sections 31 and 32, y_{n31} and y_{n32} are computed for each run. This is done to check that all backwater effects propagating upstream from the combining junction are diminished as the computations reach the dividing junction and approximately uniform flow is established at these sections. If this is not satisfied the network lengths are increased using the factor x . Table 5.3 shows that the Fr_2 values range between 0.58 and 1. For this Fr_2 range, the discharge ratio decreases gradually from 0.38 to 0.33. Fig. 5.10 shows a comparison between this variation and the design chart Fig. 5.2. Fig. 5.10 shows that the results of the discharge split for this conveyance ratio, $K_c=1/0.89$, for the network junction agrees with that in the design chart. The small discrepancy can be attributed to the differences in aspect ratios, the values of C_* , and the value of n in the non-dimensional equation for the rating curves, Eq. 5.3.

Table 5.4 presents the significance of including the dividing and combining coefficients in the momentum computations. Four cases with the same main channel

slope, $S_{o1}=0.003$, and the same factor $x=2$ (that diminishes backwater effects) are presented. In the first run all the coefficients are included in the computations, in the second run the coefficients are all set to zero, in the third only the dividing flow coefficients are included, and in the last run only the combining flow coefficients are included. The resulting discharge splits for the first two runs show that not including all coefficients in the computations causes a 7% increase in the discharge ratio. The third run indicates the importance of the dividing flow coefficients. Including the dividing flow coefficients only, produces comparable results as those obtained in the first case, where all terms are considered. The fourth run verifies the importance of the dividing coefficients and the insignificance of the combining flow coefficients because the resulting discharge split is similar to that obtained when none of the terms is considered.

Table 5.5 presents the comparison between the results of the three approaches handling the junctions in the network: the momentum approach, the energy approach, and the equal water surface elevation. Four runs are presented in four sub-tables where the main channel slopes are 0.0008, 0.001, 0.0012 and 0.0015 with factors x of 1.9, 1.9, 1.6, and 1.2, respectively. For each run, six comparison cases are presented: four for the momentum approach similar to those in Table 5.4 and the last two for applying equal water surface elevation and energy conservation. All the runs presented in Table 5.5 have backwater effects propagating upstream to the dividing junction.

Table 5.5 shows that there is a discrepancy of about 8% in the discharge ratio between the two energy approaches and the momentum approach. It can be noted that even neglecting all the secondary forces in the momentum approach (i.e setting all the coefficients to zero) gives less discrepancy, in the resulting flow split, than the energy

approaches. Fig. 5.10 indicates that the discrepancy in the flow split between the energy approaches and the momentum approach will decrease as the conveyance ratio increases because the curves become more flat and insensitive to the variation in the Froude number upstream of the junction.

Tables 5.6 and 5.7 present the results of applying the equal water surface elevations and the energy conservation, respectively, at the junctions. Different main channel slopes are tested, each with different factors, x , to create a range of Froude numbers, Fr_2 . For cases in which backwater effects are propagating up to sections 31 and 32, the y_{31} and y_{32} cells are shaded in the table. The tables show that the resulting flow split values are almost constant though the Fr_2 values are increasing from 0.34 to 1. This may be due to the effect of the backwater. Further, the case in column 2 of table 5.3 when compared to that in column 16 of Table 5.6 (same slope, and factor x and with no backwater effects) indicates a discrepancy of 6% in the discharge ratio between the momentum and the equal water surface elevation approaches.

Table 5.8 presents the results of applying the momentum model at the junctions to the river cutoff network. The table gives the variation of the discharge split with the Froude number upstream of the dividing junction for a conveyance ratio, $K_c=0.65$ and no backwater effects. It should be noted that for this case, ξ decreases from 0.64 to 0.48 with the increase in Fr_2 from 0.49 to 0.96. This variation shows that the effect of the upstream Froude number, at this conveyance ratio, on the discharge split is more significant than the case of the irrigation network. The variation of ξ with Fr_2 is plotted on the design chart in Fig. 5.2 to give Fig. 5.11. Fig. 5.11 shows that for this network also the results are coinciding fairly well with the curves in the design chart.

Table 5.9 presents the effect of including the junctions' coefficients in the computations. The set up of the table is similar to Table 5.4. The table verifies the conclusion that the dividing flow coefficients are more significant than the combining flow coefficients.

Table 5.10 presents the comparison between the different approaches for handling the junctions in the river cutoff network. The table includes two sub-tables for the two flow cases ($S_{o2}=0.001$ with $x=2.5$ and $S_{o2}=0.002$ with $x=2.2$) chosen for this comparison. The table indicates that there is a discrepancy of 7%-10% between the energy approaches and the momentum approach.

Tables 5.11 and 5.12 present the resulting discharge ratio obtained from applying the equal water surface elevation and the energy conservation approaches, respectively, at the junctions of the river cutoff. For the energy conservation approach, all the cases presented have backwater effects. For the equal water surface elevation approach, few cases can be shown with no backwater effects and can be used for comparison with the momentum approach. Comparing the run ($S_{o2}=0.003$ and $x=2.9$) presented in Table 5.10 in column 12 with that in column 3 of Table 5.8, it is concluded that there is a 10% discrepancy in the computed discharge ratio between the momentum approach and the equal water surface elevation. This discrepancy is more than the 6% noted in the irrigation network. This indicates that as the conveyance ratio increases, and the discharge split becomes less dependent of the upstream Froude number, the discrepancy between the results of the different approaches handling the junction tends to diminish.

5.4 Summary and Conclusions

Two applications for the junction models were presented. The first application based on the dividing junction model was a design chart. The second application combined the dividing and the combining junctions' models and showed their implementation into a network model.

The design chart could be developed for any dividing junction after calibrating the model coefficients K_{d1} , K_{d2} and C . The chart could facilitate the computation of the discharge split for any set of upstream and downstream boundary conditions. Further, the chart gave the limiting cases for the flow in the downstream channels where the flow became critical and was not affected by the downstream boundary condition. Sample design charts were developed for different junction geometries. The charts showed that the decrease in the lateral channel width caused the flow in that channel to reach its critical state at low values of the upstream Froude numbers. The large increase in the aspect ratio had the same effect. Finally, it was concluded that the discharge split became independent of the upstream Froude number as the conveyance ratio increased.

Two examples were presented to show the implementation of the junction models into a river network. The model equations set up for the channel segments, the combining junctions and the dividing junctions were presented. The exterior boundary conditions and the fixed variables for each network were specified. Different slopes and control volume lengths were run for each network to create different Froude numbers upstream of the dividing junctions. The variation of the discharge split with the Froude number in each network was plotted and compared to one of the design charts developed in the first application. The significance of the dividing and the combining flow coefficients was

assessed. Further, comparisons between the application of the momentum model equations, the equal water surface elevations and the conservation of energy at the junctions were performed. It was found that the variation of the discharge split with the upstream Froude number for the dividing junction in the network model conforms with the design chart when there were no backwater effects. The dividing flow coefficients were found to be more significant than the combining flow coefficients. A discrepancy in the discharge split was noted between the momentum approach and the two energy approaches. This discrepancy was found to decrease as the conveyance ratio tends to the conveyance at which the discharge ratio became independent of the Froude number upstream of the dividing junction. This indicated that for most real world cases with low Froude numbers and high conveyance ratios, employing equal water surface elevation in the computation would give good results. However, as the Froude numbers increase or the conveyance ratios decrease the accuracy of the resulting discharge ratio may be questionable.

C.V.	1	21	22	31	32	41	42	51	52	61	62	72	82	92	102	71	112	8
<i>ds</i> (m)	50	60	60	75	50	75	50	75	50	75	50	56.4	55	55	55	75.5	78.8	50

Table 5.1 The Lengths of the Control volumes for the Irrigation Network ($x=1$)

C.V.	1	21	22	31	32	41	42	51	52	61	62	71	81	91	101	111	121	131
<i>ds</i> (m)	50	60	60	60	50	60	50	60	50	60	50	60	60	55	50	50	50	50

C.V.	141	151	161	171	181	191	201	211	72	8
<i>ds</i> (m)	55	60	60	60	60	60	60	60	53.2	50

Table 5.2 The Lengths of the Control volumes for the River Cutoff ($x=1$)

F_2	0.5835	0.6739	0.7195	0.7447	0.7917	0.9396	1.0051
Q_{31} (cu.m/s)	20.9026	21.2160	21.6825	21.5712	22.0159	22.5969	22.7373
y_{31} (m)	1.0782	0.9841	0.9215	0.9213	0.8735	0.8468	0.8141
y_{n31} (m)	1.1061	1.0197	0.9636	0.9605	0.9188	0.8898	0.8567
Q_{32} (cu.m/s)	13.0974	12.7840	12.3175	12.4288	11.9841	11.4031	11.2627
y_{32} (m)	0.9225	0.8046	0.7145	0.7207	0.6586	0.6519	0.5901
y_{n32} (m)	0.9294	0.8365	0.7623	0.7666	0.7081	0.6545	0.6232
Q_9 (cu.m/s)	34	34	34	34	34	34	34
A_9 (m ²)	22.6258	20.6319	19.2135	19.2135	18.1308	17.2655	16.5509
y_9 (m)	1.5084	1.3755	1.2809	1.2809	1.2087	1.1510	1.1034
V_9 (m/s)	1.5027	1.6479	1.7696	1.7696	1.8753	1.9692	2.0543
K^*	0.2	0.2	0.2	0.2	0.2	0.2	0.2
K	0.4	0.4	0.4	0.4	0.4	0.4	0.4
C	0.1	0.1	0.1	0.1	0.1	0.1	0.1
K_{01}	0.1	0.1	0.1	0.1	0.1	0.1	0.1
K_{02}	0.8	0.8	0.8	0.8	0.8	0.8	0.8
X	3	2.3	2.5	2	2	0.9	0.85
S_{01}	0.0015	0.0020	0.0025	0.0025	0.0030	0.0035	0.0040
S_{02}	0.0010	0.0014	0.0017	0.0017	0.0020	0.0024	0.0027
K_C	1.1215	1.1215	1.1215	1.1215	1.1215	1.1215	1.1215
ξ	0.3852	0.3760	0.3623	0.3656	0.3525	0.3354	0.3313

**Table 5.3 Discharge Ratios for the Irrigation System by Applying Momentum at the Junctions
(No Backwater Effects)**

F_2	0.79169	0.87714	0.79116	0.87759
Q_{31} (cu.m/s)	22.0159	19.6969	22.0026	19.7082
y_{31} (m)	0.87347	0.79895	0.87578	0.79693
y_{n31} (m)	0.91875	0.85687	0.9184	0.85718
Q_{32} (cu.m/s)	11.9841	14.3031	11.9974	14.2918
y_{32} (m)	0.65865	0.74367	0.65915	0.74327
y_{n32} (m)	0.70811	0.79056	0.7086	0.79017
Q_9 (cu.m/s)	34	34	34	34
A_9 (m ²)	18.1308	18.1308	18.1308	18.1308
y_9 (m)	1.20872	1.20872	1.20872	1.20872
V_9 (m/s)	1.87526	1.87526	1.87526	1.87526
K^*	0.2	0	0	0.2
K	0.4	0	0	0.4
C	0.1	0	0.1	0
K_{d1}	0.1	0	0.1	0
K_{d2}	0.8	0	0.8	0
X	2	2	2	2
S_{o1}	0.003	0.003	0.003	0.003
S_{o2}	0.00205	0.00205	0.00205	0.00205
K_c	1.12146	1.12146	1.12146	1.12146
ξ	0.35247	0.42068	0.35286	0.42035

Table 5.4 The Effect of Including the Combining and Dividing Coefficients for the Momentum Approach on the Discharge Ratio (No Backwater Effects)

Approach	Momentum				WSE	Energy
Fr_2	0.3476	0.3584	0.3482	0.3577	0.3831	0.4040
Q_{31} (cu.m/s)	22.122	21.114	22.342	20.939	19.3178	19.1193
y_{31} (m)						
y_{n31} (m)	1.4007	1.3595	1.4095	1.3523	1.2845	1.2761
Q_{32} (cu.m/s)	11.878	12.886	11.658	13.061	14.6822	14.8807
y_{32} (m)						
y_{n32} (m)	1.0651	1.1214	1.0526	1.131	1.2181	1.2286
Q_9 (cu.m/s)	34	34	34	34	34	34
A_9 (m ²)	27.73	27.73	27.73	27.73	27.7297	27.7297
y_9 (m)	1.8486	1.8486	1.8486	1.8486	1.8486	1.8486
V_9 (m/s)	1.2261	1.2261	1.2261	1.2261	1.2261	1.2261
K^*	0.2	0	0	0.2		
K	0.4	0	0	0.4		
C	0.1	0	0.1	0		
K_{d1}	0.1	0	0.1	0		
K_{d2}	0.8	0	0.8	0		
x	1.9	1.9	1.9	1.9	1.9	1.9
S_{o1}	0.0008	0.0008	0.0008	0.0008	0.0008	0.0008
S_{o2}	0.0005	0.0005	0.0005	0.0005	0.0005	0.0005
Kc	1.1215	1.1215	1.1215	1.1215	1.1215	1.1215
ξ	0.3493	0.379	0.3429	0.3842	0.4318	0.4377

Momentum				WSE	Energy
0.4136	0.4314	0.4142	0.4304	0.4700	0.5263
21.968	20.855	22.132	20.731	19.2982	19.0742
1.2985	1.2561	1.3046	1.2514	1.1957	1.1869
12.032	13.145	11.868	13.269	14.7018	14.9258
1.0008	1.0583	0.9922	1.0645	1.1359	1.1468
34	34	34	34	34	34
25.79	25.79	25.79	25.79	25.7900	25.7900
1.7193	1.7193	1.7193	1.7193	1.7193	1.7193
1.3183	1.3183	1.3183	1.3183	1.3183	1.3183
0.2	0	0	0.2		
0.4	0	0	0.4		
0.1	0	0.1	0		
0.1	0	0.1	0		
0.8	0	0.8	0		
1.9	1.9	1.9	1.9	1.9	1.9
0.001	0.001	0.001	0.001	0.001	0.001
0.0007	0.0007	0.0007	0.0007	0.0007	0.0007
1.1215	1.1215	1.1215	1.1215	1.1215	1.1215
0.3539	0.3866	0.3491	0.3903	0.4324	0.4390

Table 5.5 Comparing the Momentum Approach Results with the Conservation of Energy and the Equal Water Surface Elevation Approaches at the Junctions (with Backwater Effects)

Approach	Momentum			WSE	Energy	
Fr_2	0.4602	0.485	0.461	0.4837	0.5317	0.6349
Q_{31} (cu.m/s)	22.152	20.877	22.332	20.744	19.3713	19.1069
y_{31} (m)						
y_{n31} (m)	1.2318	1.1863	1.2381	1.1814	1.1313	1.1215
Q_{32} (cu.m/s)	11.848	13.123	11.668	13.256	14.6287	14.8931
y_{32} (m)						
y_{n32} (m)	0.936	0.9981	0.927	1.0045	1.0688	1.0810
Q_9 (cu.m/s)	34	34	34	34	34	34
A_9 (m ²)	24.313	24.313	24.313	24.313	24.3126	24.3126
y_9 (m)	1.6208	1.6208	1.6208	1.6208	1.6208	1.6208
V_9 (m/s)	1.3985	1.3985	1.3985	1.3985	1.3985	1.3985
K^*	0.2	0	0	0.2		
K	0.4	0	0	0.4		
C	0.1	0	0.1	0		
K_{d1}	0.1	0	0.1	0		
K_{d2}	0.8	0	0.8	0		
x	1.6	1.6	1.6	1.6	1.6	1.6
S_{o1}	0.0012	0.0012	0.0012	0.0012	0.0012	0.0012
S_{o2}	0.0008	0.0008	0.0008	0.0008	0.0008	0.0008
Kc	1.1215	1.1215	1.1215	1.1215	1.1215	1.1215
ξ	0.3485	0.386	0.3432	0.3899	0.4303	0.4380

	Momentum			WSE	Energy	
	0.5148	0.55	0.5156	0.5483	0.6050	1.1718
	22.592	21.083	22.834	20.899	19.5387	19.2071
	1.1619	1.1122	1.1698	1.106	1.0600	1.0486
	11.408	12.917	11.166	13.101	14.4613	14.7929
	0.8523	0.9213	0.841	0.9295	0.9891	1.0033
	34	34	34	34	34	34
	22.626	22.626	22.626	22.626	22.6258	22.6258
	1.5084	1.5084	1.5084	1.5084	1.5084	1.5084
	1.5027	1.5027	1.5027	1.5027	1.5027	1.5027
	0.2	0	0	0.2		
	0.4	0	0	0.4		
	0.1	0	0.1	0		
	0.1	0	0.1	0		
	0.8	0	0.8	0		
	1.2	1.2	1.2	1.2	1.2	1.2
	0.0015	0.0015	0.0015	0.0015	0.0015	0.0015
	0.001	0.001	0.001	0.001	0.0010	0.0010
	1.1215	1.1215	1.1215	1.1215	1.1215	1.1215
	0.3355	0.3799	0.3284	0.3853	0.4253	0.4351

Table 5.5 Comparing the Momentum Approach Results with the Conservation of Energy and the Equal Water Surface Elevation Approaches at the Junctions (with Backwater Effects) (Cont.)

Fr_2	0.338	0.383	0.529	0.399	0.439	0.47	0.599	0.487	0.532	0.662	0.57	0.605	0.746	0.749	0.826	0.877	1.082
Q_{31} (cu.m/s)	19.79	19.32	18.79	19.77	19.44	19.3	18.75	19.58	19.37	18.76	19.71	19.54	18.87	18.81	18.92	18.95	19.5
y_{31} (m)													1.002	1.00	0.943	0.91	0.81
y_{n31} (m)	1.304	1.284	1.262	1.214	1.201	1.196	1.174	1.139	1.131	1.109	1.066	1.06	1.037	1.035	0.981	0.95	0.852
Q_{32} (cu.m/s)	14.21	14.68	15.21	14.23	14.56	14.7	15.25	14.42	14.63	15.24	14.29	14.46	15.13	15.19	15.08	15.05	14.5
y_{32} (m)													0.987	0.985	0.925	0.89	0.78
y_{n32} (m)	1.193	1.218	1.246	1.112	1.129	1.136	1.163	1.059	1.069	1.097	0.982	0.989	1.017	1.02	0.959	0.927	0.797
Q_9 (cu.m/s)	34	34	34	34	34	34	34	34	34	34	34	34	34	34	34	34	34
A_9 (m ²)	27.73	27.73	27.73	25.79	25.79	25.79	25.79	24.31	24.31	24.31	22.63	22.63	22.63	22.63	21.34	20.63	18.13
y_9 (m)	1.849	1.849	1.849	1.719	1.719	1.719	1.719	1.621	1.621	1.621	1.508	1.508	1.508	1.508	1.423	1.375	1.209
V_9 (m/s)	1.226	1.226	1.226	1.318	1.318	1.318	1.318	1.398	1.398	1.398	1.503	1.503	1.503	1.503	1.593	1.648	1.875
x	1	1.9	7	1	1.5	1.9	6	1.2	1.6	5	1	1.2	3	4	2.3	2	0.8
S_{o1}	8E-04	8E-04	8E-04	0.001	0.001	0.001	0.001	0.001	0.001	0.001	0.002	0.002	0.002	0.002	0.002	0.002	0.003
S_{o2}	5E-04	5E-04	5E-04	7E-04	7E-04	7E-04	7E-04	8E-04	8E-04	8E-04	0.001	0.001	0.001	0.001	0.001	0.001	0.002
Kc	1.121	1.121	1.121	1.121	1.121	1.121	1.121	1.121	1.121	1.121	1.121	1.121	1.121	1.121	1.121	1.121	1.121
ξ	0.418	0.432	0.447	0.418	0.428	0.432	0.449	0.424	0.43	0.448	0.42	0.425	0.445	0.447	0.443	0.443	0.426

Table 5.6 Discharge Ratios for the Irrigation Network by Applying Equal Water Surface Elevation at the Junctions

Fr_2	0.3462	0.3773	0.4040	0.4182	0.4749	0.5263	0.5432	0.6349	0.7023	1.1718
Q_{31} (cu.m/s)	19.5048	19.2321	19.1193	19.4685	19.1901	19.0742	19.2845	19.1069	19.3550	19.2071
y_{31} (m)										
y_{n31} (m)	1.2924	1.2808	1.2761	1.2024	1.1915	1.1869	1.1281	1.1215	1.0537	1.0486
Q_{32} (cu.m/s)	14.4952	14.7679	14.8807	14.5315	14.8099	14.9258	14.7155	14.8931	14.6450	14.7929
y_{32} (m)										
y_{n32} (m)	1.2083	1.2226	1.2286	1.1275	1.1411	1.1468	1.0729	1.0810	0.9969	1.0033
Q_9 (cu.m/s)	34	34	34	34	34	34	34	34	34	34
A_9 (m ²)	27.7297	27.7297	27.7297	25.7900	25.7900	25.7900	24.3126	24.3126	22.6258	22.6258
y_9 (m)	1.8486	1.8486	1.8486	1.7193	1.7193	1.7193	1.6208	1.6208	1.5084	1.5084
V_9 (m/s)	1.2261	1.2261	1.2261	1.3183	1.3183	1.3183	1.3985	1.3985	1.5027	1.5027
x	1	1.5	1.9	1	1.5	1.9	1.2	1.6	1	1.2
S_{o1}	0.0008	0.0008	0.0008	0.0010	0.0010	0.0010	0.0012	0.0012	0.0015	0.0015
S_{o2}	0.0005	0.0005	0.0005	0.0007	0.0007	0.0007	0.0008	0.0008	0.0010	0.0010
Kc	1.1215	1.1215	1.1215	1.1215	1.1215	1.1215	1.1215	1.1215	1.1215	1.1215
ξ	0.4263	0.4343	0.4377	0.4274	0.4356	0.4390	0.4328	0.4380	0.4307	0.4351

Table 5.7 Discharge Ratios for the Irrigation Network by Applying Equal Energy at the Junctions

Fr_2	0.4887	0.5247	0.5716	0.6543	0.7971	0.8105	0.8309	0.8612	0.8908	0.9223	0.9583
Q_{31} (cu.m/s)	12.3077	12.7141	13.1390	13.9381	15.5111	15.6788	16.0789	16.3152	16.6840	17.1032	17.8038
y_{31} (m)	0.9409	0.8648	0.8306	0.7812	0.7947	0.7912	0.7910	0.7787	0.7716	0.7670	0.7708
$y_{n,31}$ (m)	0.9421	0.8969	0.8651	0.8208	0.9797	0.9939	1.0236	1.0525	1.0886	1.1294	1.1826
Q_{32} (cu.m/s)	21.6923	21.2859	20.8610	20.0619	18.4889	18.3212	17.9211	17.6848	17.3160	16.8968	16.1962
y_{32} (m)	0.8078	0.7479	0.6908	0.5131	0.4626	0.4584	0.4225	0.4539	0.4612	0.4509	0.3797
$y_{n,32}$ (m)	0.8538	0.7876	0.7353	0.6569	0.5666	0.5573	0.5412	0.5239	0.5055	0.4876	0.4659
Q_9 (cu.m/s)	34	34	34	34	34	34	34	34	34	34	34
A_9 (m ²)	35.7099	33.2583	31.3867	28.6550	25.9191	25.6297	25.2199	24.5942	24.0292	23.5153	23.0450
y_9 (m)	1.7855	1.6629	1.5693	1.4328	1.2960	1.2815	1.2610	1.2297	1.2015	1.1758	1.1523
V_9 (m/s)	0.9521	1.0223	1.0833	1.1865	1.3118	1.3266	1.3481	1.3824	1.4149	1.4459	1.4754
K^*	0.2	0.2	0.2	0.2	0.2	0.2	0.2	0.2	0.2	0.2	0.2
K	0.4	0.4	0.4	0.4	0.4	0.4	0.4	0.4	0.4	0.4	0.4
C	0.1	0.1	0.1	0.1	0.1	0.1	0.1	0.1	0.1	0.1	0.1
K_{d1}	0.1	0.1	0.1	0.1	0.1	0.1	0.1	0.1	0.1	0.1	0.1
K_{d2}	0.8	0.8	0.8	0.8	0.8	0.8	0.8	0.8	0.8	0.8	0.8
x	3.8	3.7	2.9	2.1	0.8	0.75	0.7	0.6	0.53	0.48	0.45
S_{o1}	0.0005	0.0006	0.0007	0.0009	0.0013	0.0013	0.0014	0.0015	0.0016	0.0018	0.0019
S_{o2}	0.0020	0.0025	0.0030	0.0040	0.0055	0.0057	0.0060	0.0065	0.0070	0.0075	0.0080
Kc	0.6472	0.6472	0.6472	0.6472	0.6472	0.6472	0.6472	0.6472	0.6472	0.6472	0.6472
ξ	0.6380	0.6261	0.6136	0.5901	0.5438	0.5389	0.5271	0.5201	0.5093	0.4970	0.4764

Table 5.8 Discharge Ratios for the River Cutoff by Applying Momentum at the Junctions (No Backwater Effects)

Fr_2	0.4887	0.5321	0.4885	0.5323
Q_{31} (cu.m/s)	12.3077	10.8467	12.3152	10.8373
y_{31} (m)	0.9409	0.8621	0.9412	0.8617
y_{n31} (m)	0.9421	0.8710	0.9424	0.8705
Q_{32} (cu.m/s)	21.6923	23.1533	21.6848	23.1627
y_{32} (m)	0.8078	0.8477	0.8093	0.8464
y_{n32} (m)	0.8538	0.8890	0.8536	0.8892
Q_9 (cu.m/s)	34	34	34	34
A_9 (m ²)	35.7099	35.7099	35.7099	35.7099
y_9 (m)	1.7855	1.7855	1.7855	1.7855
V_9 (m/s)	0.9521	0.9521	0.9521	0.9521
K'	0.2	0	0	0.2
K	0.4	0	0	0.4
C	0.1	0	0.1	0
K_{d1}	0.1	0	0.1	0
K_{d2}	0.8	0	0.8	0
X	3.8	3.8	3.8	3.8
S_{o1}	0.0005	0.0005	0.0005	0.0005
S_{o2}	0.0020	0.0020	0.0020	0.0020
Kc	0.6472	0.6472	0.6472	0.6472
ξ	0.6380	0.6810	0.6378	0.6813

Table 5.9 The Effect of Including the Combining and Dividing Coefficients for the Momentum Approach on the Discharge Ratio (No Backwater Effects)

Approach	Momentum				WSE	Energy
Fr_2	0.2263	0.235	0.2279	0.2329	0.2415	0.2446
Q_{31} (cu.m/s)	10.604	8.1847	10.246	8.6379	7.9994	8.5718
y_{31} (m)						
y_{n31} (m)	1.0654	0.9068	1.0428	0.9377	0.8940	0.9332
Q_{32} (cu.m/s)	23.396	25.815	23.754	25.362	26.0006	25.4282
y_{32} (m)						
y_{n32} (m)	1.1103	1.1808	1.1208	1.1678	1.1861	1.1697
Q_9 (cu.m/s)	34	34	34	34	34	34
A_9 (m ²)	44.622	44.622	44.622	44.622	44.6216	44.6216
y_9 (m)	2.2311	2.2311	2.2311	2.2311	2.2311	2.2311
V_9 (m/s)	0.762	0.762	0.762	0.762	0.7620	0.7620
K^*	0.2	0	0	0.2		
K	0.4	0	0	0.4		
C	0.1	0	0.1	0		
K_{d1}	0.1	0	0.1	0		
K_{d2}	0.8	0	0.8	0		
x	2.5	2.5	2.5	2.5	2.5	2.5
S_{o1}	0.0002	0.0002	0.0002	0.0002	0.0002	0.0002
S_{o2}	0.001	0.001	0.001	0.001	0.0010	0.0010
Kc	0.6472	0.6472	0.6472	0.6472	0.6472	0.6472
ξ	0.6881	0.7593	0.6986	0.7459	0.7647	0.7479

	Momentum				WSE	Energy
	0.4457	0.4953	0.4489	0.4904	0.5801	0.7582
	11.792	9.6388	11.676	9.7845	8.5711	9.6063
	0.9174	0.8096	0.9118	0.8171	0.7529	0.8079
	22.208	24.361	22.324	24.216	25.4289	24.3937
	0.8663	0.9175	0.8691	0.9141	0.9423	0.9183
	34	34	34	34	34	34
	35.71	35.71	35.71	35.71	35.7099	35.7099
	1.7855	1.7855	1.7855	1.7855	1.7855	1.7855
	0.9521	0.9521	0.9521	0.9521	0.9521	0.9521
	0.2	0	0	0.2		
	0.4	0	0	0.4		
	0.1	0	0.1	0		
	0.1	0	0.1	0		
	0.8	0	0.8	0		
	2.2	2.2	2.2	2.2	2.2	2.2
	0.0005	0.0005	0.0005	0.0005	0.0005	0.0005
	0.002	0.002	0.002	0.002	0.0020	0.0020
	0.6472	0.6472	0.6472	0.6472	0.6472	0.6472
	0.6532	0.7165	0.6566	0.7122	0.7479	0.7175

Table 5.10 Comparing the Momentum Approach Results with the Conservation of Energy and the Equal Water Surface Elevation Approaches at the Junctions (with Backwater Effects)

Fr_2	0.1641	0.1835	0.1922	0.2229	0.2415	0.3493	0.3921	0.5375	0.5801	0.7046	0.6122	0.9724	1.0228	1.0934
Q_{31} (cu.m/s)	7.1905	7.7237	7.8699	7.7721	7.9994	8.007	8.2901	8.3598	8.5711	9.4856	7.3427	9.8358	8.1165	10.064
y_{31} (m)												0.6779		0.6269
y_{n31} (m)	0.8968	0.9375	0.9485	0.8782	0.894	0.789	0.8062	0.7414	0.7529	0.8016	0.6042	0.7233	0.5883	0.6714
Q_{32} (cu.m/s)	26.809	26.276	26.13	26.228	26.001	25.993	25.71	25.64	25.429	24.514	26.657	24.164	25.883	23.936
y_{32} (m)												0.7079	0.6955	0.6669
y_{n32} (m)	1.2968	1.2806	1.2761	1.1926	1.1861	1.0447	1.0376	0.9472	0.9423	0.9211	0.8556	0.8051	0.7686	0.7324
Q_9 (cu.m/s)	34	34	34	34	34	34	34	34	34	34	34	34	34	34
A_9 (m ²)	47.971	47.971	47.971	44.622	44.622	39.155	39.155	35.71	35.71	35.71	31.387	31.387	28.655	28.655
y_9 (m)	2.3986	2.3986	2.3986	2.2311	2.2311	1.9578	1.9578	1.7855	1.7855	1.7855	1.5693	1.5693	1.4328	1.4328
V_9 (m/s)	0.7088	0.7088	0.7088	0.762	0.762	0.8683	0.8683	0.9521	0.9521	0.9521	1.0833	1.0833	1.1865	1.1865
x	1	2	2.4	2	2.5	2	2.4	2	2.2	3	1	2.9	1	1.7
S_{o1}	0.0002	0.0002	0.0002	0.0002	0.0002	0.0004	0.0004	0.0005	0.0005	0.0005	0.0007	0.0007	0.0009	0.0009
S_{o2}	0.0008	0.0008	0.0008	0.001	0.001	0.0015	0.0015	0.002	0.002	0.002	0.003	0.003	0.004	0.004
Kc	0.6472	0.6472	0.6472	0.6472	0.6472	0.6472	0.6472	0.6472	0.6472	0.6472	0.6472	0.6472	0.6472	0.6472
ξ	0.7885	0.7728	0.7685	0.7714	0.7647	0.7645	0.7562	0.7541	0.7479	0.721	0.784	0.7107	0.7613	0.704

Table 5.11 Discharge Ratios for the River Cutoff by Applying Equal Water Surface Elevation at the Junctions

Fr_2	0.1643	0.1843	0.1932	0.2248	0.2446	0.3635	0.4168	0.6431	0.7582	1.1999
Q_{31} (cu.m/s)	7.9941	8.2650	8.3678	8.3982	8.5718	8.8470	9.0849	9.4217	9.6063	9.1995
y_{31} (m)										
y_{n31} (m)	0.9578	0.9778	0.9854	0.9214	0.9332	0.8393	0.8532	0.7983	0.8079	0.6941
Q_{32} (cu.m/s)	26.0059	25.7350	25.6322	25.6018	25.4282	25.1530	24.9151	24.5783	24.3937	24.8005
y_{32} (m)										
y_{n32} (m)	1.2723	1.2639	1.2607	1.1747	1.1697	1.0236	1.0175	0.9226	0.9183	0.8182
Q_9 (cu.m/s)	34	34	34	34	34	34	34	34	34	34
A_9 (m ²)	47.9712	47.9712	47.9712	44.6216	44.6216	39.1554	39.1554	35.7099	35.7099	31.3867
y_9 (m)	2.3986	2.3986	2.3986	2.2311	2.2311	1.9578	1.9578	1.7855	1.7855	1.5693
V_9 (m/s)	0.7088	0.7088	0.7088	0.7620	0.7620	0.8683	0.8683	0.9521	0.9521	1.0833
x	1	2	2.4	2	2.5	2	2.4	2	2.2	1
S_{o1}	0.0002	0.0002	0.0002	0.0002	0.0002	0.0004	0.0004	0.0005	0.0005	0.0007
S_{o2}	0.0008	0.0008	0.0008	0.0010	0.0010	0.0015	0.0015	0.0020	0.0020	0.0030
Kc	0.6472	0.6472	0.6472	0.6472	0.6472	0.6472	0.6472	0.6472	0.6472	0.6472
ξ	0.7649	0.7569	0.7539	0.7530	0.7479	0.7398	0.7328	0.7229	0.7175	0.7294

Table 5.12 Discharge Ratios for the River Cutoff by Applying Equal Energy at the Junctions

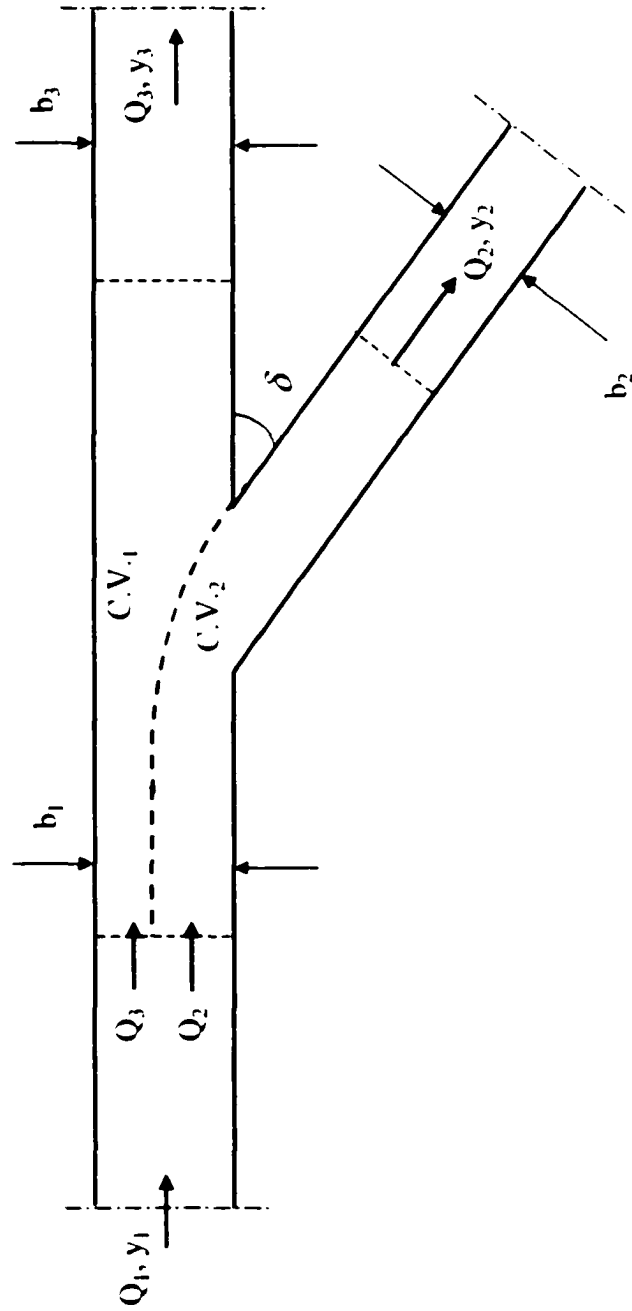


Fig. 5.1 Junction Geometry and Notation

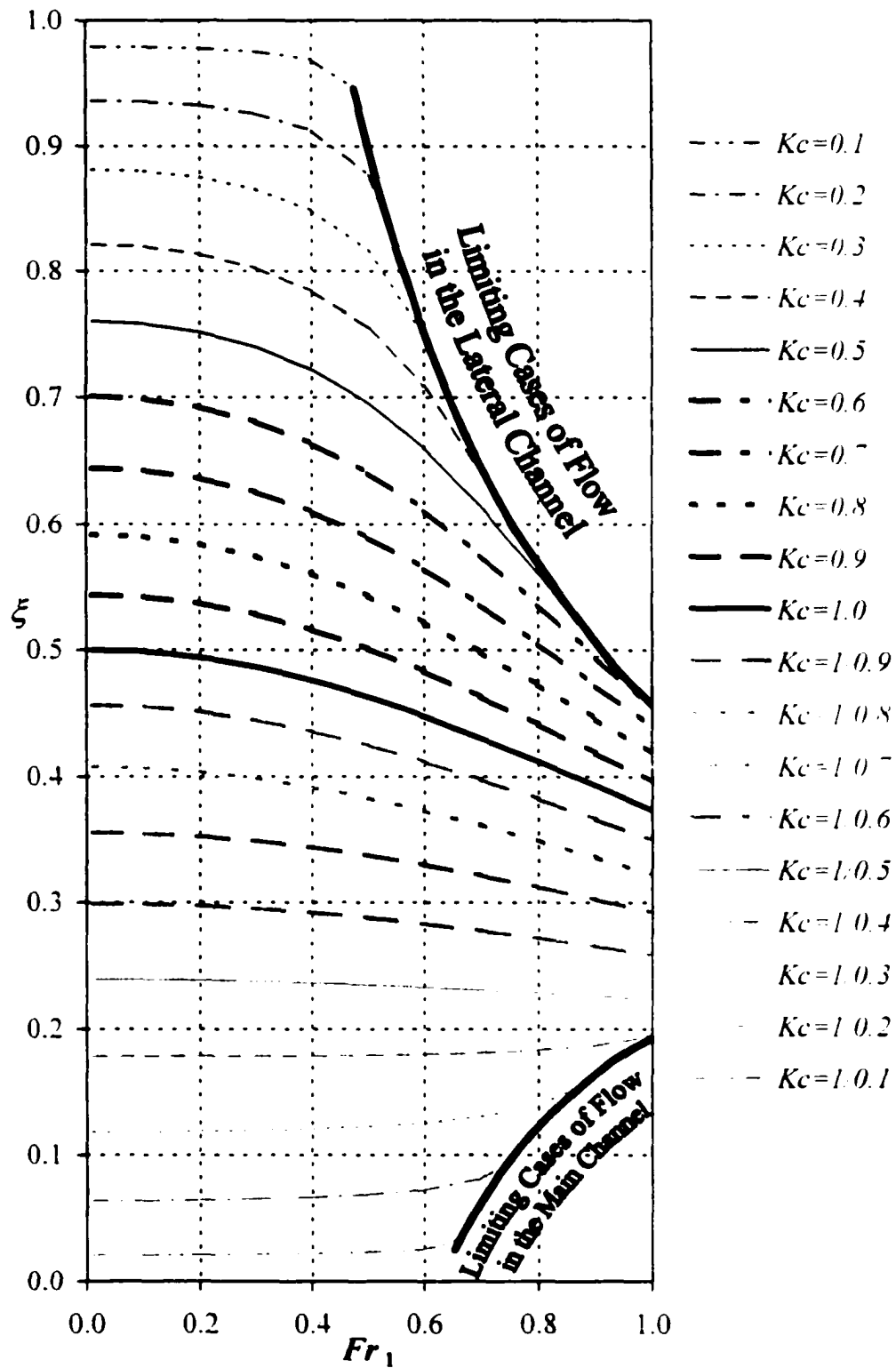


Fig. 5.2 Design Chart for an Asymmetrical Junction Geometry
 $\omega_1=1, \omega_2=1, C_1=12, K_{d2}=0.8, K_{d1}=0.1, C=0.1, a_1=8, n=0.6$

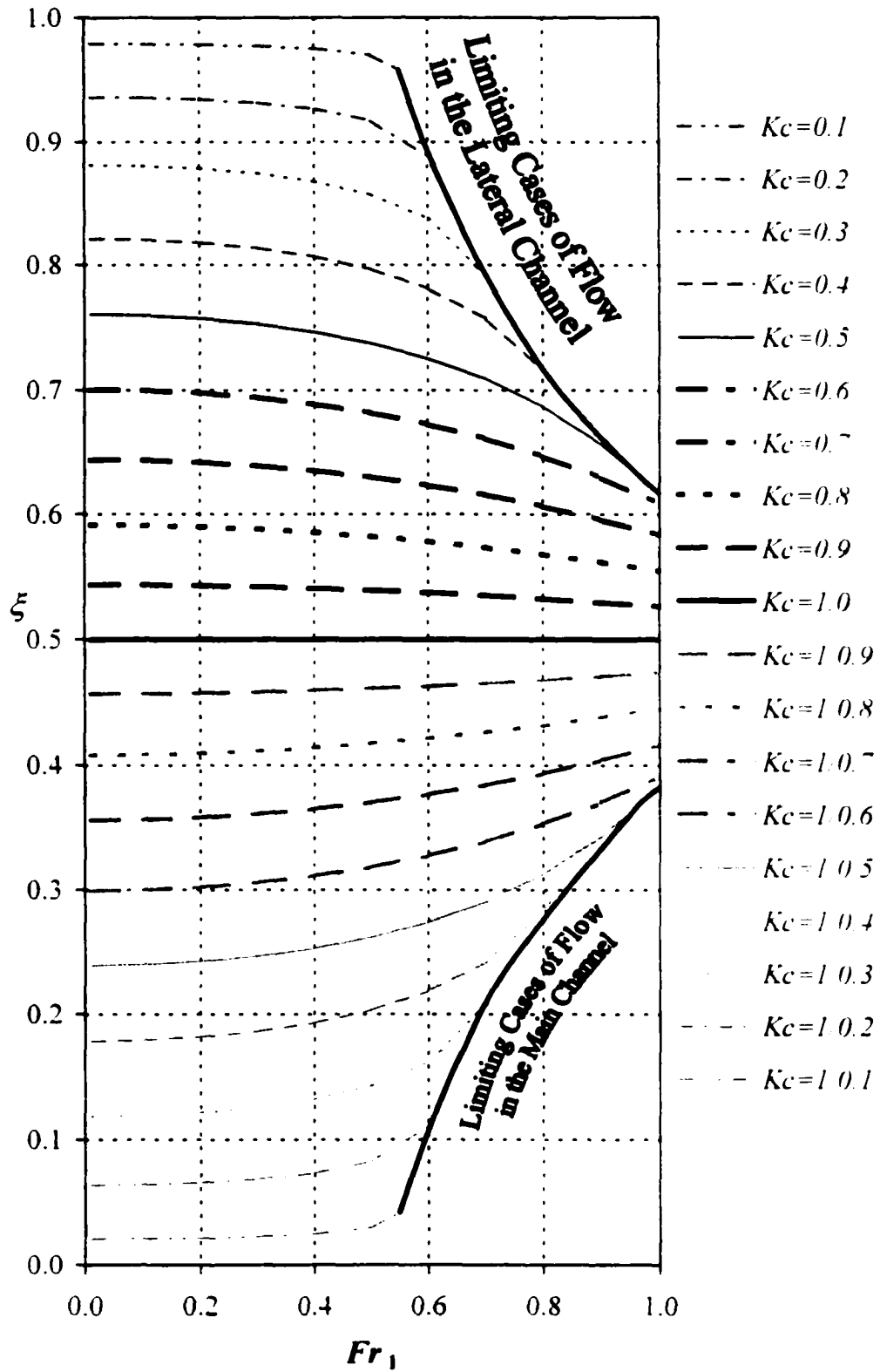


Fig. 5.3 Design Chart for a Symmetrical Junction Geometry
 $\omega_1=1, \omega_2=1, C=12, K_{d2}=0.4, K_{d1}=0.4, C=0, a_1=8, n=0.6$

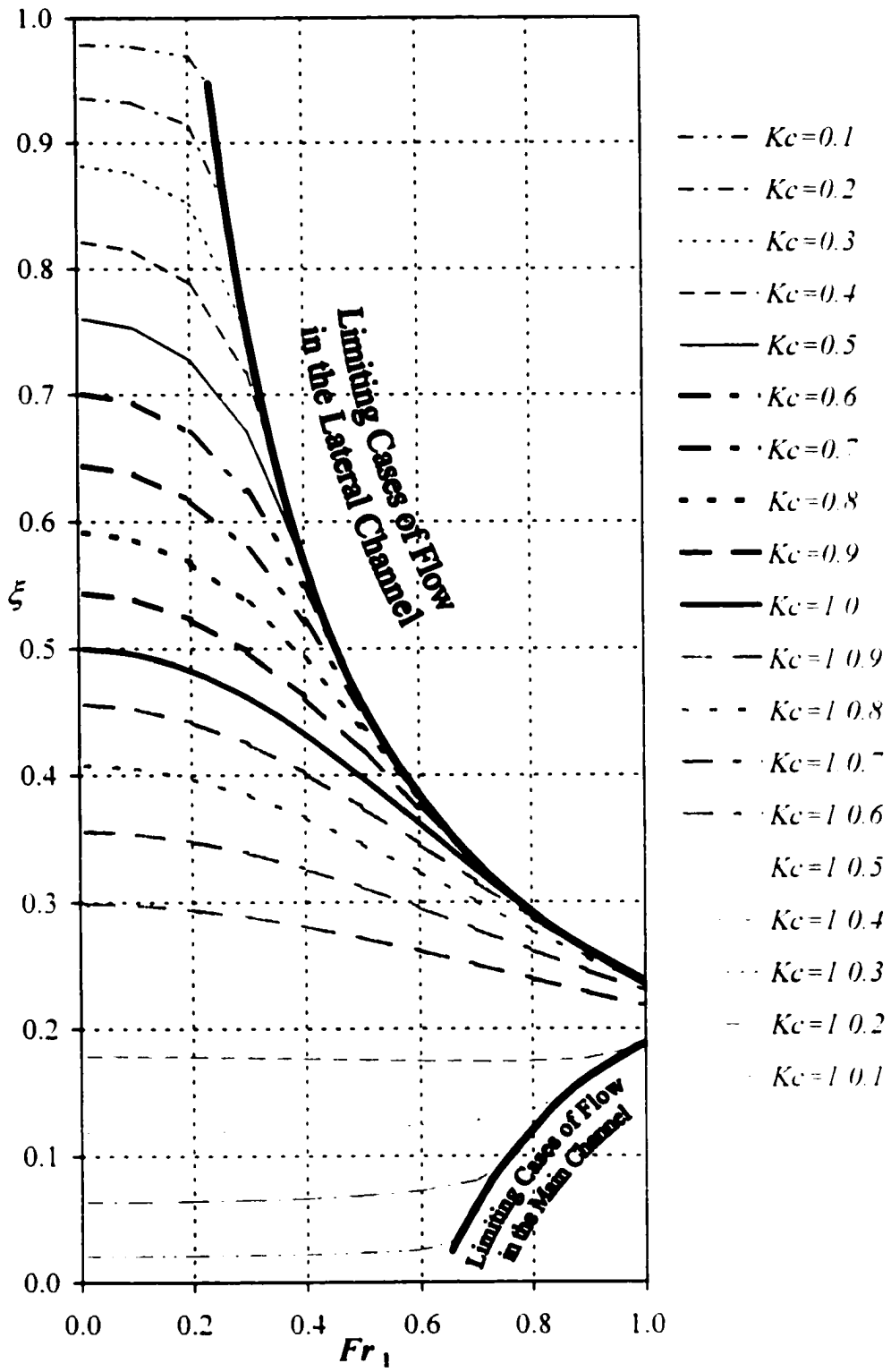


Fig. 5.4 Design Chart for an Asymmetrical Junction Geometry
 $\omega_1=1, \omega_2=0.5, C_s=12, K_{d2}=0.8, K_{d1}=0.1, C=0.1, a_1=8, n=0.6$

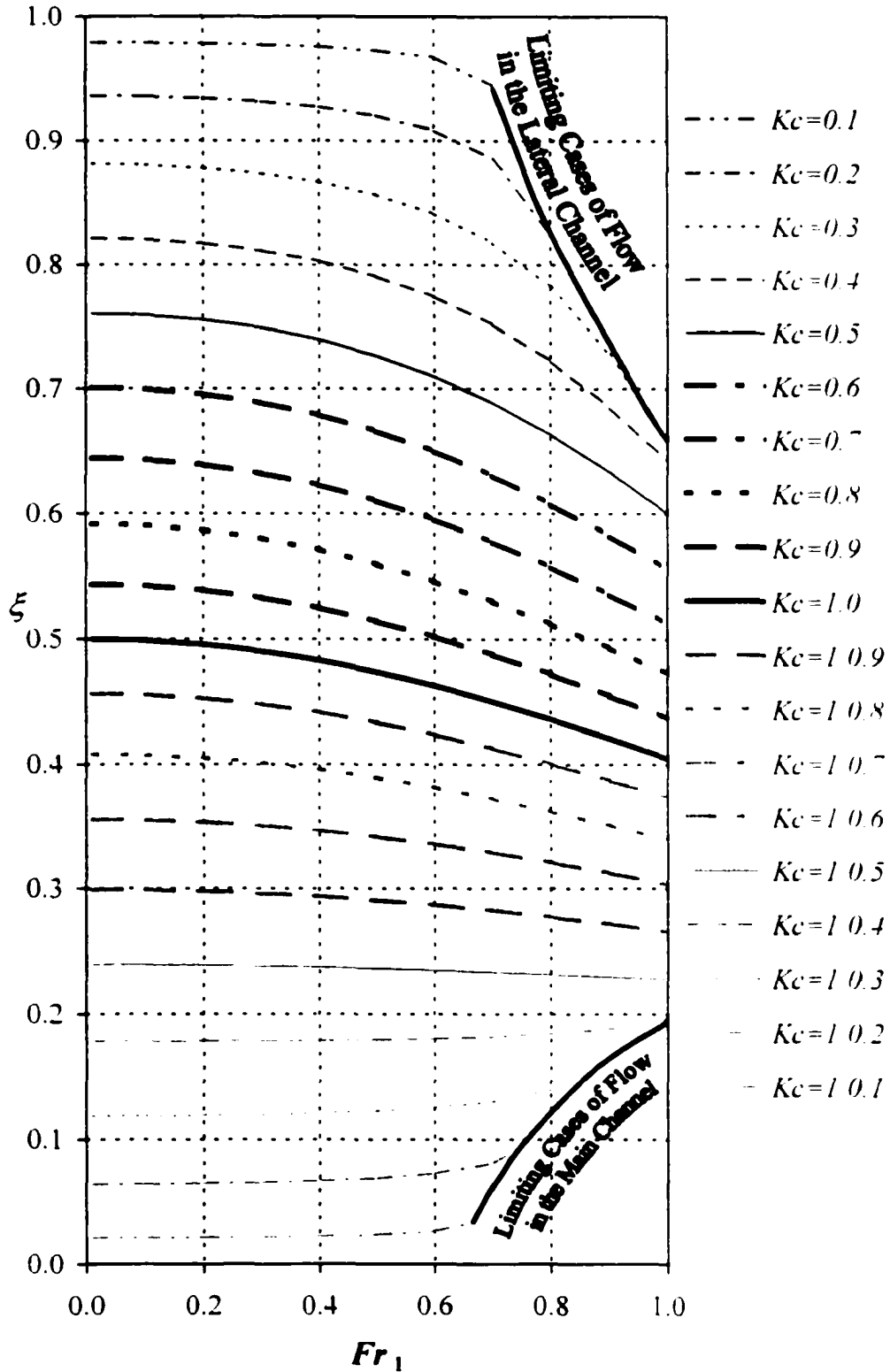


Fig. 5.5 Design Chart for an Asymmetrical Junction Geometry
 $\omega_1=1, \omega_2=1.5, C_s=12, K_{d2}=0.8, K_{d1}=0.1, C=0.1, a_1=8, n=0.6$

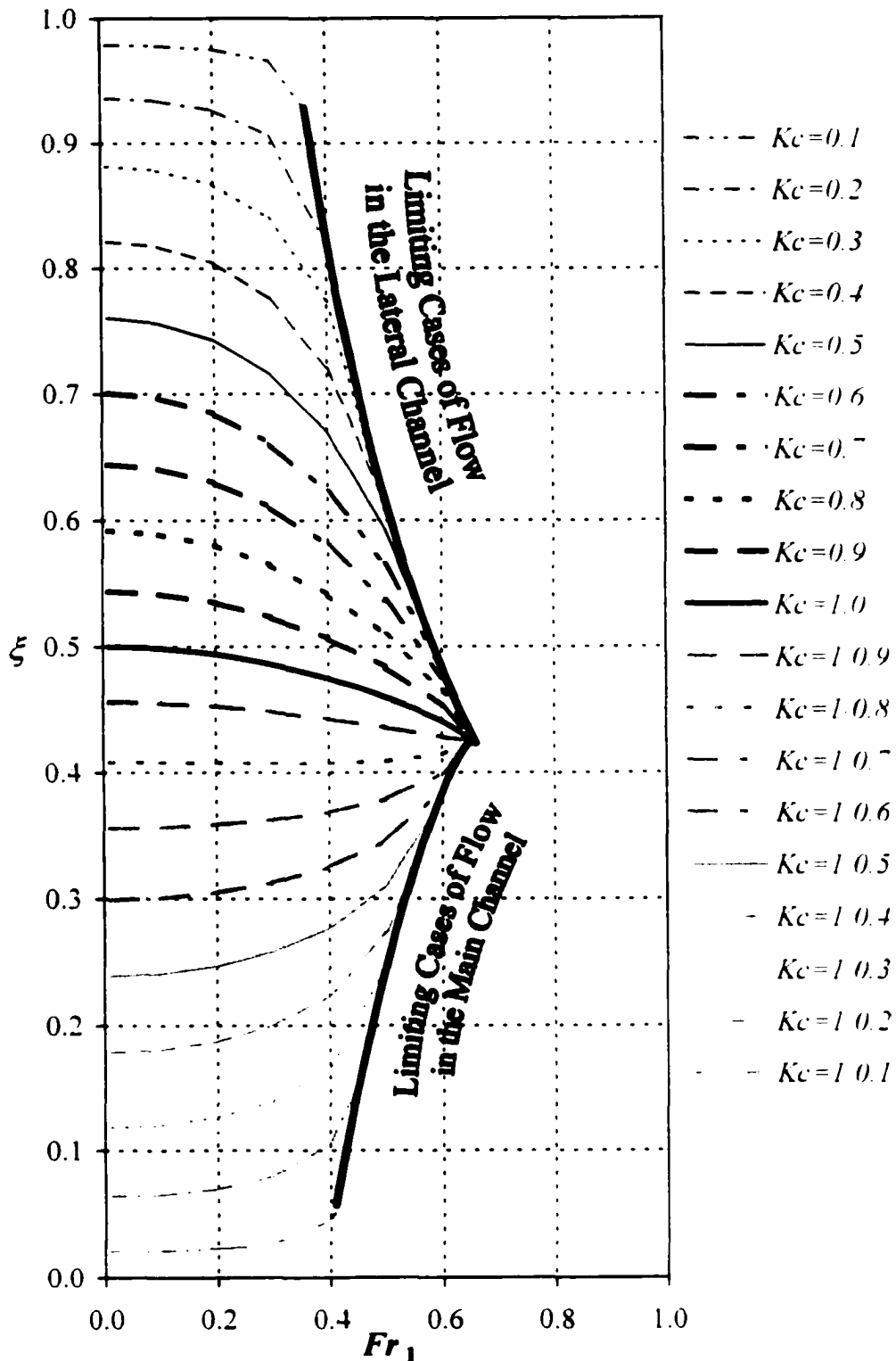


Fig. 5.6 Design Chart for a Large Scale River Junction
 $\omega_1=1, \omega_2=1, C_s=12, K_{d2}=0.8, K_{d1}=0.1, C=0.1, a_1=100, n=0.6$

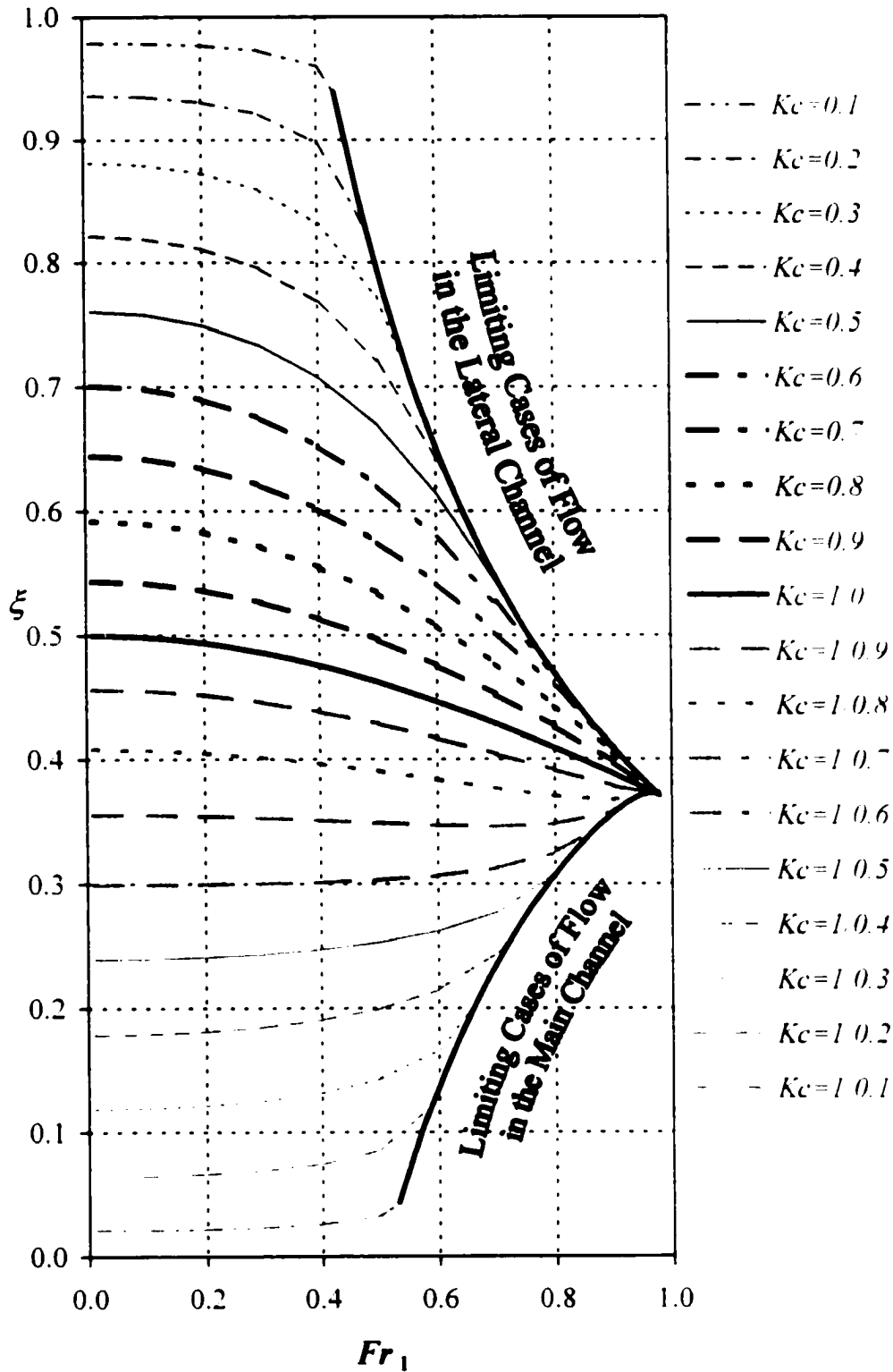


Fig. 5.7 Design Chart for a Large Scale River Junction
 $\omega_1=1, \omega_2=1, C_s=20, K_{d2}=0.8, K_{d1}=0.1, C=0.1, a_1=100, n=0.6$

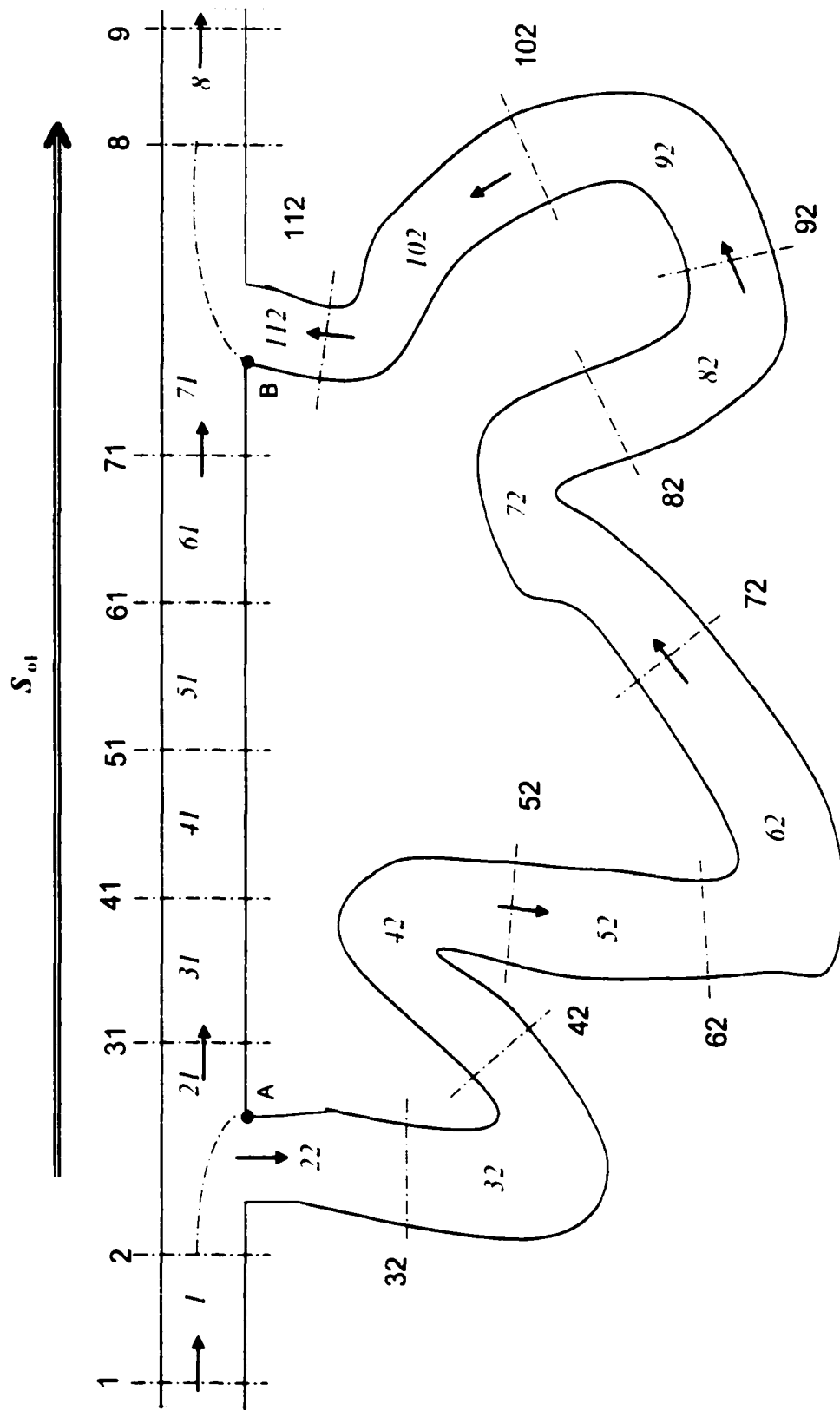


Fig. 5.8 Irrigation Network

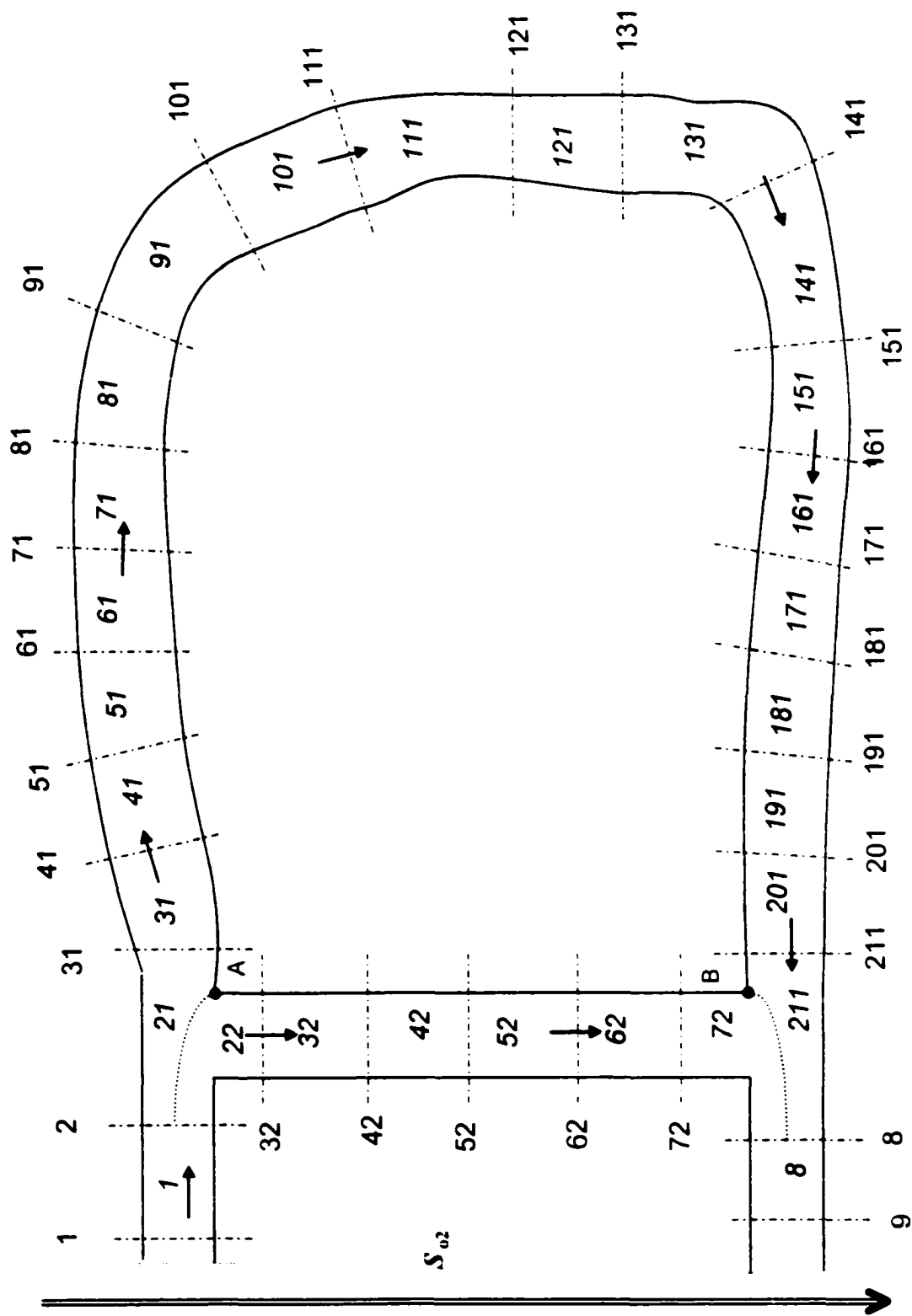


Fig. 5.9 River Cutoff

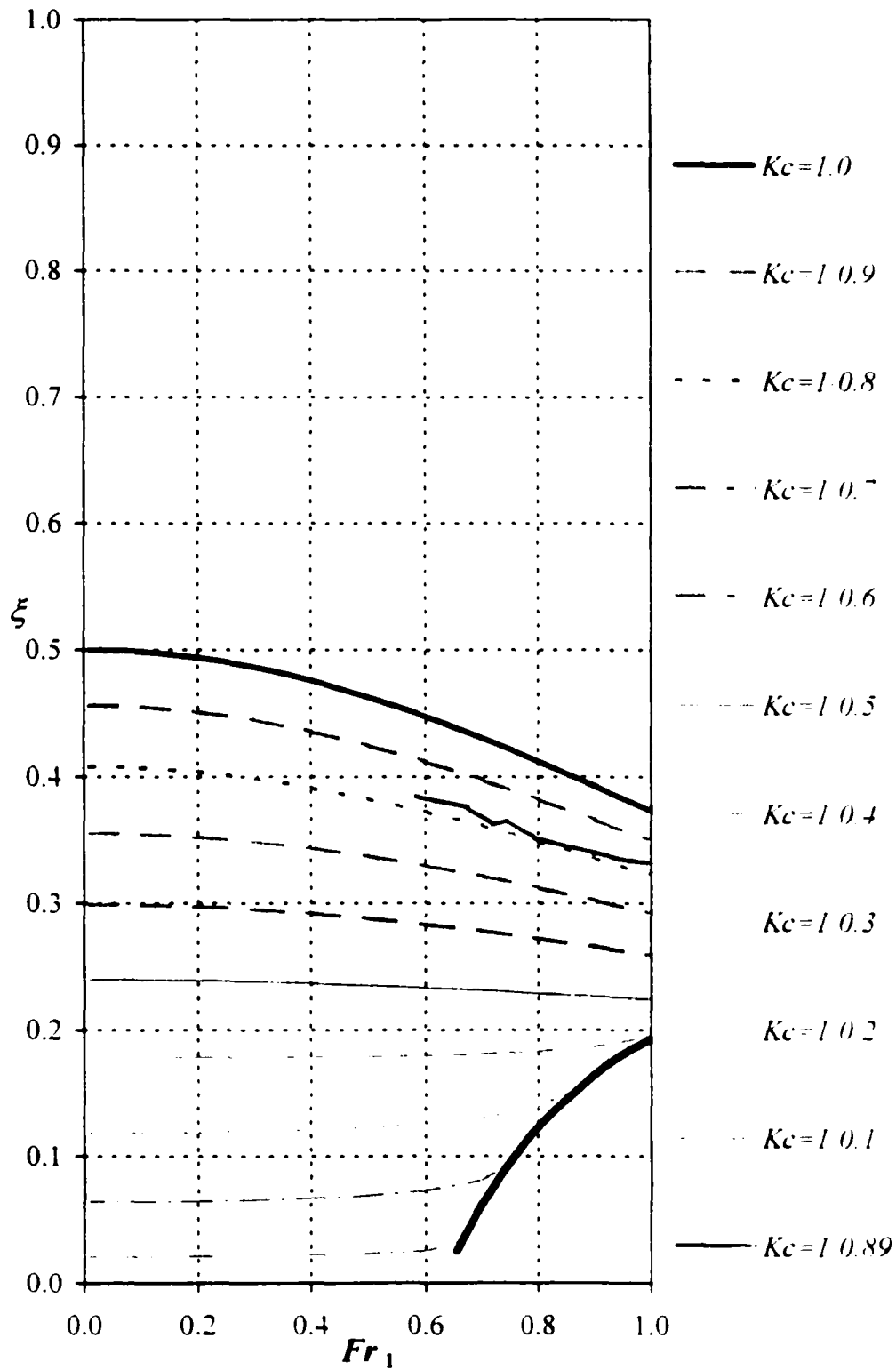


Fig. 5.10 The Variation of ξ with the Upstream Froude Number for the Dividing Junction in the Irrigation Network

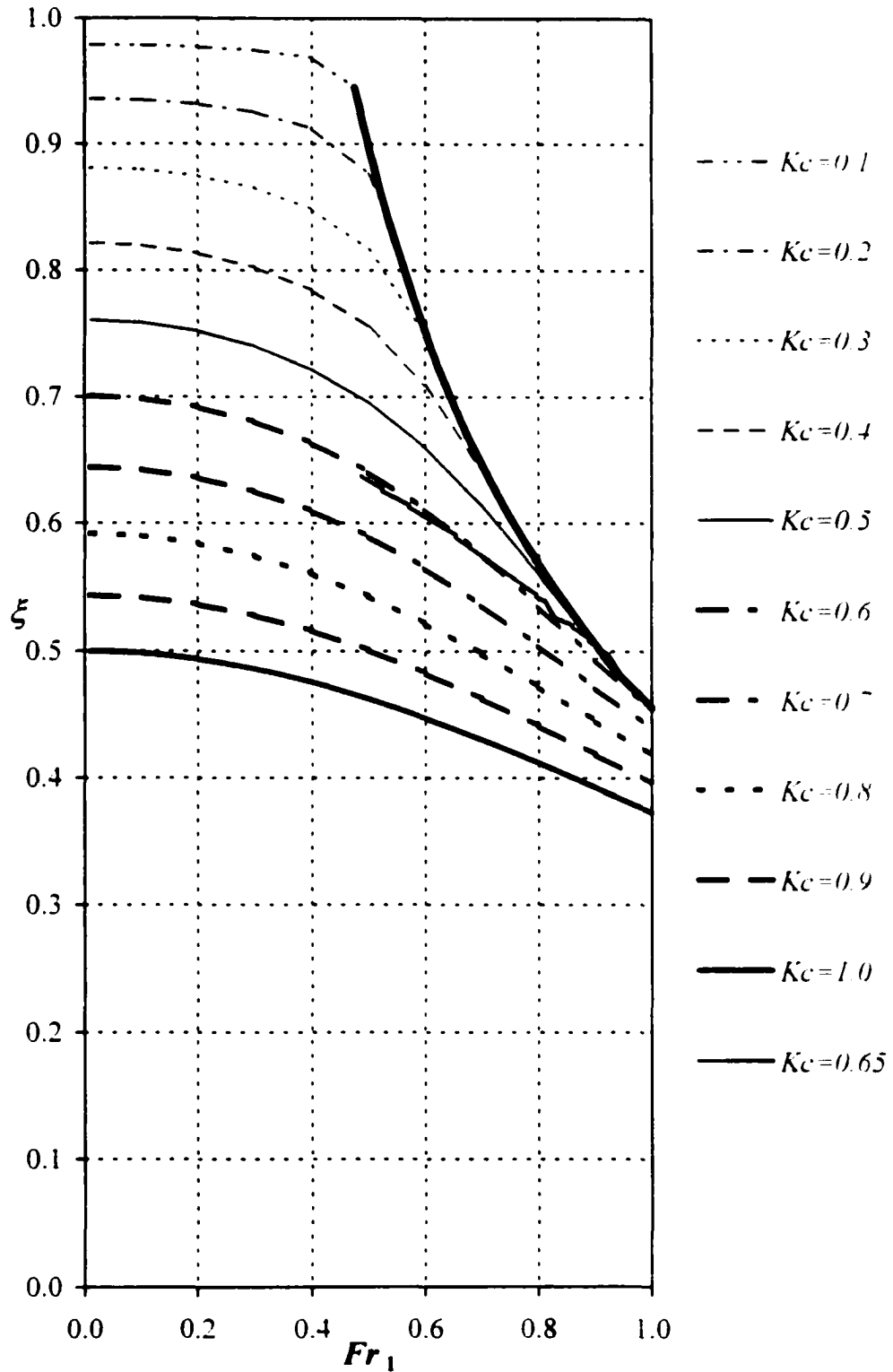


Fig. 5.11 The Variation of ξ with the Upstream Froude Number for the Dividing Junction in the River Cutoff

Chapter 6

Conclusions and Recommendations

In chapters 3 and 4 two models providing the interior boundary conditions handling combining and dividing junctions, respectively, were developed. In chapter 5, the implementation of these models into an open channel network was presented. This chapter presents a brief discussion on the models' contribution as well as recommendations for future research.

Chapter 3 presented the development of a one-dimensional model that provides the interior boundary conditions governing subcritical combining junction flows. Two control volumes were considered: one for the main channel flow, and the other for the lateral channel flow. Conservation of longitudinal momentum was applied to each control volume in the respective streamwise directions. Given the inflow discharges and a downstream boundary condition, the model could be used to calculate the upstream depths for each of the incoming channels.

The interfacial shear force between the two control volumes, the separation zone shear force acting on the lateral channel control volume, the weight component in the direction of the slope, and the boundary friction force were accounted for in the analysis. Two shear coefficients were calibrated, using the available experimental data, for the different junction angles, to evaluate the interfacial and separation shear forces. It was found that the variation in these coefficients was independent of the discharge ratio and the downstream Froude number but was dependent on the angle of intersection. From this

it was tentatively concluded that, in general, the coefficients were dependent on junction geometry, but not on flow. A comparison between the predictions of the model and those of the current energy approaches handling junctions in network models showed that the proposed model give better agreement with the experimental data.

A comparison between the proposed theory and existing momentum based approaches was performed. These existing approaches relied on the assumption of equal upstream depths and empirically accounted for the contribution of longitudinal momentum from the lateral channel. The comparison showed that the proposed model predictions were either as good as the other theories or rather superior at high discharge ratios. The advantage of the proposed theory is that it models almost all of the physical effects involved, such as the boundary friction forces, which were neglected in all of the other theories, and thus it can be scaled up to real world applications. The most important contribution of the model is to propose using two curvilinear control volumes and not to rely on the equal upstream depth assumption. Further, the application of the momentum principle in the streamwise direction allows the model to be easily implemented in network models and makes handling of the junctions consistent with that of the channel reaches.

Chapter 4 presented the development of the dividing junction flow model. The objective was to develop a model consistent with that for combining flows. Therefore, the junction was divided into two control volumes. Conservation of momentum was applied to each of the two control volumes in the respective streamwise direction together with overall mass conservation. Given the upstream Froude number and each of the main and

the lateral channel downstream depths, the model equations could be solved for the discharge ratio and the upstream depth.

In the dividing junctions the flow mechanism at the junction eliminates the interfacial shear forces. However, separation zones in the lateral channel and, for some cases, in the main channel as well, and centrifugal effects were reported in the literature. Therefore, these shear forces and the centrifugal pressure force were included in the analysis. Two separation shear coefficients and a centrifugal coefficient were introduced to facilitate the computation of these forces. Experimental measurements from the published literature were used to explore the variations in these coefficients with the different parameters governing the flow such as the upstream Froude number, the discharge ratio, the junction angle and the width ratio between the lateral channel and the main channel.

It was found that the predictions of the proposed momentum approach gave good agreement with the experimental measurements. Including the lateral channel separation zone was found to have a significant effect on the accuracy of the discharge split computations. The three dividing flow model coefficients were found to be independent of the discharge ratio for limited ranges of the upstream Froude number. They mainly varied with geometry; however, no trend for this variation could be deduced. In practice, these coefficients should be treated as calibration coefficients. For real world situations, the variations in the depth and the velocity cause small changes in the values of the upstream Froude number, therefore it is recommended that the coefficients be calibrated for certain geometry at known flow conditions and then the same values could be applied for different flow situations.

A comparison between the proposed theory and previous momentum theories proved the superiority of the proposed approach especially for high downstream depth ratios. A comparison between the currently used energy approaches which handle junctions in network models and the proposed momentum approach showed that the predictions of the momentum approach for the discharge ratio and the main channel depth ratio were better than these energy approaches.

Chapter 5 presented two applications for the models. The first was a design chart that could be developed for any dividing open channel junction after calibrating the shear and centrifugal coefficients. The chart facilitates computing the discharge split for any set of upstream and downstream boundary conditions occurring at this junction. These charts also indicate the conveyance ratio between the downstream channels at which the discharge split becomes independent of the upstream Froude number. In the second application, the implementation of the two junctions' models into an open channel network was presented. Two networks were considered for this application. The variation of the discharge split with the Froude number in each network was plotted and compared to one of the design charts developed in the first application. The significance of the dividing and the combining flow coefficients was assessed. Further, comparisons between the application of the momentum model equations, the equal water surface elevations and the conservation of energy at the junctions were performed. It was found that the variation of the discharge split with the upstream Froude number for the dividing junction in the network model conforms to the design chart. The dividing flow coefficients were found to be more significant than the combining flow coefficients. A

discrepancy in the discharge split was noted between the momentum approach and the two energy approaches. Further, this discrepancy increased as the variation in the discharge split with the upstream Froude number of the dividing junction increased.

Finally, the interior boundary conditions handling junctions that were developed in this study can be incorporated, as an option, into steady open channel network models. This can be used in validating the approach on real world situations. The model is expected to achieve results that are either as good as the currently used approaches or may be even superior since it is based on the physical effects in the problem. Further, this implementation will be a foundation on which the unsteady flow extension of the model can be built.

Recommendations for Future Research

With the addition of terms for storage of mass and momentum, the present models could be readily extended to an unsteady dynamic junction model. Conceptually, the simple junction condition of mass balance (no storage) and equal water surface elevations would now be applied across the boundary between the two junction control volumes, and the adjacent channel control volume (or computational cell). The two junction control volumes could then be treated as regular channel cells, albeit with consideration of variable width and extra interaction terms. Unfortunately, no experimental data is available at this time for verification of such a model.

It is recommended that an experimental study that focuses on investigating the different forces discussed in the present study be undertaken. This study should cover wide ranges of the flow parameters such as the discharge ratios and Froude numbers.

Also different junction geometries and rare situations, such as obtuse angled intersections and lateral channel width ratios that are greater than 1, should be investigated. This will provide an insight into the different models for these forces, and a better understanding for the parameters affecting the coefficients associated with them.

Field data is required to assess how the model scales up to real world situations. This will also help in understanding the significance of the different forces as the aspect ratio increases. These data can be used to validate the assumptions of uniform velocity distributions and hydrostatic pressure distributions and the importance of the boundary friction forces and gravitational forces.

Open channel network data is needed to verify the implementation of the two junction models into open channel networks. The data can be used to assess the quality of the results obtained when incorporating this model and comparing it with the energy based currently used approaches.

The model developed in this study can be considered a work base for a dynamic unsteady flow junction model. However, unsteady flow data is required for validating that model. Typically field data are difficult to obtain, but experimental data for unsteady combining and dividing junctions with more dynamic flow situations are valued.